

**Land-surface and boundary layer processes
in a semi-arid heterogeneous landscape**

Promotor: Prof. dr. A.A.M. Holtslag
Hoogleraar in de Meteorologie en Luchtkwaliteit

Co-Promotor: Dr. H.A.R. de Bruin
Universitair hoofddocent bij de leerstoelgroep
Meteorologie en Luchtkwaliteit

Samenstelling promotiecommissie:

Prof. Dr. A.-S. Smedman – Uppsala Universitet, Uppsala

Prof. dr. R.A. Feddes – Wageningen Universiteit

Prof. dr. P. Kabat – Alterra, Wageningen

Dr. ir. B.J.J.M. van den Hurk – Koninklijk Nederlands
Meteorologisch Instituut, De Bilt

Land-surface and boundary layer processes in a semi-arid heterogeneous landscape

Anne M. Jochum

Proefschrift
ter verkrijging van de graad van doctor
op gezag van de rector magnificus
van Wageningen Universiteit,
prof. dr. ir. L. Speelman,
in het openbaar te verdedigen
op woensdag 14 mei 2003
des namiddags te vier uur in de Aula.

ISBN 90-5808-824-3

Front cover:
Aerial photograph taken onboard the DLR Falcon flying over the EFEDA area

per me

אמ אין אני לי, מי לי?

אמ אין אכשו, מתי?

שלמה

Preface

There is a saying that all roads are leading to Rome. Well yes, some are shorter and some are longer. It seems that I took the long one... And after all, I literally went to Rome shortly after finishing the first draft of this thesis, but that is another story. Infatti sono tornata lì, tornata a casa dopo di tanti anni... grazie, Roma, per accogliermi tanto bene!

No thesis without (co-)promotors and of course, I had the chance and the luck to have the best ever... Henk, let me express my deep gratitude for being a colleague, co-promotor, and friend (in chronological order), thanks for bearing with me all the way. I thank Jon Wieringa for being my initial promotor. And thank you very much Bert, for taking over readily and for your support and patience ever since.

EFEDA would not have happened without the efforts of numerous colleagues from many countries and certainly not without the coordinating effort of Hans-Jürgen Bolle. Many further essential contributions range from the farmers in La Mancha, who offered their land for mast installations, to the Staff of Chiefs of the Spanish Air Force, who gave our EFEDA flights first priority in one of their main training airspaces.

I thank my EFEDA colleagues who have generously provided their data, most notably among them Joël Noilhan (surface dataset), Pierre Bessemoulin (radiosonde data), and Norbert Kalthoff (radiosonde data).

Thanks to Alfonso Calera for providing his landuse classification and lots of insight on vegetation phenology of the area.

Thanks also to Ernesto Rodríguez for providing the HIRLAM data.

The EFEDA field phase and analysis was partly funded by the European Commission under its Forth Framework Programme (various contracts). Some the work described in Chapter 7 was performed under EFEDA follow-up contracts (ENV4-CT95-0094, ENV4-CT97-0683) of the European Commission.

Many people at DLR have contributed in one way or the other to what I finally was able to achieve in EFEDA. To begin with, and a long time before EFEDA, thanks to Manfred Reinhardt for introducing me into the art of airborne observations and thanks to Hermann Willeke for patiently teaching me the art of landing, which was infinitely more difficult than flying, at least for me...

A large number of former colleagues at DLR had their part in the EFEDA airborne observations. In fact, too many to mention them all. Claudia Strodl, Gertrud Mergner, Robert Baumann, Reinhold Busen, Hans Fimpel, and Norbert Entstrasser jointly elaborated the airborne atmospheric data and contributed to the high quality of the Falcon in-situ dataset. Christoph Kiemle carefully processed the airborne lidar dataset.

Thanks go also to Jörg Hacker who provided his aircraft data analysis software, Larry Mahrt for his flux quality control software, and last but not least, Henk de Bruin for his coupled canopy-mixed-layer model.

Duivendaal 2 has been a very pleasant place to stay. The house has a wonderful atmosphere and the hospitality of its "inhabitants" has made it easy for me to feel at home. Thank you all for patiently speaking English with me after so many years of still not being able to communicate in Dutch! I would like to thank my former roommates, Reinder for teaching me many things about the Netherlands and Miao for teaching me about China. Thank you, Kees, for always being ready to help and always being able to find a solution, even though my notebook only spoke Spanish. There are so many reasons for thanking you, Gerrie, and it has always been a pleasure to be with you, not only during cold winter days when I could go downstairs to warm up in your office.

Mijn Nederlands is helaas niet goed genoeg om mijn samenvatting zelf te schrijven, maar gelukkig wel goed genoeg om Gerrie en Bas hartelijk te danken voer het vertalen ervan!

Special thanks go to my "paranimfen". At some point in time, each of you has been a true usher for me. Berenice, thank you for reaching out many years ago, so we could start building a set of strong bridges between "Oberpfaffenhofen" and "Duivendaal 2" and "Albacete". Hendrik, gracias por estar allí en el buen momento, para reconectarme con el mundo andino y unos cuantos más. Now, we are all coming full circle...

All those in my private world, you have supported me in many ways, thanks for being part of it and thanks for being there.

Contents

1. Background and objectives	1
1.1 General context and perspective	1
1.2 Aspects of land-surface heterogeneity	2
1.3 Observations of grid-scale fluxes in heterogeneous landscapes	5
1.4 Organization and roadmap	8
2. Consolidated datasets	10
2.1 Characteristics of the EFEDA area	12
2.2 Surface datasets	16
2.3 Aircraft datasets	18
2.4 Radiosonde datasets	24
2.5 Airborne lidar datasets	25
2.6 Composites and selection of case studies	26
3. Boundary layer budgets	29
3.1 Introduction	29
3.2 Approach	29
3.3 ABL vertical structure and state	33
3.4 Time-rate-of-change term	36
3.5 Vertical flux divergence	39
3.6 Vertical radiative flux divergence	47
3.7 Horizontal and vertical advection	49
3.8 Discussion and conclusions	51
4. Scales in flux parameterization	57
4.1 Landscape scales and forcing	57
4.2 ABL scales and heterogeneity regimes	58
4.3 Scale dependence of exchange coefficients	64
4.4 Conclusions	71
5. Flux aggregation and regional fluxes	72
5.1 Aggregation of surface flux observations	72
5.2 Area-averaged fluxes from aircraft observations	77
5.3 Regional fluxes from a conservation approach	81
5.4 Synthesis and comparison of grid-scale fluxes	87
5.5 Conclusions	91
6. Performance evaluation of the HIRLAM land-surface and boundary layer description	93
6.1 Introduction	93
6.2 Validation layout	95
6.3 ABL structure and profiles	98
6.4 Surface thermodynamic cycle	102
6.5 Surface radiation and energy budgets	106
6.6 Conclusions	115
7. Practical applications and perspectives	116
7.1 Water vapor datasets for atmospheric correction of optical satellite data	116
7.2 Assessment of water vapor datasets	118
7.3 Impact of water vapor errors on retrieved biogeophysical variables	122
7.4 Guidelines for finding the regionalbest choice water vapor data	124
7.5 Conclusions and perspectives	125
8. Summary and outlook	126

Annex A. Example of spectral analysis of airborne turbulence data	131
Annex B. The mixed layer model	133
Annex C. Landuse classification of the EFEDA area	135
Annex D. List of acronyms	136
References	137
Samenvatting	150
Curriculum vitae	155

1 Background and objectives

"En un lugar de la Mancha, de cuyo nombre no quiero acordarme..."
(*"Somewhere in La Mancha, I won't remember the name of the place..."*)

These are the first lines of the famous epic of Don Quijote (Cervantes, 1605). They might be a good start for this thesis as well, even though in our case the names of the places are well known and well remembered by all who shared this experience and by many more. Back in 1987-1990 an international group of scientists - notably among them the co-promotor, but also the author of this thesis - designed a large field experiment, which later became famous under the name of EFEDA (European Field Experiment in a Desertification-Threatened Area, Bolle et al., 1993).

Just like the story of Don Quijote, EFEDA has been a - sometimes arduous - learning endeavor. Both the hero and the EFEDA scientists set out into a challenging environment, well equipped with concepts and tools. Both encounter numerous adventures that lead the way to a new level of understanding and refined tools. As we will see, the EFEDA area presents indeed quite a few challenges to the observer and modeler.

1.1 General context and perspective

Processes at the atmosphere-land/biosphere interface mark our environment, our energy and food supply, our health, our habits of life, and our economy.

Land covers a total of 35% of the Earth's surface. Processes at the land-surface represent one of the most important climate forcings. Understanding, modeling and monitoring the physical, biological, and chemical processes occurring at the land-atmosphere interface is, therefore, crucial for the analysis and prediction of regional and global weather, climate, and climate change. A thorough understanding and high-quality monitoring capability of land-surface processes is also needed for the sustainable management of natural resources. This includes disciplines and/or economic sectors as diverse as tourism, energy supply, air pollution, water use, rural development, and agriculture.

Land-surface and atmospheric boundary layer (ABL) processes have been studied intensively (through observations and numerical and laboratory modeling) for decades, with results filling libraries. At the local scale, the early ABL experiments led to the development of the powerful framework of surface layer (SL) and mixed layer (ML) scaling and similarity theory (summarized by Stull, 1988; Sorbjan, 1989; Garratt, 1992). The advent of instrumented aircraft (e.g., Lenschow, 1986) provided access to the horizontal dimension and variability. At the same time, increasing contributions of remote sensing allowed for mapping a range of surface parameters (e.g., Myneni et al., 1995; Norman et al., 1995).

The issue of land-surface heterogeneity and its impact on ABL processes has received considerable attention ever since. Internationally coordinated research efforts in this area have focused for many years on extensive field experiments involving considerable resources in terms of ground-, aircraft-, and satellite-based observation systems. The driving forces were the global weather and climate modeling community on one hand (seeking improved and calibrated land-surface parameterizations) and the remote-sensing community on the other

(seeking calibration of satellite observing systems and algorithms to derive land-surface-related parameters).

Jointly, the World Climate Research Program (WCRP) and the International Geosphere Biosphere Program (IGBP) have played a central role in defining and implementing these land-surface experiments (LSEs). Their strategic importance lay in providing process understanding and very complete datasets for a wide range of biomes and terrain heterogeneities (Feddes et al., 1998; Jochum et al., 2000). In recent years the experimental philosophy has been extended to large river basin areas.

The general context of this thesis is given by one of the major LSEs, the European Field Experiment in a Desertification-threatened Area (EFEDA), which was conducted in 1991 and 1994 in a semiarid landscape in Spain (Bolle et al., 1993). It fills an important gap in the general LSE picture by addressing a unique area of typically Mediterranean heterogeneous land-use and of added complexity due to the simultaneous presence of mountains and the non-local influence of Mediterranean sea-breezes frequently penetrating inland.

We will look here at EFEDA from a grid-scale perspective, i.e. at the whole area of about 60 km by 80 km (in contrast to most previous studies). This work aims at providing a synthesis covering the full range from basic physical process analysis to practical applications. As such, it answers a number of open science questions and demonstrates the direct usefulness of EFEDA results in very practical issues.

1.2 Aspects of land-surface heterogeneity

Interest in land-surface processes comes from a wide range of disciplines, each addressing specific research questions and scales of heterogeneity and bringing in specific tools and perspectives. Within the atmospheric sciences, it is the micrometeorology, turbulence, and ABL community and the modeling community at any scale, in particular numerical weather prediction (NWP) and climate modeling. The remote sensing community is developing and calibrating algorithms to retrieve bio-geophysical parameters from satellite image data. To mention only a few selected aspects, the hydrology community has brought in the concept of landscape units rather than regular grid elements and plant physiology was instrumental for the development of the big-leaf and resistance framework. Having had the least immediate need for upscaling, soil physics holds some of the last open issues in aggregation (Kabat et al., 1997).

The challenge of the past decade was in scaling-up from local to regional scales. The challenge of the decade to come will be to put in practice the lessons learned and to provide well structured, high-quality, operational 4D global gridded datasets, along with simple tools and models for using them. The only way to achieve this relies heavily on NWP models and remote sensing-derived bio-geophysical data, emphasizing again the need for physically realistic surface schemes for the former and retrieval algorithms for the latter. With the increasing use of remote sensing-derived information in NWP models, both are intrinsically coupled.

Surface heterogeneity occurs on a wide range of scales, making it impossible to take into account individually. So there is no question about the necessity of spatial averaging and the need of adequate methods to achieve it. The main drivers in this area have been the NWP and climate models. Their starting point is the need to obtain grid-scale fluxes in grid cells with heterogeneous surface

properties and the desire to use a bulk framework for that purpose. So this will be the starting point for this brief review as well.

Any land surface scheme in mesoscale or large-scale NWP models has the task to diagnose the surface fluxes of heat, moisture and momentum from temperature, moisture and wind at the first prognostic model level, from atmospheric forcing (provided by the radiation scheme and precipitation), and from the model's physiographic-climatological database. Each surface scheme treats the three interrelated compartments soil, vegetation, and atmospheric surface layer in an interactive way. The current parameterizations of the soil and vegetation compartment vary over a wide range of complexity (from SiB requiring 19 input parameters (Sellers et al., 1986) to ISBA using 5 input parameters (Noilhan and Planton, 1986)). The surface layer part always uses a bulk transfer scheme based on Monin-Obukhov similarity.

Similarity theory has been used to parameterize turbulent transfer in numerical models from the mesoscale to the global scale. With significant surface forcing heterogeneity, however, the validity of the local similarity relationships cannot be automatically extended to larger areas, such as model grid elements of 10-100km size. Heterogeneous landscapes present the formidable challenge of finding spatial averaging concepts that preserve most of the simple structure of local parameterizations without missing the essence of the physics of non-linear interacting processes. This is commonly referred to as the aggregation problem.

It has early been recognized that the type of organization of the surface makes the essential difference. Initially, two types of landscape heterogeneity were distinguished by de Bruin (1987), Shuttleworth (1988) and Raupach (1991). The nomenclature varies between these and further authors, but the underlying concept is very similar. The first distinguishing criterion is the vertical extension of the response of the air flow to heterogeneous surface patches. "Disorganized surfaces", "Type A surfaces", "microscale heterogeneity", "statistical heterogeneity" all refer to small-scale patchiness conditions, where the response of the air flow is confined to the layer below the blending height (see below). "Organized surfaces", "Type B surfaces", "macroscale heterogeneity" denote landscapes where patches are "seen" by the air flow in part or all of the ABL. Further distinction within the latter regime is made according to the potential interaction between patches, e.g., significant local advection or thermally generated secondary mesoscale circulations (Raupach, 1993; Mahrt, 1996).

Numerous individual studies were performed on specific aspects of the aggregation task. Three attempts have been made to establish a general framework. Each of them is indeed general in some sense, but none of them covers all relevant aspects. Raupach (1995) identifies three major heterogeneity regimes and gives a rough estimate of the partitioning length scales. He proposes a set of aggregation tools for either case, basically a matching-term parameter aggregation scheme and an ABL slab model to obtain aggregated fluxes. Hu and Islam (1999) develop a general framework based on mathematical optimization techniques. They indeed provide an objective, physically-based framework from which to derive parameter aggregation rules for the disorganized heterogeneity regime. This allows them to integrate and evaluate previous work and represents a clear step forward, beyond the multitude of proposed approaches. However, it is still based on the assumption of equal importance of all terms in the surface energy balance. Mahrt (1996) takes up the definition of the heterogeneity regimes and gives practical estimates of the partitioning length scales (still in the sense of "order of magnitude" quantities). Without entering in the details of soil/vegetation-parameter aggregation, he focuses on the surface-layer backbone of land-surface schemes, i.e. on the bulk transfer scheme. He proposes a

generalized form of that scheme by including the subgrid mesoscale velocity in the velocity scale (similar to the convective velocity scale introduced by Beljaars, 1994). This is in principle applicable to all heterogeneity regimes, but generates the need to determine more parameterization variables. He also addresses the fundamental question of the practical handling of the aerodynamic temperature and moisture in NWP surface schemes and beyond. Sun et al. (1999) clarify the issue and show that significant errors are introduced in the surface fluxes whenever the aerodynamic surface variables are replaced with readily measured substitutes like, e.g., radiometric surface temperature. These latter are not consistent with the bulk scheme, which is valid in the surface layer, but not in the roughness sublayer.

At the same time and in parallel to theoretical work, (still tentative) parameter aggregation rules (e.g., Shuttleworth, 1991) were applied and used in practice. The fundamental question of how to provide the reference standard for their validation remains unresolved (see section 1.3 below).

On a practical level, any spatial aggregation task consists of three steps:

1. to identify the heterogeneity regime,
2. to select the aggregation approach accordingly, and
3. to provide the corresponding physiographic characterization of the surface patches.

When it comes to spatial averaging (i.e., step 2), disorganized surfaces can be treated in a statistical way. Wieringa (1986) introduced the concept of the blending height, which later was formalized by Mason (1988) and extended to non-neutral conditions by Wood and Mason (1991). Much effort has gone into the determination of effective parameterization parameters (roughness lengths, transfer coefficients). Blyth (1995) uses the architecture of a sparse-canopy SVAT model to incorporate heterogeneous patches (in what she calls a "user-friendly version of the blending height method"). It does not need effective parameters, but introduces instead new structural parameters equally difficult to determine.

The situation is different for organized heterogeneity. Effective parameters are still used in many schemes. Sun and Mahrt (1995a, b) and Frech and Jochum (1999) show that the effective exchange coefficients frequently depend on averaging scale. Subgrid-scale correlation of flux and transported quantity seems to be one of the criteria for scale dependence, another being the degree of subgrid variability of the surface-air temperature difference. On a pragmatic level, several numerical modeling studies have demonstrated that the results of parameter aggregation and flux aggregation are not dramatically different (e.g., Wood and Lakshmi, 1993; Noilhan et al., 1997).

An interesting alternative consists in accounting for sub-grid parameter variability by means of probability density functions (PDF), as proposed by Avissar (1992) in his statistical-dynamical approach. The most critical parameters to be considered are soil wetness, leaf area index (LAI) and roughness length (Avissar, 1992; Rodríguez-Camino and Avissar, 1999). The practical drawback, however, is the heavy demand on computing resources to carry along the PDFs of several parameters in the surface scheme for all grid elements.

Among the numerical modeling community Avissar and Pielke (1989) were the first to suggest the idea of treating each patch (or tile, Koster and Suarez, 1992a) separately in the lowest grid box (i.e. between the surface and the first model level). A similar concept had been launched by Wood et al. (1988), who proposed the REA (representative elementary area) as the fundamental building block for hydrological modeling. Last-generation NWP models have incorporated the tile

approach in their surface schemes, which also meant to include a vastly extended physiographic-climatological database for the new land-use classes. This still leaves the transition regime (where inter-patch advection is significant) and all kinds of secondary mesoscale circulations unaccounted for. The unified treatment proposed by Mahrt (1996) opens a physically-based formal way to include all these effects, but the task of determining some of the parameterization variables from a range of field observations remains open.

The potential of remote sensing combined with local SVAT models as a flux aggregation tool has been demonstrated for a number of cases (e.g., Gao, 1995; Peters-Lidard et al., 1997; Arain et al., 1997; Doran et al., 1998). SVAT models well calibrated for a range of biomes, like SiB (Sellers et al., 1986) and BATS (Dickinson et al., 1986) were used to calculate fluxes on a grid of 6-50 km spacing, depending on the area. Atmospheric input data for the SVAT were obtained from special downscaling algorithms, which distribute observed or NWP-derived values according to terrain features. Soil and vegetation input data for the SVAT were obtained from remote sensing derived NDVI or SR (simple ratio) (e.g., Gao, 1995). The resulting surface flux maps were shown to be able to reproduce the essential processes and patterns.

1.3 Observations of grid-scale fluxes in heterogeneous landscapes

The concept of land-surface experiments (LSEs) was developed with the objectives (Jochum et al., 2000, Feddes et al., 1998)

- to document a GCM grid-scale volume subtending the surface;
- to sample surface exchanges, and study their aggregation from sub-grid scale to landscape units;
- to collect and validate satellite data for land-surface models;
- to validate surface-atmosphere models at 10-100 km scales.

Initially motivated by the need to better understand the aggregate behavior of the landscape in the formation of weather and climate (HAPEX-MOBILHY), and by the wish to exploit the potential of remote sensing in the same context (FIFE), a series of LSEs was implemented through the Joint IGBP/WCRP Working Group on Land-Surface Experiments, to cover the ecosystem and climate zones of most interest for global change. Table 1-1 shows the timing, location and spatial scale.

Table 1-1. Major land-surface experiments (adapted from Jochum et al., 2000).

<i>name</i>	<i>Spatial scale</i>	<i>location</i>	<i>year</i>	<i>reference</i>
HAPEX-MOBILHY	100 km	France	1986	André et al. (1988)
FIFE	10 km	U.S.A. (Kansas)	1987, 1989	Sellers et al. (1992)
EFEDA	100 km	Spain	1991, 1994	Bolle et al. (1993)
HAPEX-Sahel	100 km	Niger	1992	Goutorbe et al. (1996)
BOREAS	1000 km	Canada	1993-1994	Sellers et al. (1995)
NOPEX	100 km	Sweden, Finland	1994-1998	Halldin et al. (1998)
LBA	4000 km	Amazon basin	1998-2003	Nobre et al. (1996)

Each LSE involves detailed ground-based measurements (micrometeorology, soils, vegetation) at selected sites, research aircraft with in-situ atmospheric and remote sensing instrumentation, aerological soundings, and a variety of satellite-based observations. The earlier LSEs were conducted in campaign mode, covering at best a full growing season, and focused on hydrometeorological issues in the land surface atmosphere interactions. The more recent (NOPEX, BOREAS) already extended their time frame as also more hydrological and ecological aspects grew in importance. The Large Scale Biosphere Experiment in Amazonia (LBA) is the example of the culmination of this trend. It studies the integrated functioning of Amazonia as a regional entity. It specifically addresses the effects of changes in landuse and climate on the biological, chemical and physical functions of Amazonia, including the sustainability of development in the region and the influence of Amazonia on global climate. This involves studies of the multi-annual dynamics of the tropical forest biome and its links with the global energy, water, carbon and other biogeochemical cycles (Nobre et al., 1996).

Several large field experiments beyond the official grouping of LSE are also contributing invaluable information to the understanding and parameterization of heterogeneous land-surface processes. The California Ozone Deposition Experiment (CODE) provides observations over strips of irrigated land (Mahrt et al., 1994). The Southern Great Plains Cloud and Radiation Testbed (SGP CART) hosted extended observations over mesoscale heterogeneous land (Hubbe et al., 1996; Doran et al., 1998). The most recent example is CASES (Cooperative Atmosphere-Surface Exchange Study, LeMone et al., 2000; Yates et al., 2001) conducted in a 3600 km² watershed in Kansas. The latter two provide highly spatially resolved observations across inhomogeneous areas which allow for investigating secondary mesoscale circulations.

Obviously, the analysis of observations from this kind of field experiments follows along very similar patterns, modulated by the regional context of ecosystem, climate, and (occasionally) topography. Recurring focal themes are the land-surface climate at selected supersites and its spatial variability across the area, ABL budgets and regional flux estimates, SVAT and mesoscale model validation, remote sensing, and aggregation studies. In a first instance, the results from these studies apply individually to each given field experiment and can often not be generalized. At the same time, they each contribute yet another piece of puzzle to the general understanding and modeling of land-surface processes on a global scale and they each represent an "anchor area" of ground truth data supporting global gridded datasets.

Aircraft are the prime observational upscaling tool and they are used to assess the horizontal flux variability. The design of the corresponding flight patterns is a science task and usually requires a compromise between the number of sampled surface strata and statistical significance (i.e., the number of sampled relevant eddies), which are inversely proportional. Regional differences in heat, moisture, and momentum fluxes were documented, e.g., for HAPEX-MOBILHY (Mahrt and Ek, 1993), HAPEX-SAHEL (Said et al., 1997), EFEDA (Jochum, 1993b; Michels and Jochum, 1995), NOPEX (Frech et al., 1998; Samuelsson and Tjernström, 1999), BOREAS (Desjardins et al., 1998). All have in common that at flight levels in the range of 0.05-0.15 z_i significant flux variations were detected at scales of major landscape features. In the earlier field experiments, it often occurred that surface fluxes were underestimated by aircraft. Much has been speculated about these flux-aircraft-tower intercomparison results. Initially, the design of LSE flight patterns did not always take into account the need for aircraft tracks to be long enough to sample all relevant eddies, a fact well known in the boundary layer community (Lenschow and Stankov, 1986; Lenschow et al., 1994). A great deal of early FIFE results can be explained this way. Generally, research on turbulence

aircraft sampling needs has made considerable progress since then and the uncertainties and limitations are well described (Grossman, 1992b; Mann and Lenschow, 1994; Mahrt, 1998). The remaining "underestimation" is closely linked to low level flux divergence, which is found frequently even over fairly homogeneous terrain (e.g., Gottschalk et al., 1999). Consequently, the assumption of a constant flux layer needs to be checked carefully in each case and more often than not, the flight level flux will need to be extrapolated to the surface by including the flux divergence. Grunwald et al. (1998) used a simplified version of the integral budget method proposed by Jochum (1993a) for that purpose and find good agreement within the range of uncertainties. The lessons learned here include ways to adequately sample all relevant scales and strata and to account for the flux divergence between the flight level and the ground by means of a budget analysis.

Radiosondes are able to "see" the regional flow and thus offer interesting possibilities to estimate the regional fluxes directly. Many related methods have been proposed. Mixed layer (ML) budget methods have been used widely, see Peters-Lidard and Davis (2000) and references therein. They follow the line of reasoning of McNaughton and Spriggs (1986) and de Bruin (1989) in developing a set of simplified ("slab-form") conservation equations for ML temperature and humidity. The second observational approach is based on similarity theory only, as developed by Brutsaert and Kustas (1985), Abdulmumin et al. (1987), and Munley and Hipps (1991). It was successfully applied to a variety of conditions, although in most cases it is difficult to specify the lower boundary conditions and in particular the roughness lengths. Brutsaert and Sugita (1991) extended the method by introducing the radiometric surface temperature in the calculation procedure, in order to remove some of these constraints. Since then, it has been applied in various configurations, see Sugita et al. (1997) for an assessment. Yet another approach uses radiosonde observations in the context of a simple ML growth model (Batchvarova and Gryning, 1994). Generally these simple methods are reported to work well in non-advective conditions. Hipps et al. (1994) include an adjustment for advection and subsidence, which makes his method applicable in more general conditions.

The most straightforward and simplest way to obtain grid-scale fluxes would, of course, be the averaging of surface observations. The basic requirements for this purpose are firstly, a representative coverage of all surface strata and secondly, an adequate classification to determine the areal weights from. Here is where remote sensing is able to make a significant contribution. Pelgrum and Bastiaanssen (1996) find a significant influence of the classification on the grid-scale fluxes. Notwithstanding, each surface station "sees" only its limited fetch area (or source area, Schmidt, 1994). This leaves the need to explore for each area again the question of Moore et al. (1993): "How well can regional fluxes be derived from smaller scale estimates?"

To answer this question, in the case of some field experiments an observational aggregation exercise was performed by comparing all available grid-scale flux estimates. André et al. (1990) were the first to address this from a combined observational and modeling approach using data from HAPEX-MOBILHY. Gottschalk et al. (1999) compare grid-scale fluxes for NOPEX obtained from five different methods. Radiosonde-based regional fluxes, weighted surface observations, and two mesoscale models (one hydrological and one atmospheric) give very similar results on cloud-free days, while aircraft-based heat fluxes are consistently lower. Significant low level flux divergence was observed there. Much less agreement is found whenever cloud cover provided an additional source of heterogeneity. Grunwald et al. (1996, 1998) compare weighted surface observation averages and airborne flux estimates for two sub-areas of the EFEDA

area (squares of 10-30 km sides). Including the low-level flux divergence helps them to match the flux estimates. These studies have all in common the case study view. Mahrt et al. (2001) start from a different perspective, pursuing the objective of delivering time series of observational aggregates for an entire season. They discuss a number of practical solutions to problems they find on the way to calculating area-averaged fluxes over the BOREAS area based on a combination of tower and aircraft observations. One of their main conclusions is the adjustment of weighted surface averages by means of aircraft-derived Bowen ratios. In any case, weighted surface observations are the only possible choice for the purpose of providing monthly or seasonal time series of aggregated fluxes for a given experimental area. The contribution of aircraft and other intensive short-term observations is vital to decide on potential adjustments to these values on the basis of detailed comparisons.

1.4 Objectives and roadmap

The grid-scale perspective of EFEDA shows us a semiarid, 60 km by 80 km area of heterogeneous landuse, surrounded by mountains, where regionally different boundary layers and inhomogeneous moisture fields were observed. This raises questions as to

- * the functioning of the ABL in this environment and the potential regional differences in the interplay of dominant physical processes;
- * the prevailing heterogeneity regimes and their potential implications on the applicability of parameterizations;
- * the appropriate area-averaging methods; and
- * the capability of NWP models to predict the surface and ABL processes in this environment.

This work aims at addressing these questions on the basis of a comprehensive observational dataset. In contrast to previous observational work, the grid-scale perspective is maintained throughout the analysis. The mesoscale modeling work of Noilhan (1996) and the remote sensing work of Bastiaanssen (1996) also covered the whole EFEDA area and beyond. Their results will be used for comparison.

The inherent goal is to go all the way from basic process studies towards final practical applications. Consequently, the work consists of the following steps:

- a) The unique EFEDA dataset is presented in Chapter 2. We are using here the full set of observations taken by over 30 groups. It includes a wealth of surface observations, radiosoundings, airborne flux measurements and airborne aerosol backscatter and water vapor profiling. A quality control and homogenization procedure is applied in order to achieve coherent site-specific and airborne datasets.
- b) The physical processes contributing to ML warming and drying/moistening are investigated by means of ABL budgets for part of the daytime diurnal cycle (Chapter 3). The full radiative flux divergence was measured by aircraft for the first time in an ABL budget study and is found to be significant. The heat and moisture flux divergence is analyzed in the framework of a ML slab model, where the entrainment closure parameters are derived from aircraft

observations. We analyze the budgets of two supersites separately and we discuss the relevance of the residual layer moisture structure for the results. Accurate high-resolution vertical humidity profiles play an important role here.

- c) In Chapter 4, the scales and types of heterogeneity are described in the framework of Mahrt (1996) and their impact on bulk transfer flux parameterizations is assessed on the basis of low-level aircraft observations. We find new evidence on the scale-dependence of moisture flux in the presence of surfaces with contrasting saturation deficit.
- d) Area-averaged heat and moisture fluxes for the whole EFEDA area and for several HIRLAM model grid cells are derived from observations in different ways. We identify the most appropriate landuse classification for the purpose of weighted averaging of surface flux observations in this type of Mediterranean landscape. Using results of the budget analysis, we derive area-averaged fluxes from aircraft observations. We also determine regional fluxes from radiosondes in a ML slab model framework. Based on the comparison of all approaches, we derive the methodology to obtain the consolidated EFEDA grid-scale flux dataset (Chapter 5).
- e) We use this new grid-scale dataset to evaluate the performance of the land-surface and ABL description of HIRLAM in Chapter 6. There we identify model shortcomings in several areas and propose a practical way to achieve substantial improvement of the model performance in this type of Mediterranean landscapes.
- f) In Chapter 7, we go one step further and show an example of practical applications of the results. We assess the performance of water vapor datasets from various sources in the atmospheric correction of optical satellite data and its impact on the retrieved biogeophysical parameters at the surface. There, we give recommendations on the best choice data for a given application.
- g) Chapter 8 contains the summary and addresses some perspectives.

2 Consolidated datasets

EFEDA was built upon the joint efforts of more than 30 research groups from 11 different countries (Bolle et al., 1993). In addition to the overall goal of EFEDA, each group had its individual objectives such that the observational strategy was an integrated overlay of these various aims. The resulting data (EFEDA, 1995) obviously bear the marks of the individual groups and some kind of homogenization is needed before a large subset of the total data is going to be used, as it is here. The purpose of this Chapter is twofold, firstly, to introduce the basic concepts of EFEDA and to summarize the information on the original data as far as needed here. Secondly, it serves to describe the homogenization procedure applied in the process of preparing the data for their use in the subsequent analysis, according to the objectives of this study as laid out in Chapter 1.

The general rationale of EFEDA (Bolle et al., 1993) followed along the lines of the early Land Surface Experiments (LSEs, see Chapter 1 and Jochum et al., 2000; Feddes et al., 1998). Its goal was to document the land surface state and processes in a GCM grid cell volume as in- and extensively as needed for the specific area and during a limited period of time. The observational strategy consisted of simultaneous measurements at three heavily instrumented "supersites", with instrumented aircraft and satellite remote sensing providing the observational link between these sites.

The EFEDA area was selected as to represent a GCM grid cell located in dry climate and characterized by flat terrain (yet surrounded by nearby mountains), with land uses covering natural vegetation as well as dry and irrigated agricultural lands, as typically encountered in all European Mediterranean countries. The three Intensive Study Areas ("supersites") were selected to represent these major land use types. The size of each supersite was defined to be about 10 km x 10 km, order of magnitude of previous small LSEs like FIFE or LOTREX, which were devoted mainly to remote sensing biophysical algorithm development ("ISLSCP-type", see Chapter 1). Thus, EFEDA was a combination of HAPEX/GCM- and ISLSCP-types, a configuration which was repeated successfully in second-generation LSEs like HAPEX-SAHEL, NOPEX, and BOREAS (see Chapter 1).

The observational period was selected as the entire month of June 1991, with June being the month of most actively growing vegetation and at the same time coinciding with the major dry-down after the spring rainfall. A second observational campaign was conducted during the three-months period of May-July 1994 in order to capture the full dry-down period, concentrating on the Tomelloso supersite only. Continuous observations from two anchor stations located at the two Southern supersites provide information on seasonal and annual time scales. The focus being on the whole EFEDA area, essentially the data from 1991 are used and described here. For specific purposes additional data from the anchor stations are used. They will be introduced and described where needed (Chapter 6). Data derived from remote sensing, other than from airborne lidar, are outside the scope of this thesis and therefore not described here.

Corresponding to the observational layout, a hierarchy of datasets have been derived and used. Table 2-1 summarizes the definitions and interrelationships. Following the overview and description of the major characteristics of the EFEDA area and the associated GIS-based database (section 2.1), the surface (2.2), aircraft (2.3 and 2.5), and radiosonde (2.4) datasets are introduced. The final section (2.6) provides the synoptic and other background material for the selection of case studies.

Table 2-1. Structural hierarchy of EFEDA 1991 in-situ datasets. T = Tomelloso; B = Barrax; R = Rada de Haro.

Observation type and aggregation or averaging level	Number / vegetation class / location	Sources, references
Local point observation: surface datasets		
Individual surface observation (mast)	8 masts on vine T	EFEDA CD-ROM, de Bruin et al. (1993), Berger (1997), Braud et al. (1993), van den Hurk (1996), Krikke (1994) à Section 2.2 B
	4 vetch T	
	1 bare T	
	2 irrigated crop B	
	2 fallow / bare B	
	2 natural R	
	1 vine R	
2 sunflower/ wheat R		
1-D horizontal line observation: aircraft datasets		
Individual aircraft observations	108 flight legs	Jochum et al. (1992, 1993b), Michels (1992), Jochum (1993b), Michels and Jochum (1995) à Section 2.3 B
Segmented aircraft observations	10 km segments of each flight leg	EFEDA CD-ROM, Jochum (1993b) à Section 2.3 B
1-D vertical profiling: radiosonde and airborne lidar datasets		
Radiosonde vertical profile	1 Tomelloso	EFEDA CD-ROM, Fiedler et al. (1993), Muniosguren (1993) à Section 2.4 B
	1 Barrax	
	1 Rada de Haro	
Segmented vertical profiles from airborne lidar/DIAL	Quasi-continuous (2-D) for aerosol	Jochum et al. (1992), Jochum (1993b), Kiemle et al. (1995) à Section 2.5 B
	5 km averages for water vapor	This Thesis, à Chapter 4 B
2-D horizontal area: averaged surface and aircraft observations		
Class-average surface observation (average within same vegetation class)	T vine	Linder et al. (1996), Moene (1992) à Section 2.2 B
	B bare	
	B irrigated maize	
	R natural	
Area-aggregate surface observation (aggregate of all vegetation classes within given area)	3 sites (T, B, R)	This Thesis, Linder et al. (1996) (T & R sites) à Section 2.2 B à Chapter 5 B
	6 NWP grid-elements	
	Whole EFEDA area	
Area-averaged aircraft observations	Barrax site	Grunwald et al. (1996)
	EFEDA area	This Thesis, à Chapter 5 B

2.1 Characteristics of the EFEDA area

The EFEDA experimental area is located in the region called La Mancha, part of the Castilian high plateau in the Southeast of Spain, at an average elevation of 700 m above mean sea level. It extends about 60 km in North-South direction and 80 km in East-West direction, respectively. The area is generally flat, with elevation variations of up to 100 m, but surrounded and influenced by mountain ranges. The distance to the mountains is 35 km from the South, 45 km towards the Northeast, and 40 km towards the Northwest. Figure 2-1 shows the EFEDA area in the context of the topography of the Iberian peninsula, Figure 2-2 gives the location of the supersites.

Calera (2000) has elaborated a GIS-based geographic and physiographic database of the area. The following paragraphs give an overview of the major features (as relevant for this study). These data are described in detail by Calera (2000) and references therein. The maps (GIS layers) are used here for descriptive purposes and to derive statistics for selected sub-areas. In Chapter 4 the characteristic scales of the study area will be derived from the same data.

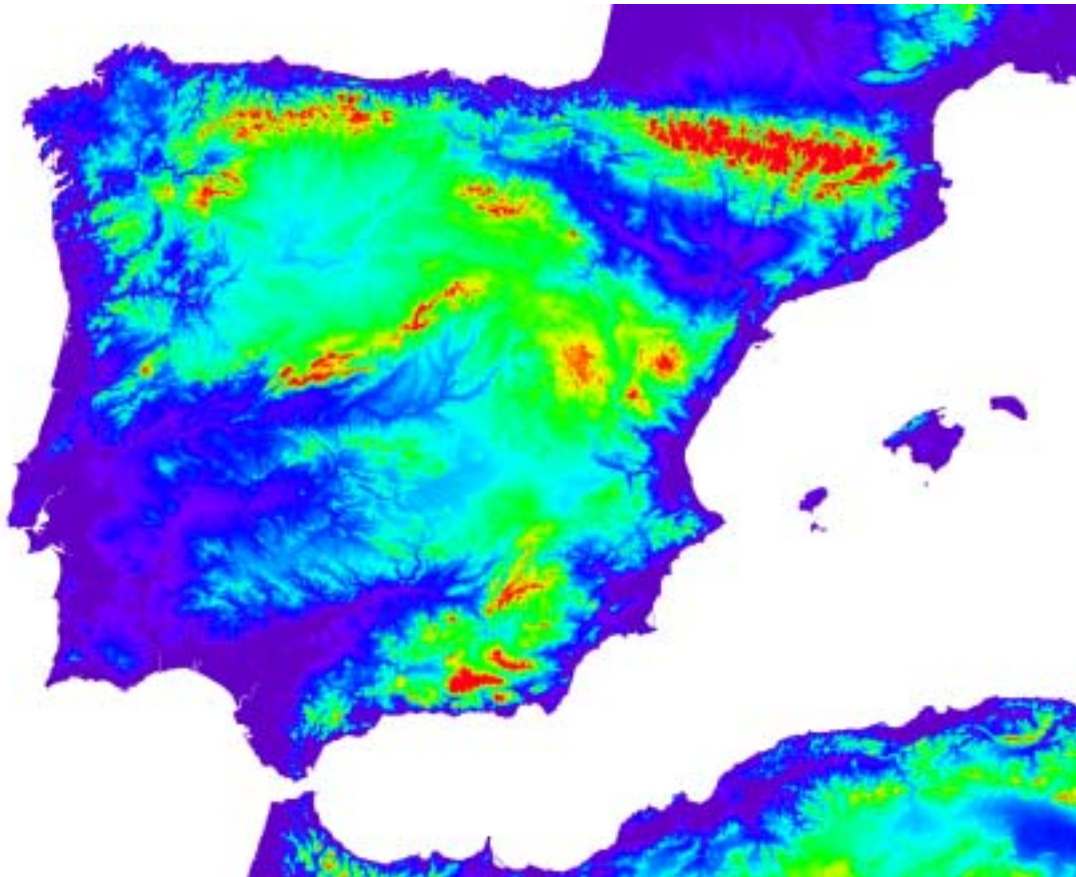


Figure 2-1. Topography of the Iberian peninsula. Color scale from sea level (dark blue) to 1700 m above sea level (red). Data from USGS (1999).

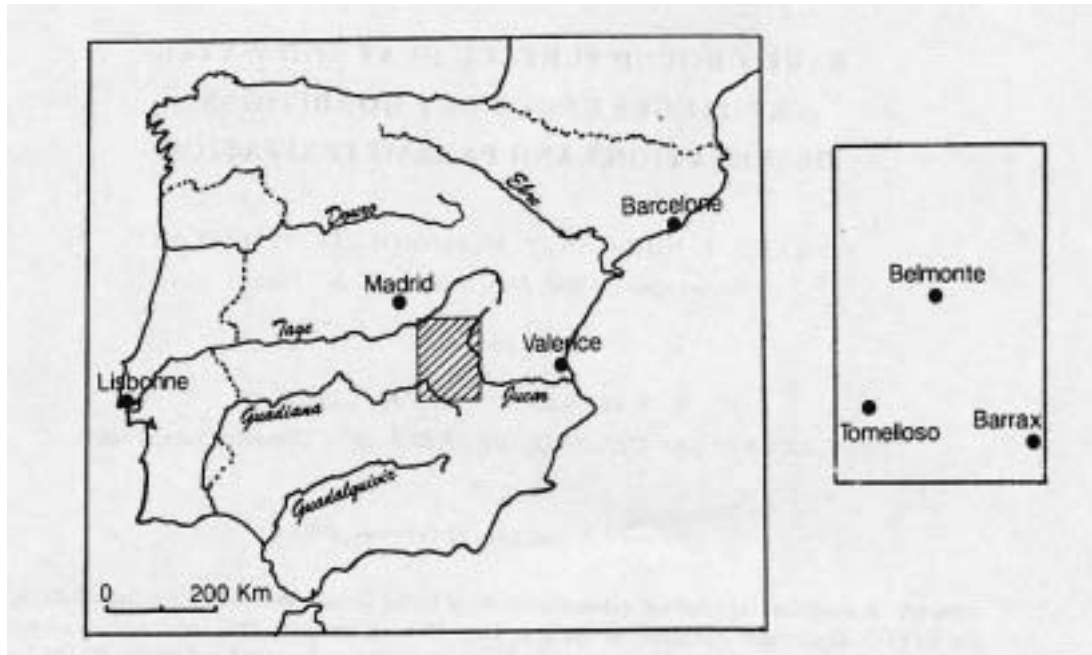


Figure 2-2. Close-up on the EFEDA area with locations of supersites Tomelloso, Barrax, and Belmonte/ Rada de Haro (from Braud et al., 1993).

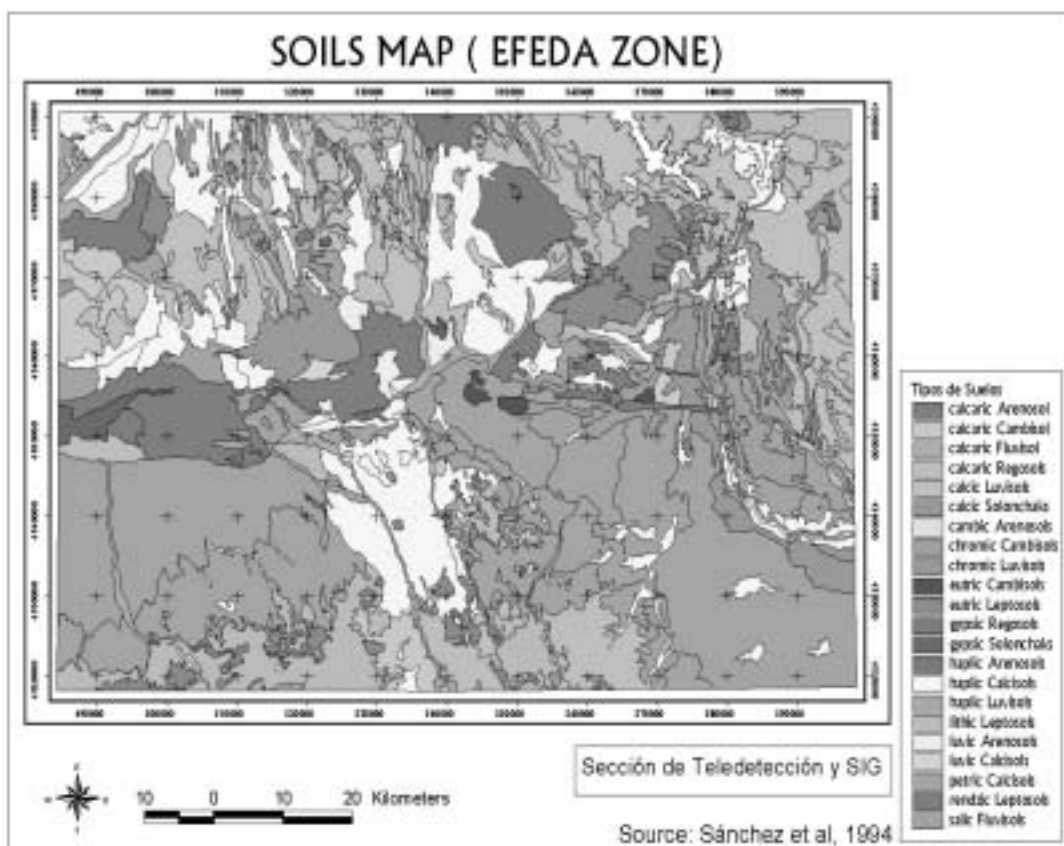


Figure 2-3. Soils in the EFEDA area (courtesy of J. Sánchez and A. Calera).

The high plateau of La Mancha (from Arabian "manxa" = dry flatland) is a geomorphologically uniform flat area, where the markedly continental Mediterranean climate and the extended agricultural activity have contributed to forming a steppe-like landscape. The soils are rather uniform, mostly calcisols with low organic matter content and thus, of moderate to low natural fertility. The soil map reproduced here (Figure 2-3) is a simplified version (Calera, 2000), which includes only the dominant soils. The complete soil classification was developed and described by Sánchez et al. (1994). The most frequent soil type, petric calcisol, is dominant in the Southern half of the study area. The most fertile soils, preferently used for agricultural purposes are calcic luvisols found in the Southeast.

The land use in the study area is divided between dry and irrigated agriculture (for moderate fertility soils) and natural vegetation zones with marginal agricultural use (for low fertility soils and hilly terrain). The land use classification as given in Annex C and Table 2-2 was developed by Calera (2000) for the main purpose of agrometeorological use, the rationale being to keep it simple and yet to discriminate the most contrasting surface types. The stratification into seven classes is based on the phenological development of each crop. As we will see in Chapter 5, this is the most adequate classification for the aggregation of surface properties and fluxes from local to GCM grid scales in the study area. The area covered by the classification of Calera (2000) is slightly different from the EFEDA area, because it corresponds exactly to the size of one Landsat scene. Therefore, the missing parts (less than 5%) have been filled with land use information derived from the CORINE database (CORINE, 1994).

The three Intensive Study Areas (supersites) are named after the village next to the center of each, Tomelloso, Barrax, and Rada de Haro, respectively. Their location is shown in Figure 2-2. Each site is roughly a square with 10 km sides. Connected with straight lines they form a triangle of approximately 70 km sides covering the whole EFEDA area.

The **Tomelloso** supersite is very flat in the Northern part and slightly undulating in the South, with maximum elevation variations of 8%. Two layers of subterranean aquifers are found here, separated by impermeable material. The soils are rather poorly developed and carry many stones. They are appropriate for the cultivation of vine (82% of the site area). Actually, the site forms part of the largest vine growing area in the world. Other uses are cereals (10%) and olive trees (3%). The remaining 3% are rolling terrain. Irrigation equipment was not installed in the zone until well after the final EFEDA period in 1994.

The **Barrax** supersite is extremely flat, with elevation variations below 2 m. Several interconnected subterranean aquifers are found below the zone, which are exploited for irrigation purposes. The soils are similar to those in Tomelloso, but less stony. Their production capacity is limited by an impenetrable petrocalcic layer at about 40 cm depth. The agricultural fields are irrigated in about 35% of the zone (mostly maize). The dominant dry farming is dedicated to winter cereals.

The **Rada de Haro** supersite (sometimes also called **Belmonte**) is located in a mountainous area at a mean altitude of 810 m above sea level. About 60% of the slopes have an inclination of over 10%. The soils are poor and agricultural activity is limited to scarce and small plots of vine, sunflower, and cereal, interspersed with olive trees.

Table 2-2. Land use classes as defined for the classification of Calera (2000) shown in Annex C. SUM-dry is also called VINE, because most of its area is vine.

Class name	Definition	Examples
BARE	Not cultivated	Bare soil, Fallow land Urban settlements
SPR-dry	Dry spring crop	Cereals Legumes
SUM-dry, VINE	Dry summer crop	Vine Sunflower (dry)
SPR-irrig	Irrigated spring crop	Cereals (barley, wheat, etc.) Garlic
SUM-irrig	Irrigated summer crop	Corn, Alfalfa, Sugar beat, Vegetables
NAT	Natural vegetation	Matorral low bushes
FOR	Forest	Forest, low mountains

Table 2-3. Fractional area covered by individual vegetation classes in different areas (in %). The coordinates given for three sites represent the center point of a 10 km² square. For additional HIRLAM grid cells used in Chapter 6, see there.

	<i>Total EFEDA</i>	<i>Tomello- so</i>	<i>Barrax</i>	<i>Rada de Haro</i>	<i>HIRLAM T05</i>	<i>HIRLAM T02</i>	<i>HIRLAM B02</i>
latitude	38°55' N- 40°05' N	39°10' N	39°03' N	39°30' N	39°00' N- 39°30' N	39°00' N- 39°15' N	39°00' N- 39°15' N
longitude	2°11' W- 3°11' W	3°01' W	2°06' W	2°20' W	2°30' W- 3°00' W	2°45' W- 3°00' W	2°00' W- 2°15' W
area (km ²)	8.000	100	100	100	2.976	475	475
BARE	5	2	22	-	6	6	22
SPR-dry	48	10	43	4	6	5	43
VINE	15	82	-	8	82	89	-
SPR-irrig	12	-	5	-	-	-	5
SUM-irrig	5	-	30	-	-	-	30
NAT	5	3	-	85	-	-	-
FOR	10	3	-	5	3	-	-

2.2 Surface datasets

Extended surface observations were performed in order to document the surface energy balance and related processes in the major land-use classes found in the EFEDA area. The sampling strategy followed the general concept of three supersites as described above, but was also influenced by the research interests of the participating groups.

The research questions addressed by the individual groups include process analysis and modeling of soil-vegetation-atmosphere exchange in sparse canopy, bare soil, in very dry conditions, the contrast between dry and irrigated crops, and the influence of topography. Results from these observations were published, among others, by van den Hurk (1996), Oliver and Sene (1992), Braud et al. (1993), Grunwald et al. (1996), Blümel (1998), and Berger (1997).

Here, the individual field observations are not analyzed as such, but rather used in the context of regional scale aggregation (Chapter 5) and NWP model validation (Chapter 6). Corresponding to this purpose, it is important to describe the surface energy balance of each major vegetation class, its uncertainty, its variability within the class, and the significance of differences between classes.

A total of 21 surface flux stations of different configurations was deployed by 10 groups, some operating only during part of the EFEDA period. Several mobile instruments were used in addition. The major concentration (13 stations) was found in the Tomelloso supersite, along with the most complete temporal coverage of the entire month of June 1991. Eight of these stations were installed on vine, which is the dominant crop within the site but also is considered to be representative of a much larger area. Less spatial and temporal coverage was dedicated to the other two supersites, where each major vegetation class (including bare soil) was monitored by 1 or 2 flux stations (see Table 2-1). The details of the location and instrumentation of these stations are described in the EFEDA Final Report (de Bruin et al., 1993). The data from each station were quality-checked and processed by each group before introducing them in the corresponding database, which has been established at the Department of Meteorology of Wageningen Agricultural University (Krikke, 1994). The same data are also included in the EFEDA CD-ROM (EFEDA, 1995).

Moene (1992) and de Bruin et al. (1993) performed a detailed assessment of the observational errors of the surface energy balance components as measured by the individual flux stations. Their conclusions are summarized in Table 2-4. The 7% error of net radiation is basically the calibration error. A 30% error of soil heat flux is assumed for all methods. The heat and moisture flux errors vary widely according to the methods used (eddy correlation, profile method, Bowen ratio, or temperature variance).

Table 2-4. Uncertainty of surface flux observations for daytime hours. Estimates for profile method apply to individual measurements. After Moene (1992) and de Bruin et al. (1993).

Method	Sensible heat flux	Latent heat flux	Soil heat flux	Net radiation
All	-	-	30 %	7 %
Eddy correlation	10 %	10 %	-	-
Profile / profile	20 %	72 %	-	-
Profile / residuum		70 %		
Bowen ratio	20 %	55 %	-	-

Linder et al. (1996) have derived representative, standardized datasets for the four major vegetation classes for the purpose of intercomparing surface schemes. Their datasets consist of atmospheric forcing data, general soil and vegetation data (input needed to run the schemes), and flux data for comparison. Table 2-5 summarizes the datasets and gives a list of parameters. Note that the vegetation and soil data listed include the full set given by Linder et al. (1996), while only a subset is used here, according to the input data requirements of the models used (see Chapters 3 and 5). For Tomelloso, a within-vegetation-class aggregation was performed for the flux data by arithmetically averaging the data of the four most consistent stations. In the other sites, one flux station was selected in each class. All atmospheric and flux data were interpolated to standardized height and time intervals. Due to the large scatter (and inherent difficulties of measuring moisture flux in very dry conditions), the latent heat flux was recalculated for all stations as the residual in the energy balance equation. The soil and vegetation data needed as model input were sometimes not available from observations, so they were inferred from ancillary information. The time periods selected by Linder et al. (1996) cover 27 days (Tomelloso), 26 days (Barrax irrigated maize), 11 days (Barrax bare soil), and 5 + 8 days (Rada de Haro).

For the purpose of NWP validation (Chapter 6), grid-element-averaged datasets are needed. Chapter 5 is dedicated to area-aggregation for various grid-cell area sizes and for the entire EFEDA area.

Table 2-5. Coverage and contents of consolidated surface datasets of Linder et al. (1996). SW = shortwave radiation; LW = longwave radiation.

<i>General</i>	<i>Atmospheric forcing data</i>	<i>Surface flux data</i>	<i>Vegetation and soil data</i>
4 major vegetation classes:	Half-hourly values of	Half-hourly values of	2 roughness lengths emissivity, albedo vegetation fraction leaf area index minimum stomatal resistance soil texture saturation-, field capacity-, & wilting point water content B-parameter thermal conductivity saturated hydraulic conductivity & head soil depth root density profile initial profiles of soil temperature & moisture
*Vine *Natural *Irrigated crop *Bare / fallow	air temperature 2m relative humidity 2m wind speed 10m air pressure incoming SW outgoing SW incoming LW precipitation	sensible heat flux latent heat flux soil heat flux net radiation friction velocity radiative surface temperature	

2.3 Aircraft datasets

Aircraft play a key role in land-surface experiments such as EFEDA in several aspects. They represent the only observational means to bridge the gap between local scale point measurements and regional- to global-scale models. It was the aim of the EFEDA aircraft missions

- * to document land-surface and atmospheric boundary layer parameters on a range of scales from 10 to 10⁴ km²; and
- * to derive area-averaged heat and moisture fluxes.

Two different instrumented aircraft were used for in-situ measurements during the second half of June 1991, the twin-engine fan jet Dassault Falcon 20 owned by DLR (now German Aerospace Centre) and the twin-engine turboprop aircraft Dornier Do 128 owned by the Technical University of Braunschweig. Two further aircraft provided high-resolution remote sensing data on two days each (coordinated with Landsat overpasses), a Douglas-McDonald DC-8 and a Lockheed ER-2, both owned by NASA (National Air and Space Administration). Table 2-6 gives an overview of the instrumentation.

The subsequent detailed analysis (Chapters 4 and 5) uses only Falcon data, so only this aircraft dataset is described below. However, the results obtained from the analysis of the other aircraft datasets are used in Chapter 3. The intercomparison of data from the two flux aircraft shows that their data are compatible within the observational error limits (Kratzsch and Jochum, 1993). Flux data from the Do 128 were analyzed by Kratzsch (1994) and Grunwald et al. (1996). Results of the remote sensing aircraft were summarized by Bolle et al. (1993). A detailed description of the Falcon observations and data is given in the corresponding data report (Jochum et al., 1992).

The timing of the various aircraft missions is summarized in Table 2-7, along with the radiosonde operations.

Table 2-6. EFEDA aircraft and their instrumentation.

<i>Aircraft type</i>	<i>Parameters obtained (in-situ aircraft) / instrumentation (remote sensing aircraft)</i>
Falcon 20	Basic meteorological parameters (temperature, humidity, pressure, wind) Turbulent fluxes Radiation fluxes (all four) Water vapor and aerosol backscatter vertical profiles (DIAL, see 2.5) Video images of ground
Do 128	Basic meteorological parameters (temperature, humidity, pressure, wind) Turbulent fluxes Radiometric temperature
DC-8	C-, L-, and P-band, full polarization synthetic aperture radar (AIRSAR)
ER-2	Thematic mapper simulator (TMS) Visible / infrared imaging spectrometer (AVIRIS) Metric camera

Table 2-7. Time periods covered by aircraft and radiosonde observations. All times are UTC, local noon is about 12:00 UTC. The flight pattern codes are explained in Box 2-1. For lidar/DIAL see Section 2.5; Y=yes; N=no. Sondes launched before 8:00 and days with less than two radiosonde operations are not included.

day (June)	radiosonde Tomelloso (number)	radiosonde Barrax (number)	aircraft time (pattern)	lidar / DIAL	clouds
9	8:20 - 20:20 (8)		-	-	1/8
11	8:20 - 20:20 (8)		-	-	0/8
12	9:30 - 16:10 (3)		-	-	4/8
19	12:00 (1)	7:35-16:30 (4)	10:00 - 12:47 (N)	N / N	5/8
20	7:30 - 13:30 (5)	6:00 -16:10 (4)	10:10 - 12:58 (B)	Y / Y	2/8
21	7:00 - 17:40 (8)	4:10 - 22:35 (17)	10:21 - 13:13 (M)	Y / Y	4/8
22	8:55 - 14:00 (4)	10:00 - 14:20 (3)	10:20 - 13:09 (B)	N / N	0/8
23	4:10 - 17:30 (8)	5:00 - 18:00 (10)	7:05 - 9:11 (P) 11:13 - 13:33 (P) 15:22 - 17:38 (P)	Y / Y	0/8
25	6:00 - 16:30 (7)	4:00 - 18:15 (12)	12:04 - 15:09 (M)	Y / Y	4/8
26	8:00 - 14:00 (4)	7:30 - 16:10 (4)	10:23 - 12:49 (B)	N / N	2/8
27	10:00 - 14:00 (3)	11:05 (1)	-	-	4/8
28	8:00 - 14:20 (4)	10:35 - 14:05 (2)	11:25 - 14:17 (M)	Y / Y	1/8
29	6:00 - 16:30 (9)	4:00 - 17:40 (11)	9:29 - 11:57 (N)	Y / Y	0/8
14.7.	-	-	9:38 - 12:09 (N)	Y / Y	0/8

2.3.1 The Falcon in-situ observations

The observational strategy is defined and illustrated in Box 2-1. Four different flight patterns were designed as to meet the complete set of objectives set out above, yet at the same time providing a sufficient statistical sample in each case. Some of the flight lines (called "legs") were common to more than one pattern, in order to obtain a higher statistical significance in some parts of the area.

The aircraft carries a complex high-precision instrumentation package to measure atmospheric parameters plus all aircraft parameters needed to eliminate the influence of the aircraft and its motion from the resulting data. Fimpel (1987) describes the instrumentation configuration used in EFEDA (see Figure 2-4). It includes a Honeywell Lasernav inertial reference system and an air motion sensing system based on a Rosemount 585J five-hole probe mounted on a noseboom with Rosemount transducers for static, dynamic, and differential pressure. Humidity is measured with three sensors, all located within the nose of the jet. A Vaisälä Humicap and a Lyman- α , both located in a humidity measuring duct, are combined to derive long-term stable fast-response moisture data. The inlet to the duct lies at the bottom of the nose. To correct for compression effects, the temperature and pressure of the air inside the duct are measured as well. A dewpoint sensor General Eastern 1011 is located at one side of the nose. Two temperature sensors are used, both PT100's (Rosemount 102). The open element for fast measurements responds to frequencies up to 13 Hz. The PT wire of the slower sensor is protected within an aluminum tube. The output of the various sensors used for turbulence calculation is sampled at 100 Hz after undergoing analog filtering at 50 Hz to remove aliasing effects. The accuracy of the derived meteorological parameters is listed in Table 2-8.

Box 2-1. Falcon flight patterns: layout and objectives.

<i>Flight pattern outlay</i> (from Jochum et al., 1992; sketch approximately to scale)	<i>Flight pattern name (code)</i> <i>Principal objective</i>
	BOX (B)
	Terms in budget equations and area averaged fluxes by means of integral balance method (Jochum, 1993a)
	FLUX PROFILE (P)
	Diurnal cycle of ABL state and flux profiles Michels and Jochum (1995)
	NASA (N)
In-situ validation of flux estimates derived from airborne and satellite remote sensing data (Jochum et al., 1994; Brasa et al., 1997)	
MAP (M)	
Area-averaged fluxes and horizontal variability of ABL state and fluxes across the whole EFEDA area (Jochum, 1993b)	

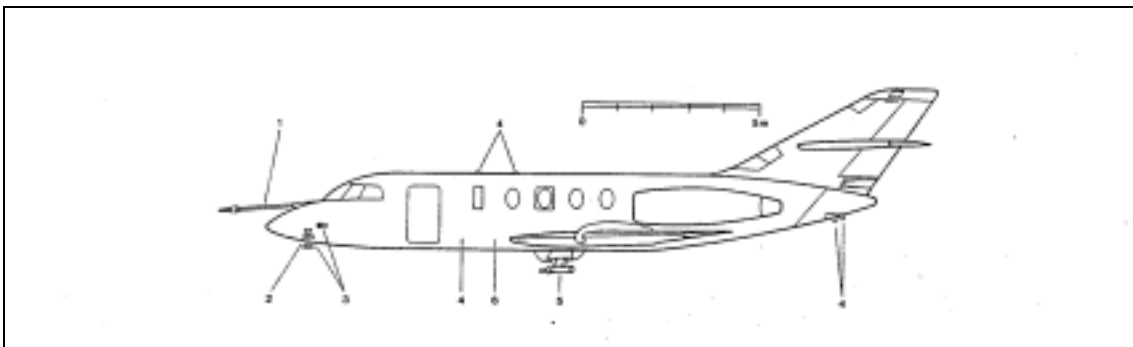


Figure 2-4. Location of sensors on DLR Falcon: Air motion (1), temperature (2), humidity (3), radiation (4), droplet spectrometers (5), lidar/DIAL (6). From Fimpel (1987).

Table 2-8. Absolute longterm and relative short-term accuracy of basic meteorological parameters derived from Falcon measurements. The three moisture parameters are obtained from three different sensors. Parameters marked with *) are not used for flux calculation. From Jochum et al. (1992).

Parameter	Absolute accuracy	Relative accuracy
Static pressure	1.0 hPa	0.1 hPa
Temperature	0.5 K	0.03 K
Dew point	1.0 K	*)
Relative humidity	2 %	*)
Absolute humidity	0.5 g m ⁻³	0.01 g m ⁻³
Horizontal wind	1.5 m/s	0.10 m/s
Vertical wind	0.5 m/s	0.05 m/s

2.3.2 The Falcon in-situ dataset

In accordance with the observational objectives described above, four different types or processing levels of data are included in the Falcon in-situ dataset. Table 2-9 summarizes its contents and characteristics. Levels A and B provide directly the time series, which are obtained from the basic processing, quality control, and data conversion procedure. There, the raw data are first converted to physical units by applying calibration curves. From the entire flight time series the individual flight legs and ascents or descents are cut and dealt with separately. A sophisticated analysis software, especially developed for this aircraft configuration (Baumann and Bögel, 1991), is used to remove all known influences of the aircraft and its motion from the data and to calculate the meteorological parameters of an undisturbed atmosphere. It also serves to remove spikes and to control the quality of the data. For horizontal flight legs, the original high resolution of 100 Hz is maintained in the resulting time series (level A) in order to enable subsequent turbulence statistics calculation, whereas for ascents or descents the rate is reduced to 10 Hz (level B).

The level A time series for each flight leg are detrended and highpass-filtered before fluxes and other turbulence statistics are computed. After careful inspection of the response functions of various filters a Lanczos square filter was selected for the EFEDA data. A cut-off wavelength of 20 km was used for all legs longer than 60 km. Only for shorter legs, a 9 km cut-off was applied. This ensures that long-wavelength contributions to the turbulent fluxes are retained (see below). Spectral analysis is used for further quality control of each individual horizontal flight leg. Annex A shows an example. Fluxes are then computed by means of the eddy-covariance method. This implies that quasi-stationarity is assumed (Stull, 1988). The time series of instantaneous covariances are included in the level A data. Finally, the resulting kinematic fluxes are converted into energy fluxes using the measured mean air density. The Webb correction is applied whenever appropriate. Level C data contain the mean fluxes and other turbulence parameters for each flight leg. Level D data are the 10 Hz time series of the four radiation components.

Table 2-9. Contents and characteristics of Falcon in-situ dataset. TAS: true air speed of aircraft.

Type	Form	Parameters	Uncertainty / Error	Purpose / Used in
A	100 Hz time series for each leg	θ , θ_v , q , u , v , w , p , z , TAS; instantaneous variances & covariances	Table 2-8	Detailed process analysis; Terms in budget equations
B	10 Hz time series for each ascent/descent	θ , θ_v , q , u , v , p , z	Table 2-8	To complete radiosonde data: ABL state & budget; NWP validation
C	leg-average	mean θ , θ_v , q , u , v , w ; heat & moisture flux, momentum flux; all variances, TKE; further covariances & correlations; skewness & kurtosis	see text and Box 2-2	Vertical flux profiles; Flux divergence in budget equation; Areal variability and area average
C1	segment-averages	mean parameters & fluxes	see 2.3.3	Mesoscale model comparison
D	10 Hz time series for each leg	upward & downward short- & longwave radiation (4 components)	7%	Radiation flux divergence in budget equation; Areal variability; NWP validation

Calculating fluxes from aircraft measurements is a complex procedure and a research topic in its own, where instrumental aspects are blended with considerations on how to adapt optimally the flight strategy to the turbulence characteristics to be observed. In most cases, a first guess of the potential observational results is needed to develop the most adequate approach. In-flight real-time processing and display of key data is a prerequisite to fine-tuning the flight strategy for that purpose.

The accuracy of the basic derived parameters, as given in Table 2-8, is not crucial for flux calculations, since it is well within the limits required for that purpose. It is relevant, however, for the very demanding calculation of advective and other terms in the budget equations. The information given in Table 2-8 will be used later (Chapter 3) to estimate the corresponding errors.

Errors in turbulent fluxes can arise from five fundamental sources. A sufficient level of *instrumental accuracy* is guaranteed by the rigorous quality assurance and control procedure described above.

Systematic errors are associated with (in)adequate sampling of the dominant wavelength(s). Lenschow and Stankov (1986) were the first to investigate this problem for their airborne dataset. Lenschow et al. (1994) and Mann and Lenschow (1994) have further developed their line of reasoning into a set of formulae to estimate the corresponding errors. These formulae are based on simplified assumptions about the properties of mixed layer profiles, so the underlying premises need be checked when applying the formulae. Basically, the requirement for the time series (i.e. the flight leg) is here to be "long enough" to capture well the dominant wavelength. The "length" in this sense is influenced by data detrending and filtering, so these data manipulations need to take into account the scales under investigation. The relevant scales of the EFEDA area will be determined in Chapter 4. Table 2-10 shows an example of the resulting flux uncertainty estimates for one leg flown at two different altitudes, based on the analytical expressions given in Box 2-2.

Random errors arise from sampling only a finite number of turbulence events (eddies) along the flight leg, i.e. from a sample too small to be statistically representative. Very long legs, e.g., over homogeneous terrain will keep this error small. Another means to overcome this problem, especially in heterogeneous areas, are repeated aircraft passes over the same track and/or compositing several days of similar characteristics. Mann and Lenschow (1994) provide another set of analytical formulae to estimate these errors. The example in Table 2-10 and Box 2-2 show that both the systematic and random error grow with normalized height (z/z_i) and with the leg length (LL) relative to the dominant eddy size (z_i/LL), where the ML depth (z_i) is taken as a measure of dominant eddy size.

Further error sources are *mesoscale flux contributions*, which can be estimated roughly from the given data (Mahrt, 1998), and *non-stationary conditions* prevailing over heterogeneous surface or under heterogeneous cloud cover. Vickers and Mahrt (1997) developed a series of tests for (non-)stationarity of a given time series. Non-stationarity of the time series implies that the traditional error definitions and estimates (discussed above) are not valid. From a purely statistical point of view, these records need to be discarded. In cases such as EFEDA, however, they contain valuable information that cannot be obtained in any other way. The solution consists of carefully inspecting each individual record in order to sort out the scales of motion and of interest. At any rate, eddies not adequately sampled by a given leg need to be removed by appropriate filtering.

Box 2-2. Analytical formulae to estimate sampling errors of airborne fluxes. After Mann and Lenschow (1994). z = flight altitude; z_i = ML depth; LL = leg length.	
Error type	Estimated uncertainty
Systematic error	$1.16 * (z / z_i)^{1/6} * (z_i / LL)^{1/2}$
Failure to capture dominant eddy wavelength	
Random error	$1.75 * (z / z_i)^{1/4} * (z_i / LL)^{1/2}$
Failure to capture enough eddies (sample size too small, statistically not representative)	

Errors in the radiative flux components (Table 2-8) are basically calibration errors. Wendling et al. (1985) describe the procedure of continuous in-flight calibration. The radiative fluxes are measured directly, so they are not affected by sampling or non-stationarity errors.

2.3.3 Segmented Falcon in-situ data

For the purpose of mesoscale model comparison (Noilhan et al., 1997) and to assess the areal variability (Jochum, 1993b), the individual flight legs were cut into segments of 10 km length, overlapping by 5 km. Segment averages were calculated for all parameters. This segmented dataset is included in the EFEDA CD-ROM. The errors in the mean meteorological parameters and radiation fluxes given in the previous section apply to the segments as well. The uncertainty of the turbulent fluxes, however, needs careful revision. The analytical error formulae given in Box 2-2 can be used to infer the error estimates of the shorter segments. Taking the example of one leg flown at two different altitudes, Table 2-10 shows the difference in systematic and random errors for the original 106 km leg and for a 10 km segment. Both errors increase about threefold, due to their dependence on the square root of the leg length. Compositing or repeating the same 10 km segment 2 (4) times reduces the random error to about the same size as (60 % of) the systematic error.

Table 2-10. Example of systematic (SE) and random (RE) error in heat flux calculation from 106 km leg and 10 km segment. RE (2x): random error for 10 km segment repeated 2 times, RE (4x): analogous.

z_i	z/z_i	LL	SE	RE	RE (2x)	RE (4x)
1220 m	0.23	106 km	10 %	13 %	-	-
		10 km	32 %	41 %	29 %	20 %
1550 m	0.55	106 km	13 %	18 %	-	-
		10 km	41 %	56 %	40 %	28 %

2.4 Radiosonde datasets

Radiosondes were launched regularly at the three supersites in order to document the atmospheric boundary layer (ABL) state during the entire month of June and to investigate differences in the ABL over the three sites. The data are used here for three objectives, firstly, in the ABL budget analysis of Chapter 3, secondly, to estimate the regional heat and moisture fluxes from a budget method (Chapter 5), and thirdly, to evaluate the performance of HIRLAM (Chapter 6). For this purpose, a homogenized and normalized radiosonde dataset was derived (as described below), based on the original data as provided by the Principal Investigators (Pierre Bessemoulin, personal communication; Norbert Kalthoff, personal communication).

Three different sounding systems were used by three groups. At Tomelloso, Météo France operated an Omega navigation system in conjunction with Vaisälä sondes. At Barrax, the University of Karlsruhe used a radar tracking system together with Graw sondes. The data from these systems differ with respect to humidity sensor accuracy at higher altitudes or low humidities (humicap capacitor vs. carbon element), ascent speed, sampling rate, final altitude, and vertical resolution of wind profiles. Details are described in the EFEDA Final Report (Fiedler et al., 1993; Muniosguren, 1993). Table 2-11 gives those sounding system characteristics, which are relevant for using the dataset.

Table 2-11. Characteristics of the radiosonde dataset.

Site	Accuracy humidity *)	Accuracy temperature	Vertical resolution	Vertical resolution wind	Average final altitude
Tomelloso	0.5 g/kg	0.5 K	30-50 m	30-50 m	5-6 km
Barrax	0.5 g/kg	0.5 K	30-50 m	150-300 m	10-12 km

*) below 5 km altitude.

Due to technical problems, the data taken at Rada de Haro are of rather limited use. The data of two days were adjusted, recalibrated and included in the EFEDA CD-ROM, but they are not used here. Data from aircraft ascents and from airborne lidar were used instead to infer mixed layer (ML) depth over that site.

The scheduling provided daily launches at each site, plus an intensive program on selected days to cover the ML diurnal cycle. The timetable of launches at Tomelloso and Barrax is included in Table 2-7.

The data were interpolated to 50 m (Barrax) and 100 m (Tomelloso) height increments by Fiedler et al. (1993) before including them in the EFEDA CD-ROM. In order to retain the maximum achievable vertical resolution, the original data are used here (as quality controlled and processed by the Principal Investigators; Pierre Bessemoulin, personal communication; Norbert Kalthoff, personal communication) and prepared for the subsequent analysis by means of a normalizing procedure introduced by Betts (1973). The purpose of this procedure is to create a conserved variable framework for easy comparison and compositing of vertical profiles. The data are first interpolated to equidistant pressure intervals (0.05 hPa), using pressure as the vertical coordinate rather than height. Before compositing, each profile is vertically normalized with the pressure difference between ML depth and the surface.

2.5 Airborne lidar datasets

A downward-looking near-infrared Differential Absorption Lidar (DIAL) was flown onboard the DLR Falcon in order to measure the aerosol backscatter and water vapor fields within and above the ABL. The data are used here mainly to quantify the variability and scales of ML depth and vertical humidity profiles across the EFEDA area (Chapter 4).

The DIAL system (Ehret et al., 1993) is based on a two-wavelength lidar measurement using narrowband transmitters. During the "on-line" measurement, typically performed at the peak of a suitable water vapor absorption line, an extinction enhancement occurs when the laser beam penetrates the atmosphere because of atmospheric water vapor absorption. A second, "off-line" lidar sounding, typically performed in the wing of a water vapor line, is needed as a reference measurement. The latter basically relates to aerosol backscattering and extinction as known from conventional lidar techniques. From both on- and off-line measurements probing the same atmospheric volume, water vapor density can be determined as a function of range.

EFEDA was the first operational deployment of the (then) recently developed DIAL system. Uncertainties remaining after careful calibration of all system components were therefore removed by occasional cross-calibration with the Tomelloso radiosondes (Kiemle et al. 1995). The vertical and horizontal resolution of the aerosol backscatter data is 15 m (given a typical aircraft speed of 135 m/s). To reduce the statistical error of the water vapor data, the lidar signals have to be averaged on a case-to-case basis, which results in a typical vertical resolution of 300 m and a typical horizontal resolution of 5 km.

The timetable of lidar observations is included in Table 2-7, where all days with validated water vapor data are listed as Y (yes) in the DIAL section. Depending on the intended use of these data, the signal-to-noise ratio needs to be checked in each case.

The DIAL data are typically displayed as distance-height crosssections of aerosol backscatter and water vapor content (see example in Chapter 4). The former allow high-resolution (15 m) determination of ABL structural features and localization of ML depth, residual layer (RL) depth, entrainment zone (EZ) structure, and associated wavelengths and scales, information which will be used mainly in Chapter 4. The latter give a qualitative idea of the water vapor field structure, which however, is sometimes difficult to separate from numerical artifacts due to the required averaging. In a strictly quantitative sense, the individual vertical profiles along the flight line are averaged over 3-5 km to yield statistically significant water vapor profiles together with a measure of the horizontal variability (in terms of standard deviation).

2.6 Composites and selection of case studies

The synoptic situation during the observational period of 1-30 June 1991 was mostly characterized by anticyclonic conditions. The only major perturbation occurred in the first three days, when cyclonic flow over Spain and a blocking anticyclone over the eastern Atlantic ocean produced strong convective activity and some precipitation in the EFEDA area (Rodríguez-Camino and García-Moya, 1992). During the rest of the month, a small number of weak frontal systems passed over Spain. They affected the EFEDA area on a total of five days, mostly associated with increased cloudiness.

The synoptic situation offers a natural classification of the experimental days into the two broad categories of "anticyclonic" and "slightly unstationary" conditions, excluding the first three days. Except for these initial days, there was no significant precipitation in the area. Therefore, soil wetness does not serve as a further stratification criterion. The irrigation events in the Barrax site do, of course, influence the soil wetness significantly. However, this situation is very local and thus, is dealt with by means of the corresponding category of land-use rather than of external forcing (see Chapter 5).

The "anticyclonic" cases represent a rather large sample (22 days) of fairly homogeneous conditions, well covered by surface observations and 1-2 daily radiosoundings. The second half of June 1991 (with its added datasets from aircraft and frequent radiosoundings) holds eight of these cases, with 23 June most densely covered by observations. Figure 2-5 to Figure 2-8 show the essential features of the composite of all anticyclonic cases, based on the Linder et al. (1996) surface dataset for the Tomelloso vine class. Without entering in any details of interpretation (to be discussed in Chapter 3), the emphasis is here on the spread of the curves (indicating the intra-sample variability) and the relative position of the individual day curves of 23 June (day 23). The variability of net radiation (Figure 2-5) is small (less than 14%) and apparently related to differences in cloud cover in the early afternoon. Ground heat flux and sensible heat flux (Figure 2-6) vary by less than 20% and 23%, respectively. The moisture flux variability is highest (up to 43%), but the shape of the individual curves is generally preserved. The individual day 23 observations are almost identical to the composite, except for ground heat flux, where day 23 exhibits higher values close to the upper limit of the standard deviation bars. Yet the daytime evaporative fraction (Figure 2-7) of day 23 again corresponds closely to the composite values. The variability of screen level temperature and specific humidity (Figure 2-8) reflects the general synoptic picture of anticyclonic episodes interrupted by short frontal passages, which bring in different air masses. This affects the absolute values of temperature (standard deviation up to 3.5 K) and specific humidity (up to 1.5 g/kg), but not the shape of the curves. Day 23 again maps very well the composite.

The situation is very similar for the other two dry vegetation classes (Belmonte-natural and Barrax-bare). The irrigated vegetation (Barrax) needs special treatment (see Chapter 6) due to the cyclic irrigation timing. Compositing all days without taking into account the irrigation cycles would result in large scatter and loss of essential information. Day 23 was one of only three isolated irrigation events in the anticyclonic sample.

In conclusion, the individual day 23 dataset can be considered equivalent to the composite of the full anticyclonic sample of 22 days. Therefore, an individual case study approach will be adopted in most of the following Chapters. The focus will be on 23 June 1991, complemented with other days whenever additional data and/or increased sample size (e.g., for aircraft-derived fluxes) needed.

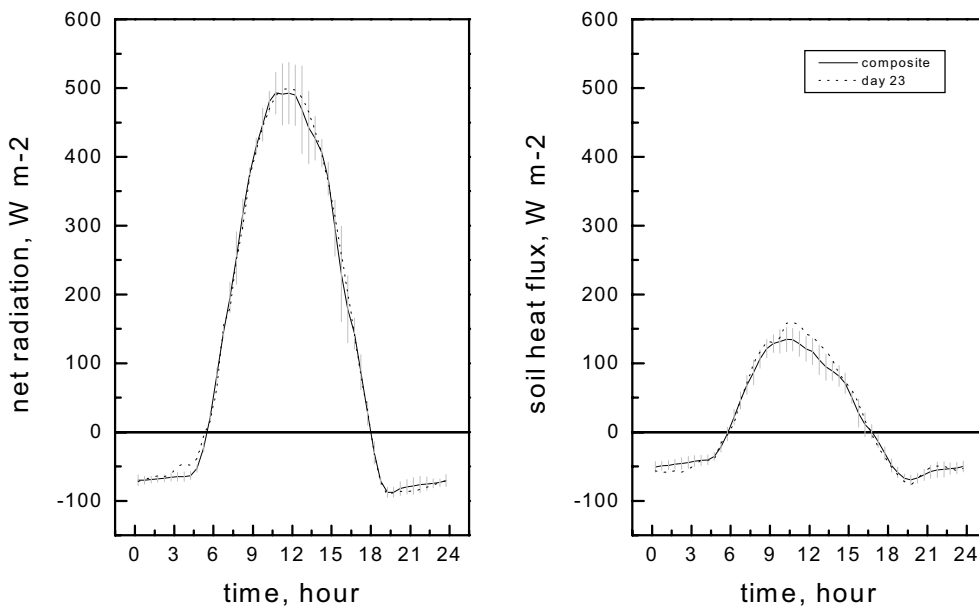


Figure 2-5. Diurnal cycle of net radiation (left panel) and soil heat flux (right panel) at Tomelloso (vine): Composite of all (22) anticyclonic days (solid line) and 23 June (dotted line). Error bars indicate standard deviation of the mean. Dataset from Linder et al. (1996).

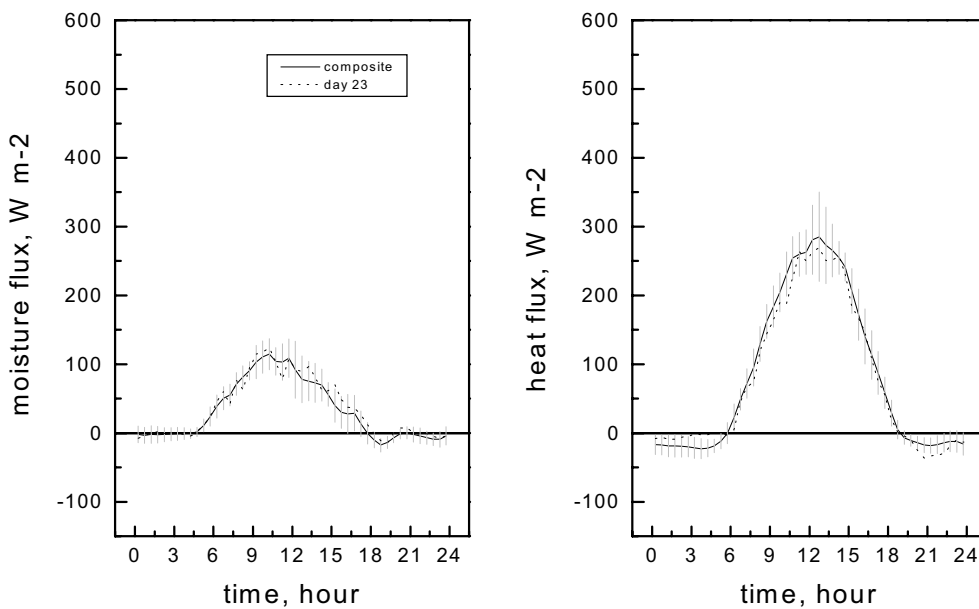


Figure 2-6. Same as Figure 2-5 for moisture and heat flux.

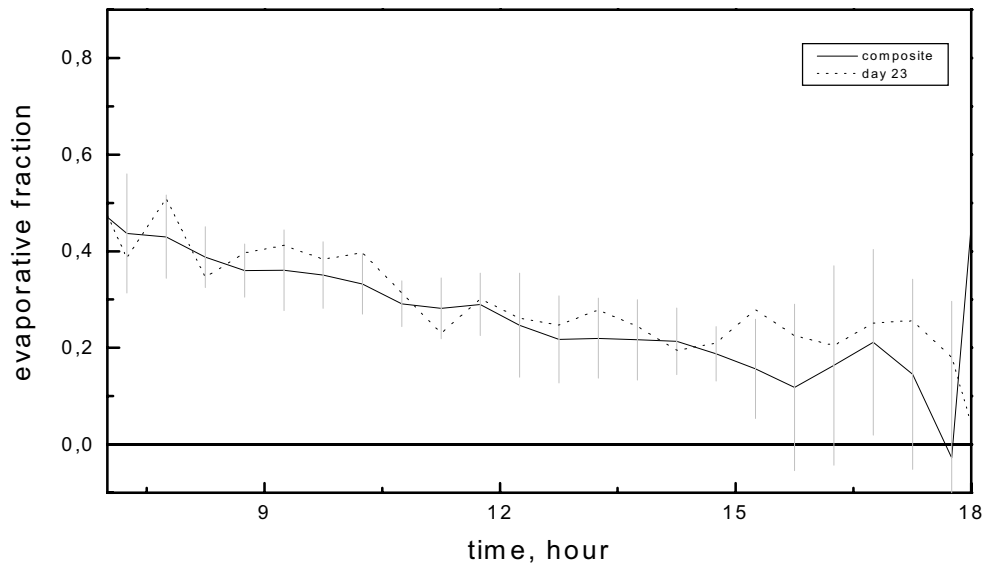


Figure 2-7. Same as Figure 2-5 for evaporative fraction.

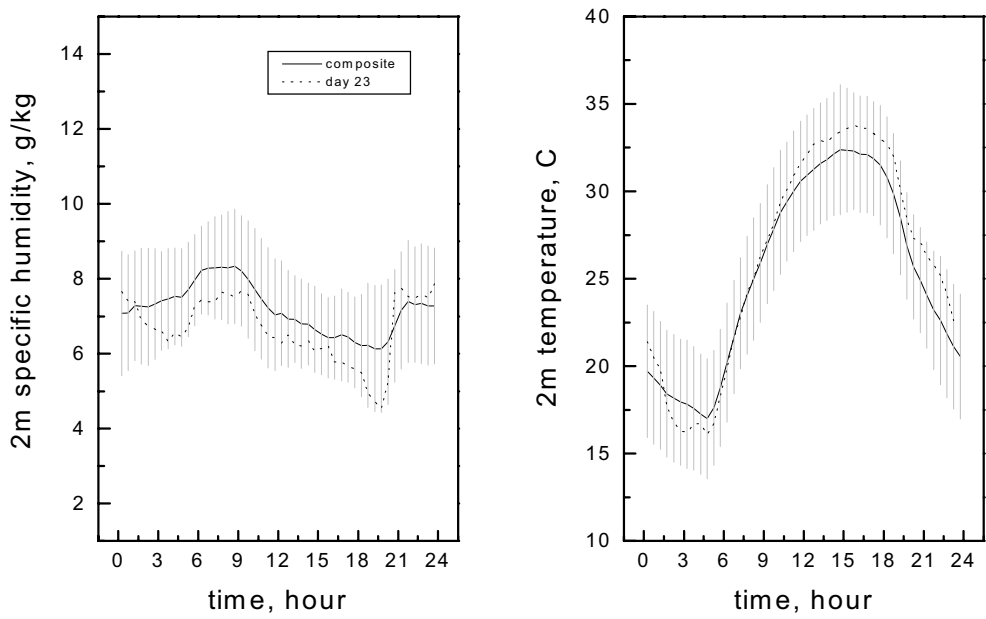


Figure 2-8. Same as Figure 2-5 for temperature and specific humidity at 2 m.

3 Boundary layer budgets¹

3.1 Introduction

The EFEDA area provides an interesting background for atmospheric boundary layer (ABL) budget studies. Mixed layers of different characteristics were observed at rather short geographical distance (80 km) between the two main supersites. Moisture plays the key role here. The Tomelloso site is an extensive wine-growing area representative of semiarid conditions, with a surface energy balance dominated by the sensible heat flux. The Barrax site is characterized by additional moisture supply from two sources, one at the ground from irrigation and one aloft from the Mediterranean sea breeze often penetrating inland in the afternoon. The resulting ABL at Barrax is generally moister, slightly cooler and less deep than at Tomelloso.

We study the ABL budgets separately for each site, the objective being

- i) to determine the processes contributing to the mixed layer (ML) structure and state changes during daytime; and
- ii) to assess the relative importance of the different terms in the energy and moisture budget equations, including horizontal and vertical advection and radiative flux divergence.

Our budget analysis is based on the synergistic combination of a comprehensive observational dataset and a simple coupled canopy-ML model. The observational dataset consists of distributed micrometeorological surface stations, radiosondes, flux aircraft, and an airborne water-vapor differential absorption lidar (DIAL). In particular the unique aircraft dataset includes the four radiation flux components, from which the full radiative divergence can be derived. By providing a large sample of heat and moisture flux observations throughout the ML depth, it supports the analysis of the vertical flux divergences in a ML slab framework.

Airborne DIAL- and radiosonde-derived humidity crosssections and profiles show that the residual layer (RL) above both sites is characterized by a layered moisture structure. The resulting entrainment moisture fluxes vary in magnitude and sign over a large part of the diurnal cycle. The determination of the vertical moisture flux divergence becomes a challenging task under these circumstances.

We first describe the budget methods (section 3.2) and the observations along with relevant aspects of the data analysis (section 3.3). The estimation of the budget terms starts with the "classical" time-rate-of-change (section 3.4) and flux divergence terms (3.5) and then proceeds to the radiative flux and horizontal and vertical advection terms (sections 3.6 - 3.7). The complementary analysis of the individual budget terms provides new information on the relative role of entrainment and surface forcing and on the importance of radiative warming in this semi-arid environment, which is discussed and summarized in section 3.8.

3.2 Approach

We consider the whole EFEDA area of 60 km by 80 km, as well as two sub-areas of 10 km by 10 km centered at the radiosonde launch sites located within the two

¹ Manuscript in preparation for Boundary-Layer Meteorol.

supersites Tomelloso and Barrax. In either case we decompose the atmospheric variables into their horizontal mean over the area and their smaller scale fluctuations, i.e. $\theta = \bar{\theta} + \theta'$ for potential temperature, $Q = \bar{q} + q'$ for specific humidity, and analogously for the wind components u , v , and w . The overbar (used to denote horizontal averages) is omitted in single variables and is only used in covariances. The distinction between sub-areas will be clear from the context, so we will not use any subscript for that purpose.

Then the ABL budgets of energy and moisture are described by equations (3.1) and (3.2) (e.g., Stull, 1988):

$$\frac{\partial \theta}{\partial t} + u \frac{\partial \theta}{\partial x} + v \frac{\partial \theta}{\partial y} + w \frac{\partial \theta}{\partial z} + \frac{\partial \overline{u'\theta'}}{\partial x} + \frac{\partial \overline{v'\theta'}}{\partial y} + \frac{\partial \overline{w'\theta'}}{\partial z} + \frac{1}{\rho C_p} \frac{\partial R_n}{\partial z} = 0 \quad (3.1)$$

I

II

III

IV

V

VI

$$\frac{\partial q}{\partial t} + u \frac{\partial q}{\partial x} + v \frac{\partial q}{\partial y} + w \frac{\partial q}{\partial z} + \frac{\partial \overline{u'q'}}{\partial x} + \frac{\partial \overline{v'q'}}{\partial y} + \frac{\partial \overline{w'q'}}{\partial z} = 0 \quad (3.2)$$

where R_n is the net radiation flux, ρ air density, and C_p the specific heat of (moist) air.

The terms in either equation denote, from left to right, the time rate-of-change (I), the along- and crosswind component of the horizontal advection (II), the vertical advection (III), the two components of the horizontal flux divergence (IV), and the vertical flux divergence (V), respectively. The last term on the left-hand side of equation (1) represents the vertical radiative flux divergence (VI). In absence of cloud processes, there is no source or sink term in equation (3.2).

The ABL budgets for the sub-areas are now obtained by vertically integrating the equations (3.1) and (3.2) over the surface and mixed layers, i.e. from screen level to the ABL top.

The individual terms in the integrated equations have been calculated or estimated in different ways, depending on the available data in each case. The horizontal flux divergence terms were found to be at least one order of magnitude smaller than the main terms in all cases. The same applies to the vertical advection of potential temperature. Therefore, we eliminate terms IV from both equations and term III from equation (3.1). Since moisture is not always well mixed, its vertical advection is in many cases not negligible. Therefore, term III in equation (3.2) was retained.

The final set of simplified and vertically integrated equations is

$$\int \left(\frac{\partial \theta}{\partial t} \right) dz + \int \left(u \frac{\partial \theta}{\partial x} + v \frac{\partial \theta}{\partial y} \right) dz + \int \left(\frac{\partial \overline{w'\theta'}}{\partial z} \right) dz + \int \left(\frac{1}{\rho C_p} \frac{\partial R_n}{\partial z} \right) dz = 0 \quad (3.1a)$$

$$\int \left(\frac{\partial q}{\partial t} \right) dz + \int \left(u \frac{\partial q}{\partial x} + v \frac{\partial q}{\partial y} \right) dz + \int \left(w \frac{\partial q}{\partial z} \right) dz + \int \left(\frac{\partial \overline{w'q'}}{\partial z} \right) dz = 0 \quad (3.2a)$$

where the integral sign stands for integration from screen level to ABL top.

The observational analysis is imbedded in the conceptual framework of a simple ML slab model. This type of model (Betts, 1973; Carson, 1973; Tennekes, 1973) has been used widely in boundary layer studies. Its simplest configuration uses prescribed surface fluxes. We use here a coupled canopy-ML model (de Bruin, 2001, personal communication), which consists of two sub-models. The ML part is the slab model of Tennekes (1973) with the entrainment formulation of Tennekes and Driedonks (1981). The canopy sub-model is based on the Penman-Monteith formulation of moisture flux. The surface heat flux is then obtained from the surface energy budget. The coupling is established through Monin-Obukhov similarity. The model equations are given in Annex B.

Figure 3-1 illustrates the conceptual background of the ML model. The ML is considered as a one-dimensional (1-D) vertical slab with well-mixed (vertically constant) potential temperature θ and humidity q . The figure (from Hipps et al. 1994) shows the idealized form of the θ -profile and gives the relevant definitions. The top of the EZ, h_e , is defined as the height where the gradients reach the free atmosphere (FA) lapse rates. The ML top h_i is located at the height of the first temperature inversion and/or a marked drop in specific humidity and/or a clear minimum of saturation pressure deficit. Then, the linear FA profile is extrapolated down and the ML profile is extrapolated upwards. Finally, the ABL top h is obtained by making areas A and B of equal size. The temperature jump $\Delta\theta$ and the humidity jump Δq at level h are calculated as the difference between the FA- and ML-gradient lines at that level. The average ML depth z_i , defined as the height where 50% of the air has ML (and 50% FA) characteristics (Stull, 1988) roughly coincides with h .

In the case of moisture, the idealized form of the specific humidity profile is not universal. Depending on the sign of the jump Δq and/or of the FA gradient γ_q , the air above the ML can be drier or moister than the ML. A ML capped by dry air will give rise to ML drying by entrainment (positive entrainment moisture flux). In contrast, a ML capped by moister air is moistening by entrainment.

The slab model is based on the simplified conservation assumption that the storage term balances the flux divergence, i.e. that only terms I and V in Equations (3.1) and (3.2) are retained. As such, it will not work in conditions of strong advection. We will see below (section 3.6) that horizontal advection is small at the scale of the whole EFEDA area. But the data were not always conclusive enough on the supersite scale. We will see later (Chapter 5) that this slab model works well for the supersites, so this is be an indirect confirmation that advection is of secondary importance also at that scale. The other terms in the complete budget, like vertical advection and radiative divergence, are retained in this model in simple parameterized ways (see Annex B).

The model will be shown (in Chapter 5) to reproduce well the surface fluxes observed at each vegetation class and the ML at Tomelloso. Using a set of input parameters obtained through parameter aggregation, it also reproduces well the ML at Barrax (see Chapter 5). Thus, we can consider it as a validated tool, adapted for each area through the appropriate set of input data. Obviously, we are using here the same set of input data.

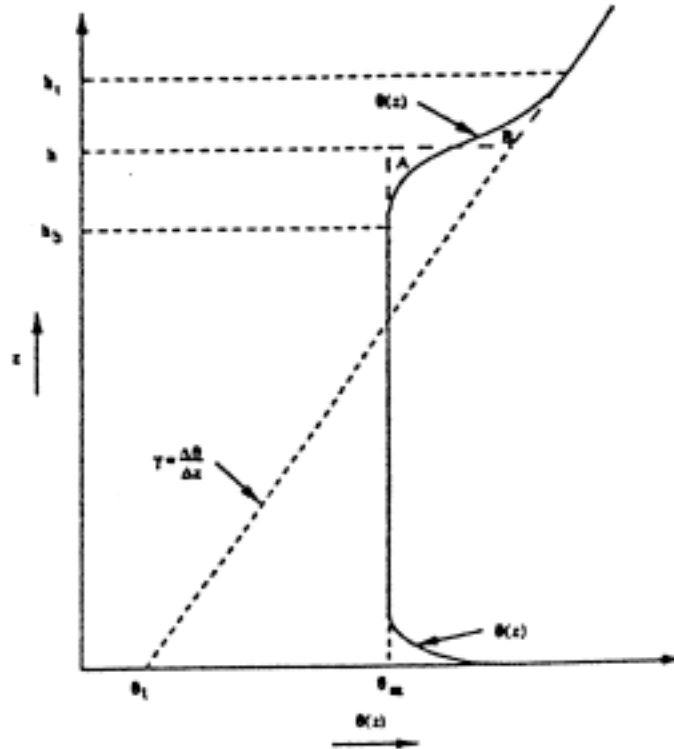


Figure 3-1. ML slab model concept: Schematic procedure to determine ML depth (from Hipps et al., 1994)

We present in detail the case study of 23 June 1991, where the most complete dataset is available. The daytime diurnal cycle of 23 June was most densely covered by aircraft observations (a total of five flights performed by two different aircraft). Radiosondes were launched roughly every 2 hours at Tomelloso and Barrax. The day was almost cloud free with weak northerly winds. This day was shown to be representative of the full set of 22 individual days with anti-cyclonic conditions. Figures 2-6 through 2-9 of Section 2.6 show that the 23 June surface thermodynamic state and surface energy balance are almost identical to the composite of the full sample.

As described in Chapter 2, the two sites, Tomelloso and Barrax, are characterized by very different land use, dry vineyards around Tomelloso and partly irrigated fields in the Barrax area. The surface energy budget of the dry fields is dominated by the sensible heat flux, while that of the irrigated fields shows a dominant latent heat flux. Figure 3-2 shows the site-aggregated surface fluxes for 23 June. The aggregated fluxes were obtained by weighted averaging of observed fluxes in each vegetation class, using areal fractions from the vegetation classification of Calera (2000). The sensible heat flux is similar at both sites. The moisture fluxes are very low at Tomelloso (mean daytime Bowen ratio of 2.5) and much higher at Barrax (daytime Bowen ratio range of 0.1-0.2 at individual irrigated fields; 0.6-1 for the site-aggregate), which reflects the different moisture availability at the surface. The net radiation is significantly higher at Barrax due to higher surface temperature and albedo and lower elevation at Tomelloso.

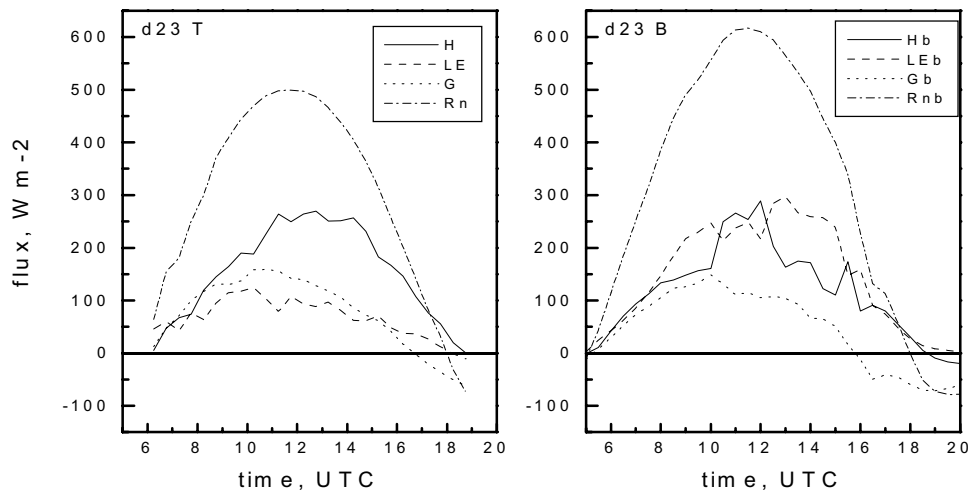


Figure 3-2. Surface fluxes at Tomelloso (left) and Barrax (right) on 23 June 1991.

The budget terms were calculated at four times during the daytime diurnal cycle. At 10:00 UTC, the ML is still growing into the nocturnal stable boundary layer (NBL). The rapid ML growth phase starts around 12:00 UTC and slows down around 14:00 UTC, where the surface fluxes have reached their peak values already and where ML warming has slowed down. The ML depth peak phase around 16:00 UTC coincides with the decay of the surface fluxes and the onset of surface cooling.

3.3 ABL vertical structure and state

A prerequisite for the analysis in this and the following sections is the determination of the ABL vertical structure and state from a set of radiosonde ascents. This is a non-trivial task, especially for EFEDA conditions, where the ML was topped by a deep residual layer (RL) during a significant part of the day and where the moisture fields were rather inhomogeneous. An example of profiles observed on 23 June 1991 at Tomelloso (Figure 3-3) illustrates the difficulties associated with delineating the ML and entrainment zone (EZ) boundaries from these data. In any case, this is done manually, so it involves a certain degree of subjectivity. The first step of analyzing each radiosonde profile consists in delineating the ML and EZ by locating the first temperature inversion and/or a marked drop in specific humidity and/or a clear minimum of saturation pressure deficit in the plotted profiles. The subsequent analysis uses the graphical approach (based on Driedonks, 1982) as schematically depicted in Figure 3-1.

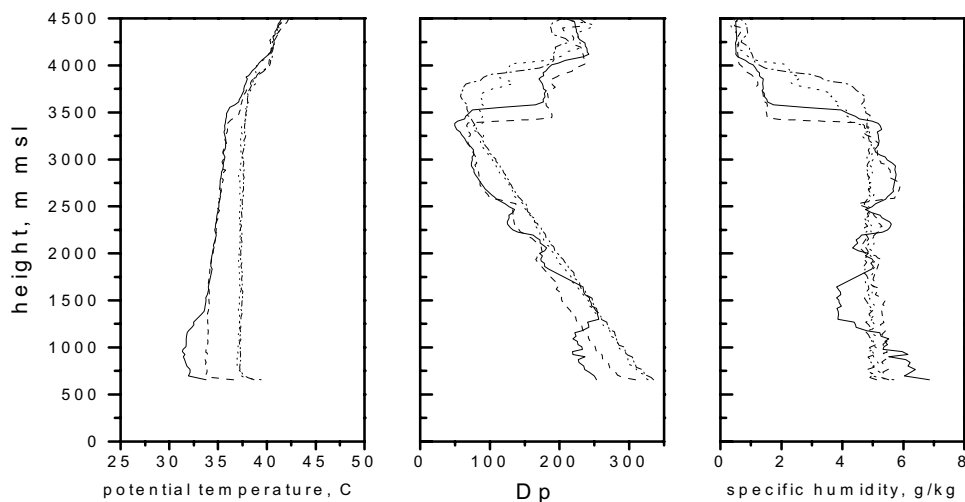


Figure 3-3. Vertical profiles of potential temperature (θ), specific humidity (q), and saturation pressure (p^*) deficit ($Dp = p - p^*$) on 23 June 1991 at Tomelloso. Solid line: 10:00 UTC; dashed: 11:30 UTC; dotted: 16:00 UTC; dash-dotted: 17:30 UTC.

The error in delineating the layers by means of radiosonde data comes from three different sources. Firstly, the vertical resolution of the radiosonde is 25-30 m for the altitudes in question. Secondly, the uncertainty of the manual procedure itself is essentially due to the sometimes erratic profiles of individual soundings. It is estimated at about 100 m. The third and most important uncertainty (not present in the early morning hours) is introduced by the undulating nature of the EZ, which is due to the motions of large thermals penetrating into the EZ. The analysis of airborne lidar data (Jochum, 1993a) reveals ML depth and EZ undulations of about 10-15% of its depth, i.e. of over 300 m in the afternoon. An individual radiosounding is like a needle pin into the atmosphere, successively crossing the ML, EZ, RL (if it were), and FA. Depending on its position in troughs or ridges of the EZ, it would "miss" the actual mean ML depth by a maximum amount equal to the amplitude of the EZ undulations. The overall uncertainty in h resulting from these three error sources is taken as 15%.

Figure 3-4 (from Michels and Jochum, 1995; MJ95 hereafter) shows the diurnal cycle of the ABL structure on 23 June 1991, as obtained from all available data (radiosonde, aircraft ascents, airborne lidar). The stable nocturnal boundary layer (NBL) is twice as deep at Barrax than at Tomelloso. The ML is growing more rapidly and reaches a larger final depth at Tomelloso. Both features are due to the larger amounts of water vapor available from the irrigated fields. The residual layer, which originated from the ML of the day before is about 3 km deep and slightly stable in both sites. It is maintained a very long time, until finally the ML has fully grown in the afternoon. Moisture advected by the sea breeze penetrating inland in the afternoon inhibits further growth of the ML at Barrax (Fiedler et al., 1996).

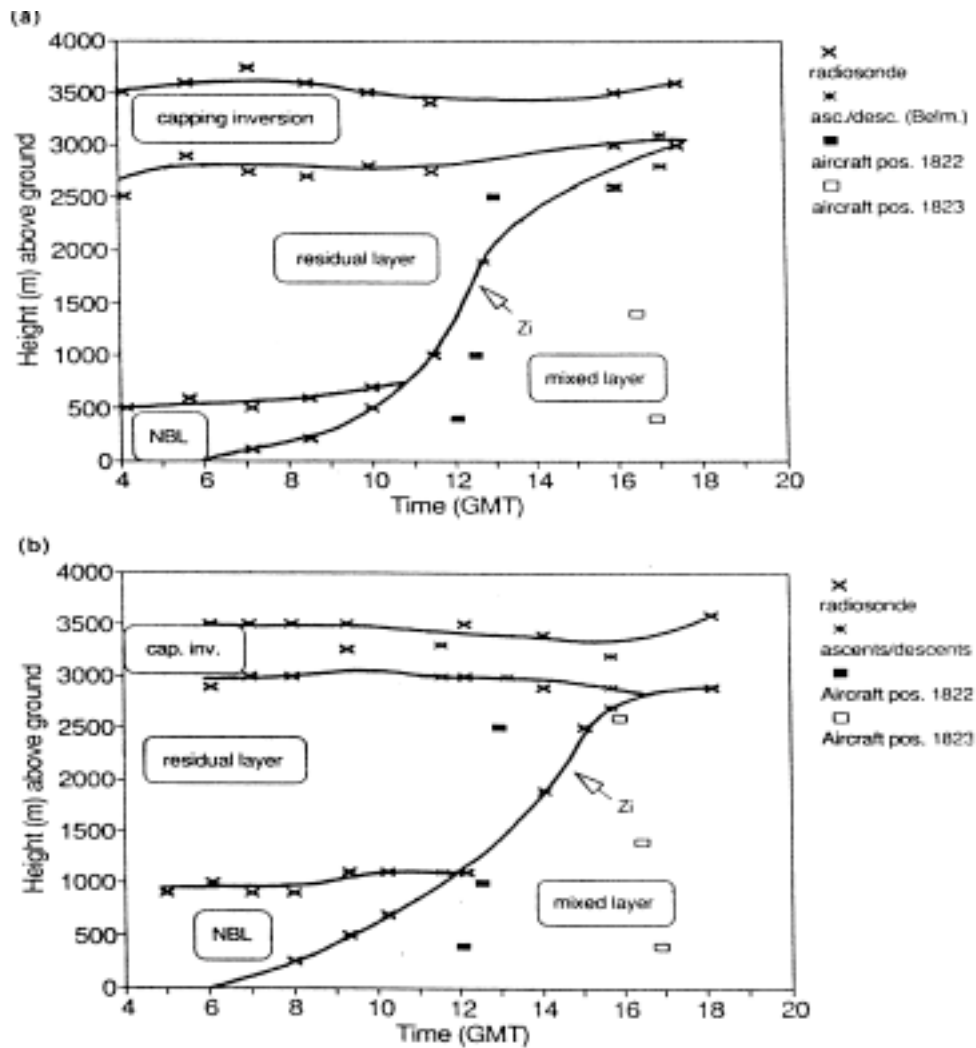


Figure 3-4. ABL development in Tomelloso (top panel) and Barrax (bottom panel) areas (from MJ95). The solid lines marking transitions between the different layers were obtained from manually interpolating the individual data points.

Figure 3-5 and Figure 3-6 illustrate the daytime evolution of the temperature and moisture stratification at the two sites along with the time-space reference of the flux aircraft data. Radiosondes were launched every 1-3 hours, with occasional sonde failures adding to the data gaps. Aircraft ascents and descents were used to complete the sounding data, but they are limited to the flight times and the height ranges covered by the flight legs. This density of vertical soundings is sufficient to give a qualitative picture of the situation, but any method of gridding introduces some degree of numerical artifact in this case. Furthermore we will see later that the (short) period of moisture flux divergence is not captured here. Therefore, Figure 3-5 and Figure 3-6 are used here for qualitative illustration of the general features, while quantitative conclusions will be drawn only directly from the datasets involved, as described below. We find ABLs that are well-mixed in temperature at both sites, with a warming maximum centered around 14:00 UTC. The specific humidity is hardly well-mixed at Tomelloso and not well-mixed at all at Barrax. The ML warming is roughly uniform with height, whereas the drying or moistening is not.

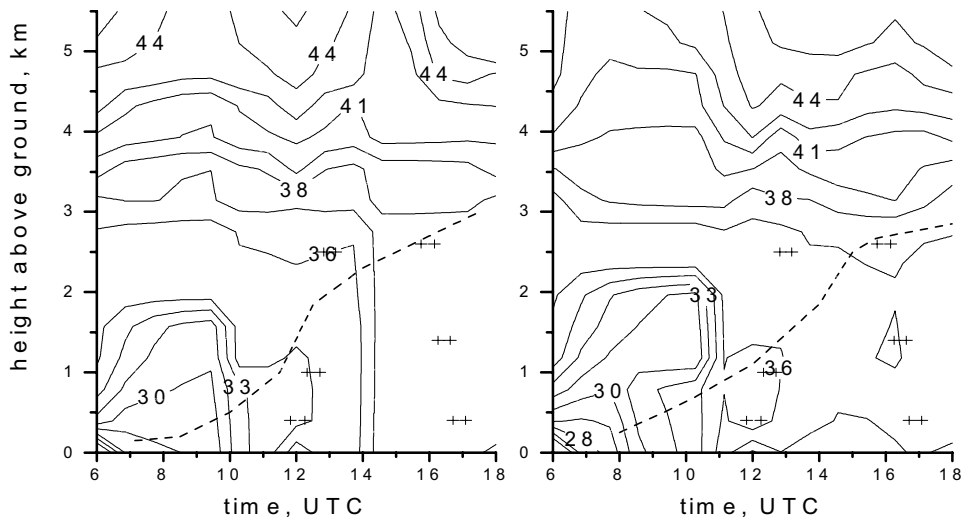


Figure 3-5. Stratification of potential temperature (in °C) during 23 June 1991 at Tomelloso (left panel) and Barrax (right panel). The dashed line indicates ML depth as given in Figure 3-4. The crosses mark positions of aircraft legs.

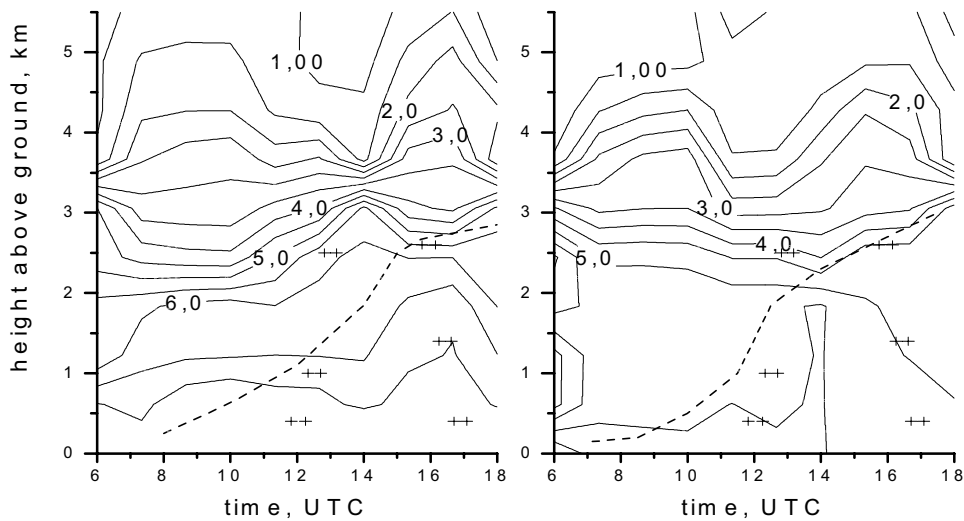


Figure 3-6. As in Figure 3-5 for specific humidity (in g/kg) at Tomelloso (right) and Barrax (left).

3.4 Time rate-of-change term

The ML warming/cooling and drying/moistening was calculated from three different kinds of observations in a complementary way (aircraft, radiosonde, surface stations). Figure 3-7 shows the mean potential temperature evolution during the day as obtained from all available observations. We consider none of the observing systems alone as sufficient to obtain an accurate estimate. Aircraft data alone give only a small number of point values along the day and across the

area. Due to the size of the area and the associated length of the aircraft legs, there was no continuous series of legs flown over the same area at regular time intervals. Mean values over all segments of aircraft legs flown in the ML over the two test areas are used directly (solid symbols in Figure 3-7). Some of the aircraft legs are too close in time to give a meaningful time gradient. Potential temperature is well mixed, so all segment-averages are representative of the ML mean. Since this is not the case for specific humidity, two height ranges are retained for analysis. The same applies to the radiosonde data, where ML averages were used for potential temperature and height-bin-averages for humidity. Least squares quadratic fits were used in either case to obtain the instantaneous time change. Using a linear fit, e.g., in the case of Tomelloso, obviously would underestimate the actual trend at noon, because the two observations closest in time (viz., at 12 and 16 UTC) also include the low-trend early afternoon period. Surface observations offer the necessary continuity in time, but are not necessarily representative of the whole area nor of ML trends. Figure 3-7 shows clearly the higher potential temperature in the superadiabatic layer at Tomelloso, but not at the moister Barrax area. The time gradients of ML and surface are very close in the afternoon, while in the morning they reflect the time lag between surface and ML warming. Equally, Figure 3-8 shows the higher moisture in the superadiabatic layer, with the difference being larger in the irrigated zone of Barrax. Again, the time gradient is similar in the ML and surface at Tomelloso, but not at Barrax, indicating an afternoon decoupling of moisture transport at low ML levels. Both the surface and ML are moister at Barrax than at Tomelloso. Thus, the irrigation-generated moisture supply is mixed upwards well into the ML.

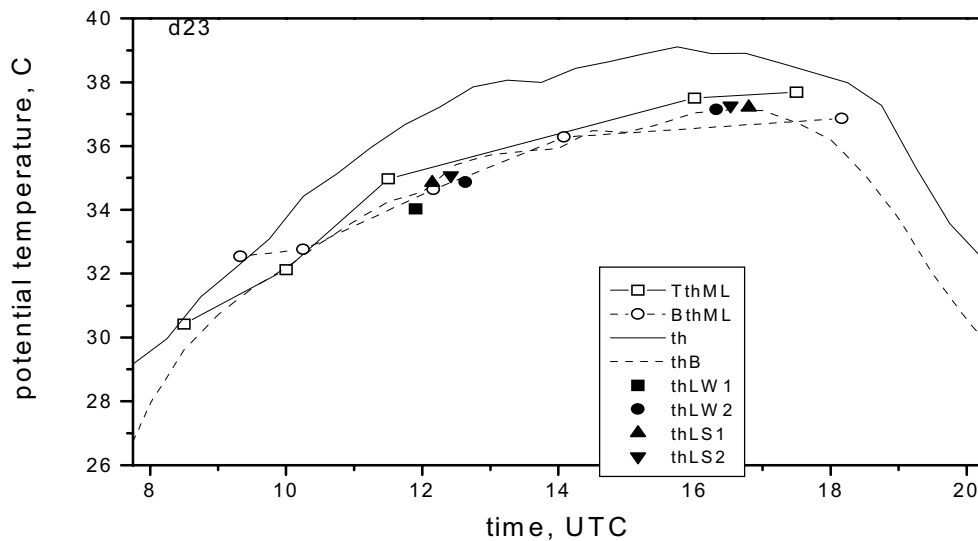


Figure 3-7. Mean potential temperature observed by different systems during 23 June 1991. Solid line: surface Tomelloso; dashed line: surface Barrax; solid line with open squares: radiosonde Tomelloso, dashed line with open circles: radiosonde Barrax, solid symbols: aircraft segment means.

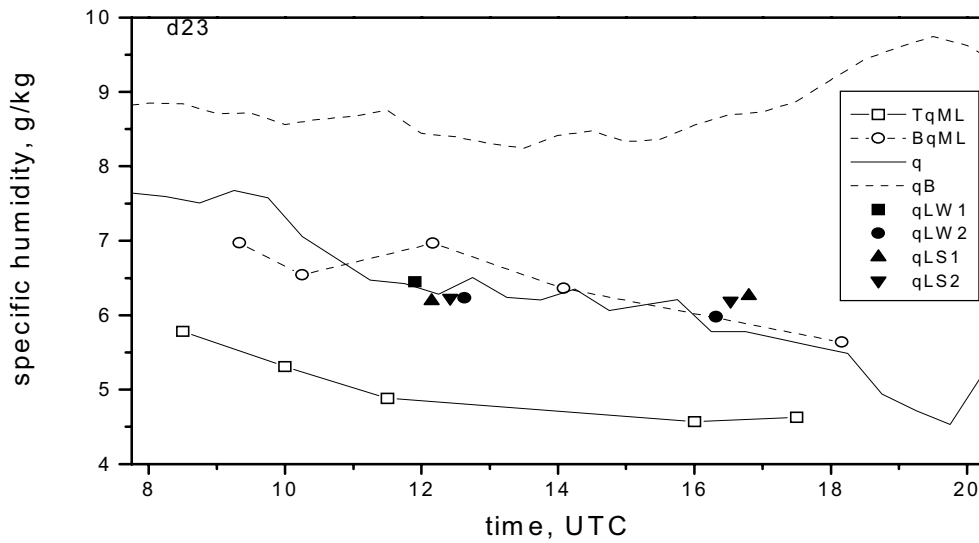


Figure 3-8. As Figure 7 for specific humidity.

The surface warming peaks in the early morning, shortly after sunrise (6-8:00 UTC) and then decays rapidly. while the ML warming peaks around 10:00 UTC at Tomelloso (12:00 at Barrax, where the additional moisture supply slows down the warming process). The surface cooling sets on around 16:00 UTC, the ML follows some 2 hours later. At Tomelloso, the surface drying peaks at 10:00 and increases again after 16:00 UTC (about the time when stomatal resistances increase strongly; van den Hurk, 1996). The ML drying decreases steadily there until late afternoon, when it stops at very low humidity. The ML at Barrax is drying all over the day (least before noon, most in the afternoon), while the surface alternates between drying at noon and slight moistening in the early morning and afternoon.

In conclusion, a weighted combination of results obtained from the individual observing systems was adopted. The errors given in Figure 3-9 are obtained from the standard deviations of aircraft segment-means and radiosonde layer-averages, respectively. The uncertainty in surface trends was assumed to be 0.1K and 0.5 g/kg per 2.5 hour period, similar to Betts et al. (1992) and LeMone et al. (2001). The noon warming rates of all observational systems are rather close, so the synthesis value was obtained by simple weighted averaging (with highest weight given to radiosondes, lowest to aircraft). The same applies to the noon drying rate. For the afternoon period, the data reflect the time-lags between surface and ML warming and drying (moisture decoupling in the case of Barrax). Therefore, the radiosonde values were taken. The aircraft values marked with asterisk were discarded because the legs were too close in time, resulting in large errors.

In summary, Figure 3-9 shows that the ML warming rate at Tomelloso is always larger than at Barrax. At both sites, the warming decreases along the day. The Tomelloso ML is drying, with decreasing drying rate over the day. In contrast, the Barrax ML is moistening around noon. We will come back to the ML drying/moistening in Section 3.8.

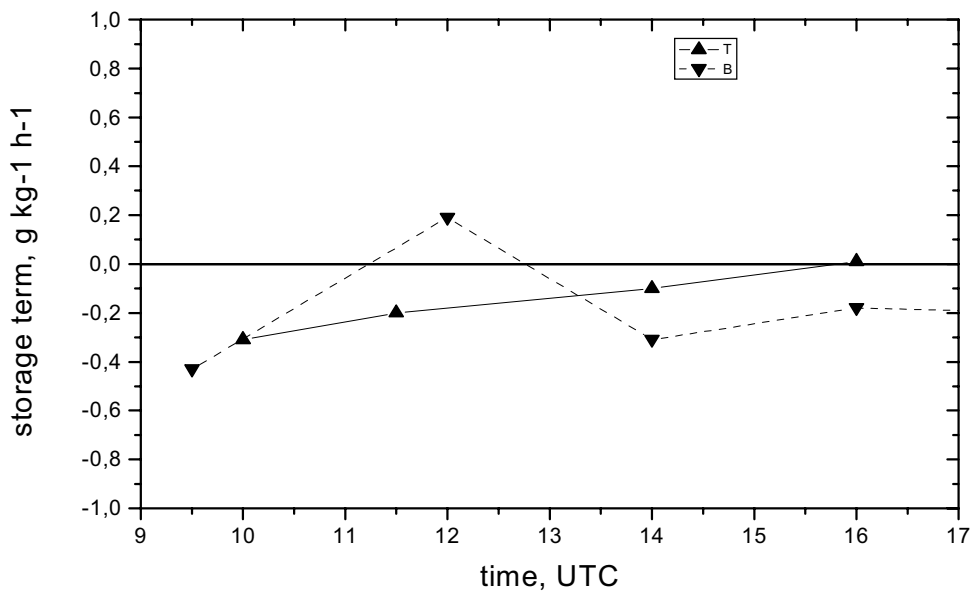
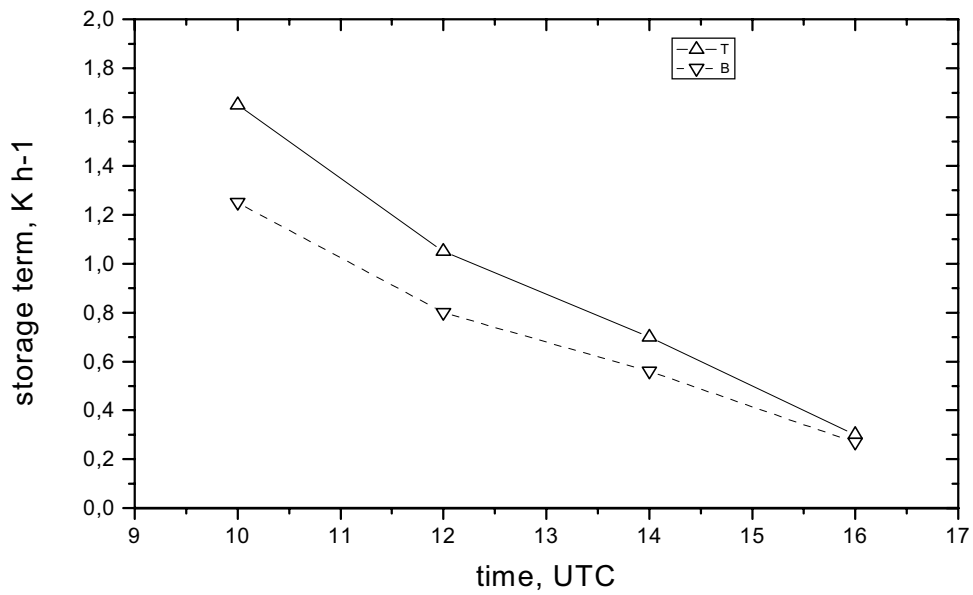


Figure 3-9. Time rate of change of potential temperature (top) and specific humidity (bottom) as obtained from synthesis of observing systems.

3.3 Vertical flux divergence

The heat and moisture flux was measured onboard the aircraft at different height levels (see Chapter 2). ML95 and Kratzsch (1994) have performed a detailed analysis of four "flux profile" flights conducted at different times during 23 July 1991. Their results are used here in the process of estimating the vertical flux divergence. Obtaining vertical flux profiles from single aircraft observations, however, is generally limited by the uncertainties associated with sampling the

large eddies at higher ML levels, especially in deep MLs. The limitations become more severe over heterogeneous surfaces and during rapid growth/decay phases. The flux sampling and stationarity requirements outlined in Chapter 2 are very difficult to meet simultaneously in single aircraft observations at any one level. The effect of combined single-level uncertainties on the errors of a whole profile is complex. Therefore, we have opted for a combined approach based on the ML slab model framework and using the aircraft observations to determine the entrainment closure parameter.

We start with the sensible heat flux. The moisture flux will be treated later in a different way.

The conceptual framework of a ML slab model (see Section 3.2 and full set of model equations as given in Annex B) applies to a horizontally homogeneous, well-mixed layer. Figure 3-5 confirms that at both sites, potential temperature is well-mixed and that the heating rate is uniform over the whole ML. Therefore, the vertical profiles of sensible heat flux are linear, i.e. $\overline{w'T'(z)}$ is a linear function of z between surface ($z=0$) and ABL top ($z=z_i$):

$$\overline{w'T'(z)} = \overline{w'T'(0)} + az, \text{ with the gradient } a = \frac{\overline{w'T'(z_i)} - \overline{w'T'(0)}}{z_i}. \quad (3.3a)$$

Assuming advection and radiative flux divergence to be of minor importance, the flux divergence balances the storage term:

$$\frac{\partial \theta}{\partial t} = \frac{\overline{w'T'(0)} - \overline{w'T'(z_i)}}{z_i} \quad (3.3b)$$

Combining Equations (3.3a) and (3.3b), we get the general expression:

$$\overline{w'T'(z)} = \overline{w'T'(0)} - \frac{\partial \theta}{\partial t} z \quad (3c)$$

A closure assumption is needed to proceed. Tennekes and Driedonks (1981) give the general formulation for the entrainment flux

$$\overline{w'T'_i} = A\overline{w'T'_0} + A' \frac{u_*^3 T_0}{gh} \quad (3.4a)$$

where the first term describes the buoyancy-generated flux and the second term corresponds to shear-generated flux and A, A' are constants. Shear generation of flux is important mainly in the early morning hours, when the ML is very shallow and the surface heat flux is small. During the time period of interest for this budget estimation, however, the shear generation is negligibly small. Therefore, we can use the simplified entrainment flux parameterization in form of the flux ratio model (Ball, 1960; Stull, 1988)

$$\overline{w'T'_i} = A\overline{w'T'_0} \quad (3.4b)$$

This allows us to obtain the sensible heat flux divergence from the combination of surface flux and ML depth z_i at any given time during the day:

$$\frac{\partial \overline{w'T'}}{\partial z} = \frac{(A-1)\overline{w'T'_0}}{z_i} \quad (3.4c)$$

In combination with Equation (3.3c), we obtain the sensible heat flux at a given height z from

$$\overline{wT}(z) = \overline{wT}(0) \left(1 - (1+A) \frac{z}{z_i} \right). \quad (3.4d)$$

We are using aircraft observations to derive the closure parameter A . It is generally taken to be 0.2 (Stull, 1988; Garratt, 1992), but higher values have been reported, e.g., by Betts (1992), van den Hurk (1996), and Tjernström and Smedman (1993). Angevine (1999) attempts a classification according to wind regime, aerosol load and inversion strength.

Figure 3-10 shows that the dependence on the value of the entrainment parameter is not overly critical here. We compare values of A from 0.2 to 0.4 for Tomelloso and Barrax on 23 June 1991, based on the site aggregated surface flux observations of Chapter 2. The calculation starts at 10:00 UTC, when the ML has grown sufficiently so that shear effects are not important any more. Throughout the day, the value of the closure parameter does not make any significant difference. The results for Barrax (shown here only for $A=0.3$) are very similar to those for Tomelloso during most of the day.

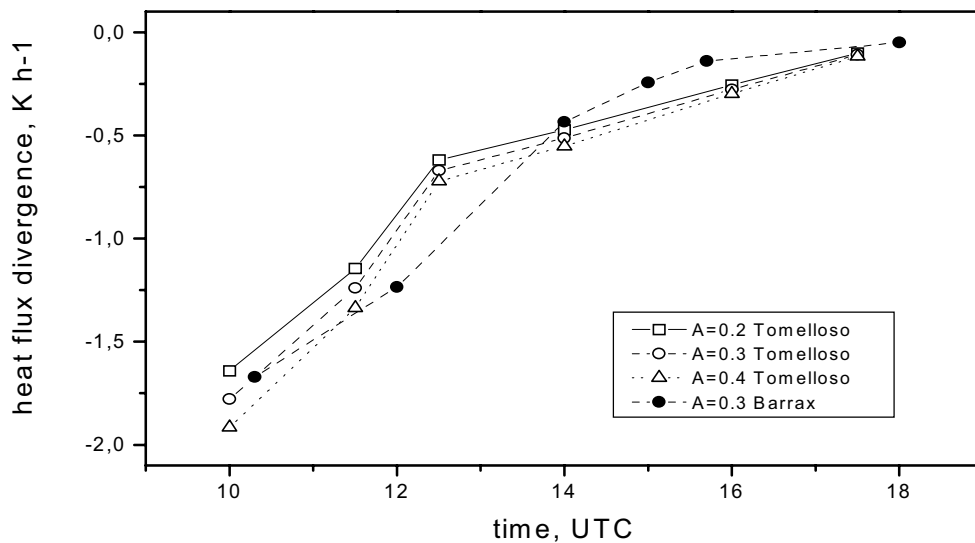


Figure 3-10. Vertical heat flux divergence estimated from surface flux observed at Tomelloso (open symbols) and Barrax (solid symbol) and different values of the entrainment parameter A (square/solid line: 0.2; circle/dashed line: 0.3; triangle/dotted line: 0.4).

We now proceed to derive the entrainment closure parameter A from aircraft observations. First we compare individual case vertical flux profiles and secondly, we perform a statistical comparison with a larger sample. For the 23 June case, we use the full set of available airborne observations (ML95 and Kratzsch, 1994) to cover the daytime evolution. Figure 3-11 gives the vertical profiles obtained with a range of closure parameters from 0.2 to 0.4, calculated from observed surface fluxes at Tomelloso averaged over 2-hour periods centered at 10:00,

12:00, 14:00, and 16:00 UTC, respectively. These periods coincide with the aircraft observations shown as symbols (circles: Falcon observations by MJ95; squares: Do 228 observations by Kratzsch, 1994, personal communication). Results from intercomparison flights have confirmed that the fluxes from the two aircraft are consistent (Kratzsch and Jochum, 1993). The error bars are based on flux uncertainty estimates after Mann and Lenschow (1994), using the integral scales of Lenschow and Stankov (1986). For the Falcon, only parts of flight legs in the vicinity of Tomelloso are included. We find very good agreement with the $A=0.3$ line. For the Do 228, all full legs are used, since segment data are not available. Therefore, the agreement is less good, especially in the early morning rapid ML growth phase, which is difficult to reproduce by a simple model anyway (see Chapter 4). At 14:00, the data points of legs over "Tomelloso-like" surfaces are close to both $A=0.3$ and $A=0.4$ lines. We conclude from this comparison that the simple approach yields realistic vertical heat flux profiles, valid from mid-morning to late afternoon. For the Tomelloso area, the closure parameter is around 0.3. A similar exercise for the Barrax area (not shown here) leads to values of A around 0.15-0.2. Both are in line with the classification ranges of Angevine (1999).

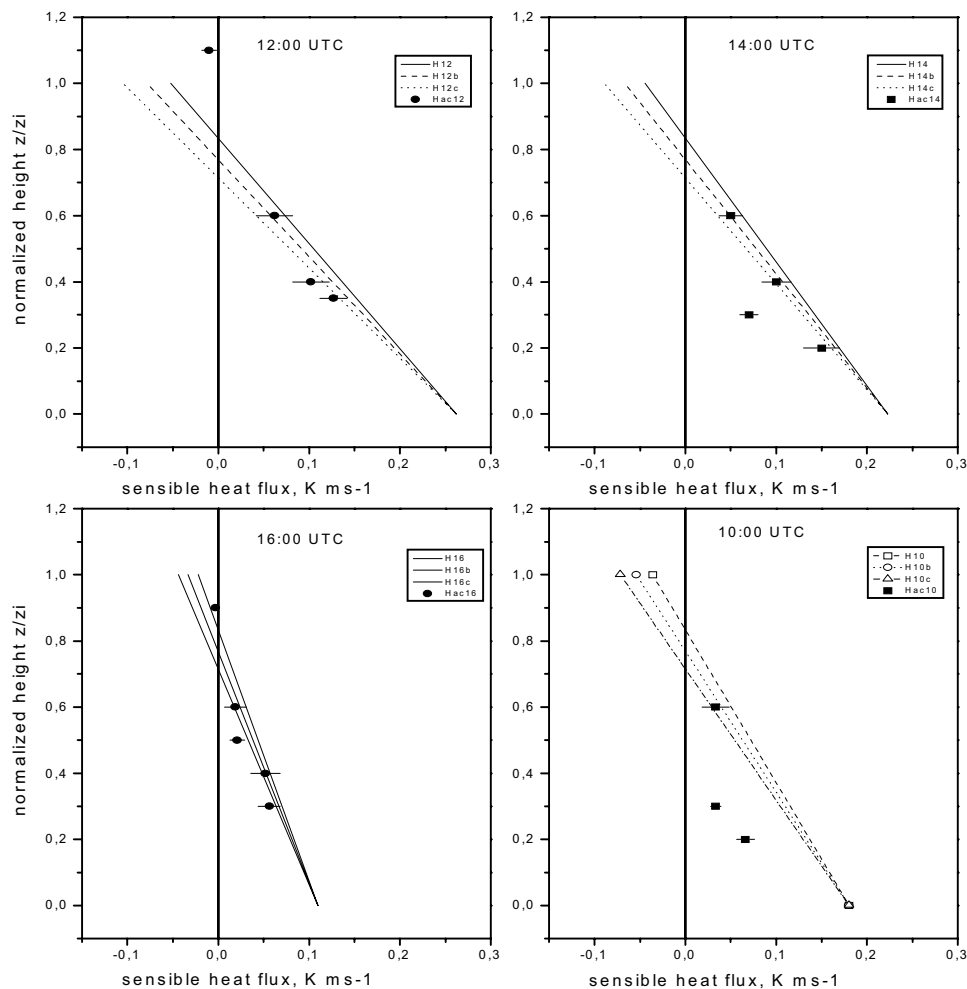


Figure 3-11. Vertical profiles of sensible heat flux at Tomelloso at four different times on 23 June 1991. Lines were obtained from observed surface fluxes and different values of closure parameter A (solid: 0.2; dashed: 0.3; dotted: 0.4). Symbols denote leg-averaged aircraft observations (circles: Falcon 20 covering Tomelloso only; squares: Do 228 covering all areas) with error estimates after Mann and Lenschow (1994).

For the statistical analysis, all Falcon observations during June 1991 were stratified into transects (i.e. parts of whole legs, generally 30 km or longer) flown in the vicinity of Tomelloso, Barrax, and Rada de Haro. Figure 3-12 shows the resulting scatter plots of sensible heat flux for the Tomelloso and Barrax class. The linear regression line gives a closure parameter of 0.3 for Tomelloso and of 0.16 for Barrax, at a significance level of 92% and 88%, respectively. The different closure parameters found in the two areas reflect the differences in the relative importance of surface- and entrainment-generated flux. As such, they are consistent with the ABL description at both sites given above (Section 3.3).

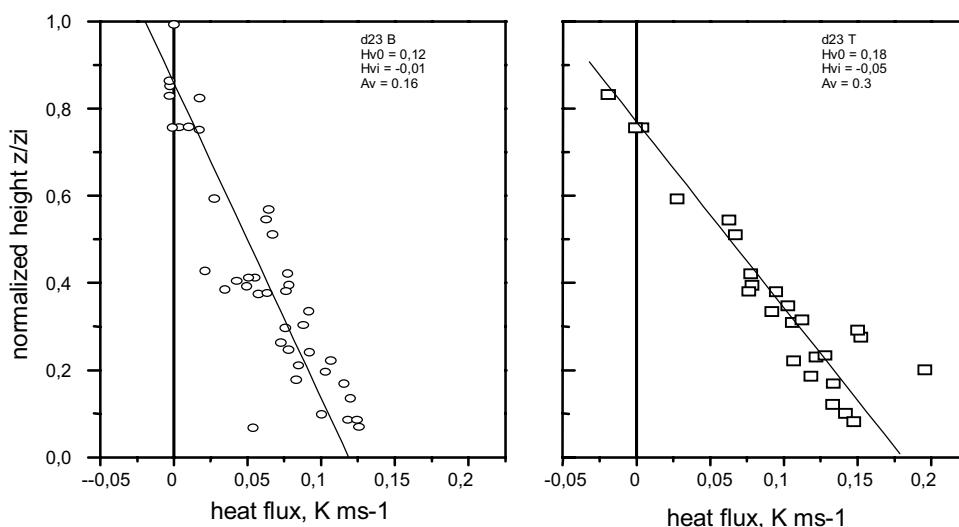


Figure 3-12. Noon vertical profiles of sensible heat flux at Tomelloso (right panel) and Barrax (left panel) for all fair weather days during June 1991. Solid lines give linear fit, with regression parameters as indicated in top right corner of each panel.

In conclusion, the entrainment closure approach was adopted to estimate vertical heat flux divergence from Equation (3.4c), with $A=0.3$ for the Tomelloso area and $A=0.16$ for Barrax, respectively. The errors introduced by this approach were estimated as $\pm 20\%$. The resulting final error in the flux divergence term does not significantly depend on A , as shown above. It is largely determined by the uncertainty of ML depth and to a lesser extent of the surface flux observations.

For moisture flux, the situation is different. Figure 3-6 shows that specific humidity is not well-mixed during a large part of the day and that the drying/moistening rate is not uniform over the layer. This means that the vertical moisture flux profiles are not necessarily linear and that the ML slab framework is not necessarily applicable. There is, however, observational and model-generated evidence on the quasi-linearity of the flux profiles, confirming that the approach is viable.

Two different three-dimensional mesoscale models were implemented and validated for the area. Fiedler et al. (1996) used a non-hydrostatic mesoscale model in the Barrax area. They find non-linear local scale flux profiles, but on an average over a 10 km by 10 km area their profiles are almost linear. Using a hydrostatic mesoscale model, Noilhan et al. (1997) find linear profiles at the whole-area scale as well. Aircraft observations of MJ95 and Grunwald et al.

(1996) confirm these findings. So the assumption of almost linear moisture flux profiles seems to be fairly well justified on scales relevant for this budget estimate.

Still, the closure is not as straightforward as in the case of heat flux. For moisture, the entrainment flux can be either positive or negative (according to the sign of the humidity jump) and depending on the relative importance of surface and entrainment flux, the vertical flux profiles can be convergent or divergent. This can be easily seen from Equation (3.5), which is the moisture counterpart to Equation (3c)

$$\overline{w'q'}(z) = \overline{w'q'}(0) - \frac{\partial q}{\partial t} z \quad (3.5)$$

Moisture flux divergence corresponds to an overall moistening ML, while flux convergence corresponds to a drying ML. The ML humidity remains constant whenever the surface evaporation balances the entrainment drying.

The inversion moisture flux is not driven by the surface flux alone, but is influenced by inhomogeneous moisture fields at meso- and larger scales (Chapter 5; Mahrt, 1991). Therefore, there is no simple closure assumption relating the inversion moisture flux to surface moisture flux. Consequently, additional observational information on the inversion moisture flux is needed to estimate the moisture flux divergence.

Direct airborne observations of inversion moisture flux are hardly available. Adequate flux sampling is more difficult than in the case of heat flux, because the integral scales (Lenschow and Stankov, 1986) are larger and variability is higher. The statistical scatter plots (Figure 3-13) are not conclusive either, even if stratified into the Tomelloso and Barrax areas. Some generic differences can be detected, like, e.g., the low surface flux combined with high entrainment flux at Tomelloso and the opposite at Barrax. But the scatter is still very large, not only due to inherent sampling uncertainties of moisture flux, but also reflecting the range of individual cases (where the degree of interplay between surface and large-scale processes varies from day to day).

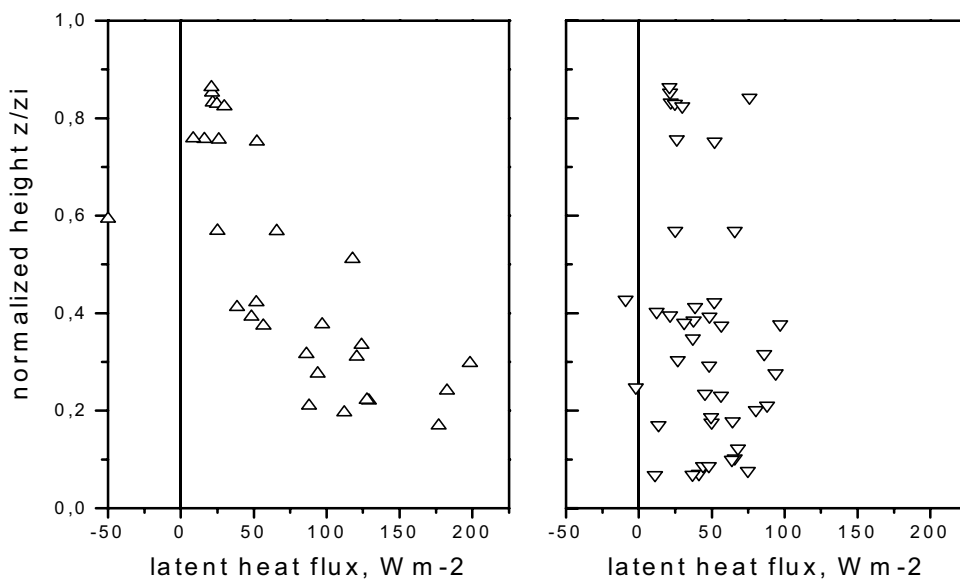


Figure 3-13. Noon vertical moisture flux profiles at Tomelloso (right) and Barrax (left) for all fair weather days in June 1991.

There is an observational alternative, however, since the entrainment-level Bowen ratio ($\beta_i = H_i/LE_i$) is more accessible to measurements. It is not affected by the sampling problems of eddy-flux measurements. Following Betts (1992) and others, the inversion level Bowen ratio can be obtained from radiosonde observations, using

$$\beta_i = H_i/LE_i = \frac{C_{pd} \overline{w'T'_i}}{L \overline{w'q'_i}} \approx C_{pd}/L \delta\theta/\delta q. \quad (3.6a)$$

Rearranging Equation (3.6a) shows how the inversion moisture flux can be obtained directly from the $\delta\theta/\delta q$ gradient and the inversion heat flux

$$\overline{w'q'_i} \approx \frac{\overline{w'T'_i}}{\partial\theta/\partial q} \quad (3.6b)$$

The $\delta\theta/\delta q$ gradient is found from mixing line diagrams like in Figure 3-14. Due to the sometimes erratic radiosonde profiles, the uncertainty is rather high ($\pm 50\%$).

Figure 3-14 shows the (θ, q) mixing lines for two soundings (noon and afternoon) at either site. Data points plotted for Barrax are averages over 100 m layers. Data points for Tomelloso give the original vertical resolution of 30-50 m for near-surface and near-inversion layers. The near-surface Bowen ratios obtained from the Tomelloso soundings agree fairly well with those calculated from surface observations. The inversion level Bowen ratios are determined by means of linear regression of all relevant data points. Selecting the relevant data points is straightforward only in the case of a clearly marked ML-FA transition with well-defined jumps in potential temperature and specific humidity, like in the afternoon soundings. The noon soundings present a real challenge, due to the RL structures overlying the ML as apparent in Figure 3-3 and Figure 3-14. The error depends very much on the adequate delineation of the ML top.

In the context of the ML slab framework, the inversion moisture flux can now be related to the surface moisture flux using the observed Bowen ratios in combination with the simple heat flux closure of Equation (3.3b). Introducing the definition of Bowen ratio $\beta (= H/LE)$ into Equation (3.3b) at both the surface (index 0) and entrainment level (index i) gives the following simple model for the inversion moisture flux

$$\overline{q'w'_i} = \overline{w'T'_i} / \beta_i^* = -A \overline{w'T'_0} / \beta_i^* = -A \beta_0 / \beta_i \overline{q'w'_0}. \quad (3.7)$$

where $\beta_i^* = \beta_i L/C_{pd}$ and $\beta_0^* = \beta_0 L/C_{pd}$. A is the same closure parameter as in the case of heat flux. The inversion-level Bowen ratio is found from equation (3.6b) and the surface Bowen ratio is easily obtained from the site-aggregated surface flux observations.

The vertical moisture flux divergence is finally estimated from the difference between the entrainment and surface fluxes and the ML depth. In a strict sense (i.e. without assuming linearity of the flux profile), this is a first order approximation of the ML average flux divergence. As such, it is consistent with other terms in the budget estimated on similar grounds.

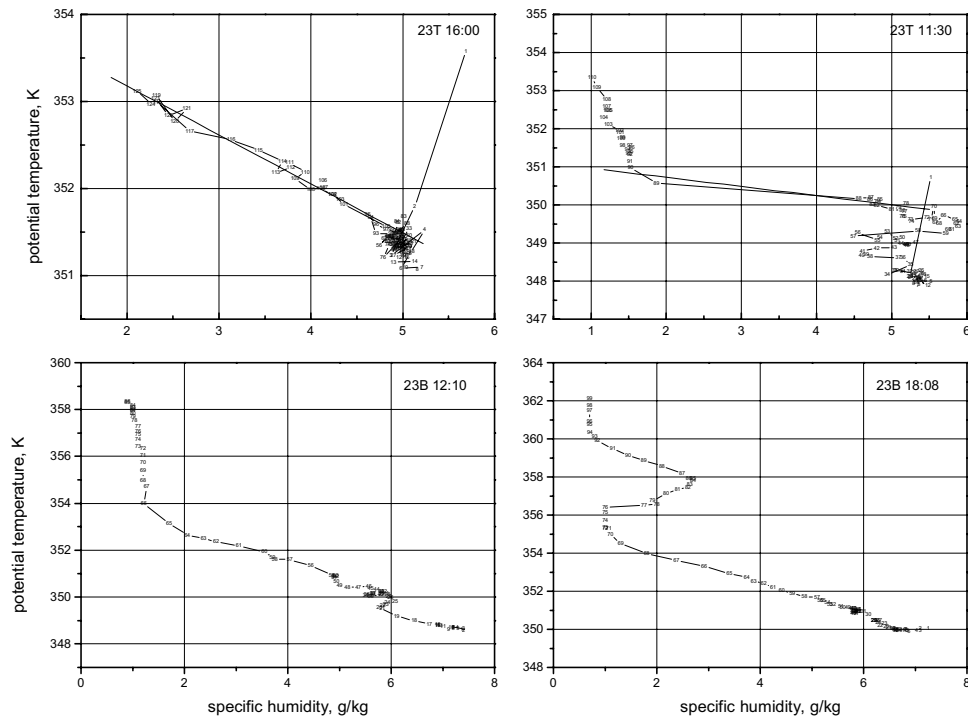


Figure 3-14. (θ, q) mixing lines for Tomelloso (top) and Barrax (bottom) radiosoundings at noon (left) and in the afternoon (right) of 23 June 1991. See text for determination of inversion Bowen ratio.

Table 3-1 summarizes the Bowen ratios and the resulting moisture flux divergences. There are a small number of aircraft data points available from the analysis of MJ95, which can be used as a qualitative check of plausibility rather than for validation. The orders of magnitude and signs of the near-inversion fluxes do agree. The mesoscale model simulation of Noilhan (1996) gives a much higher flux convergence at Tomelloso.

Table 3-1. Vertical moisture flux divergence at Tomelloso (T) and Barrax (B) on 23 June 1991. β = Bowen ratio. $\overline{w'T'}$ in K m s^{-1} , $\overline{w'q'}$ in $\text{g kg}^{-1} \text{m s}^{-1}$, divergence in $\text{g kg}^{-1} \text{h}^{-1}$.

	Inversion β	Inversion $\overline{w'T'}$	Inversion $\overline{w'q'}$	Surface $\overline{w'q'}$	$\overline{w'q'}$ divergence
T 10:00	-0.26	-0.0064	0.098	0.043	0.35 ± 0.22
T 12:00	-0.66	-0.0077	0.0468	0.0396	0.06 ± 0.08
T 14:00	-0.36	-0.0073	0.0812	0.356	0.086 ± 0.06
T 16:00	-0.34	-0.0047	0.05	0.0164	0.042 ± 0.015
B 10:00	-0.12	-0.0022	0.073	0.0704	0.015 ± 0.04
B 12:00	-0.255	-0.0033	0.0129	0.0848	-0.075 ± 0.008
B 14:00	-0.15	-0.0031	0.0828	0.078	0.006 ± 0.003
B 16:00	-0.3	-0.0019	0.0252	0.058	-0.02 ± 0.008

3.6 Vertical radiative flux divergence

This term is very often neglected due to lack of observations. Betts et al., (1992) and Barr and Betts (1997) give a rough estimate of 0.02 K/h radiative ML warming based on a general assessment of the meteorological situation, which helps them to close the energy budget. Frech et al. (1998) included the longwave (LW) radiative divergence into their budget estimates for the NOPEX area, using LW radiation measured onboard an aircraft. They find cooling on the order of 0.02-0.03 K h⁻¹ (about 50% of their ML warming). Even though this helps them to close the budget on one of two days, there is still the shortwave (SW) part of radiative divergence (which may be of equal magnitude and opposite sign) not accounted for. LeMone et al. (2001) used radiative transfer modeling to determine the vertical profiles of SW and LW flux divergence, accounting both for clear air and aerosol absorption processes. They obtain values of 0.02-0.05 K h⁻¹ of net warming due to clear air radiative processes. Depending on aerosol load (expressed in terms of visibility), the additional warming due to aerosol absorption processes was estimated in the range 0.03 - 0.19 K h⁻¹. All these studies refer to Northern or mid-latitudes (NOPEX, BOREAS, FIFE, CASES). Similar studies for the semiarid Mediterranean environment have not been reported so far.

For the first time, the SW and LW flux divergence is calculated here on the basis of spatially and temporally resolved aircraft observations at different altitudes. As explained in Chapter 2, the four components of radiative flux (SW and LW up- and downward flux) were directly measured onboard the aircraft and on the ground. We have calculated net radiation at the various levels and obtained its vertical divergence from these data. Since there is no flux sampling problem associated with these fluxes, local vertical profiles can be obtained from measurements along the same flight leg at different altitudes. The horizontal variability of radiative fluxes is discussed in more detail in Chapter 5. Figure 3-15 shows net radiation mean values over segments of 10 km length along a transect near Tomelloso. Figure 3-16 puts selected segment means into the context of the corresponding surface observations at Tomelloso (net radiation curve identical to Barrax). The apparent non-linearity in time and space is not surprising, given the space-time variability of the moisture and aerosol fields (see Chapter 4). Figure 3-16 was used to obtain the time trends from a sinusoidal fit, in order to remove them before calculating the vertical flux divergence between the different layers. Figure 3-17 gives the results for the same transect. All segment mean values close to Tomelloso and Barrax (from a total of 6 flight legs) were used to obtain the final source term estimates as summarized in Table 3-2. For the lowest level divergence, surface data were used in conjunction with the lowest aircraft level. Radiative transfer modeling was used to check the consistency between surface and aircraft observations. It indicates a slight high-bias for the surface data. For the late morning/noon transition period, the average low level radiative flux divergence is 0.11 K h⁻¹, which corresponds to a ML warming of 0.3 K over that period. The lower part of the ML experiences more warming than the upper ML. Since the values are comparable, a vertical ML average was derived for use in the energy budget. In the afternoon, however, the differences across the ML depth are pronounced. Warming continues in the mid- and upper ML, while the lowest layer is cooling strongly at a rate of 0.2 K h⁻¹.

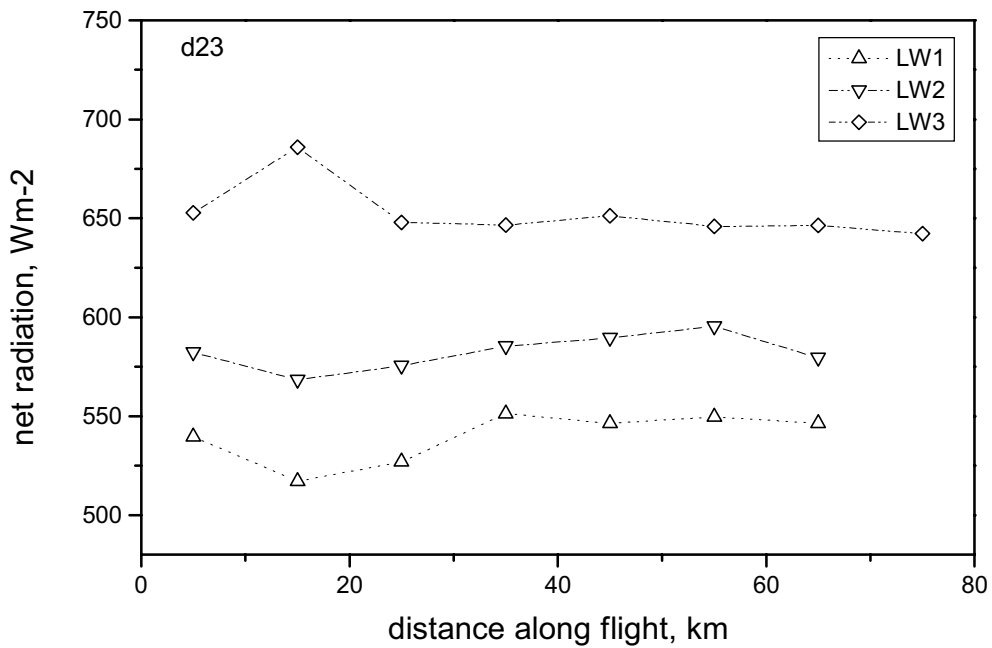


Figure 3-15. Net radiation around noon at three altitudes along a transect near Tomelloso on 23 June 1991. LW1 was flown at an average height above ground of 330 m, LW2 at 900 m, and LW3 at 2500 m.

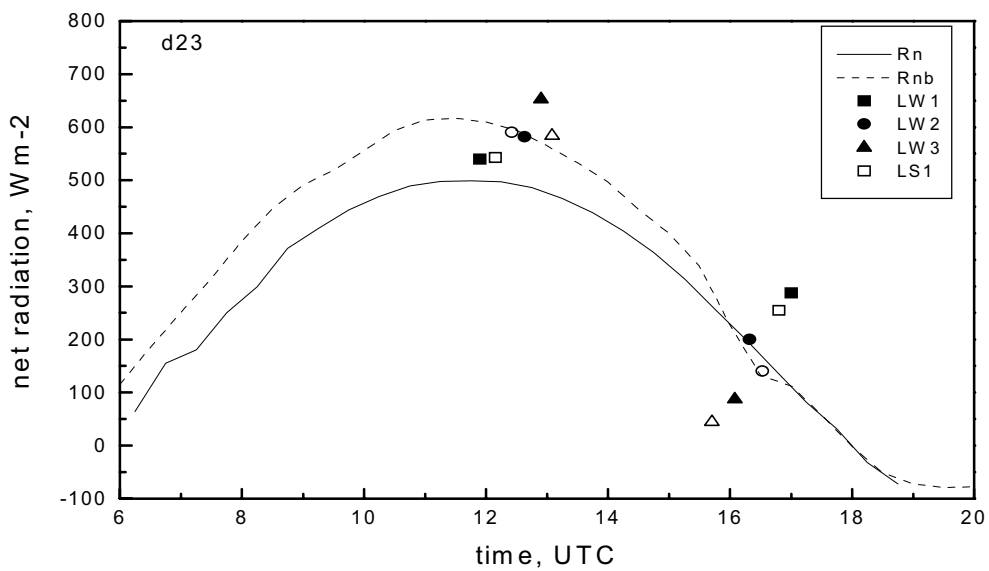


Figure 3-16. Net radiation at the surface and at three altitudes above Tomelloso and Barrax on 23 June 1991.

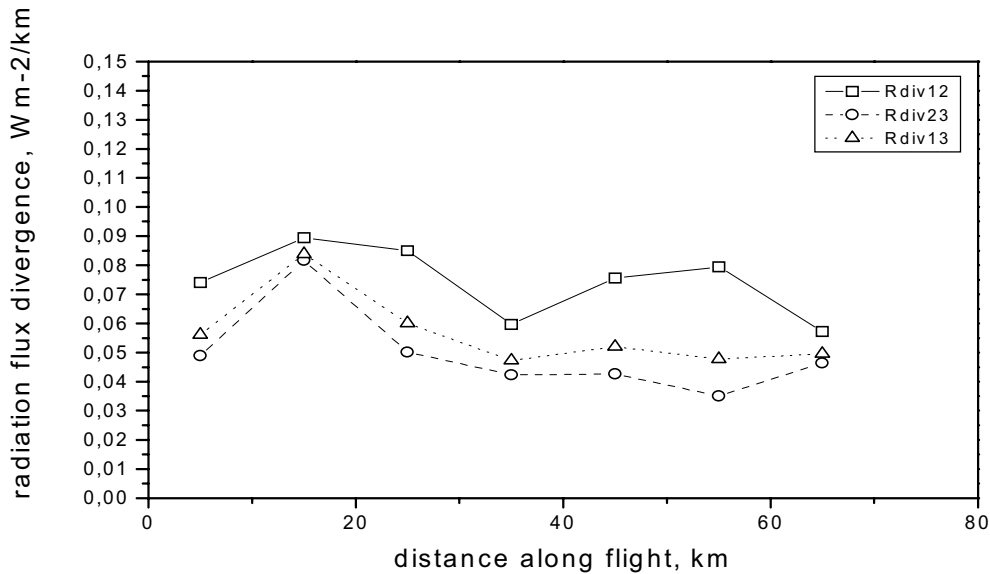


Figure 3-17. Net radiation flux divergence between the flight levels of Figure 3-15. Rdiv12 gives the divergence between levels LW1 and LW2, and accordingly for the other level combinations.

Table 3-2. Vertical divergence of net radiation flux (in $K h^{-1}$) of different layers on 23 June 1991. Errors are given in terms of standard deviation.

	Approximate height range	Tomelloso noon	Tomelloso afternoon	Barrax noon	Barrax afternoon
Low	sfc - $0.3 z_i$	0.13 ± 0.03	-0.2 ± 0.02	0.10 ± 0.03	-0.12 ± 0.03
Mid	$0.3 - 0.6 z_i$	0.07 ± 0.005	0.12 ± 0.005	0.05 ± 0.01	0.1 ± 0.008
High	$0.6 - 1.0 z_i$	0.04 ± 0.008	0.08 ± 0.005	0.04 ± 0.008	0.08 ± 0.005

3.7 Horizontal and vertical advection

As outlined in Chapter 2, the flight patterns were selected according to the structure of the underlying landscape rather than according to wind direction. In contrast to FIFE, e.g., (Betts et al., 1990) the alignment with the actual wind direction was not a dominant criterion here due to the rather low wind speed. As a consequence, both the alongwind and crosswind components of horizontal advection have to be calculated for each leg. On 23 June 1991 the wind in the lower and mid ABL was weak ($2-3 m s^{-1}$) and from the North ($u < 1 m s^{-1}$). Wind speeds consistently larger than $5 m s^{-1}$ were observed on two days only.

The u - and v -components of advection were calculated for the two lower aircraft levels (flown at approximately $0.3 z_i$ and $0.5 z_i$). The time trend was removed from each time series using the storage term as estimated in section 3.4. The results, as summarized in Table 3-3, show that the horizontal advection term is an order of magnitude smaller than the time rate-of-change and flux divergence terms. However, this result applies to the advection across the whole EFEDA area, since the full length of the flight legs was used in the calculation. This helps to keep the error at a reasonable size on one hand, but does not resolve any smaller scale horizontal gradients.

The time series of potential temperature along both flight legs (not shown here) suggest negligible differences in spatial gradients across the whole area. The specific humidity time series, however, reveal gradient variations between Barrax and Tomelloso in the afternoon (Figure 3-18 bottom). During the noon flight, the only marked differences concern the humidity fluctuations, which are much more pronounced over Barrax than in any other area (Figure 3-18 top). Using these local gradients, an attempt was made to estimate horizontal advection at the scales of the Tomelloso and Barrax areas. Due to the short distance, the absolute errors are larger, but the relative error remains on the order of 50%. We find increased moisture advection in the Barrax area during the afternoon (Table 3-3). Grunwald et al. (1996) did not perform a full budget analysis, but their results for the Barrax area corroborate these findings.

Table 3-3. Components of horizontal advection (in $W m^{-3}$) on 23 June 1991, at the scale of the whole EFEDA area.

	Noon, $S=\theta$	Noon, $S=q$	Afternoon, θ	Afternoon, q
$v*\partial S/\partial y$	0.0034 ± 0.002	0.01 ± 0.006	0.0041 ± 0.003	0.018 ± 0.006
$u*\partial S/\partial x$	$-6.1 E-5 \pm .001$	$-4.3 E-5 \pm .005$	$-3.2 E-5 \pm .001$	$-6.2 E-5 \pm .005$
Total hor. adv.	0.0034 ± 0.002	0.01 ± 0.006	0.0041 ± 0.003	0.02 ± 0.006

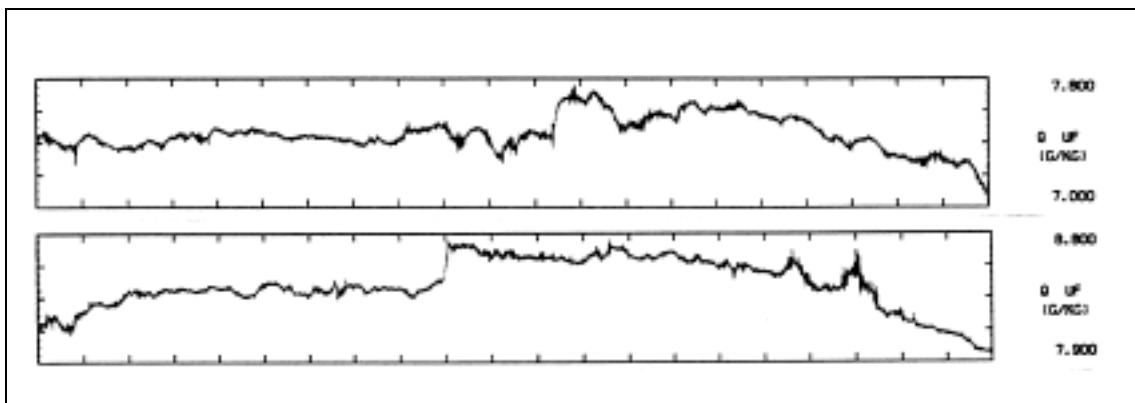


Figure 3-18. Spatial series of specific humidity along the Tomelloso-Barrax transect at noon (top) and in the afternoon (bottom) of 23 June 1991 (from Jochum, 1993b). A spatial series is obtained from the observed time series by means of conversion to distance along flight track using actual true air speed of the aircraft.

The vertical advection term in the budget is usually neglected, based on the assumption that temperature and moisture are very well mixed. As we have seen in section 3.1, temperature is reasonably well mixed here, while moisture is not, especially in the Barrax area (Figure 3-6). In fact, several features in the radiosonde vertical profiles and in the horizontal flight leg time series might indicate the presence of divergence and/or convergence and the associated vertical air motion.

To obtain this term from measurements is extremely difficult (Stull, 1988). It means moving within the very limits of observational uncertainty with respect to each contributing variable. Therefore, an initial simple estimate was made to determine the order of magnitude of divergence and subsidence. For the case of Barrax, the vertical moisture gradient is about $1 g/kg/km$. Assuming a rather weak vertical air motion of $0.1 m s^{-1}$, we obtain a vertical moisture advection of $0.18 g kg^{-1} h^{-1}$. This is the same order of magnitude as the storage and flux

divergence terms. Even for much less pronounced vertical gradients of about 0.1 g kg^{-1} per km, a vertical air velocity of 0.1 m s^{-1} still gives a vertical advection of $0.036 \text{ g kg}^{-1} \text{ h}^{-1}$. In conclusion, the vertical advection of moisture may significantly contribute to ML drying or moistening.

3.8 Discussion and conclusions

We have investigated the physical processes that contribute to heat and moisture transport in the EFEDA area by means of an atmospheric boundary layer (ABL) budget study. Mixed layers of different characteristics were observed at rather short geographical distance (80 km) between the two main supersites. Moisture plays the key role here. The Tomelloso site is an extensive wine-growing area representative of semiarid conditions, with a surface energy balance dominated by the sensible heat flux. The Barrax site is characterized by additional moisture supply from two sources, one at the ground from irrigation and one aloft from the Mediterranean sea breeze often penetrating inland in the afternoon. The resulting ABL at Barrax is generally moister, slightly cooler and less deep than at Tomelloso.

Our budget analysis is based on the synergistic combination of a comprehensive observational dataset and a simple coupled canopy-ML model. The observational dataset consists of distributed micrometeorological surface stations, radiosondes, flux aircraft, and an airborne water-vapor differential absorption lidar (DIAL). In particular the unique aircraft dataset includes the four radiation flux components, from which the full radiative divergence can be derived. By providing a large sample of heat and moisture flux observations throughout the ML depth, it supports the analysis of the vertical flux divergences in a ML slab framework.

Airborne DIAL- and radiosonde-derived humidity crosssections and profiles show that the residual layer (RL) above both sites is characterized by a layered moisture structure. The resulting entrainment moisture fluxes vary in magnitude and sign over a large part of the diurnal cycle. The determination of the vertical moisture flux divergence becomes a challenging task under these circumstances.

The results for the temperature budget are summarized in Figure 3-19. As we have seen in Figure 3-9, the overall ML warming is larger at the dry Tomelloso site at any time during the observed period (10-16 UTC). At both sites, the warming peaks in the morning and slows down along the day. This behavior is fairly typical of summertime convective boundary layers. Again at both sites, the ML warming is balanced by a combination of heat flux divergence and radiative flux divergence (Figure 3-19). Horizontal temperature advection is found to be small at the whole EFEDA area scale. At the individual site scale (where the observations did not resolve this term), the budget residual is small at all times, which indicates that horizontal advection is small also there. The absolute values of the radiative flux divergence vary only slightly with time and between sites, but their relative importance in the budget is greater at Barrax and in the afternoon. The magnitudes are consistent with the high aerosol load and low visibility observed in the area most of the time. LeMone et al. (2001) find slightly lower values from radiative transfer modeling.

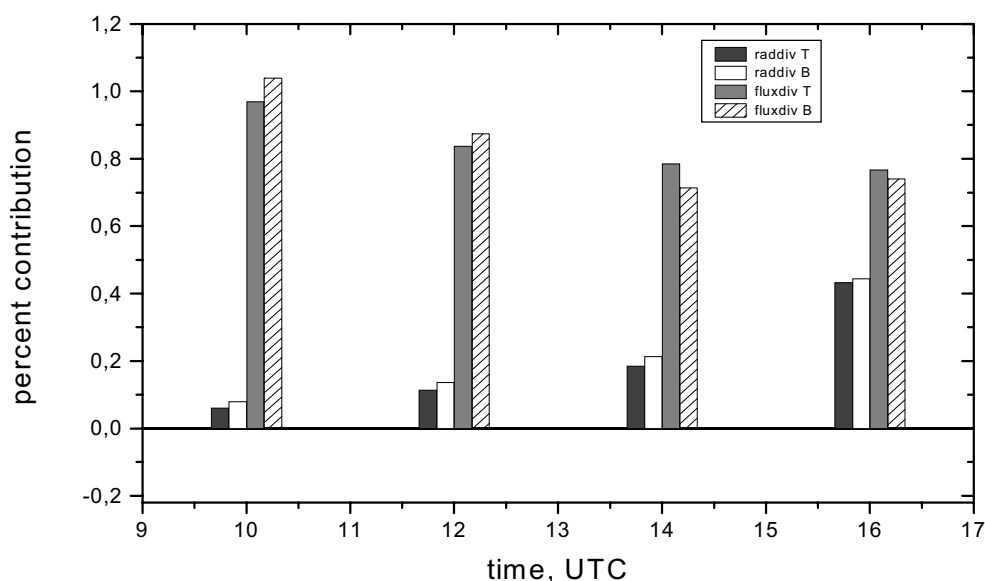


Figure 3-19. Budgets of temperature at Tomelloso and Barrax for 23 June 1991: percent contribution of heat flux divergence ("fluxdiv") and radiative divergence ("raddiv").

The vertical heat flux divergence was estimated from a simple entrainment flux closure parameterization in the framework of a ML slab model, where the entrainment closure parameter A was derived from aircraft measurements on the basis of the entire midday anticyclonic sample. This increases greatly the statistical significance of the A -estimate and the resulting flux divergence. Determining the flux divergence directly from aircraft observations on each day would have led to higher uncertainties. Given the limited sample size of aircraft observations at other times of the day, the same value of A is used for the entire period of the budget estimate (10-16:00 UTC). We have seen that the errors thus introduced in the temperature budget are small. In general, however, A may well vary over the day. Our midday values (0.3 for Tomelloso and 0.16 for Barrax) are within the range of values found by others. It has become clear that the textbook value of $A=0.2$ applies to a limited range of conditions and needs to be checked in any given situation. Angevine (1999) finds a dependence of A on radiative warming, wind regime, and inversion strength. The EFEDA data sample is too uniform to allow for any such stratification.

In contrast, the moisture flux divergence is not accessible through such a simple and general approach. Given the day-to-day variability of the entrainment flux forcing (see below), inversion level moisture fluxes were estimated for each individual day.

The results for the moisture budgets are summarized in Figure 3-20. In the moisture budget, we have two main terms resolved by the observations, storage and vertical flux divergence. These are mostly again of comparable importance, but sometimes of the same sign. Consequently, the residual would sometimes be quite large if only these two terms were accounted for.

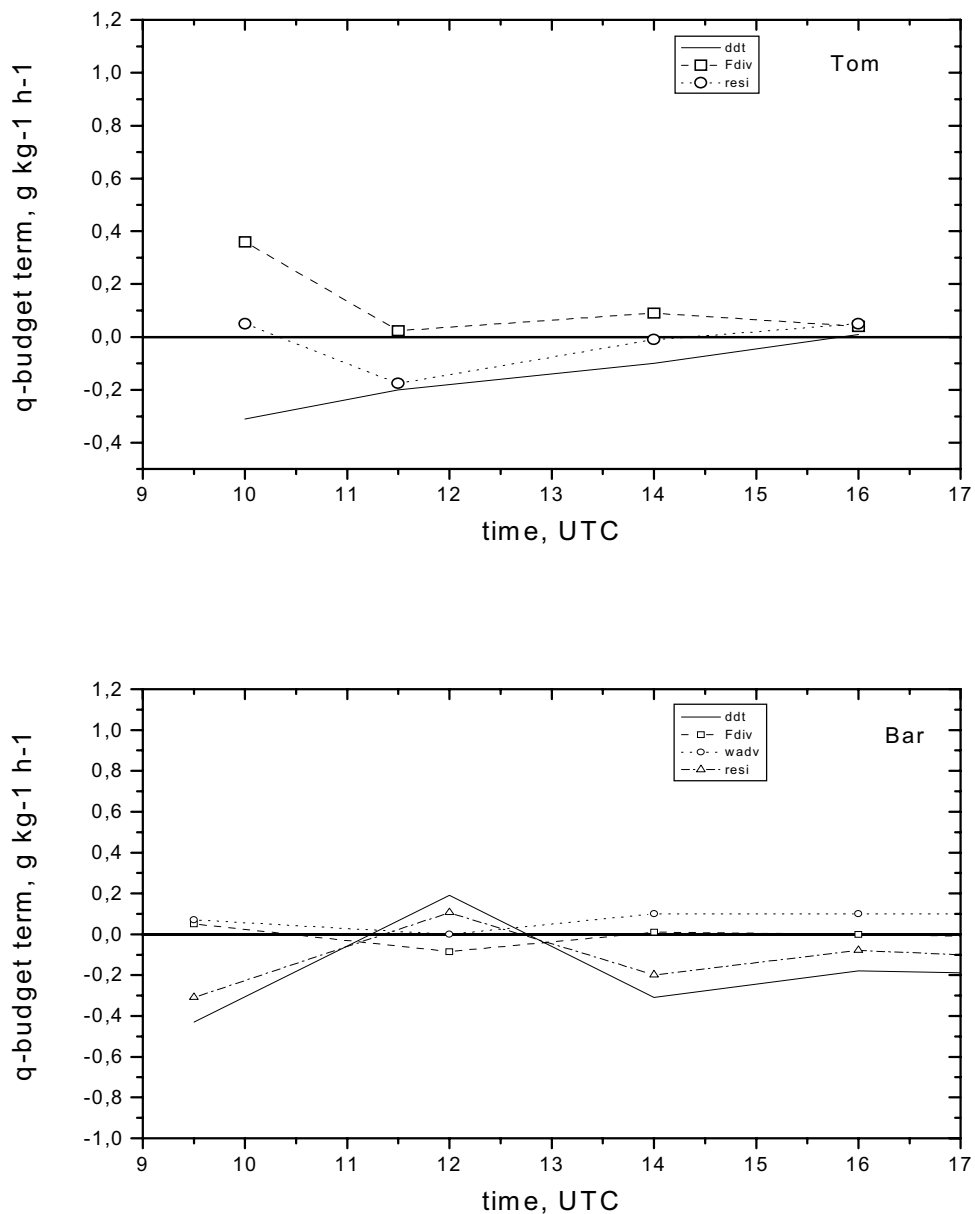


Figure 3-20. Components of moisture budget at Tomelloso (top) and Barrax (bottom) for 23 June 1991. All units are $\text{g kg}^{-1} \text{h}^{-1}$. Errors as given in Tables 1-4.

The situation at Tomelloso (Figure 3-20 top) may look simple, but actually requires some further consideration. The ML part of the successive vertical humidity profiles gives a clear picture of continuous ML drying throughout the day. The RL part of the same soundings, however, draws the attention to the positive q -gradients in the morning hours (Figure 3-3). Once the ML comes in contact with this RL, it will entrain moist air. Then, the entrainment moisture flux will become negative and the moisture flux profile will become divergent. The inversion Bowen ratio is then positive and the inversion-Bowen-method of Equation (3.6b) or (3.7) would correctly give a negative inversion moisture flux.

Running the ML slab model with the observed RL q -gradients (i.e. with differing γ - q for different time periods) leads indeed to a short period (about one

hour) of divergent moisture flux and associated ML moistening (Figure 3-21). However, the RL moisture structure is not preserved in the afternoon. Due to the Tomelloso sounding data gap in the decisive period (12-16:00 UTC), this cannot be validated observationally. Aircraft ascent data taken in the North of the EFEDA area (with comparable q -profiles) indicate a slight ML moistening between 12 and 13:00 UTC. Aircraft-derived inversion level Bowen ratios obtained at/after 13:15 give values characteristic of entrainment-drying (-0.36). Thus the q -budget entry at 11:30 UTC in Figure 3-20 may correspond to the time just before the transition from drying to moistening, while the following entry (13:30) may already reflect the time after the moistening event has occurred. We can only speculate that the q -budget of the (instationary) midday moistening event would look very differently from Figure 3-20.

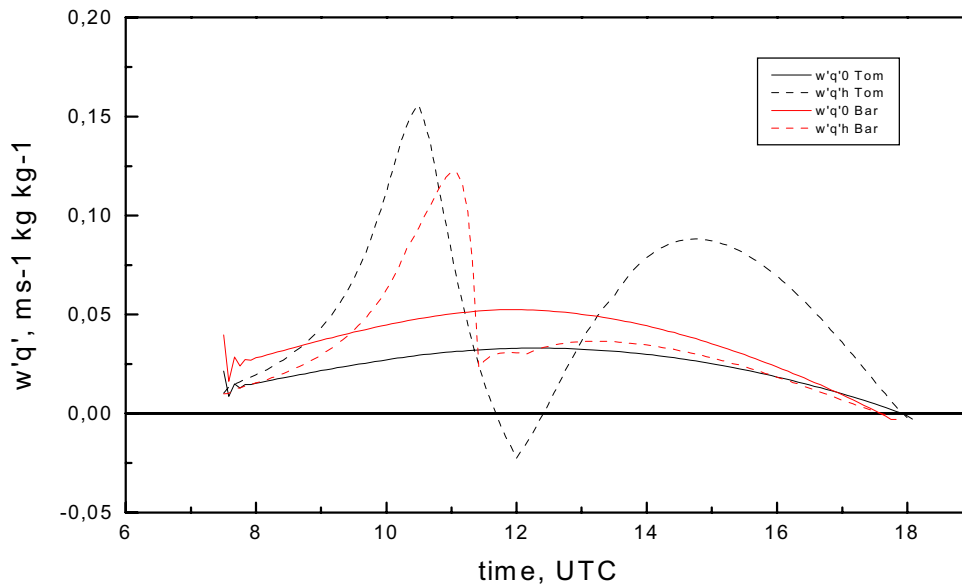


Figure 3-21. ML slab model-calculated surface and inversion level moisture fluxes.

The situation is different for the Barrax site (Figure 3-20 bottom). There, we have clearly identified a midday moistening period in the vertical soundings, along with a divergent ("moistening") flux profile. The strong morning ML drying corresponds to a convergent moisture flux profile, which is in accordance with entrainment-drying and with an inversion level moisture flux even larger than the irrigation-enhanced surface flux. The afternoon budgets show moderate drying and weakly convergent flux profiles. At all times we find pronounced vertical slopes in the q -profiles. The vertical moisture advection term (see section 3.6) is therefore included in the budget estimates. The remaining residual could well be explained by horizontal advection, which is difficult to assess from observations at the scale of Tomelloso or Barrax, except for the afternoon moisture advection. We have seen in Section 3.5 that horizontal temperature and moisture advection at the whole EFEDA area scale is small compared to the main budget terms. Estimation of local gradients in the afternoon gives increased moisture advection at Barrax. The observational analysis of the Barrax ABL by Grunwald et al. (1996) supports these findings. This also agrees with results from model simulations (Fiedler et al., 1996, and Noilhan et al., 1997) that local advection of moist air from the Mediterranean does play a role in the Barrax area in the afternoon.

The origin of the observed differences between the moisture budgets at the two sites can be explored by means of a simple consideration relating the ML drying/moistening to the Bowen ratios at the surface and the inversion. Following Betts (1992) we have used the inversion level Bowen ratio β_i to estimate the inversion moisture flux in a ML slab framework. Similar to his critical surface Bowen ratio, we define the critical inversion Bowen ratio as that β_i where $\frac{\partial q}{\partial t} = 0$ and obtain β_{ic} as a function of the surface Bowen ratio β_0 :

$$\beta_{ic} = A(\beta_0 + 0.07) - 0.07, \quad (3.8)$$

where A is the entrainment closure parameter and the value of 0.07 corresponds to the Bowen ratio of the virtual adiabat. The dependence on A is more pronounced here than in the case of the heat flux divergence.

From Figure 3-22 we see that at Tomelloso, after 10:00 UTC we are always in the drying regime, as long as the inversion Bowen ratios remain within a summer convective range (-0.2 to -0.4). Within this same range, we are much closer to the separating curve at Barrax. Obviously, this is related to the role of surface evaporation, which is enhanced by irrigation at Barrax. However, advection-generated inversion level Bowen ratios (as found in part of the EFEDA RLS) can give rise to crossing the critical curve at any given time. This means that the entrainment moisture fluxes could then be of any sign and would not be related to ABL processes and scales only. Consequently, the driving forces of ML warming/cooling and drying/moistening are partly independent of each other. Heat transport occurs mainly at local ABL scales, while moisture transport is influenced by a wider range of scales. Similar non-local scales of moisture transport were also observed in HAPEX-Mobilhy and NOPEX, e.g., by Mahrt (1991) and Frech et al. (1998).

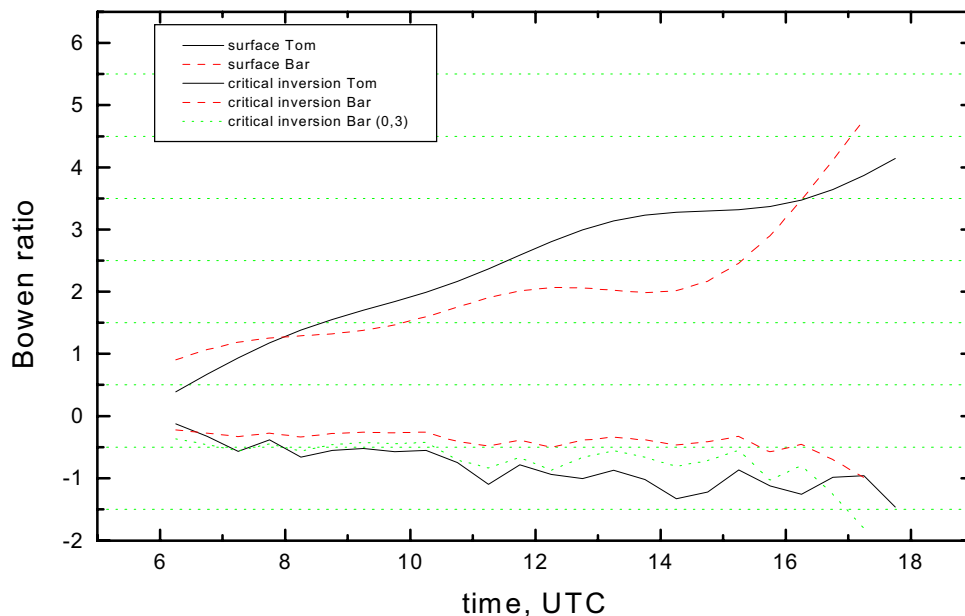


Figure 3-22. Critical inversion Bowen ratio and surface Bowen ratio at Tomelloso and Barrax. Inversion level Bowen ratios smaller than critical (absolute magnitudes) correspond to drying regime. See text for details.

In conclusion, the ML warming is balanced by a combination of the heat flux divergence and the radiative divergence. The radiative flux divergence was directly obtained from aircraft measurements here. Its absolute values vary only slightly with time and between sites, their relative importance is greater at Barrax and in the afternoon. The magnitudes are consistent with the high aerosol load and low visibility observed in the area most of the time. Temperature advection is found to be small and the heat budgets are fairly closed using aircraft-derived midday entrainment closure parameters of 0.3 (Tomelloso) and 0.16 (Barrax), respectively. These values are well within the range of other observations (e.g., Angevine, 1999).

The evolution of the moisture budgets over the observed period is more complex. It is related to the inhomogeneous moisture structure of the RL, with gradients of changing sign. The ML is drying at both sites as long as it erodes the dry NBL. As soon as it gets in contact with the positive humidity gradients in the RL, the entrainment flux becomes negative until the moister air has been fully entrained. This midday moistening event lasts only a short time (1-2 hours) before the ML starts drying out again from above. This sequence was clearly identified in the series of four moisture budgets at Barrax. At Tomelloso, it was probably missed by the data, but it is evident in the ML slab model calculation. Thus, the moisture budgets show clearly the influence on non-ABL scales on the moisture transport, which is also reflected in the lack of simple entrainment closure parameterization for moisture flux. A simple model relating the surface and inversion level Bowen ratios is used to derive the moisture flux divergence. With inversion level Bowen ratios generated by advection (like in the case of the inhomogeneous RLs), the entrainment moisture fluxes are not related with ABL processes and scales only. Accurate high-resolution vertical humidity profiles are needed to properly estimate these fluxes. The coupled canopy-ML slab model proves to be a valuable tool in this complex environment, if it is regularly provided with updated RL gradients.

This non-local characteristic of moisture transport is found at both sites. However, the ML drying or moistening may evolve differently at either site on any given day, because it depends on the relative importance of surface vs. entrainment flux. A simple model confirms that the potential for moisture flux divergence and associated ML moistening is higher at Barrax, where irrigation enhances the surface evaporation.

4 Scales in flux parameterization

The EFEDA area is heterogeneous in many ways and at many scales. A quantitative assessment is needed before the topics of aggregation and flux parameterization can be addressed. This is the objective of the present chapter. More specifically, it aims at performing the following steps:

1. to identify landscape features that generate heterogeneity in the surface and atmospheric forcing and to quantify the scales of the heterogeneous forcing;
2. to assess its impact on ABL processes and turbulent transfer in a general framework for spatial averaging to large-scale model grid scale;
3. to assess the impact on flux parameterization and its dependence on scale.

We analyze the scale dependence of the bulk aerodynamic relationship using low-level aircraft observations. For the first time, this is investigated here for semiarid Mediterranean landscapes.

4.1 Landscape scales and forcing

Landscape scales originate essentially from the topography, geomorphology, soils, hydrology and land-use of a given area, which are all interrelated to a certain degree. In the case of the EFEDA area, the topography is the most prominent landscape feature. As described in Chapter 2, the EFEDA area is generally rather flat, with elevation variations of less than 20 m in the South and 100 m in the North. The elevation spectra of the EFEDA area are not conclusive, due to the rather small variations within the area. Terrain undulations in the South and the North are on scales larger than the area.

The EFEDA area is part of the Southern sub-plateau, which extends on a scale of 200 km in the East-West and about 100 km in the North-South directions. The plateau is almost completely surrounded by mountain ranges. It is open only to the Southwest (following the Guadiana river basin to the Atlantic ocean) and to a small extent to the Northeast (following the narrow Júcar river basin to the Mediterranean sea).

The topography of the Iberian peninsula further affects the mesoscale to synoptic scale circulation in and around the EFEDA area in two special ways. One is the frequent generation of thermal lows in the summer, with their preferred center located around 3°W / 37.5°N, i.e., about 150 km to the South of Tomelloso (Portela and Castro, 1996). The other is the sea breeze frequently penetrating up to 70 km inland from the Mediterranean coast in the afternoon (Habets, 1994; Noilhan, 1996; Fiedler et al., 1996; Miao et al., 2002).

The landuse varies according to the fertility of the soils and the water availability. Irrigation agriculture is concentrated in the Southeast and to a lesser extent in the West. Field sizes range from 4 to 30 ha. The major landuse-induced influence on the surface forcing comes from irrigation, which generates distinctly different surface energy budgets as compared to dry fields (see Chapter 5). Differences between dry land-use classes (dry agriculture, natural vegetation, fallow land) are much less significant.

The scales of land-use-induced surface forcing were determined by means of spectral analysis, using the reflective properties of the surface (albedo and NDVI) as indicators. Figure 4-1 shows the example of an albedo spectrum obtained from

airborne radiation measurements. We use the measured true air speed of the aircraft (on average 120 m s^{-1}) to convert frequency into length scale. Given the leg length of 60-100 km, frequencies above 0.006 s^{-1} (corresponding to roughly 20 km) are considered resolved. Figure 4-2 shows the probability distribution of these albedo-related length scales as obtained from all relevant flight transects. We find a concentration on 4-6 km scales (close to the maximum boundary layer eddy size, see below), then again on 10-12 km and on 18 km.

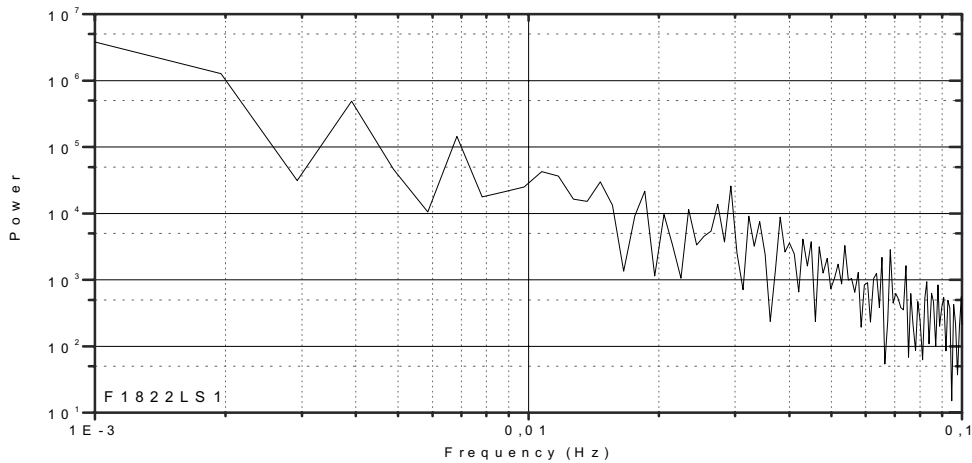


Figure 4-1. Albedo spectrum along low-level aircraft transect Tomelloso-Barrax on 23 June 1991.

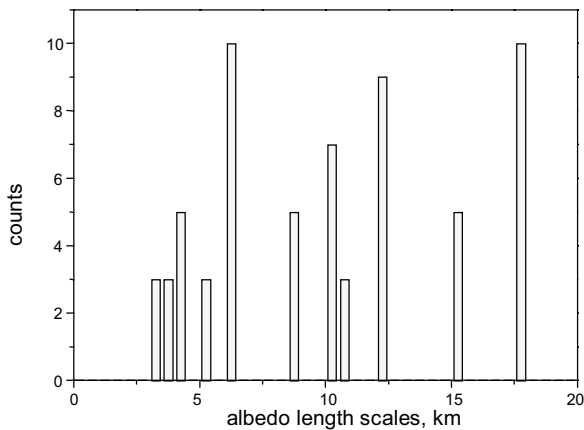


Figure 4-2. Histogram of length scales based on analysis of albedo spectra from all relevant flight transects.

4.2 ABL scales and heterogeneity regimes

We first determine the scales relevant for surface and ML similarity scaling. Dealing with daytime ABLs, the first important scale is ML depth z_i . As described

in Chapter 3, z_i has been determined from radiosoundings at the two supersites Tomelloso and Barrax. There is much more detailed information on mean values and horizontal variability in airborne lidar observations (see below) which on the other hand are limited to a few case studies. Resuming here, the final ML depth is about 3 km, often reached in the late afternoon. This is then the scale of the boundary layer eddies.

The Obukhov length L was determined from surface and aircraft observations as

$$L = \frac{-u_*^3}{\kappa \left(\frac{g}{\theta_v} \right) \overline{w'\theta_v'}} \quad (4.0)$$

with the von Karman constant κ and the buoyancy parameter g/θ_v . The local (flight altitude) values obtained from low-level aircraft agree quite well with the surface observations. L varies in the range of -2 to -20 m (daytime). Momentum flux (and thus, L) data are not available at the irrigated Barrax field. The largest values were observed at Belmonte, due to the higher momentum flux in the slightly hilly terrain.

The stability parameter z_i/L indicates the strength of convective activity and the respective role of buoyancy and shear-generated turbulence. It ranges from -5 to -60. We find moderately buoyant convection in the morning (smaller values) and vigorous mixing in the afternoon (larger values).

The variability of these basic ABL scales across the area is rather small. The ML depth difference between Tomelloso and Barrax is up to 10%. Variability on the same order of magnitude is revealed by airborne lidar along horizontal transects through the whole area (Jochum, 1993b). Spectral analysis of these ML depth transects shows the major dominating wavelength at the scale of the boundary layer eddies (3-6 km). The Obukhov length varies less than 20% between the supersites and less than 10% along low-level aircraft transects.

In contrast, the variability of the forcing-related scaling parameters (e.g., the surface fluxes) is significant and mainly tied to contrasting surface evaporation in dry and irrigated land (see Chapter 5). Therefore, the validity of the local similarity relationships (e.g., Stull, 1988) cannot automatically be extended to larger areas. This applies equally to the bulk surface and ABL parameterizations in large-scale models, which are based on these similarity relationships. This is commonly referred to as the aggregation problem in heterogeneous landscapes, where spatial averaging concepts are sought that preserve most of the simple structure of local parameterizations by means of effective parameters. As a first step in that task, we seek to identify heterogeneity regimes of the EFEDA area.

As described in Chapter 1, the scales of heterogeneity have been classified according to their aggregation properties (de Bruin, 1987; Shuttleworth, 1988; Raupach, 1991, 1993; Mahrt, 1996). The first discrimination criterion is how far in the vertical the effect of a given surface feature extends, before it is mixed by/into the horizontal flow. At the local scale, this has been investigated in the framework of internal boundary layers (IBLs). When air passes above a surface discontinuity, an IBL is formed. Well below the IBL top, the air is in equilibrium with the new surface. Above the IBL top, the flow carries the characteristics of the upwind surface. Wieringa (1986) introduced the concept of the blending height l_b for a patchy landscape as the level above all IBLs where surface heterogeneities are no longer felt. Mason (1988) formalized this concept and Wood and Mason (1991) extended it to non-neutral ABLs. Mahrt (1996) (M96

hereafter) has further extended these ideas into a general framework of spatial averaging for heterogeneous landscapes. He proposes a hierarchy of scaling regimes characterized by conceptual models and delimited by simple length scales. In a way, he is re-organizing the results of previous and his own work in a scheme that can serve as flow-chart in actual spatial averaging tasks. This framework is used here to assess the scaling properties of the EFEDA area and at the same time to assess the applicability of those length scales for this type of area.

Figure 4-3 (from M96) shows the different regimes as a function of the observing level (assumed well below the ML top). We are in the blending regime as long as we are above the blending height. There, local time-averaging is still valid. As soon as the top of the equilibrium layer is higher than the observation level, each surface patch needs to be treated separately as a homogeneous sub-area. In between the two regimes we find the transition zone (above the equilibrium layer and below the blending height), where any flux estimate represents local conditions only. The homogeneous sub-areas are commonly referred to as tiles (Avisar and Pielke, 1989; Koster and Suarez, 1992) or patches (Raupach, 1991, 1993). Equations (4.2)-(4.5) give the definition of the corresponding length scales. The partitioning scale L_p is defined as that horizontal scale where the blending height coincides with the reference level. Frech and Jochum (1999) derived an additional blending regime scale for heat L_{ph} . The minimum horizontal scale for homogeneous subareas L_{hom} is defined as that scale where the top of the equilibrium layer reaches the reference level.

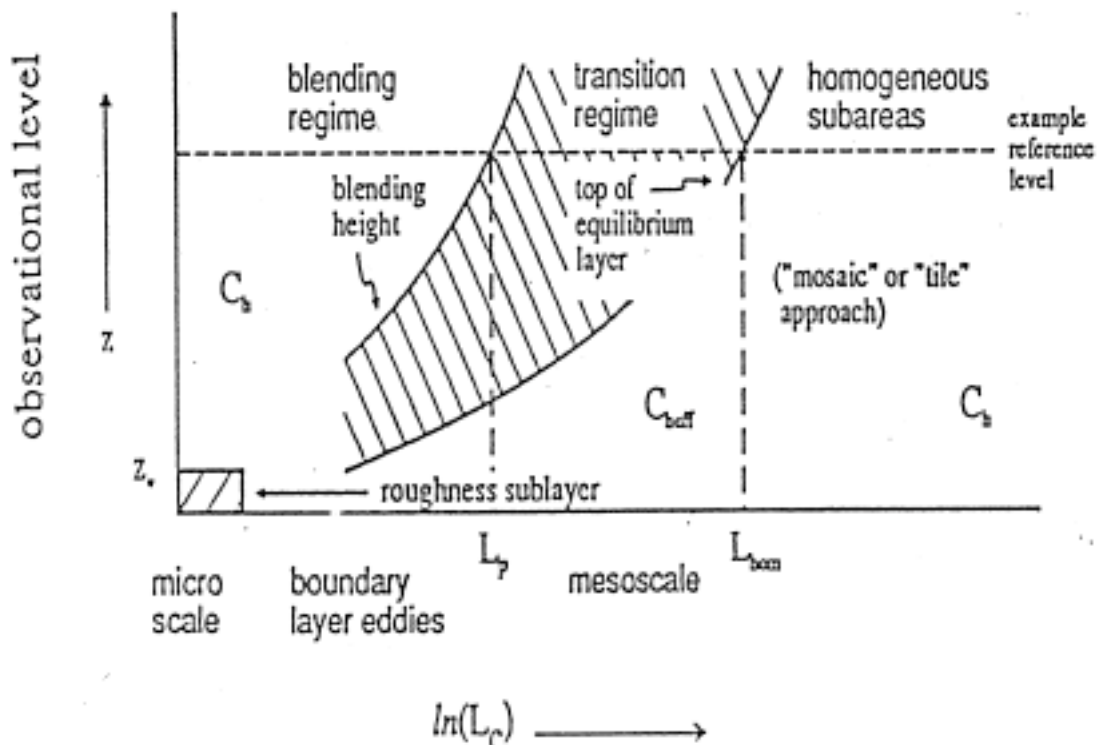


Figure 4-3. Spatial averaging regimes and associated length scales in heterogeneous terrain (from Mahrt, 1996). See text for details and definitions of length scales.

Mahrt (1996) gives a simple estimate of the blending height l_b as a function of the surface forcing scale L_c

$$l_b = 2 C_m L_c \text{ (neutral)} \quad (4.1a)$$

$$l_b = 2 (\sigma_w/U)^2 L_c \text{ (non-neutral)} \quad (4.1b)$$

where C_m is the drag coefficient.

The partitioning length scales after M96 and Frech and Jochum (1999) are

$$L_p = \frac{zU^2}{2\sigma_w^2} \quad (4.2)$$

$$L_{ph} = \frac{z}{w'\theta'} \frac{U\sigma_\theta}{\sigma_\theta/\theta + \sigma_U/U} \quad (4.3)$$

$$L_{hom} = \frac{zU}{c_E \sigma_w} \quad (4.4)$$

$$L_{therm} = \frac{T c U^3}{g w'\theta'_0} \quad (4.5)$$

where c and c_E are constants and with the notation as in Chapter 3.

Surface forcing heterogeneity at still larger scales has been shown to have the potential of inducing mesoscale circulations, the most common of which is the sea breeze (e.g., Miao et al., 2002). Anthes (1984) first introduced the idea of secondary circulations generated by vegetation heterogeneity. The topic has been studied intensively by means of numerical modeling (e.g., Chen and Avissar, 1994; Lynn et al., 1995; and Avissar and Schmidt, 1998). It has been concluded that inhomogeneous surface forcing at scales larger than about 10 km has the potential to generate secondary circulations and that the minimum scale depends on wind speed. M96 includes the regime of secondary circulations in his scheme (Figure 4-3) and suggests a simple formulation of the minimum scale necessary to generate thermal circulations (Eq. (4.5)). A similar relationship to Eq. (4.5) was proposed by Doran et al. (1995).

The full set of midday aircraft observations in the surface and lower ML (0.06-0.3 z_i) was used to estimate the first three scales from Equations (4.2)-(4.4). In the given height range, there is hardly any height dependence in L_p , L_{ph} , and L_{hom} . The limiting scale for the blending regime L_p can be interpreted as the maximum upwind fetch scale that is felt at the reference level z . It has rather low values for EFEDA, ranging from 200 m to 4 km, with most of the observations concentrated at 500-1500 m. This is obviously due to the generally low wind speeds combined with strong vertical mixing. The thermal blending regime scale L_{ph} is somewhat larger, in the range 2-15 km. Frech and Jochum (1999) find ranges of 1-5 km (L_p) and 2-16 km (L_{ph}) in the NOPEX area, where wind speeds were higher and the mixing less vigorous.

The limiting scale for the tile regime (homogeneous sub-areas) L_{hom} is smaller than L_p , which would suggest that the blending regime is not applicable in our

case. On the other hand, Eq. (4.4) contains a free constant c_E (set equal to 1 by M96), which can be used to adapt the order-of-magnitude regime boundaries to specific cases. The scale dependence analysis in the following section shows that the blending height approach is indeed applicable, which means that C_E is smaller than 1 here.

Figure 4-4 suggests a weak dependence of L_p on the stability parameter z_i/L (except for the very few extreme cases of $-z_i/L$ higher than 30), while there is hardly any correlation between L_{hom} and z_i/L . We will discuss the further implications of these scales in the next section.

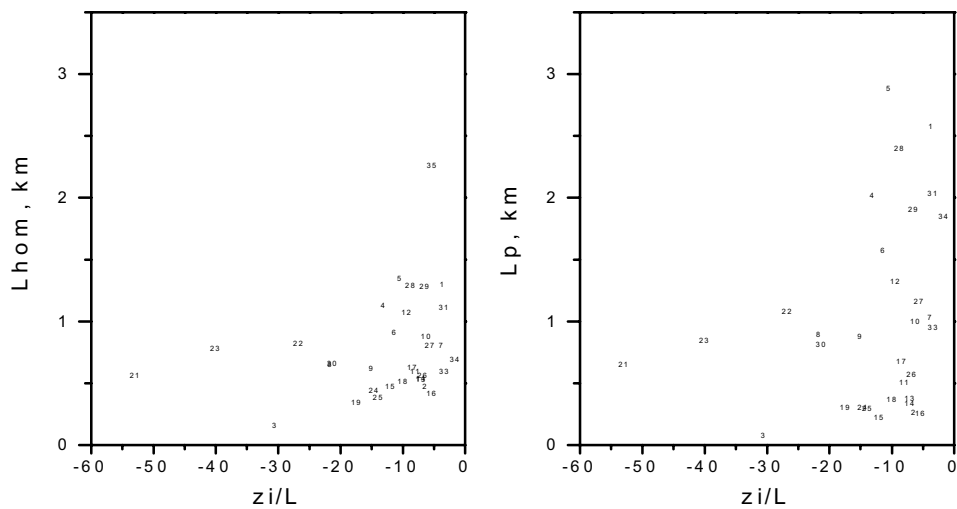


Figure 4-4. Length scales L_p and L_{hom} versus stability parameter z_i/L .

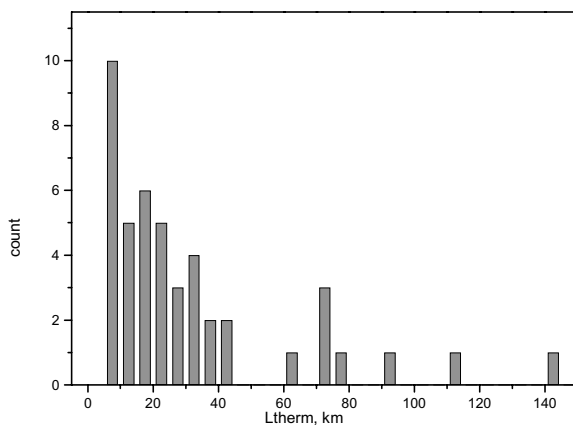


Figure 4-5. Histogram of minimum scales for generation of thermally-induced mesoscale circulations (L_{therm}) after M96 and Doran et al. (1995).

The minimum scale length for thermally-induced circulations L_{therm} (Eq. (4.5)) depends strongly on ambient wind speed and to a lesser extent on surface heat flux. The wind was mostly weak during the EFEDA period, thus creating the

opportunity for secondary circulations to develop and to be maintained. Figure 4-5 shows the distribution of L_{therm} estimates from all surface layer and up to mid-ML flight legs. We find the major concentration in the 5-30 km range. The values above 60 km are all "seen" from the flight transect height range 0.3-0.5 z_i . The observed range of L_{therm} indicates that potential thermally-induced circulations are well within the scales of the area and thus, could potentially occur. Now it would be up to each case study to find observational evidence in pro or contra.

The observational area coverage and spacing of EFEDA is not sufficient to perform a rigorous analysis of secondary mesoscale circulations. The study of Shaw and Doran (2001) has been quite unique in that respect. Yet, their major conclusion might apply to the EFEDA area as well, even though the area is smaller and some of the conditions are different. Shaw and Doran (2001) demonstrate observationally the existence of secondary circulations on the scale postulated by numerical modeling (Lynn et al. 1995; Avissar and Schmidt, 1998), but conclude that "topographical variations appear to be more important than land use differences in generating these circulations". In the case of EFEDA, several observational results give indications of secondary circulations. One of them is the different ABLs over the dry Tomelloso area and over the irrigated Barrax area (Fiedler et al. 1996; Chapter 3). Simultaneous radiosoundings of wind fields at both locations reveal horizontal divergence (Chapter 3). Aircraft flux measurements reveal significant mesoscale flux contributions (Chapter 5). The generally complex flow field is also reflected in the highly inhomogeneous aerosol backscatter and moisture fields observed by airborne differential absorption lidar (DIAL). Figure 4-6 shows an example of a vertical cross-section along an East-West transect. The challenge lies in identifying a unique source of these circulations. The land use differences capable of generating thermal circulations result from irrigation. Now there is a concentration of irrigation in the Barrax area, but only less than 30% of the fields are actually irrigated there, which probably would not generate the gradient in surface heating required for thermal circulations to develop. Additional sub-synoptic circulations (due to the sea breeze, the surrounding topography, and/or thermal lows) will probably interfere and overlay any area-specific circulation. Miao et al. (2002) have performed 3D numerical simulations with a non-hydrostatic mesoscale model. They find strong impact of the topography on the sea breeze and on the wind field divergence/convergence pattern in the EFEDA area.

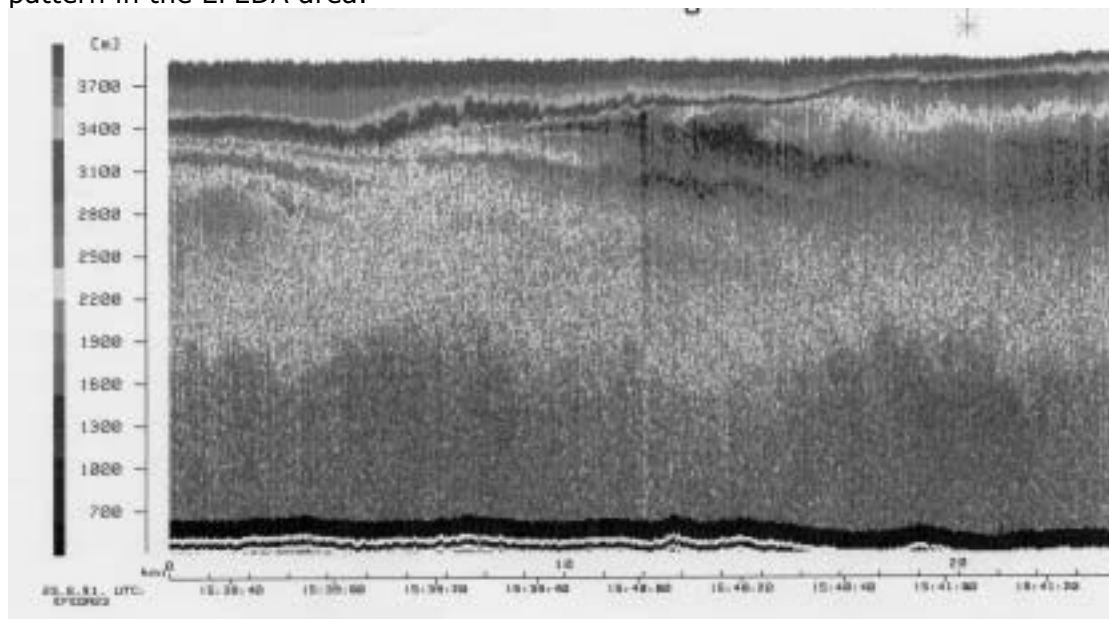


Figure 4-6. Aerosol backscatter cross-section along East-West transect obtained from airborne DIAL on 23 June afternoon.

4.3 Scale dependence of exchange coefficients

Current surface parameterization schemes in NWP and climate models use some version of the bulk aerodynamic relationship to obtain the grid-scale turbulent fluxes. This relationship is based on similarity theory, which in a strict sense is valid only at the local scale. Its application to grid-size scales is not automatic, nor straightforward, because of the inherent non-linearity of the processes involved. Aggregation methods provide a framework for scaling-up from the local to the grid scale. Many modeling studies have been performed to study the aggregation mechanism (see Chapter 1). A much smaller number of observational studies is available on the subject. In spite of many limitations, aircraft observations are the only adequate data source for this purpose. Mahrt and Sun (1995a) showed the implications of averaging scale on exchange and drag coefficients in the bulk aerodynamic relationship by using aircraft data from four different field experiments. There, the drag coefficient showed a notable dependence on averaging scale, whereas the exchange coefficients for heat and moisture transfer only exhibit a weak dependence. In the case of scale-independence, the local similarity theory may still be used.

Frech and Jochum (1999, hereafter FJ99) investigated the scale-dependence of exchange coefficients for momentum and heat transfer in a forest dominated heterogeneous boreal landscape by comparing the results of four different flux aggregation methods with aircraft observations from NOPEX (Halldin et al., 1997, 1999). Their main result is a strong scale dependence of the heat transfer coefficient, which is explained by the generally small temperature difference between atmosphere and surface and the negative temperature difference over lakes. These findings were corroborated by a control experiment with increased surface temperature and by comparing with observations from EFEDA (Table 7 of FJ99), which do not reveal any scale dependence of the heat transfer coefficient.

The approach of FJ99 has the advantage of directly addressing the grid-scale exchange coefficients, as defined in Equations (4.6)-(4.8), without entering in their calculation from surface layer similarity (Equations (4.9)-(4.12)). Thus, it circumvents the problem of determining effective roughness lengths for momentum and heat discussed by Beljaars and Holtslag (1991) and van den Hurk and Holtslag (1997). We have performed a similar analysis as FJ99, using aircraft observations from EFEDA. Four aggregation methods were evaluated, viz., the bulk, tile, blending height, and block approaches. The bulk approach applies the similarity relationships at grid-scale. The block approach does the same for a regularly spaced sub-grid, thus mimicking the effect of a higher-resolution grid. The blending height approach (Wieringa, 1986; Wood and Mason, 1991) assumes that the internal boundary layers above each land-use class have been blended by turbulent mixing and will not be recognizable above the blending height. The tile approach deals with the surface layer above each land-use class separately before spatially averaging the resulting fluxes (Avissar and Pielke, 1989). These concepts were discussed in the preceding section.

The bulk aerodynamic relationship parameterizes the fluxes in terms of the vertical gradients of the mean quantities. It is commonly expressed as in Equations (4.6) to (4.8) (Stull, 1988; Garratt, 1992; Beljaars and Holtslag, 1991), where the overbars denote time averages:

$$\overline{u_*^2} = C_m \overline{U^2} \quad (4.6)$$

$$\overline{w'\theta'} = C_h \overline{U} (\overline{\theta_a} - \overline{\theta}) \quad (4.7)$$

$$\overline{w'q'} = C_q \overline{U} (\overline{q_a} - \overline{q}) \quad (4.8)$$

with exchange coefficients C_m and $C_h=C_q$ that include the stability correction of Paulson (1970)

$$C_m = \kappa^2 \left(\ln \left(\frac{z}{z_0} \right) - \Phi_m \left(\frac{z}{L} \right) \right)^{-2} \quad (4.9)$$

$$C_h = \kappa^2 \left(\ln \left(\frac{z}{z_0} \right) - \Phi_m \left(\frac{z}{L} \right) \right)^{-1} \left(\ln \left(\frac{z}{z_{0h}} \right) - \Phi_h \left(\frac{z}{L} \right) \right)^{-1} \quad (4.10)$$

$$\Phi_m = 2 \ln \left(\frac{1+x}{2} \right) + \ln \left(\frac{1+x^2}{2} \right) + \frac{\pi}{2} \left(1 - \frac{4}{\pi} \tan^{-1} x \right) \quad (4.11)$$

$$\Phi_h = 2 \ln \left(\frac{1+x^2}{2} \right), \text{ where } x = \left(1 - 16 \frac{z}{L} \right)^{1/4} \quad (4.12)$$

The bulk aerodynamic relationship has been derived for time averaged local variables. It is defined for stationary, horizontally homogeneous conditions. Mahrt (1996) discusses the problems that arise when it is applied to heterogeneous landscapes. As explained above, there are two issues to consider, first, the scale of the heterogeneity of the surface (section 4.1) and second, how far up into the ABL the flow experiences the heterogeneity (section 4.2). When applying the bulk aerodynamic relationship to heterogeneous conditions, the time-averages in Equations (4.6) - (4.8) are redefined as spatial averages and the local exchange coefficients C_m and C_h become effective exchange coefficients $C_{m,eff}$ and $C_{h,eff}$. Mahrt and Sun (1995a) propose new empirical effective exchange coefficients that include the effects of sub-grid heterogeneity in conjunction with an extended velocity scale that equally includes the subgrid mesoscale velocity.

Our evaluation is based on midday aircraft observations from low-level transects (0.06-0.15 z_i). The aircraft height is taken as the reference level and is conceptually assumed to represent the lowest model level. The whole flight leg (60-100 km long) is assumed to represent the model grid scale. Segments of the flight leg will then correspond to model tiles, which are defined by means of the land-use classification of Calera (2000). We show the results from two different legs (composited from several flights under similar conditions) crossing the area in East-West direction and statistics from all relevant legs. Leg ML1 in the very South of the area connects the Southern part of the Barrax and Tomelloso pilot zones and passes over slightly hilly terrain in between. Leg ML4 crosses near the center and covers very flat terrain only. Table 4-1 gives the leg characteristics. Six segments were defined for ML1 and four for ML4, based on an objective segment selection algorithm (Howell, 1994) applied to airborne albedo measurements.

Table 4-1. Aircraft leg characteristics ML1 and ML4. Fluxes in $W m^{-2}$.

	Length (km)	Elevation variation (m)	H whole leg	H segment average	LE whole leg	LE segment average	w^* ($m s^{-1}$)
ML1	69	146	219	207	111	106	1.45
ML4	63	33	185	180	123	112	1.35

Applying the bulk aerodynamic relationship in the four aggregation methods results in the expressions of the grid-scale exchange coefficients as given in Box 4-1.

Box 4-1. Exchange coefficients in four aggregation approaches (after FJ99).	
$[C_m]_G = \frac{[u_*^2]}{[U^2]}$ $[C_h]_G = \frac{[w'\theta']}{[U][\{\theta_s\}] - [\theta(z)]}$ $[C_h]_G = \frac{[w'\theta']}{[U][\{\theta_s\}] - [\theta(z)]}$	<p><u>Bulk (index G):</u></p> <p>All input variables are averaged over the whole leg. This is the exchange coefficient corresponding to the grid resolution of the model.</p>
$[C_m]_B = \sum_{i=1}^n f_i \frac{u_{*i}^2}{[U^2]}$ $[C_h]_B = \sum_{i=1}^n f_i \frac{\{w'\theta'\}_i}{[U][\{\theta_s\}_i] - [\theta(z)]}$ $[C_h]_B = \sum_{i=1}^n f_i \frac{\{w'\theta'\}_i}{[U][\{\theta_s\}_i] - [\theta(z)]}$	<p><u>Blend (index B):</u></p> <p>The mean variables at the reference level are averaged over the whole leg, whereas the fluxes are averaged over segments of land-use. This corresponds to the blending height approach. The reference values are grid average values, which are assumed to be at the blending height.</p>
$[C_m]_T = \sum_{i=1}^n f_i \frac{u_{*i}^2}{U_i^2}$ $[C_h]_T = \sum_{i=1}^n f_i \frac{\{w'\theta'\}_i}{\{U\}_i (\{\theta_s\}_i - \{\theta(z)\}_i)}$ $[C_h]_T = \sum_{i=1}^n f_i \frac{\{w'\theta'\}_i}{\{U\}_i (\{\theta_s\}_i - \{\theta(z)\}_i)}$	<p><u>Tile (index T):</u></p> <p>Both the mean values and the fluxes are averaged over the land-use segments. This corresponds to the tile approach.</p>
$[C_m]_R = \frac{1}{m} \sum_{i=1}^m \frac{u_{*i}^2}{U_i^2}$ $[C_h]_R = \frac{1}{m} \sum_{i=1}^m \frac{\{w'\theta'\}_i}{\{U\}_i (\{\theta_s\}_i - \{\theta(z)\}_i)}$ $[C_h]_R = \frac{1}{m} \sum_{i=1}^m \frac{\{w'\theta'\}_i}{\{U\}_i (\{\theta_s\}_i - \{\theta(z)\}_i)}$	<p><u>Block (index R):</u></p> <p>The mean values and the fluxes are averaged over a fixed segment length of 5 km without taking the land surface heterogeneity into account. This can be interpreted as using results from a model with regularly spaced, fixed higher spatial resolution.</p>
<p>Square brackets indicate grid-scale averages, curled brackets represent sub-grid scale averages (tiles and segments). n and m are the numbers of tiles and segments, respectively. f_i are the area fractions of the tiles (Σf_i=1).</p>	

Figure 4-7 shows the exchange coefficient for heat transfer along ML1. The open symbols mark the values of the exchange coefficient for the individual segments (which are identical for the blend and tile approach and 5 km fixed-length for the block approach). The horizontal lines with open symbols at either end represent the grid-scale mean (effective) exchange coefficients as computed from Box 4-1 for the four approaches. The latter show no significant difference between the four approaches, which clearly indicates that in this case the bulk aerodynamic relationship can be applied at grid-scale without any problems due to sub-grid heterogeneity. There is sub-grid scale variation in the exchange coefficients along the leg, with the three approaches following a similar pattern. Blending and tile approach are very close, so we are above the blending height. The variation is due to variations of heat flux. The results for leg ML4 and other transects (Table 7 of FJ99) are very similar and confirm the main conclusion of scale independence of the exchange coefficient for heat. This contrasts the situation and results of FJ99, who do find scale dependent heat transfer. However, our results from the EFEDA analysis confirm the conclusion of FJ99 and of Ronda and de Bruin (1999) that the main criterion for scale (in-)dependence of heat transfer was the magnitude of the air-land temperature difference. In NOPEX, this difference was small or even negative (over lakes). In the case of EFEDA, the surface is always much warmer (up to 20K) than the air, so the heat transfer parameterization does not depend on scale.

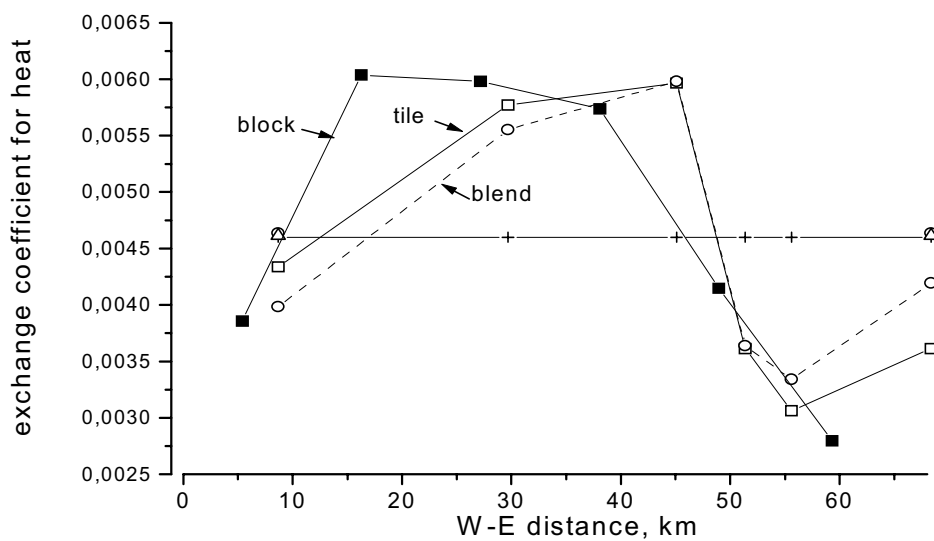


Figure 4-7. Exchange coefficient for heat transfer along flight leg ML1 (Barrax-Tomelloso), composite of three days in June 1991. Line marked with + denotes the grid-scale bulk approach, open circles give the blending height approach, open squares the tile approach, and closed squares the block approach. The corresponding aggregated (grid-scale) effective exchange coefficients are given by the horizontal lines marked with symbols at both ends.

The drag coefficient behaves differently. Figure 4-8 shows that again the blending and tile approaches give almost identical results, indicating that the reference level is indeed above the blending height. The grid-scale effective drag coefficients (horizontal lines), however, do not agree. Assuming the tile and blending approaches give the "correct" value, we find an underestimation of -17% for the bulk approach and an overestimation of +14% of the block approach. In order to explore this result further, we first inspect the along-leg

variations of momentum flux and wind speed (Figure 4-9). The wind speed is almost constant along the leg, the variations of 0.2 m s^{-1} are at the limit of observational accuracy. The momentum flux does vary in the range of $0.2\text{-}0.4 \text{ m}^2 \text{ s}^{-2}$, its components vary even more and change sign. According to Mahrt and Sun (1995a), the latter might be an indication of a dominating sub-grid scale wind fluctuation, which in turn would lead to scale dependence of the drag coefficient. The standard deviation of the wind speed is indeed rather high (1.5 m s^{-1}), while the mean wind speed is rather low (3.5 m s^{-1}). This combination suggests the presence of mesoscale motions. Transient motions could be one option. The topography could be another explanation. Leg ML1 is located near the Southern edge of the area, rather close to the mountains and with elevation variations underneath the flight track of 146 m. For leg ML4, e.g., which is located over very flat terrain in the center of the area, the along-leg variations are smaller and the grid-scale effective drag coefficients of all four methods agree quite well. In other words, the drag coefficient does not depend on scale there.

The available flight tracks of EFEDA do not cover a large range of topography variations. Therefore, this aspect cannot be studied more systematically. Flight legs in the flat center of the area may be less affected, but in general we conclude that the scale dependence of the drag coefficient is related to the mesoscale circulations discussed in section 4.2. Thus, the sub-grid scale velocity variations due to these mesoscale motions would need to be explicitly included in the effective drag coefficient, e.g., using an empirical approach proposed by Mahrt and Sun (1995b).

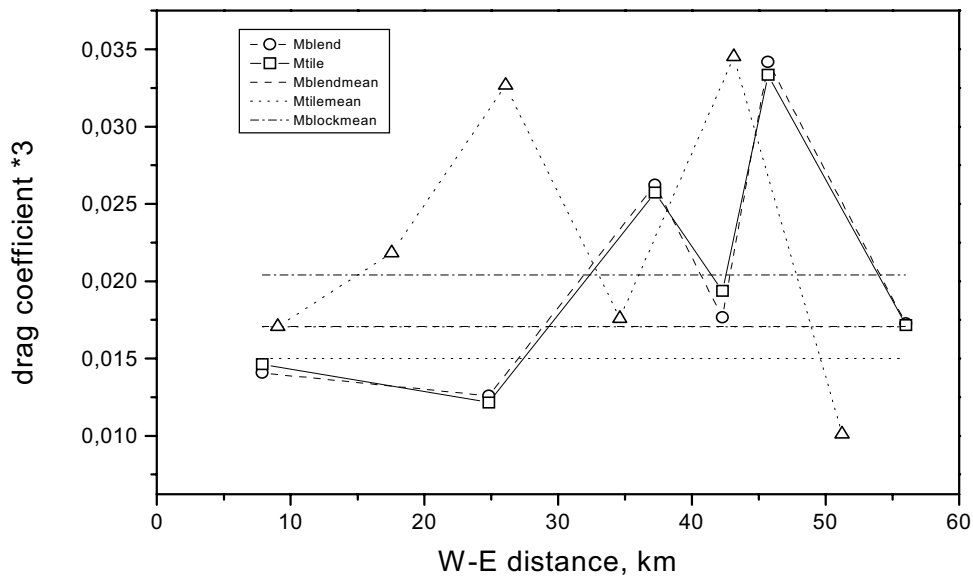


Figure 4-8. Drag coefficient along flight leg ML1. Same as Figure 4-7.

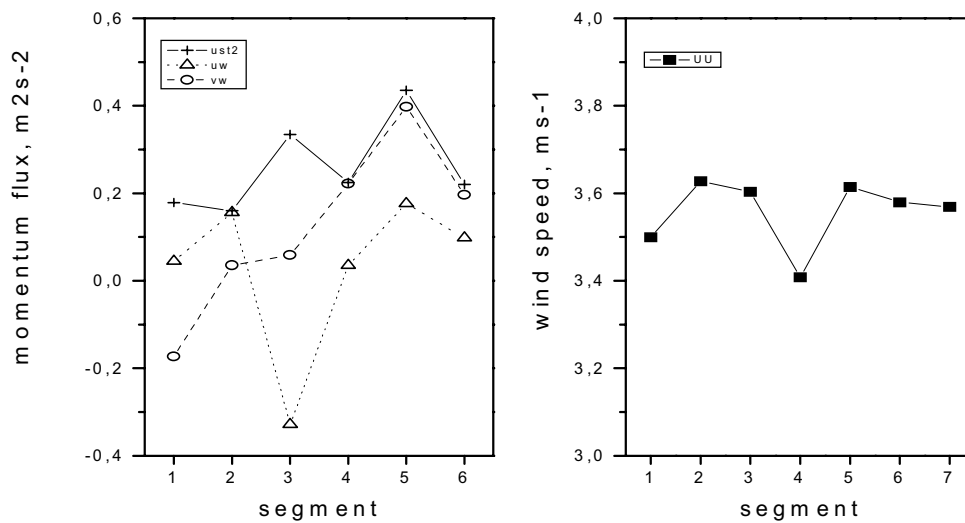


Figure 4-9. Momentum flux (left) and wind speed (right panel) along flight leg ML1. Symbols denote segment averages.

The case of moisture transfer is again different. Figure 4-10 suggests that the exchange coefficient for moisture is completely independent of scale. There is, however, an important point to consider. The bulk aerodynamic relationship for moisture uses the saturation specific humidity at the surface temperature as a lower boundary condition. This is consistent with the parameterization of heat transfer, where the surface temperature is used. Sun et al. (1999) show that large errors in surface fluxes can be introduced by the use of radiometric instead of aerodynamic surface temperature. This equally translates to aerodynamic surface humidity and its common substitutes. Similarly detailed observations are not available to assess the differences here. An important point can be made nevertheless. The saturation deficit is very large over dry zones with sparse canopy, but it can become very small over irrigated fields, especially with sprinkler or pivot irrigation installations, which almost saturate the air above the plants. So we might be in a similar situation as with heat transfer in the NOPEX area, where precisely the small air-land temperature difference was found to be responsible for the scale dependence of heat transfer (FJ99).

Since the observations do not allow for testing this hypothesis, we recur to performing a set of simple control experiments. This consists of either subtracting 25K from the surface temperature T_s (test 1) or subtracting 95 g kg^{-1} from the saturation specific humidity q_s corresponding to T_s (test 2). Both tests are performed for leg ML2, which is 8 km to the North of ML1 and includes the largest part of the irrigated fields in the East. The summary in Table 4-2 shows that in both cases, we do find a scale dependence of moisture transfer.

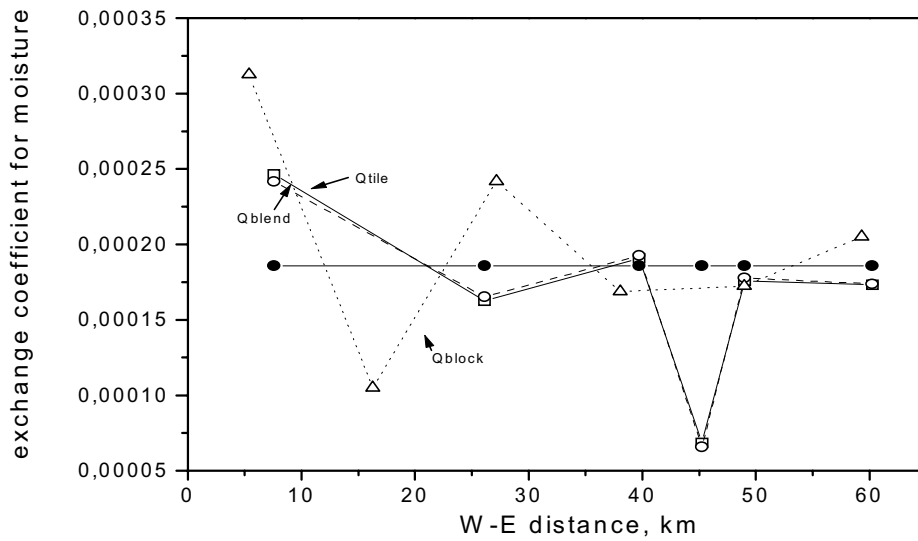


Figure 4-10. Exchange coefficient for moisture, same as Figure 4-7.

Table 4-2. Grid-scale effective exchange coefficients: percent differences between the four approaches. T-B = $(CT-CB)/CT \cdot 100$, others analogous. Average values for all cases are given. NOPEX results from FJ99 are included for comparison.

	T-B	B-G	T-G	R-B	R-G
momentum EFEDA hilly	0	-17	-17	-12	-31
momentum EFEDA flat	0	-4	-6	5	4
momentum NOPEX	0	-5	-5	-1	-6
heat EFEDA	0	-1	-1	0	0
heat NOPEX	-29	28	8	37	55
heat NOPEX+5 K	-13	1	-12	7	8
heat NOPEX- no lakes	28	43	32	20	22
heat EFEDA-25 K	2	10	9	-10	13
moisture EFEDA	0	1	1	-1	1
moisture EFEDA-25 K	2	9	13	-15	19
moisture EFEDA-95g/kg	-2	11	-16	-19	22
moisture NOPEX	0	-2	-2	2	0

4.4 Conclusions

We have investigated the scales of heterogeneity of the EFEDA area and their impact on flux parameterization. The scale dependence of the bulk aerodynamic relationship was evaluated using low-level aircraft observations. For this purpose, we compared airborne estimates of grid-scale fluxes obtained from the bulk aerodynamic relationship at different grid resolutions and from the corresponding blending height and tile approach, respectively.

We find scale dependence of the flux parameterization due to two different heterogeneity features of the EFEDA area, one related to topography and the other to landuse.

1. Momentum transfer becomes scale dependent in the presence of sub-grid velocity variations due to mesoscale motions. The observations give evidence of mesoscale circulations induced by the topography and influenced by the sea breeze, which is corroborated by mesoscale model results (e.g., Miao et al., 2002). The four approaches give different grid-scale momentum fluxes.
2. Heat transfer is found to be independent of scale, which is explained by the large temperature difference at the air-land interface. We recall complementary results of Frech and Jochum (1999) from NOPEX, where heat transfer was found to depend on averaging scale due to the small positive or negative temperature difference (over adjacent land and lake areas).
3. The moisture transfer scales are analogously linked to the land-air saturation deficit. The saturation deficit is very large over dry zones with sparse canopy, but it can become very small over irrigated fields, where often the air above the plants is almost saturated. Thus, moisture transfer becomes scale-dependent in the presence of contrasting dry and irrigated fields.

5 Flux aggregation and regional fluxes²

One of the objectives of EFEDA was to obtain a consolidated dataset of area-averaged surface fluxes for the duration of the field experiment and for the scale of the entire area. Surface fluxes at grid scale are needed for the evaluation of turbulent transport parameterizations in large scale numerical models. However, they are not immediately obtained from any kind of observations. Different methods are combined to achieve this goal.

Surface observations provide continuous time series of observational grid-scale fluxes through weighted averaging. Notwithstanding, each surface station "sees" only its limited fetch area (or source area, Schmidt, 1994). The question is, therefore, how representative a weighted tower average is and if any adjustments are necessary (for strata, processes, and/or scales not covered). Comparison exercises serve exactly that purpose (see review in Chapter 1).

Airborne flux observations provide an area-wide view at single points in time on single days. So they offer independent reference values for comparison, often around local noon and on fair-weather days. Radiosondes offer another alternative of areal perspective. In conjunction with a simple ML model framework, they can provide semi-observational continuous regional fluxes during daytime. Mesoscale model data complete the comparison data, once the model has been validated (e.g., Noilhan et al., 1997).

The objective of this chapter is to discuss the individual approaches on the grounds of the available data. Using the results from the previous chapters, we will derive grid-element average fluxes from the observations in all possible ways. Based on the comparison of all estimates, we then determine the methodology for calculating grid-scales fluxes for the whole month of June. This has not been done so far in a systematic way for the EFEDA area.

The concept of scale aggregation plays a role in several of these steps. So we briefly recall the relevant definitions. A grid-scale flux or an area-averaged flux is simply the mean flux across a given area (or model grid element). Parameter aggregation is defined as the "spatial averaging of heterogeneous surface variables to obtain effective values which are representative of the area" (Michaud and Shuttleworth, 1997). Flux aggregation refers to the spatial averaging of the patch-scale fluxes.

Flux aggregation through weighted surface averages will be the topic of section 5.1. Aircraft-based flux estimates are discussed in section 5.2. Section 5.3 is dedicated to the regional flux estimation from radiosondes in a ML slab model framework. A comparison of results from all relevant methods will be presented and discussed in section 5.4, before general conclusions are drawn in section 5.5.

5.1 Aggregation of surface flux observations

Local-scale surface observations were performed at 21 micrometeorological stations distributed across the three supersites, see Chapter 2 for a summary of the locations and the measured parameters. Linder et al. (1996) have developed standardized datasets for the four major vegetation classes (see again Chapter 2). We have used their datasets and complementary individual site data when

² Material of this chapter (complemented with some of chapter 2) is used in manuscript submitted to J. Appl. Meteorol.

needed. This section describes the process of aggregating the local-scale surface observations to the regional scale.

The regional flux F (of sensible heat or moisture) is here obtained through flux aggregation in a straightforward manner. It simply consists of weighted averaging of the fluxes f_i observed in each vegetation class. The weights are taken as the fractional contributions α_i of each vegetation class to the overall area:

$$F = \sum_{i=1}^N \alpha_i f_i, \quad \text{where} \quad \sum_{i=1}^N \alpha_i = 1 \quad (5.1)$$

The cornerstone of any such flux aggregation is an adequate land-use classification with realistic partitioning between the most contrasting surface types, that reflects properly the seasonal cycles of natural vegetation and cultivated land. Pelgrum and Bastiaanssen (1996) have shown that different classifications produce different area-aggregates. The classification of Calera (2000) (see Annex C) is simple and functional. The classes are defined according to the different phenological growth cycles of the individual crops (Table 5-1). This provides the best solution for Mediterranean land-uses, which are characterized by natural vegetation and bare soils on one hand and seasonal dry or irrigated agricultural fields on the other. The phenological growth cycles are directly related with those parameters that play a key role in the surface energy budget (SEB). These are the vegetation fraction, LAI, albedo, roughness length, soil texture and moisture content. The parameters listed here are also key input parameters into the ISBA land-surface scheme and thus, will be used in Chapter 6 for the performance evaluation of HIRLAM.

Table 5-1. Definition of vegetation classes in Calera (2000) and range of relevant crop parameters for June 1991. Arrows indicate change from beginning to end of month. Soil moisture ranges from Allen et al. (1998); emissivity from Rubio (1997); all other from Linder et al. (1996) and Calera (2002, personal communication).

	BARE	SPR-dry	SPR-irrig	SUM-dry	SUM-irrig	NAT	FOR
Description	bare & fallow	spring dry crop	spring irrigated	summer dry crop	summer irrigated	natural veget.	forest
Albedo	.23-.28	.23-.28	.23-.28	0.28	.15 - .25	0.2	0.2
Emissivity	0.972	0.959	0.986	0.976	0.98	0.99	0.99
Vegetation height (m)	0	1 → 0	1 → 0	0.6	.2 → 1.5	1	3
Fraction of vegetation	0	0.6 → 0	.8 → .1	0.1	.1 → .8	0.15	0.30
LAI	0	.3 → 0	.4 → .1	.1 → .4	.2 → .4	0.5	1
Soil texture class	sandy-clay-loam (15-25% clay, 60-75% sand)					sand (<10% clay, >85% sand)	
Field capacity vol. moisture content	0.18 - 0.28 m ³ m ⁻³					0.07-0.17 m ³ m ⁻³	
Wilting point vol. moisture content	0.06 - 0.16 m ³ m ⁻³					0.02 - 0.07 m ³ m ⁻³	

Table 5-1 gives the definition of the classes (partly repeating Table 4 of Chapter 2) and adds the relevant information on the crop phenological status for June 1991. The phenological cycles of most crops are rather short, with the timing depending on local climate and elevation. In the EFEDA area, the spring crops (dry and

irrigated) have either been harvested or are senescent by mid-June. Therefore, their SEBs are similar to those of fallow land and there is no need to represent these classes separately in the surface flux aggregation. The forest class occupies a very small area fraction and will be regrouped into the natural vegetation class (which has similar characteristics, since both are on similar soils). The remaining four classes match perfectly the vegetation types covered by the EFEDA observations. Tomelloso corresponds to "Summer-dry", Belmonte/Rada de Haro to "Natural", Barrax-bare to "Bare", and Barrax-irrigated to "Summer-irrigated".

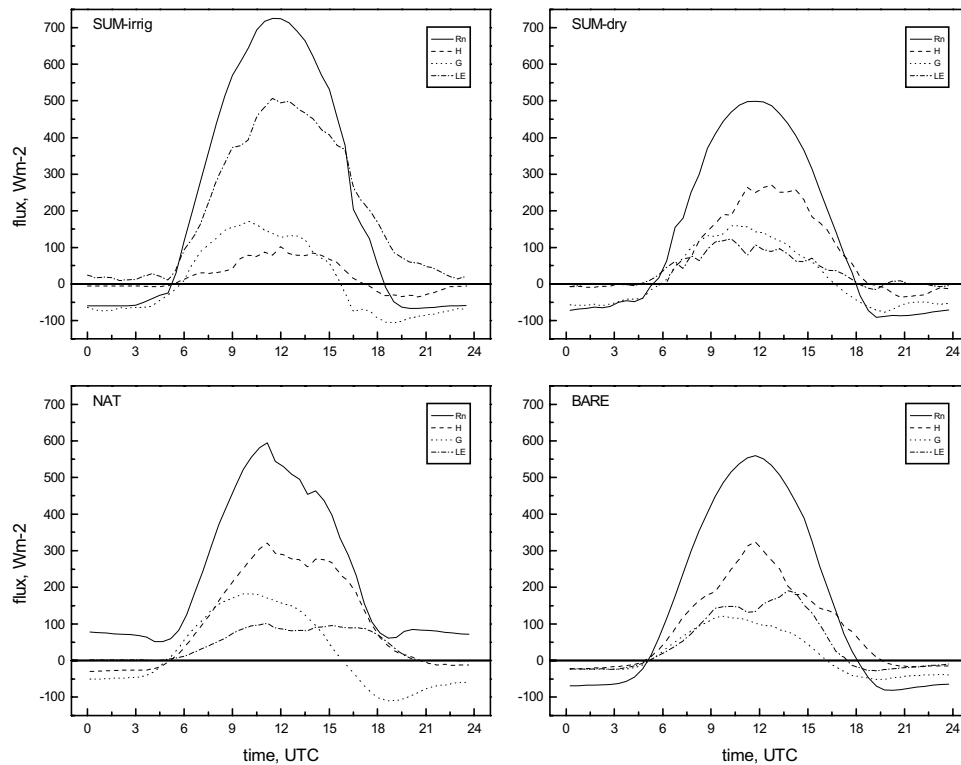


Figure 5-1. 23 June surface energy budget for each vegetation class. Top left: SUM-irrig; top right: SUM-dry; bottom left: NAT; bottom right: BARE.

The SEBs of the three dry land-use classes are rather similar to each other (SUM-dry, BARE, and NAT in Figure 5-1). The most notable influence on the surface energy budget comes from irrigation (SUM-irrig in Figure 5-1), which is not performed in any continuous way across all fields and at all times. Without entering into the details of irrigation scheduling (Allen et al., 1998), we can still assess its effect on the local SEB. Panels (a)-(c) of Figure 5-2 show the diurnal cycle of the SEB components of an irrigated field during three consecutive days. Panel (d) gives the dry field reference for the middle day, which does not vary significantly over the three days. The irrigated field SEB shows clearly the big differences induced by the irrigation on the second day (starting in the evening of the first day) and the very gradual relaxation into a drier ("irrigation-off") mode. The most notable difference is in the moisture flux, which reaches values of 500 W m^{-2} instead of less than 200 W m^{-2} towards the end of the irrigation cycle (first day). The sensible heat flux is reduced accordingly, but the overall available energy (through the net radiation) is also increased on the irrigation day, since both the albedo and the surface temperature are reduced during the period of high water availability. One day after irrigation (d24), the moisture and heat

fluxes are still close to their wet extremes. Around the fifth or sixth day (corresponding to the first day, d22, in Figure 5-2), the SEB is normally back to a state of minimum water availability and on the sixth or seventh day the irrigation cycle starts again.

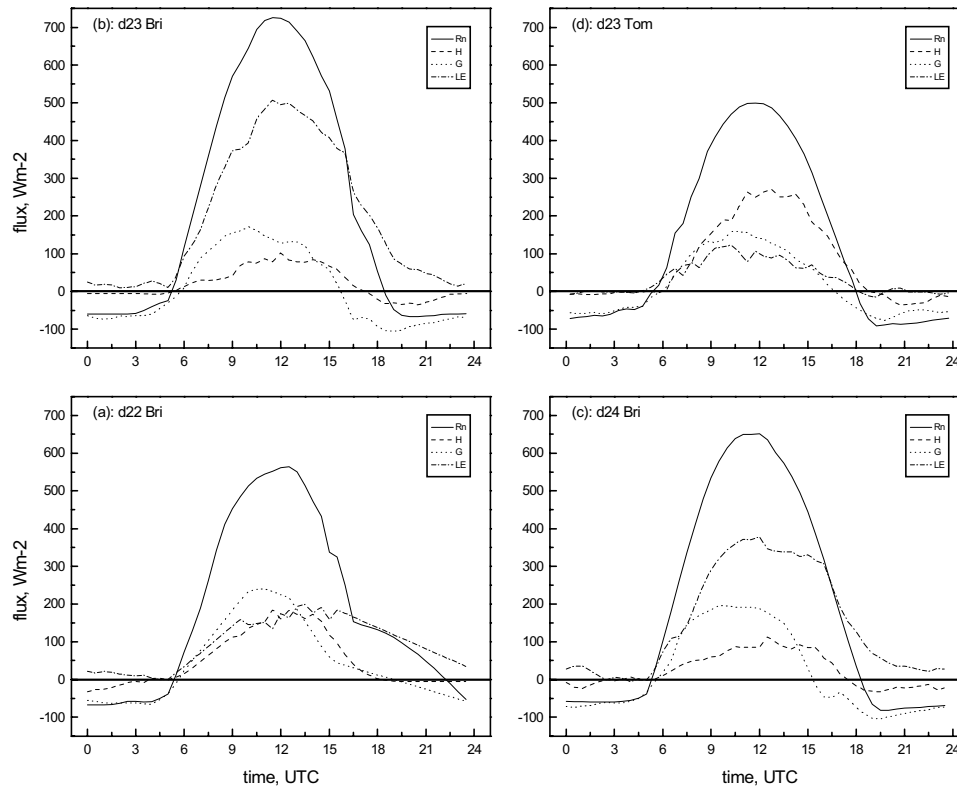


Figure 5-2. Surface energy budget on three consecutive days (22-24 June 1991), in maize with irrigation on the middle day (panels (a) to (c)) and in dry vine (panel (d), middle day).

During the month of June 1991, there were four irrigation events in that particular field (the observing mast was maintained in the same location all the time). On the other fields within the "Summer-irrigated" crop class, these events possibly took place on other dates. According to information from the regional Irrigation Association, the average frequency would have been about 4-6 times per field in one month, with a range of 10-80% of all fields in this class actually irrigated on any given day.

Due to their markedly different SEB, the irrigated fields have a major effect on the area-aggregated fluxes. The challenge lies in the high time-space variability induced by the day-to-day irrigation practice. In principle, the irrigation scheduling (timing and geographical distribution) would need to be taken into account when calculating area-aggregated surface fluxes for a given area. This is practically feasible for a number of cases only (depending on the availability of the Irrigation Association's registers on water use and high-resolution satellite data). Grunwald et al. (1996) recognized the importance of the irrigated fields in the Barrax area average. They use the seven-day history of a moisture indicator

(based on the fraction of evaporation in global radiation) to derive area-averaged fluxes for the Barrax site on a single day.

Here, we are interested in obtaining a time series of regional fluxes for the whole month of June and for different grid-element areas. So we are aiming at a simpler approach. First, we seek to quantify the dependence of the area-aggregated moisture and heat fluxes on the fraction of actually irrigated fields. The range of space-time variability of irrigation water supply as given above results in an approximate range of 10-30% of actually irrigated fields (represented by the observed SEB at "Barrax-irrigated" on irrigation days). So we calculate the aggregated fluxes for this range of areal fractions. Figure 5-3 shows the results of this simple sensitivity assessment. The peak aggregated moisture flux on the irrigation day ranges from 150 to 220 $W m^{-2}$. In other words, raising the irrigated area fraction from 10 to 30% results in enhancing the peak aggregated moisture flux by about 50%. At the same time, the peak aggregated sensible heat flux is reduced by about 15% (from 250 to 215 $W m^{-2}$).

In conclusion, the skill in aggregating surface fluxes in this type of area consists of estimating the percentage of actually irrigated fields, which depends on the land-use and the irrigation practices of the area. The land-use classification of Calera (2000) provides the appropriate differentiation according to the crop phenological cycles. It is used here in conjunction with the observed surface fluxes from the vegetation-class-averaged dataset of Linder et al. (1996). Irrigation scheduling in the area is based on weekly cycles. In a statistical sense, all irrigated fields are maintained close to potential evaporation. Without entering in details of the irrigation history of each field, we therefore obtain a realistic area estimated of actually irrigated fields by reducing the irrigated class peak values by 15-20%. The corresponding fractional areas of each vegetation class are summarized in Table 5-2, which also comprises a regrouping of Table 2-3 in Chapter 2. In section 5.4 below, we calculate the actual area averages for these (sub-)areas.

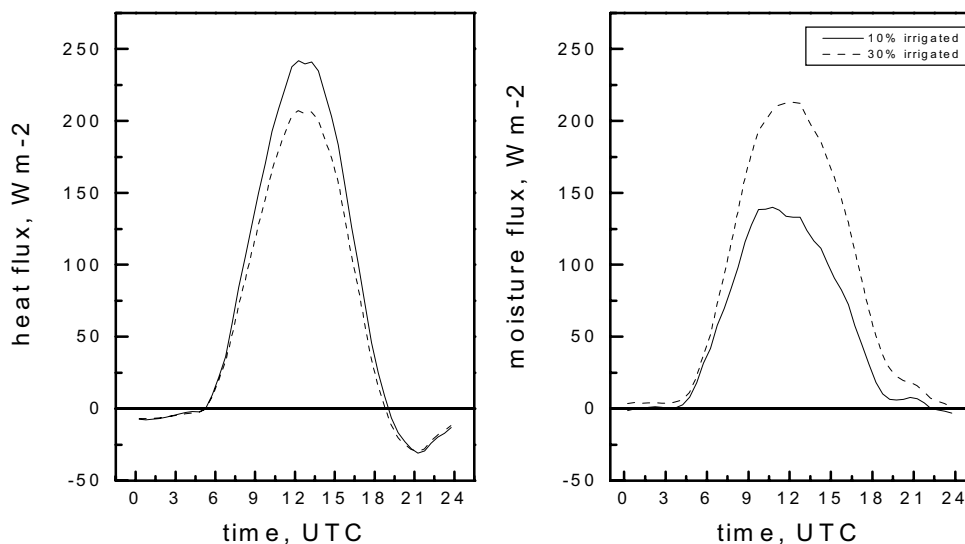


Figure 5-3. Area-aggregated surface moisture and heat fluxes for different area fractions of irrigated fields (solid line: 10%; dashed line: 30%).

Table 5-2. Fractional area covered by each vegetation class in the EFEDA area and in the corresponding model grid elements within and around that area (in %).

	Total EFEDA	HIRLAM T05	HIRLAM B05	HIRLAM T02	HIRLAM B02
latitude	38.917°-40.083°N	38.75° N-39.25° N	38.75° N-39.25° N	39.1° N-39.2° N	38.9° N-39.1° N
longitude	2.183°-3.183° W	2.75° W-3.25° W	1.75° W-2.25° W	2.9° W- 3.1° W	1.9° W- 2.1° W
area (km ²)	8.000	2976	2976	475	475
Tom (SUM-dry)	45	88	48	97	25
Brb (BARE, SPR-dry, SPR-irrig)	45	9	32	3	35
Bri (SUM-irrig)	5	0	20	0	40
Bel (NAT, FOR)	5	3	0	0	0

5.2 Area-averaged fluxes from aircraft observations

Flux aircraft offer two alternatives to obtain regional fluxes. The first approach is analogous to the flux aggregation of surface observations by means of weighted averaging. It requires very low flying aircraft that samples individual patches along its transects (legs). Flying repeated transects is necessary to achieve a meaningful sample size of each vegetation class. The second approach aims at observing the effective flux at the flight level (assumed to be at least a local variant of the blending height), where some aggregation has already been performed by the turbulent mixing (see Chapter 4). Ideally, these observations would physically cover the whole area in a short period of time. The two approaches are conceptually different and require different types of aircraft. Given the size and heterogeneity of the EFEDA area, the emphasis was on the second approach. The DLR Falcon is a fast jet aircraft equipped for high-resolution turbulence measurements (see Chapter 2), thus it is able to cover a large sample of the area in one hour. In either case, the flux divergence between the flight level and the surface has to be accounted for.

Transects (legs) in the height range of 0.07-0.2 z_i are used to derive area-averaged fluxes. The most complete aggregation flight pattern (flown three times) consists of a set of five East-West transects of 60-80 km length, with a North-South spacing of 5-10 km (MAP in Box 2-3 of Chapter 2). It takes about one hour to complete the whole pattern. Therefore, the time trend (as obtained in Chapter 3) between the segments was removed. Each individual leg takes about 10 minutes, so it would not be necessary to remove any time-trend along the tracks if we analyzed a single transect. Linear spatial detrending was performed to remove advective gradients. Other flight patterns were used as secondary priority, in order to obtain a more complete sample of cases and composites. The MAP pattern is attributed higher priority, because it provides the most comprehensive coverage of the area.

The area-averaged flux (again of sensible heat or moisture) at flight level is derived from any such low-level pattern through arithmetic averaging of leg-mean fluxes. If a low-level pattern consists of N legs and the leg-mean flux for

leg number l is f_l^* , then the whole area average flux F^* (the star indicating flight level values) is obtained from

$$F^* = \frac{1}{N} \sum_{l=1}^N f_l^*. \quad (5.2)$$

In the most complete mapping pattern, we have a low-level set of $N=5$ legs of 60-80 km length. In the minimal configuration low-level pattern, we have $N=2$ legs of 60 and 105 km length.

The use of flux aircraft in heterogeneous terrain presents a formidable challenge, where a compromise between turbulence sampling needs and stationarity requirements has to be found on a case to case basis. Thus, the first step in any use of airborne flux data is to analyze their potential errors. As outlined in Chapter 2, these arise from five fundamental sources, of which the first (instrumental accuracy) is not critical at all. The next two are related to inadequate sampling of turbulent eddies, either by missing the dominant wavelengths or by having too small a sample. These are the systematic and random errors, respectively. They were estimated here from the equations of Mann and Lenschow (1994) (see Box 2-2 in Chapter 2). Due to the long flight legs (60-100 km), both errors are below 15-20% for heat flux (Figure 5-4) and below 20-24% for moisture flux (not shown). The mesoscale flux contributions were estimated from a combination of detrended and high-pass filtered data. They were found to be significant in some cases (see below). The most restricting error source in our case is non-stationarity, which affects many transects. However, these records contain valuable information for the purpose of this work, which was made available by careful inspection (visual and analytical) of each time series. A slightly relaxed version of the tests developed by Vickers and Mahrt (1997) was used and individual flight legs were composited whenever possible. We found undersampling in a few cases, which was included in the uncertainties given below.

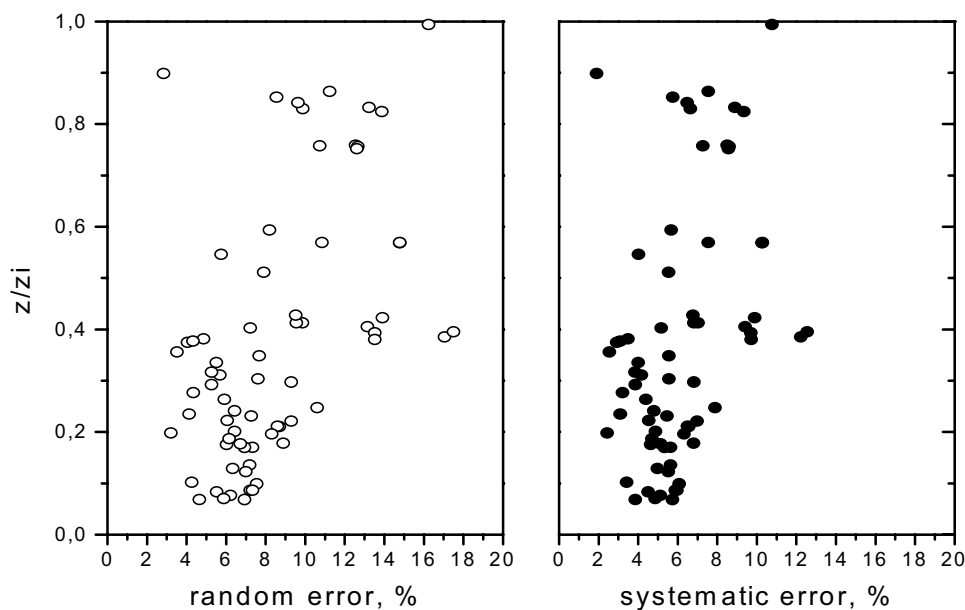


Figure 5-4. Systematic and random errors of airborne heat flux estimates after Mann and Lenschow (1994), as relative errors in percent of leg-mean flux.

The spatial pattern of sensible heat flux exhibits slightly enhanced values over rolling terrain and somewhat reduced values over irrigated areas. There is inherent variability, not related to any terrain feature, of about 30% (Jochum, 1993b). Mesoscale contributions enhance the heat flux by 10-15%. The behavior of moisture flux is more difficult to assess. The variability is much higher and in many cases not clearly related to landscape features. Mesoscale contributions are particularly variable. Figure 5-5 shows a striking example of heat and moisture flux along several low-level tracks on a slightly cloudy day. We observe overall low fluxes (due to the low net radiation) with low spatial variation, except for a marked peak in the moisture flux (over a dry zone). This peak does not appear in the flux filtered to ABL scales (up to 5 km, which corresponds to about 1.5 times the maximum ML depth), but is obviously of mesoscale origin. High and irregular moisture variability was also found in many individual aircraft time series at all levels (Figure 17 in Chapter 3; Michels and Jochum, 1995) and in airborne differential absorption water vapor lidar (DIAL) crosssections (see example in Chapter 4). Additional atmospheric moisture becomes available from the irrigation installations (which often provide more water to the air than to the plants). Additional moisture may also be introduced by the sea breeze, which has been shown to enter the Eastern part of the EFEDA area (Habets, 1994; Fiedler et al., 1996; Miao et al., 2002). We have seen above (Chapter 4) that there is evidence of mesoscale terrain-induced circulations, which are assumed to be the mechanism to distribute the additional moisture from both sources throughout the EFEDA area, thus generating the observed highly inhomogeneous moisture fields and fluxes. This remains speculative, however, since the data coverage is not sufficient for a quantitative investigation of mesoscale circulations.

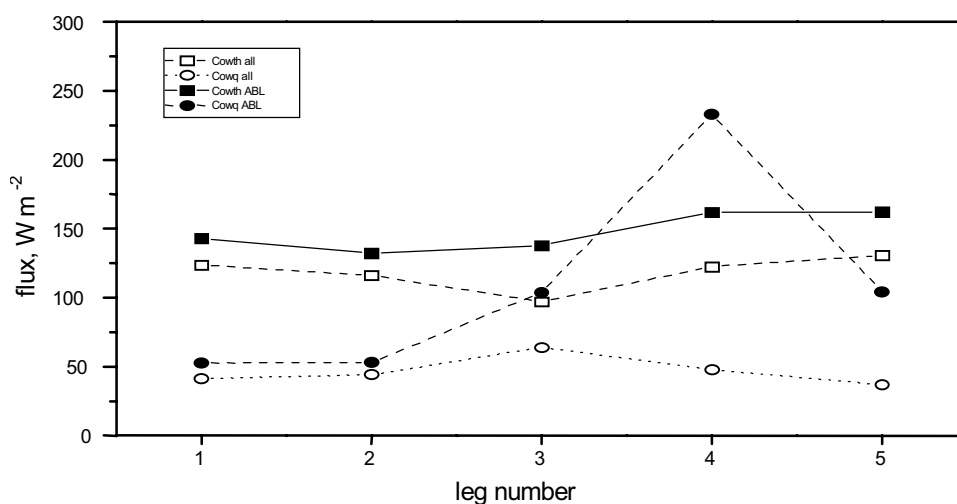


Figure 5-5. Heat and moisture flux variations along five East-West transects at different latitudes (spacing 5-10 km). Each symbol corresponds to an average over a 20 km segment. Solid symbols denote flux filtered to ABL scales (5 km), open symbols contain both ABL and mesoscale contributions.

Obtaining now the surface fluxes from flight level fluxes involves some method to account for the low-level flux divergence. Several approaches have been proposed and used (e.g., Betts et al., 1992; Jochum, 1993a; Grunwald et al., 1998; Bange et al., 2002). We use here the results from the budget analysis of Chapter 3 as explained below.

In a first step, the consistency of airborne and surface observations of fluxes was assessed for the extended homogeneous area of the Tomelloso supersite, which is perfectly adequate for this purpose. Given the height difference of up to 300 m, there was no classical "aircraft-tower flyby" (which rather serves for instrument intercomparison purposes). The strategy of the consistency check is essentially an intercomparison of the surface energy budget components obtained from both platforms, as referring to an area of about 10 km by 10 km. The area is homogeneous enough for the Tomelloso site-averaged dataset of Linder et al. (1996) to provide local as well as areal fluxes. It is also homogeneous enough to offer patch scales large enough to be "seen" by the aircraft. In view of the low wind speed, we are not concerned with footprint issues here. We will use the following strategy to derive the surface energy budget from aircraft observations. First, we select all flight segments located within 5 km of the Tomelloso centerpoint. Then we calculate the mean heat flux and net radiation from the segment averages (previously calculated and detrended as explained above). The flux divergences obtained in the budget analysis of Chapter 3 are used to estimate the surface values of heat flux and net radiation. Both flux divergences have been shown to vary only slightly across the area. From net radiation, we calculate the ground heat flux using the G/R_n relationship ($G/R_n=0.26\pm0.02$) obtained from the surface observations for the noon period. Finally, the moisture flux is obtained as the residual of the other terms in the surface energy budget equation ($LE=R_n-H-G$).

The moisture flux was, of course, measured onboard the aircraft and the errors are sufficiently small. However, the vertical flux divergence is very uncertain and depends on many factors. We have seen in Chapter 3 that it is not necessarily always constant across the whole area. Using the energy balance approach circumvents this problem conveniently. Actually, the moisture fluxes in the surface dataset were also obtained from the energy balance method, because the direct observations (via eddy correlation or profile method) were found to be problematic in this very dry environment (Linder et al., 1996). Table 5-3 shows the procedure and the results for an example case. The heat flux at the surface is underestimated by the aircraft even after correcting for the vertical flux divergence. This is probably due to the undersampling of some energy-carrying eddies by the segment averages of 10 km length. Given the very deep MLs observed in the area, the ABL scales range up to 5 km (assuming 1.5 times the ML depth). Testing this hypothesis with 20 km segments (and thereby reducing the Tomelloso sample from 7 to 3 in our example) yields heat fluxes closer to the surface observations.

The results of the intercomparison confirm the consistency of airborne and surface-based flux observations for the homogeneous sub-area of Tomelloso. This forms the basis for proceeding to derive area-aggregated fluxes for the whole EFEDA area from airborne flux data in Section 5.4, using the same approach.

Table 5-3. Comparison of surface energy budget components in the Tomelloso area. Example of case 25 June 1991, all fluxes in $W m^{-2}$. Errors are standard deviations of mean.

	Surface observations	Aircraft-level flux (10 km segments)	Surface flux from aircraft observation	Surface flux from aircraft 20 km segments
H	252 ± 21	158 ± 45	198 ± 38	231 ± 37
R_n	458 ± 61	502 ± 51	460 ± 16	449 ± 12
G	123 ± 18	--	124 ± 10	121 ± 8
LE	84 ± 29	64 ± 28	138 ± 42	97 ± 39

5.3 Regional fluxes from a conservation approach

Radiosondes are able to "see" the regional flow and thus, offer interesting possibilities to estimate the regional fluxes directly. Radiosonde-based mixed layer (ML) budget methods have been used widely, see Peters-Lidard and Davis (2000) and references therein. Many of them follow the line of reasoning of McNaughton and Spriggs (1986) and de Bruin (1989) in developing a set of simplified conservation equations for ML temperature and humidity in a ML-slab framework. For a review of these and other related approaches, see Chapter 1.

We use here the same coupled canopy-ML model (de Bruin, 2001, personal communication) as in Chapter 3 as a tool to estimate the regional fluxes. The model description and the complete set of equations are given in Annex 2. We first perform a simple validation in the Tomelloso and Barrax sub-areas, in order to obtain a well-adjusted set of input parameters for these areas.

Table 5-4 lists all input parameters required by the model along with the sets of input data used in the subsequent analysis. Driedonks (1982), Jacobs (1994), and van den Hurk (1996) discussed the sensitivity of this and a similar model. Their results are used here when needed. The canopy input data for the three vegetation classes were determined from surface observations (basically from Linder et al., 1996; see Chapter 2). The ratio of soil heat flux to net radiation ("G-factor") was initially taken as the average value of the morning period (which is the more critical period for ML growth). In fact, it changes quite a bit during the daytime hours (Figure 5-6), so we have finally modified the model to account for a time-dependent G-factor. The roughness lengths were taken from Linder et al. (1996), while the surface resistance was estimated very roughly according to "very dry" (500 s/m) or "very wet" (0) (de Bruin, 2001, personal communication).

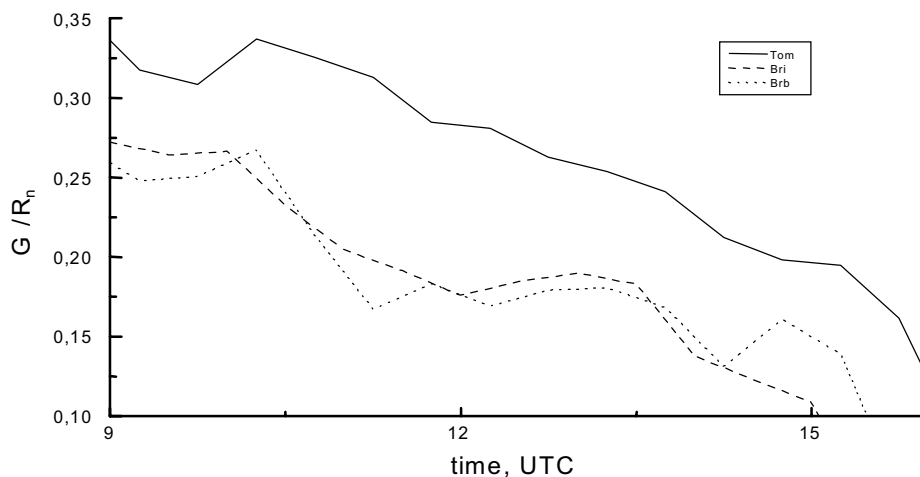


Figure 5-6. Daytime behavior of G-factor (ratio of soil heat flux to net radiation) on 23 June 1991 for the vegetation classes Tom, Brb, and Bri.

The entrainment factor A was set according to the discussion in Chapter 3, where it was derived from aircraft observations. The ML input data were obtained from radiosoundings shortly after sunrise. The task of extracting the required parameters from the vertical sounding profiles is the same as in Chapter 3 and

was described there. The gradients ("gamma θ " and "gamma q") above the ML require special attention here again. Since the model allows for time-dependent gradients, the observed FA temperature gradient is introduced around model-noon. The RL moisture structure is more complex (see humidity profiles in Figure 2 of Chapter 2). So a new humidity gradient is introduced whenever a new moisture layer was reached.

Table 5-4. Input parameters for coupled canopy-mixed layer model. Tom = vine; Bri = Barrax irrigated maize; Brb = Barrax fallow; Barrax aggregate see text. gamma is the gradient above the ML. Times in UTC.

	Tom	Bri	Brb	Barrax aggregate
Wind speed, m s ⁻¹	2.2	2.9	2.9	2.9
Amplitude of incoming solar radiation, W m ⁻²	923	961	961	961
Albedo	0.28	0.14	0.23	0.21
G-factor = G / R _n	0.24	0.20	0.20	0.20
z ₀ , m	0.04	0.06	0.01	0.022
z _{0h} , m	0.004	0.006	0.001	0.0022
r _s , s m ⁻¹	500	0	500	375
Entrainment factor	0.3			0.2
Initial ML depth, m	350			400
Initial θ (ML), K	300			299
Initial q (ML), g kg ⁻¹	6.3			7.3
Jump θ , K	4			7
Jump q, g kg ⁻¹	-2.1			-2
gamma θ , K m ⁻¹	0.0025 0.001 after 12:00			0.001
gamma q, g kg ⁻¹ m ⁻¹	0.00011 0.002 after 10:30 -0.001 after 12:00 -0.0013 after 13:30			-0.0005 0.005 after 10:30 0 after 11:20 -0.00015 after 12:00

The ML input data cells in Table 5-4 are left blank on purpose for the vegetation classes Bri and Brb. The surface energy budgets of these fields are substantially different enough to generate different MLs. The settings in the last column were used to run the model in both cases, with widely differing ML results (not shown). Since the Barrax area consists of a statistically heterogeneous (see Chapters 1 and 4) mixture of irrigated and non-irrigated patches, the ML is not in equilibrium with any single patch, but rather with the effective properties of all patches. The radiosoundings will "see" the ML above the blending height only. We will come back to this issue (and to the last column in Table 5-4) below.

First we compare the model results with observations at Tomelloso. The net radiation is slightly underestimated, with a noon maximum 5% below the observed 500 W m⁻². Since the albedo and the incoming solar radiation are both taken from the observations, this is due to the longwave parameterization, where the emissivity was already modified according to the observations. The difference is well within the range of observational uncertainty, so no further adjustments were made. The moisture flux follows closely the observed values, whereas the heat flux is not quite in phase. It reaches the maximum earlier than observed and decreases earlier in the afternoon. The reason is in the soil heat flux, which is modeled by means of a constant G-factor (as a percentage of net radiation). As

we have seen already from Figure 5-6, it is far from constant at the three sites. Therefore, the input value as given in Table 5-4 is a compromise, which always leads to a time-dependent bias. Since the surface heat flux is calculated as the residual from the surface energy budget, this bias propagates directly into it. Modification of the model to allow for a time-dependent G-factor (see below) improves the agreement with observations.

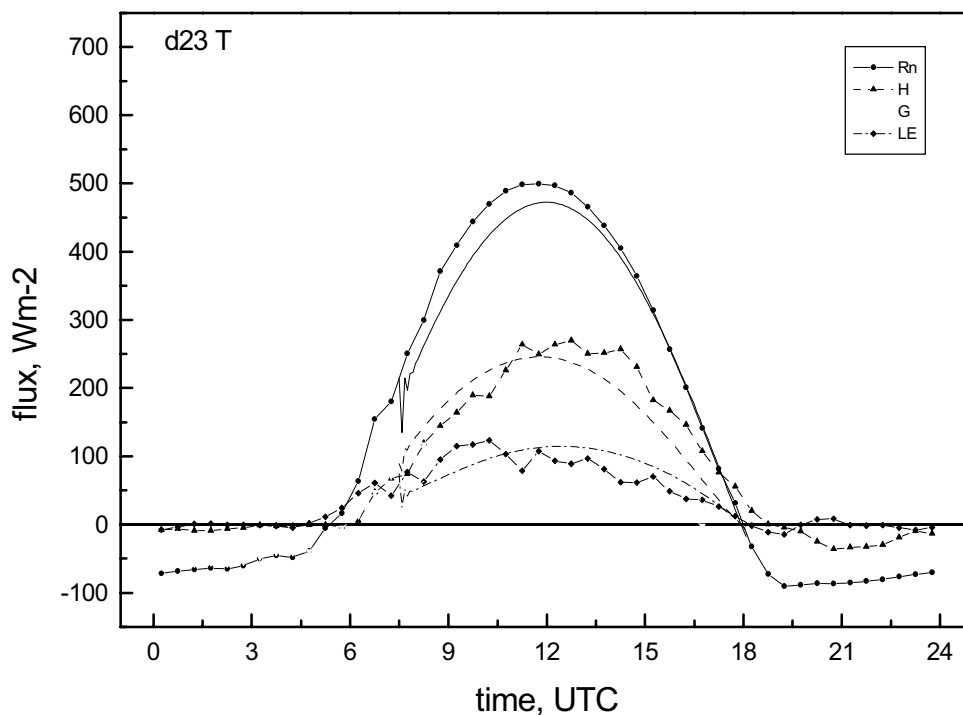


Figure 5-7. Comparison of surface energy budget terms from observations and canopy-ML model at Tomelloso on 23 June 1991.

With the surface energy budget reproduced well, we now compare the ML behavior. The model ML temperature (red dotted line in Figure 5-8) remains below the observed ML average (black dotted line with open symbols). This might be an indication of significant radiative warming. This was indeed found from the budget analysis in Chapter 3. Introducing constant radiative warming as foreseen in the model results in a time-dependent bias, which does not improve the model performance. This suggests an area of model improvement, to allow for time-dependent radiative warming or cooling. The modeled surface temperature is much lower than the observed radiative surface temperature. It is difficult to enter into an explanation here, since the model uses the aerodynamic surface temperature, which can actually be very different from the radiometric surface temperature (e.g., Sun et al., 1999). The ML specific humidity (Figure 5-9) is reproduced equally well as the ML depth (Figure 5-10). The consistency of the modeled inversion level fluxes was assessed in the context of the budget analysis of Chapter 3. In summary, we conclude that the model in this configuration reproduces the Tomelloso surface and mixed layer well.

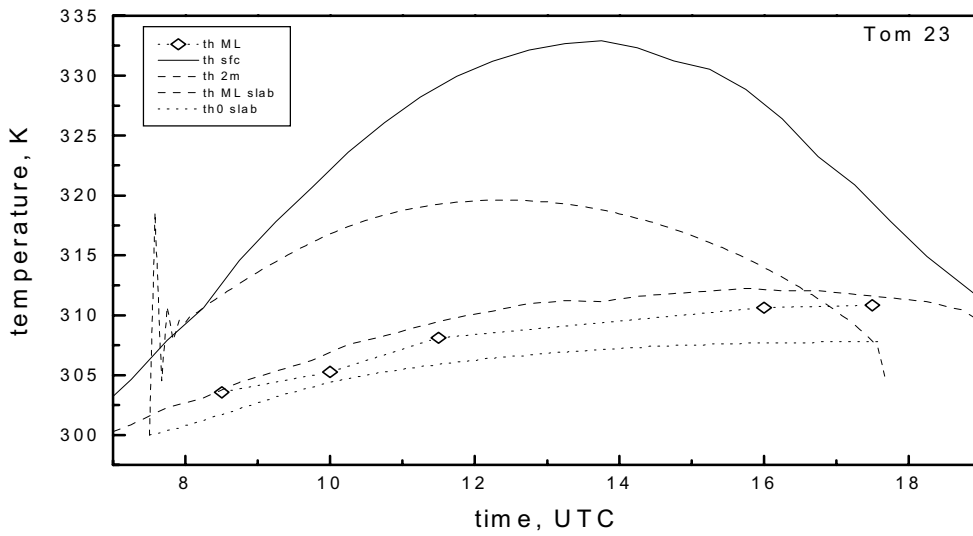


Figure 5-8. Comparison of surface and ML air temperatures at Tomelloso.

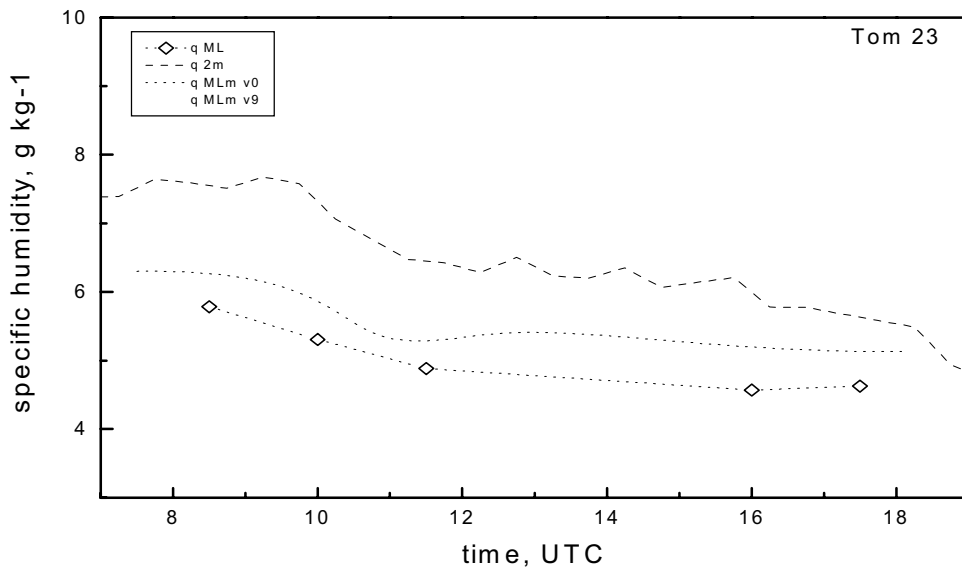


Figure 5-9. Comparison of surface and ML specific humidities at Tomelloso.

The comparison for the Barrax site is different. As said above, the Barrax ML is not in equilibrium with none of the individual field classes, which are interspersed across the area. Consequently, a column-type comparison is not possible here. Instead, we focus the comparison on the surface energy budget for now. Later in a follow-up step, we will use the resulting surface fluxes to perform a flux aggregation. The results of the surface energy budget comparison in either vegetation class (irrigated maize and dry fallow land, not shown) are very similar to those for Tomelloso. The net radiation and moisture flux are within the observational uncertainty, while the soil and surface heat fluxes show again a time-dependent bias, which is removed by introducing a time-dependent G-factor as observed (Figure 5-6).

Now the model is used to perform a simple aggregation task in order to access the Barrax ML. This is done in a rather experimental way, following the set of simple parameter aggregation rules recommended by Shuttleworth (1993) (which he calls "strawman" aggregation rules). Our measure of success is the agreement of the modeled "Barrax aggregate" ML with the observed. The input parameters given in the last column of Table 5-4 are the aggregated parameters obtained this way. Albedo and G-factor are obviously averaged linearly. The roughness lengths are treated after Wood and Mason (1992). The surface resistance is the most uncertain issue. Shuttleworth (1993) gives two alternatives, either linear averaging of the resistances or linear averaging of the corresponding conductances, depending on the importance of mixing. The first alternative turns out to be the suitable option for our case. All averages are weighted according to the areal fraction of each vegetation class, which is taken as 20% irrigated and 80% dry (corresponding to HIRLAM grid element H05B). The model is run with these effective parameters and with the ML input parameters obtained from the Barrax radiosounding as given in Table 5-4. The resulting ML depth is very close to the observed (Figure 5-10). So is the modeled ML temperature (Figure 5-11), indicating less radiative warming here. The modeled surface temperature is again lower than the observed radiometric surface temperature (see comments above). The ML specific humidity (Figure 5-12) is less well predicted than in the case of Tomelloso, but still within a reasonable range (close to the limit of observational accuracy).

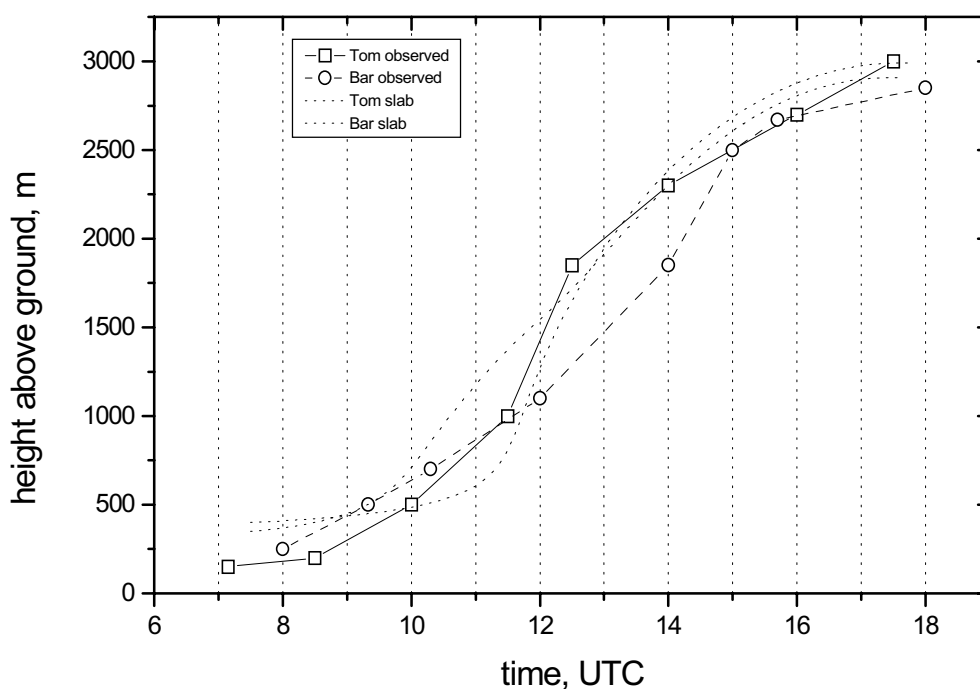


Figure 5-10. Comparison of ML depth at Tomelloso and Barrax (aggregate, see text). Observations (squares and circles) are taken from Michels and Jochum (1995).

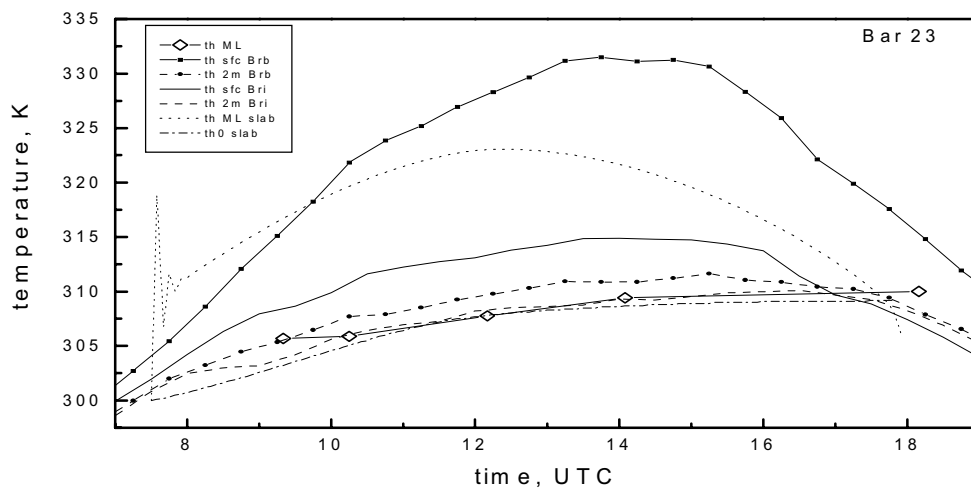


Figure 5-11. Comparison of temperatures for Barrax aggregate.

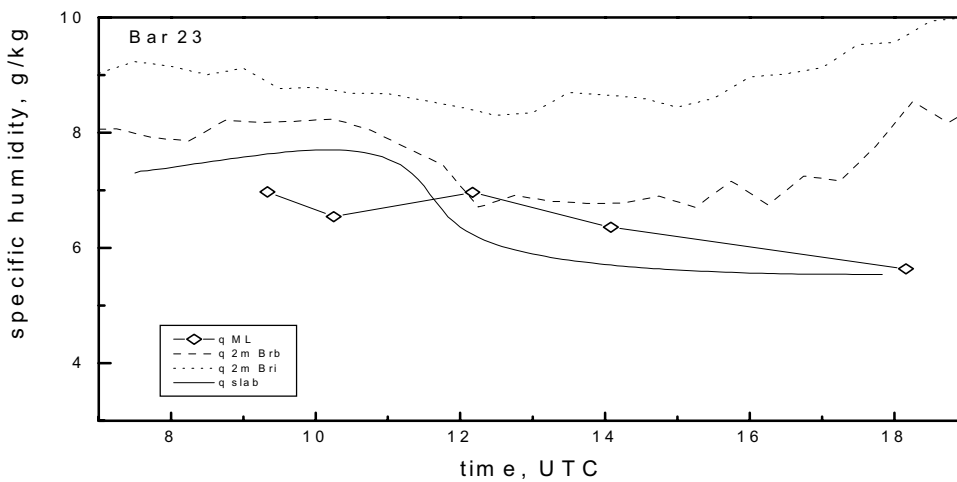


Figure 5-12. Comparison of specific humidity for Barrax aggregate.

The main conclusions from the comparison can be summarized so far:

1. The canopy-ML model with the set of input parameters given in Table 5-4 reproduces well the surface fluxes observed at each vegetation class. The heat fluxes (soil and surface) have a time-dependent bias, which was removed by introducing a time-dependent G-factor as observed.
2. It also reproduces well the ML depth and state at Tomelloso and, with a set of input data obtained through parameter aggregation, at Barrax. The resulting fluxes are the regional fluxes for the Barrax area (i.e. at 10 km scale).
3. The "strawman" parameter aggregation rules of Shuttleworth (1993) work well for the Barrax case.

This confirms that the model is a suitable tool for diagnostic studies at the EFEDA sites and that it can be used to derive regional fluxes for the whole area in the following section.

5.4 Synthesis and comparison of grid-scale fluxes

We are now comparing grid-scale fluxes obtained from the following methods

- * Weighted averages from surface observations;
- * Airborne flux observations;
- * Regional fluxes from a radiosonde-based conservation approach; and
- * Results of the mesoscale model simulations of Noilhan (1996).

We show the grid-scale flux comparison for 23 June 1991, because on that day also the mesoscale model results are available, even though the flight pattern coverage of the whole area is less complete than on other days. The starting point for the comparison are the weighted surface observations. We focus on the areas of interest given in Table 5-2. One is obviously the whole EFEDA area, while the others are sub-areas (some only partly overlapping with the whole area) defined according to the grid cells of HIRLAM. Both the standard resolution of the operational HIRLAM version (0.5°) and the high-resolution version (0.2°) are used, so the sub-areas differ by size and by geographical location and therefore, by fractions of land-use classes (Table 5-2). Figure 5-13 and Figure 5-14 show the area-aggregated heat and moisture fluxes for each area. Following the discussion in section 5.1 above, it is clear that the actual aggregated fluxes depend on the fraction of irrigated land and thus, on size and location. Mahrt et al. (2001) observe a similar phenomenon in the case of BOREAS, where the area-aggregates depend on the fraction of coniferous vs. deciduous forest. The influence of irrigated land, however, is much stronger. The difference is most dramatic in the moisture flux, where we find a range of $110\text{--}280\text{ W m}^{-2}$ for midday maxima and a phase shift of the occurrence of the maximum from 10 to 13:00 UTC. The overall EFEDA area behaves similarly to the "dry" grid-cells, but at the level of 0.5° resolution (i.e. about 50 km sides), the character of the grid-scale fluxes is rather "wet" in the vicinity of Barrax. With smaller grid-cells, zooming in on the irrigated zone (H02B), this effect increases. The sensible heat flux varies less dramatically. The whole area aggregate resembles closely the dry cells, with a midday peak of about 260 W m^{-2} , whereas the wettest grid-cell reaches a maximum of 210 W m^{-2} .

The aircraft estimate of surface heat flux at 12:00 noon is within the range of the wet cells and thus, remains below the whole area surface aggregate, but the uncertainty ranges overlap. The aircraft estimate of surface moisture flux is slightly higher than the weighted surface average, but well within the range of uncertainty. The "airborne surface flux" uncertainty is composed of four factors. Direct flux errors and the range of spatial variability at flight level can be assessed from the data (about 33% for heat flux and 50% for moisture flux). Errors in the low-level flux divergence and in the ML depth (which propagate into the normalized height z/z_i) are estimated to be roughly of the same order.

Mesoscale model data provide another area-aggregate for the whole EFEDA area. Noilhan (1996) and Noilhan et al. (1997) used the Météo France hydrostatic model PÉRIDOT in conjunction with an AVHRR-based land-use classification (Champeaux and Jullien, 1993) and the soil classification of Mascart et al. (1993). After validation with the surface datasets of Linder et al. (1996), the model was used for aggregation studies. Figure 5-15 (from Noilhan, 1996) shows the surface moisture flux obtained from the mesoscale model. There, the area-aggregate was calculated in two different ways. Firstly, the input parameters to the land-surface scheme (ISBA, see Chapter 6) were averaged over the whole area, before the fluxes were computed using a 1D column version of the model (parameter aggregation approach). Secondly, the same input parameters were used with the same ISBA scheme to compute surface fluxes for each grid cell (10 km wide),

before these grid cell fluxes were averaged over the area (flux aggregation approach). It follows from Figure 5-15 that parameter aggregation gives a satisfactory area-aggregate in this case, which is not only within the range of variability (vertical lines give the standard deviation of the mean) of the individual grid cell values, but practically equal to the flux aggregated values. For the purpose of our comparison, we notice that all daytime model fluxes are consistently higher than the observational surface aggregate, which is surprising, because the model has been validated with EFEDA surface observations previously (Noilhan, 1996). A simple explanation would be that their land-use classification might be biased towards wet (irrigated) crops.

Additional runs of the coupled canopy-ML slab model were made with a new set of input parameters aggregated for the whole area, following the same approach as in section 5.3 above. There, the results of parameter aggregation and flux aggregation do not agree as in the mesoscale model. This affects in particular the partitioning between sensible and latent heat fluxes (Figure 5-16). Sensible heat fluxes are larger with parameter aggregation, moisture fluxes are larger with flux aggregation. This could be an effect of the Penman-Monteith method introducing more non-linearities than the bulk transfer scheme of ISBA. The difference is largest with high fractional areas of irrigated crop (see Figure 5-16 for the Barrax area).

The flux uncertainties are of the same order of magnitude as of aircraft flux estimates. Moreover, some of the data and methodology is the same in both, so the flux estimates are not completely independent of each other.

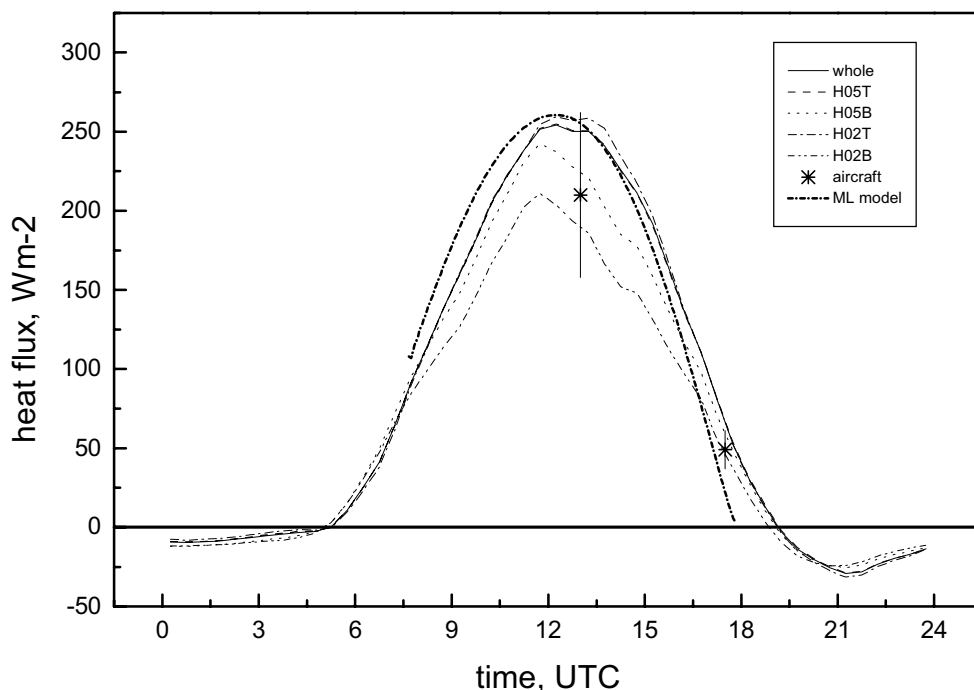


Figure 5-13. Area-aggregated sensible heat flux for the whole EFEDA area (solid line) and for different sub-areas on 23 June 1991. The sub-areas are defined according to the HIRLAM grids. H05T and H05B are the grid cells of the HIRLAM 0.5° resolution version that include the Tomelloso and Barrax supersites, respectively. H02T and H02B refer to the 0.2° resolution version. The star with error bars represents the airborne estimate. Short-dashed line gives radiosonde-ML slab model results.

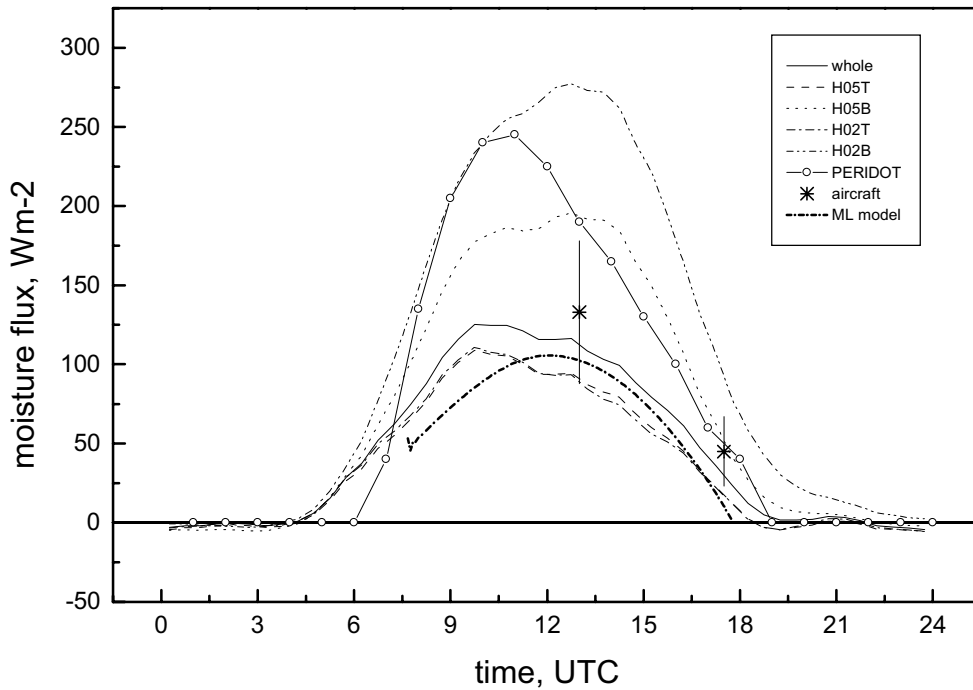


Figure 5-14. Area-aggregated moisture flux, same as Figure 5-13. The open circles represent a selection of the mesoscale model results of Figure 5-15.

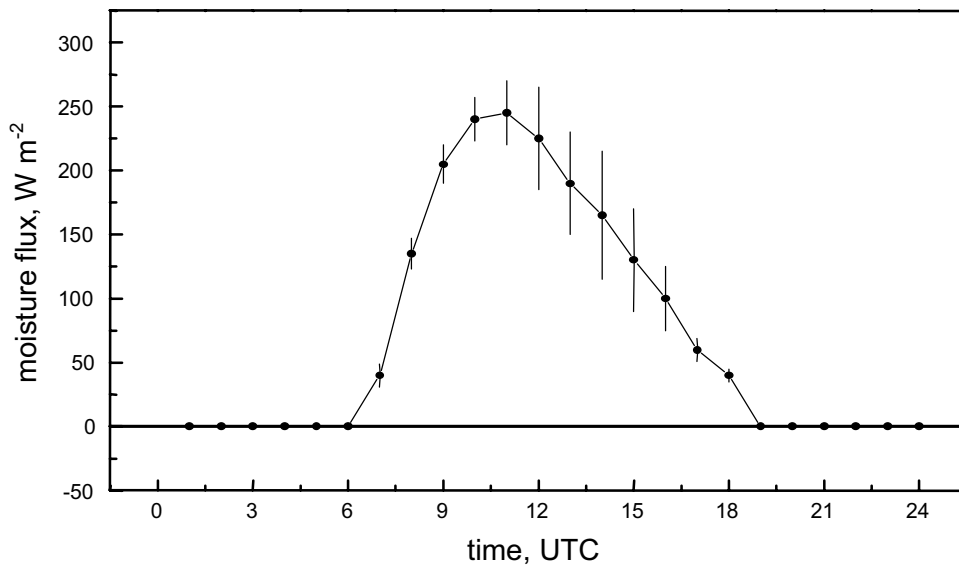


Figure 5-15. Area-aggregated moisture flux from mesoscale model (Noilhan et al., 1996). Solid line corresponds to parameter aggregation, dots to flux aggregation (see text for details).

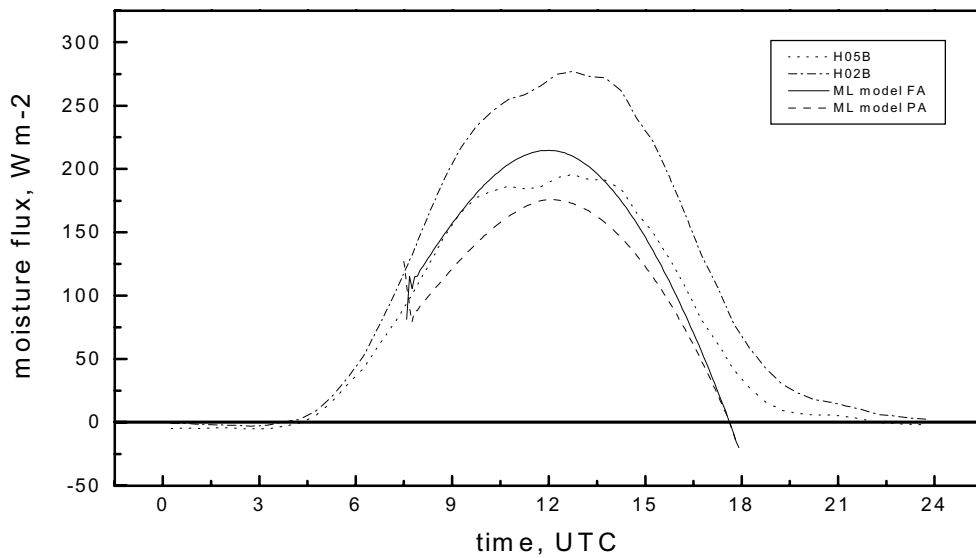


Figure 5-16. Area-aggregated moisture flux from coupled canopy-ML model for Barrax site and related HIRLAM gridpoints. ML model uses same areal fraction of irrigated land as H05B. FA indicates flux aggregation, PA parameter aggregation. See text for details.

Figure 5-17 shows the grid-scale flux comparison of the remaining SEB terms. The net radiation peak ranges from 500 to 600 W m^{-2} , while ground heat flux gives visibly different values only during the afternoon transition. The spread of net radiation is explained by the behavior of albedo and surface temperature (not shown). The aircraft estimate of surface net radiation ($505 \pm 35 \text{ W m}^{-2}$) is within the range of the whole area, but closer to the dry cells. This is due to the specific flight pattern (Flux, Chapter 2) flown on that day, which does not "see" much irrigated land. The indicated uncertainty is a combination of cross-area variability (standard deviation of 19 W m^{-2}) and uncertainty of the "effective" low-level divergence (taken as the mean of local values). Accordingly, the aircraft estimate of ground heat flux is within the (narrow) range of surface observations.

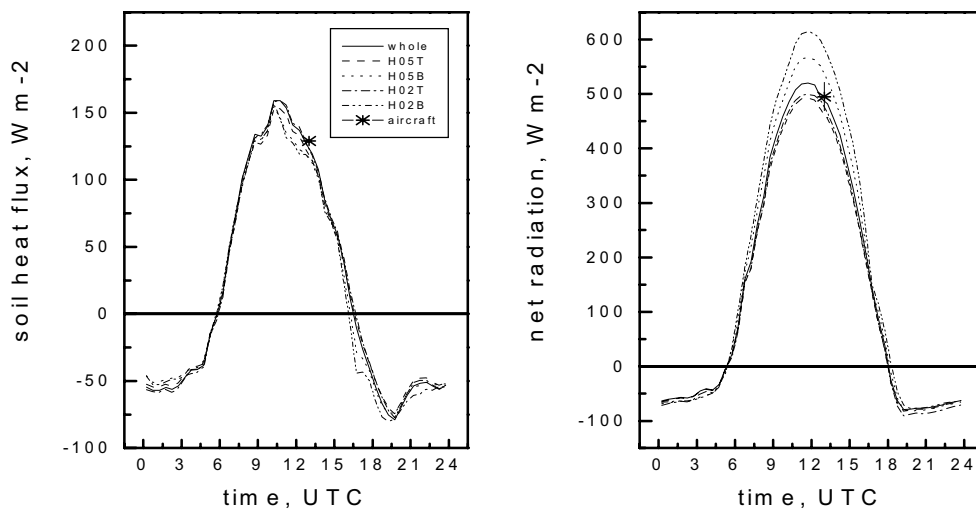


Figure 5-17. Area-aggregated net radiation (left) and ground heat flux (right), same as Figure 5-13.

According to the large spread of aggregated moisture flux and the non-linearities introduced by the moisture indicators, the Bowen ratio and evaporative fraction extend over a wide range as well (Figure 5-18). Moreover, their diurnal behavior is different in dry and wet grid cells. Evaporative fraction is commonly taken as constant over a large part of the daytime period. This applies indeed to the wet cells, but the dry cells and the whole area average are characterized by decreasing values. The opposite occurs with the Bowen ratio, which remains almost constant in the wet cells, but increases strongly in the dry cells and the whole area average.

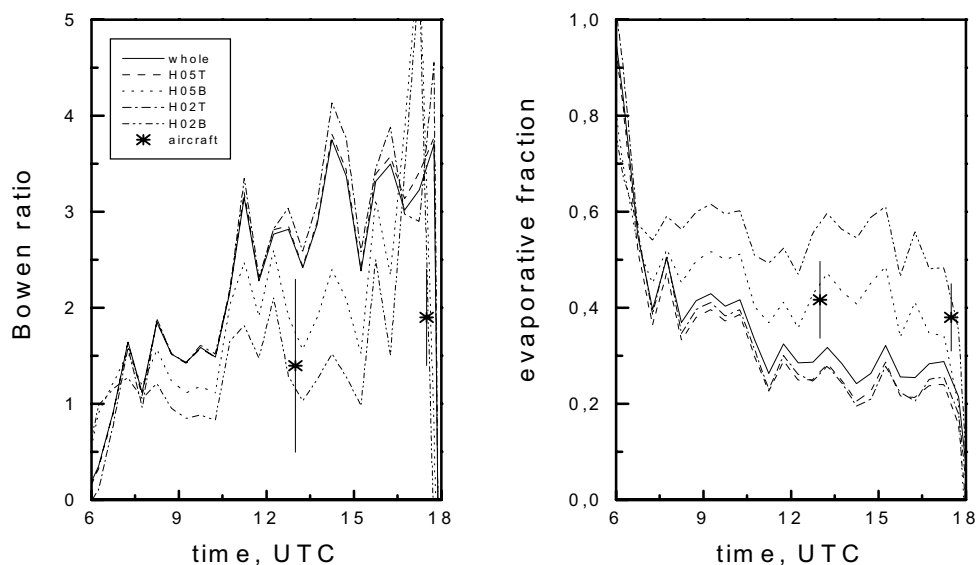


Figure 5-18. Area-aggregated Bowen ratio and evaporative fraction, same as Figure 5-13.

5.5 Conclusions

Summarizing the results of the grid-scale flux comparison, we have seen that the results of the different methods agree within the range of uncertainty. Similar comparison exercises for other days confirm the results. On some days, the airborne estimate of sensible heat flux is low, which could indicate that either the low-level flux divergence was underestimated or that the ML depth was overestimated. The PERIDOT mesoscale model latent heat fluxes are consistently high, which we suppose is due to a wet bias in its land-use database. The area-aggregated fluxes are highly sensitive to the fraction of irrigated land, which (even if trivial in itself) highlights the need of its correct identification (in the land-use classification and in the delineation of the area). Occasionally, large mesoscale moisture flux contributions were observed by the aircraft, which would be consistent with the inhomogeneous moisture fields observed by airborne lidar. We speculate that they originate from a combination of sub-grid scale circulations and the influence of irrigation and the sea breeze, but the data coverage is not sufficient to investigate this quantitatively (see also Chapter 4).

Based on these conclusions, the following statements apply to the consolidated dataset of grid-scale fluxes in EFEDA.

1. The weighted surface averages do provide an adequate estimate of the area-aggregated fluxes for daytime conditions. Given the lack of independent reference results for nighttime, this will be the default assumption for the entire diurnal cycle. Adjustments due to the limited range of "view" of the surface observations, like in the case of BOREAS (Mahrt et al. 2001), are not necessary here. However, adjustments will need to be made for the timing in the crop growth and irrigation cycle and for relative cloud cover (see below).
2. The area-aggregated fluxes (in particular of moisture) depend strongly on the exact area boundaries, whenever a significant fraction of irrigated land is present. A prerequisite is the capability of the land-use classification to properly identify irrigated fields and their water status in different seasons. This implies discerning spring and summer irrigated crops and their respective phenological cycles.
3. To a lesser extent, the area-aggregated fluxes are also sensitive to heterogeneity of cloud cover. An adjustment needs to be made in the form of a factor expressed as the relation between tower cloud cover and areal cloud cover of each vegetation class.
4. Although the impact of locally hilly terrain on the surface fluxes is small, the overall topography of the area may generate subgrid-scale circulations, which either alone or jointly with sea breeze effects give rise to very heterogeneous moisture fields and fluxes across the area. The grid-scale moisture fluxes may be enhanced by mesoscale contributions, which are obviously not captured by the weighted surface average.

Some of these results are not surprising, yet they demonstrate clearly the importance to adequately account for tiles of irrigated land in surface schemes and the corresponding physiographic databases of large scale models. The simplest way to accommodate a minimum information on plant water status would be via the distinction of two classes of irrigated crops, one of spring and one of summer growth cycles. The classification approach of Calera (2000) offers a viable solution for this purpose.

These statements apply to the computation of grid-scale fluxes for the EFEDA area during the whole month of June 1991, where intensive surface tower observations are available. In a more general sense though, they offer the perspective of obtaining seasonal and annual time-series of grid-scale fluxes from the permanent observing stations located in the area, using additional information on crop phenological status as provided by the local Irrigation Association (Martín de Santa Olalla et al., 1999).

6 Performance evaluation of the HIRLAM land-surface and boundary layer description³

6.1 Introduction

The parameterization of land-surface and ABL processes has made considerable progress during the last decade. Advanced surface schemes have recently been incorporated in the major numerical weather prediction (NWP) models. A series of comparison and validation studies (Betts et al., 1993, 1998, 2002, Yucel et al., 1998, and others) have contributed significantly to this progress.

These previous comparisons have all one feature in common, in that the observational sites are located in fairly homogeneous areas, with only small variations in topography and gross vegetation type. All but the Arizona site of Yucel et al. (1998) (who do not provide a detailed study of boundary layer development) are furthermore located in semi-humid or humid climate zones. Yet they all identify problems related to the transport of moisture. An interesting question is, therefore, how the models behave in arid or semiarid climate zones. One step further is the study of possible effects of complex terrain on model performance.

It is the objective of this work to evaluate the surface and ABL performance of the HIRLAM model for a semi-arid environment, with additional emphasis on two aspects of heterogeneity, one related to topography, and one to land-use. For this purpose we will use a consolidated dataset from the European Field Experiment in a Desertification-threatened Area (EFEDA; Bolle et al., 1993). Several characteristics of the EFEDA dataset make it very useful for this kind of comparison. Firstly, the EFEDA area is located at an elevation of 700 m and is surrounded by mountains at distances of several tens of kilometers. Secondly, the surface evapotranspiration is inhomogeneous on scales of several tens of kilometers (i.e. in principle resolvable by limited area models) due to partly irrigated land-use. Observations show clearly that these surface variations affect the whole atmospheric boundary layer (ABL) and can introduce differences of up to 40% in mean ABL moisture. This allows us to test the local (grid element) coupling between surface and mixed layer. In addition, on some days effects of the sea-breeze from the Mediterranean were observed as far inland as in the southeastern part of the EFEDA area, causing moisture advection in the upper boundary layer and the overlying free atmosphere (Noilhan et al., 1996; Miao et al., 2002).

The datasets used in previous comparisons came from a series of land-surface experiments (LSEs) in a wide range of ecosystem and climate zones. These field experiments represent a concentrated effort to document a general circulation model (GCM) grid-scale volume and to study the aggregation of surface exchanges from sub-grid scale to landscape units (Jochum et al., 2000; Feddes et al., 1998). Each LSE involves detailed ground-based measurements (micrometeorology, soils, vegetation) at selected sites, research aircraft with in-situ and remote sensing instrumentation, aerological soundings, and a variety of satellite observations, and thus, a complete dataset for model evaluation. The First ISLSCP (International Satellite Land-Surface Climatology Project) Field Experiment (FIFE, Sellers et al., 1987) was the first LSE to be used for NWP model evaluation. For that purpose, a single mean time series of surface and near-surface parameters was generated by Betts and Ball (1998).

³ Extended version of manuscript submitted to Mon. Wea. Rev. (co-authors: E. Rodríguez-Camino and H.A.R. de Bruin)

Betts et al. (1993) compared this time series with 24 hour forecast time series obtained from the European Centre for Medium Range Weather Forecast (ECMWF) operational model at the grid point next to the FIFE area. They found a number of systematic errors associated with overpredicted incoming solar radiation, too slow ground-surface interaction, surface and boundary layer drying out due to deficiencies in the formulations for soil moisture and surface evaporation, the roughness length for heat, and the description of entrainment at the top of the boundary layer. Based on these results and further studies, improved land-surface parameterizations were developed (Viterbo and Beljaars, 1995) and introduced in the ECMWF operational model and used in the ECMWF Reanalysis Project (ERA). Betts et al. (1998) evaluated the performance of ERA by comparing the corresponding model output time series with the same FIFE dataset. They find that some of the earlier model biases were now removed, but still identify model errors and areas for further model improvement, such as the longwave radiation code and the incorporation of a seasonal cycle of vegetation and ground storage. An area of concern remains also the diurnal cycle of boundary layer development and the transport of moisture.

In a similar way and using the same FIFE dataset, Betts et al. (1997) evaluated the performance of the National Center of Environmental Prediction (NCEP) – National Center of Atmospheric Research (NCAR) reanalysis model and of the NCEP Eta model and contributed to improving the land-surface parameterization in those models. Yucel et al. (1998) compared data from the NCEP Eta model with longer time series of surface data from two observational networks, located in semihumid, continental climate (Oklahoma and Kansas) and in semiarid climate (Arizona). They again find systematic biases in the model solar radiation and in parts of the surface formulation.

Betts et al. (2002) also used data from the old black spruce site of the Boreal Ecosystem-Atmosphere Study (BOREAS, Sellers et al., 1998) in Manitoba, Canada for comparison with the ECMWF and NCEP-NCAR reanalysis models. Here they find again shortcomings of the surface and boundary layer parameterizations related with radiation, soil processes, evaporation, boundary layer development and moisture. The work led to improved land-surface parameterization for high-latitude forests.

Bosveld et al. (1999) performed a comparison of ERA data with fluxes and profiles observed at the Cabauw mast. They find a high bias in incoming shortwave radiation, essentially due to shortcomings of the cloud parameterization. This error propagates into an overestimated summertime net radiation, which in turn leads to overestimated sensible and latent heat fluxes. Comparison of prognostic variables at model level 30 with mast levels reveals discrepancies in the lower ABL structure, which probably result from a combined effect of the surface and ABL schemes.

Bringfelt et al. (1999) evaluated the tile approach (Avissar and Pielke, 1989; Koster and Suarez, 1995) implemented in a new experimental version of the operational HIRLAM. Their reference observations are from three sites of different land-use (agricultural and forest) included in the Northern Hemisphere Climate Processes Land-Surface Experiment (NOPEX, Halldin et al., 1999). They find that the model results depend critically on a realistic description of the vegetation physiology and the initial soil moisture. The tile approach is found to work well there. The new tiled surface scheme of the ECMWF model is shown to improve the surface energy budget in a three-year NOPEX comparison (Gustafsson et al., 2002).

We evaluate here the performance of the current HIRLAM land-surface and boundary-layer description for a semi-arid environment. The output of the fully coupled 3-D model is compared with a comprehensive observational dataset from the European Field Experiment in a Desertification-threatened Area (EFEDA, Bolle et al., 1993). Distributed micrometeorological surface stations, radiosondes, flux aircraft, and airborne lidar provide a unique validation dataset of the diurnal cycle of surface and boundary layer processes.

The purpose of our comparison is twofold. Firstly, the results will provide indications for further model improvement. This corresponds to the classical model validation. Secondly, the information on model output errors enables us to assess uncertainties arising from the use of 4DDA and forecast data in practical applications, such as impact studies and the atmospheric correction of satellite image data (Chapter 7).

The observational dataset, the model versions, and the evaluation strategy are described in section 6.2. The comparison starts with the atmospheric boundary layer (ABL) structure and profiles (section 6.3). We then investigate the surface thermodynamic cycle in section 6.4, before comparing the surface radiation and energy budgets (section 6.5) and summarizing the conclusions (6.6).

6.2 Validation layout

The HIRLAM (High-Resolution Limited Area Model) system is a complete NWP system including 4DDA (Four-dimensional Data Assimilation) with analysis of observations and a limited area short-range forecasting model (Unden et al., 2002). HIRLAM uses the ISBA (Interaction Soil-Biosphere-Atmosphere) surface scheme (Noilhan and Planton, 1989; Mahfouf and Noilhan, 1996; Bringfelt, 1996) and the tile approach to represent fractions of land-use classes present within a single grid element (Rodríguez et al., 2002; Avissar and Pielke, 1989; Koster and Suarez, 1995). The convective mixed layer is parameterized according to Cuxart et al. (2000), while the stable layer formulation is based on Louis (1979). The fast radiation scheme is derived from Savijärvi (1990).

Surface, w_s , and total layer, w_d , water contents, are assimilated separately at each tile. Water intercepted by vegetation, w_r , is not analysed, being simply copied from the first guess to the analysis. The method to initialize w_s and w_d is based on the sequential assimilation developed by Mahfouf (1991), with optimum coefficients approximated analytically by Bouttier et al. (1993a,b), and further modified for operational implementation in the Arpege model by Giard and Bazile (2000).

The operational version 5.2 of HIRLAM (as currently implemented at ECMWF) is used for the validation, while a research version of HIRLAM (as currently used by the Spanish Weather Service INM, Instituto Nacional de Meteorología) serves to analyze details. The comparison focuses on the six-hour forecast (fc06). Whenever there is a notable difference in prognostic variables introduced by the analysis increment, we take a moment to discuss it.

The observational datasets were collected during the EFEDA field phase in June 1991 (Bolle et al., 1993). A large sample of 22 case studies is available of anticyclonic conditions typically encountered in the area during the summer months. Day 23 (23 June 1991) is most densely covered by observations (Michels and Jochum, 1995). The sample composite is almost identical to the individual day 23 observations. Therefore, we have adopted the individual case study

approach in this work. The month of June is perfectly in line with the needs of applications to atmospheric correction of optical satellite data, which are tied to dry, fair weather conditions. The diurnal cycles of surface and ABL processes are compared in detail with observations of 23 June 1991. The performance evaluation at seasonal and annual time-scales is the subject of a follow-up study, which uses data from two permanent observing stations in the same area.

The EFEDA experimental area is located in the region called La Mancha, part of the Castilian high plateau in the Southeast of Spain, at an average elevation of 700 m above mean sea level. It extends about 60 km in North-South direction and 80 km in East-West direction, respectively. The area is generally flat, with elevation variations of up to 100 m, but surrounded and influenced by mountain ranges. The distance to the mountains is 35 km from the South, 45 km towards the Northeast, and 40 km towards the Northwest. Three Intensive Observation Sites (supersites) were selected as to represent the major Mediterranean ecosystems found in the area.

Figure 6-1 shows the location of the two main supersites, Tomelloso (o) and Barrax (+), along with the model grid elements and the locations of operational radiosonde stations. The symbols mark the centerpoints of a 10 km by 10 km square of each site. These centerpoints coincide with the high-resolution radiosonde launch sites in either case. A regular 1° by 1° grid (solid lines) serves to give a rough orientation about the HIRLAM grids. We use two different resolutions of HIRLAM, 0.5° and 0.25°, which would subdivide each 1° by 1° grid element into 4 and 16 smaller elements, respectively. Table 6-1 summarizes the model grid dimensions.

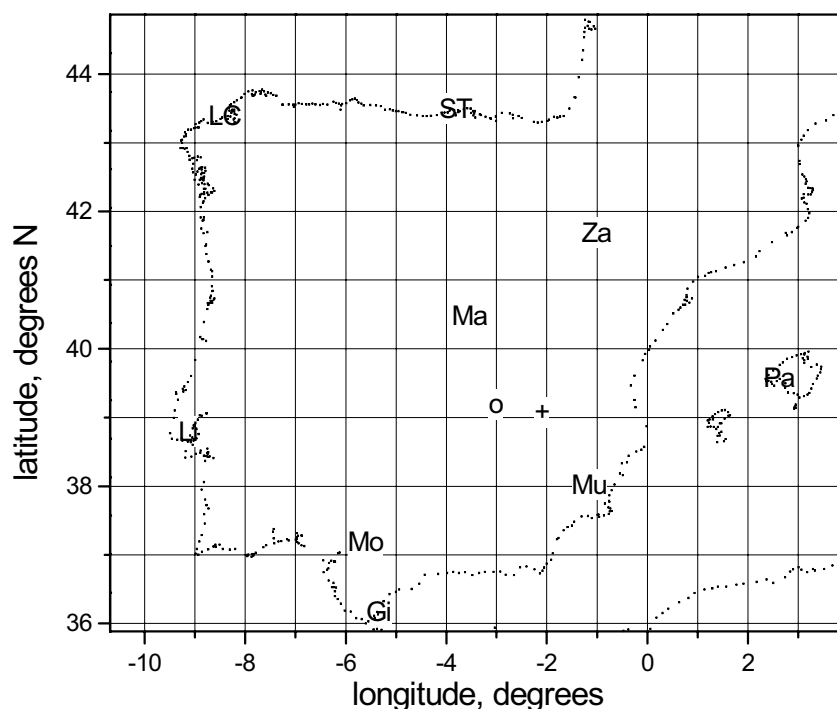


Figure 6-1. Model grids and locations of radiosonde stations for the Iberian peninsula. The solid grid lines mark a regular 1° by 1° grid, which holds four HIRLAM 0.5° grid elements or 16 HIRLAM 0.25° grid elements, respectively. Research radiosondes were launched during EFEDA from the center of the Tomelloso site (o) and from the center of the Barrax site (+). The letter codes indicate the location of the available operational radiosondes.

Table 6-1. Model grid characteristics. Grid size in km gives average values for the Iberian peninsula.

	Resolution latitude	Resolution longitude	N-S grid size, km	E-W grid size, km
HIRLAM-0.25	0.25°	0.25°	24	31
HIRLAM-0.5	0.5°	0.5°	48	62

This comparison focuses on the Tomelloso site, which is representative of fairly undisturbed semi-arid conditions and thus, would be expected to be well reproduced by the models. The Barrax site is characterized by two additional sources of moisture, one at the ground from irrigation and one aloft from the Mediterranean sea-breeze penetrating inland in the afternoon. The latter feature is normally not resolved in operational NWP models. We use the Barrax comparison occasionally, whenever it provides additional insight. Both represent typically Mediterranean landuse. We use the site-aggregated dataset for Tomelloso from Linder et al. (1996). The site-aggregated dataset for Barrax was developed on the basis of Linder et al. (1996) and the vegetation classification of Calera (2000), as described in Chapter 6. The radiosonde and aircraft datasets are used as described in Michels and Jochum (1995) and Jochum (1993b).

Table 6-2. Location and characteristics of HIRLAM gridpoints within the EFEDA area and fixed model parameters for these cells (and tiles when applicable). Values of albedo, LAI, and roughness length are given for June. Data for the EFEDA supersites from Linder et al. (1996). Model landuse classes after Manzi and Planton (1994). Supersite landuse classes after Calera (2000).

	Tomelloso	HIRLAM T	HIRLAM TB	Barrax
longitude	3°01' W	2° W	2°30' W	2°06' W
latitude	39°10' N	39° N	39° N	39°03' N
elevation, m	655	755	891	700
vegetation percentage	.05-0.15 (1-30 June)	0.5	0.4/0.9	.07 (23 June)
landuse class	summer dry (vine)	17 (100%) deciduous shrub	1 (87%) crop, 5 (13%) decid. broadleaf	30% irrigated, 70% bare or summer dry
soil texture type	3	5	11 / 5	4
emissivity	.98	.95	.95	.98
albedo	.28 (23 June)	.17	.18 / .16	.15 irrigated, .23 bare / dry
LAI	0.1-0.4 (1-30 June)	1.5	2.0 / 4.0	.26-.36 (11-29 June)
$r_{s \text{ min}}, \text{ s m}^{-1}$	~ 140	150	40 / 250	(irrigated) 180
roughness length, m	.01-.05 (1-30 June)	0.0391 *)	0.0488 *)	.01 bare / dry .001-.06 irrigated
roughness length for heat, mm	~ $z_0/200$	0.096	0.042 / 0.8	.001 bare

*) includes orography

Due to the presence of mountainous terrain at model scales, the selection of model grid-elements for comparison needs great care. The principal and obvious idea is to have the observational site inside the model grid cell, which in practice

matches the nearest grid-point concept of Betts et al. (1993, 1998). Both FIFE and BOREAS, however, are located within extended areas of similar characteristics and of small topographic variations. In contrast, the EFEDA area itself is rather flat, but is surrounded and influenced by mountain ridges, which come closest to the area from the South (35 km) and East. In a pragmatic way, we have still identified the nearest grid-point to the location of each observational set of profiles (see Table 6-2 for all relevant coordinates). But we also monitor the differences to a set of adjacent grid-points, in order to assess the influence of the model orography. All points included in the comparison are located within the same climate regime. The model grid elements, which include the Tomelloso and Barrax sites, also contain part of the Southern mountains. The model grid elements covering the northern part of the EFEDA area include more mountain ranges towards the North and East. The models use a mean orography, which is adapted to the needs of the mountain drag parameterization. This results in a notable difference in elevation between grid element and site, depending on the model type and resolution. For Tomelloso, the HIRLAM-0.5 grid surface is at 100 m above ground.

6.3 ABL structure and profiles

The daytime diurnal cycle of 23 June 1991 was very densely covered with aircraft observations. Radiosondes were launched roughly every two hours at Tomelloso and Barrax. The day was almost cloudfree with weak northerly winds. Figures 3-5 and 3-6 (Chapter 3) illustrate the daytime evolution of the temperature and moisture stratification at the two sites along with the space-time reference of the radiosonde and aircraft data. Michels and Jochum (1995) performed a detailed analysis of the diurnal cycle of the ABL structure at both sites, as obtained from all available observations (radiosoundings, aircraft ascents, airborne lidar).

At Tomelloso, the stable nocturnal boundary layer (NBL) is about 500 m deep and remains until very late in the morning (11:00 UTC). The ML grows rather slowly until then. Its rapid growth phase starts only after complete erosion of the NBL and is furthermore slowed down by the slightly stable stratification of the very deep (3 km) residual layer (RL). The ML reaches its full depth by late afternoon (17:30 UTC) only, when finally the RL has been eroded as well. The maintenance of the RL for most of the day is rather unusual, but was observed quite often during EFEDA (Michels and Jochum, 1995). It might be explained by the cirrus cloud cover reducing the incoming solar radiation, as well as by the slightly stable stratification of the RL. More energy is needed to remove a stable RL than a neutral one. The RL would be slightly stable for the combined effect of two processes. On one hand, entrainment of warm air at the top of the ML will continue for a short while after the ML has decoupled from the surface in the evening. On the other hand, nighttime cooling due to aerosol and water vapor occurs in the NBL and lower RL (Michels and Jochum, 1995).

At Barrax, the NBL is twice as deep and takes until noon to be eroded. The ML is growing more slowly and reaches a lower final depth. Both features are due to the larger amounts of water vapor available from the irrigated fields. Moisture advected by the seabreeze penetrating inland in the afternoon inhibits further ML growth here. The RL is similar to the one at Tomelloso.

The comparison of the vertical profiles of potential temperature at Tomelloso (Figure 6-2) shows small differences between model forecast and observations. At 06 UTC, the model NBL temperature is about right, whereas the model RL is slightly (-1 K) too cool. At 12 noon, the ML temperature is reproduced very well. However, the model does not capture the weakly stable RL and therefore,

produces a ML top at about 740 hPa, which is almost 100 hPa too high. By 18 UTC, the model ML top is about right, but the ML is 1K too cool. There are no observations available at midnight.

These differences in potential temperature are just above the limit of significance. Taking into account that we are comparing with a single radiosonde profile (which gives a "snapshot" only) and that the results for other fair weather days (not shown here) are similar, we can conclude that the model performs well on daytime potential temperature.

In the 06-12 UTC period, the model-diagnosed warming (Figure 6-3) of the lower ABL is too high, especially at the lowest gridpoint (by 0.3 K h^{-1}). This period is characterized by erosion of the NBL and incipient growth of the ML, so a combination of factors could contribute to the overprediction. Part of the rapid ML growth phase occurs in the afternoon period 12-18 UTC. Therefore, the overall observed ML warming during that period is stronger in the lower layers. This feature is not captured by the model, which gives rise to a slight underprediction (0.1 K h^{-1}) of lower ML warming. The RL warming/cooling is reproduced fairly well in both periods.

For moisture, the situation is different. At 06 UTC, the radiosonde shows a complex layered structure, with a deep relatively dry ($\sim 4 \text{ g kg}^{-1}$) RL and a moist NBL ($6-7 \text{ g kg}^{-1}$) on top of the shallow drier incipient ML. The model forecast comes close to the NBL moisture ($\sim 0.5 \text{ g kg}^{-1}$ more), but is unable to resolve the rest of the layers. This means also that the incipient ML is too moist. At 12 UTC, the model gives a ML top between 800-760 hPa, with humidity slightly decreasing upwards. The radiosonde-derived ML extends only up to 950 hPa, while the rest is the RL. The model ML average of specific humidity ($\sim 7 \text{ g kg}^{-1}$) is about 1.5 g kg^{-1} (27%) too moist. At 18 UTC, the model ML is again about 1.5 g kg^{-1} too moist. The ML top around 660 hPa agrees reasonably well.

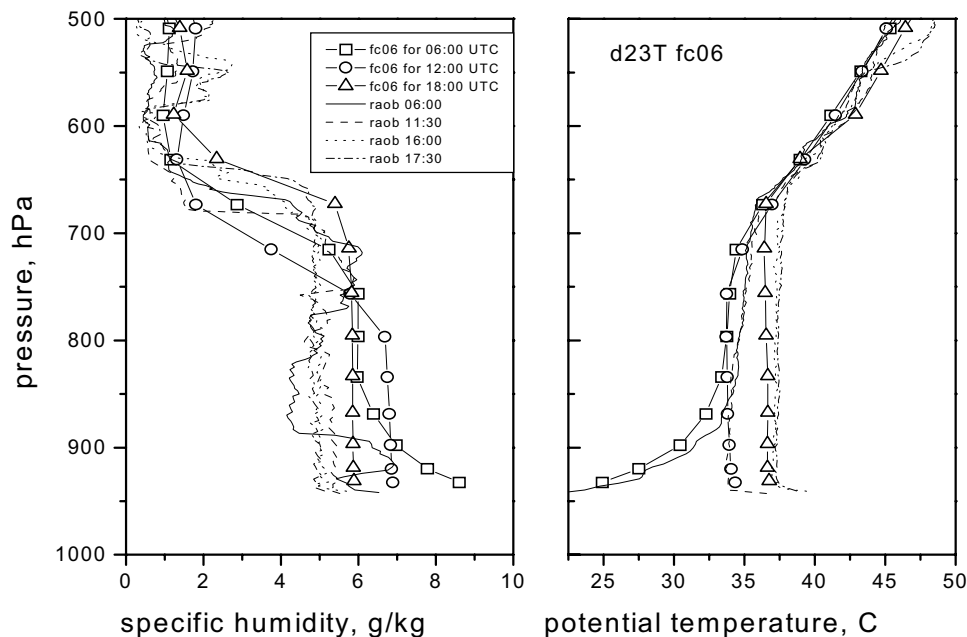


Figure 6-2. Comparison of vertical profiles of potential temperature (right) and specific humidity (left panel) from HIRLAM fc06 (symbols) and Tomelloso radiosonde (no symbols) on 23 June 1991.

The observed drying or moistening varies vertically according to the layered structure (Figure 6-4). During the morning period (06 to 12 UTC) the erosion of the NBL leads to drying of the lowest layers. The lower RL is moistening by entrainment, while the upper RL is strongly drying by entrainment of very dry FA air. The model is able to reproduce the general shape of the vertical profile in this case even though the RL top is too low. During the afternoon period (12-18 UTC), the model ML dries out more than observed, which helps to partially offset the low bias in the 12 UTC humidity profile (such that the 18 UTC profile is less biased). The seemingly good agreement of the upper RL moistening is due to another compensating effect rather than to the model's ability to reproduce the corresponding physical processes. This moistening peak results from the final ML growth going on in the early afternoon, when the remnants of moist RL air are entrained down into the ML. As explained above, the RL erosion takes most of the afternoon. The model does not resolve the moist RL, neither at 12 UTC nor at 18 UTC. The model-produced moistening peak results rather from the underpredicted RL moisture at 12 UTC.

The analysis increment results in several changes in the vertical profiles. Their tendency is to make the 06 UTC and 18 UTC profiles moister and the noon ML profile warmer (~1.5 K) and drier (0.5-1 g kg⁻¹). The overall accuracy is not really improved though. The analysis noon ML is now warmer, but still moister than observed.

Figure 6-5 shows the comparison of model forecast profiles at adjacent gridpoints. The Tomelloso gridpoint elevation is 755 m msl (above mean sea level), the Barrax gridpoint is at 891 m msl. Other than altitude effects, there are small differences in moisture (0.3-0.6 g/kg), but not in temperature. The comparison for the Barrax gridpoint is slightly more favorable due to the enhanced moisture observed there. However, this cannot be attributed to the model performance, since both moisture sources (irrigation and sea breeze) are not represented in the model.

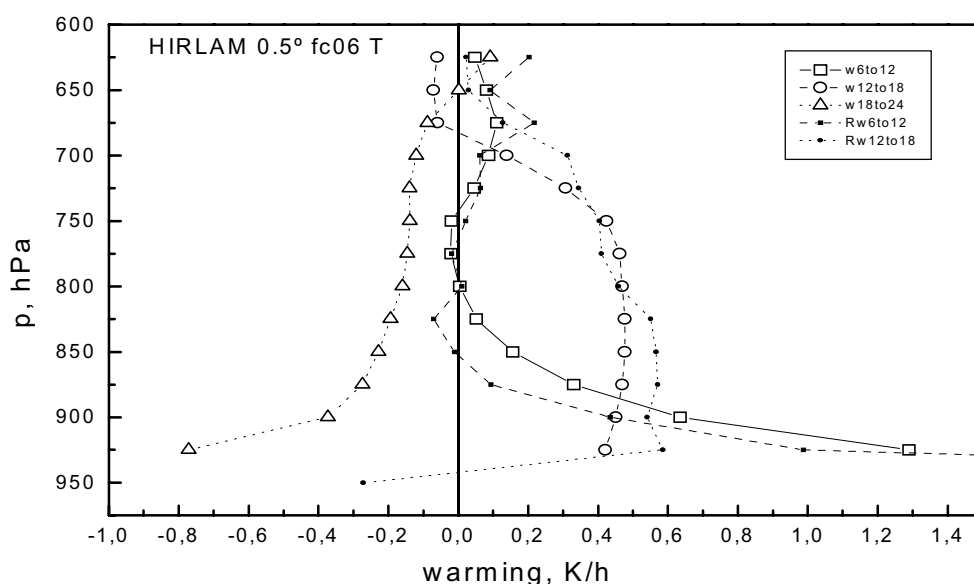


Figure 6-3. Comparison of vertical profiles of warming and cooling rates from HIRLAM fc06 (large open symbols) and Tomelloso radiosonde (small solid symbols) on 23 June 1991.

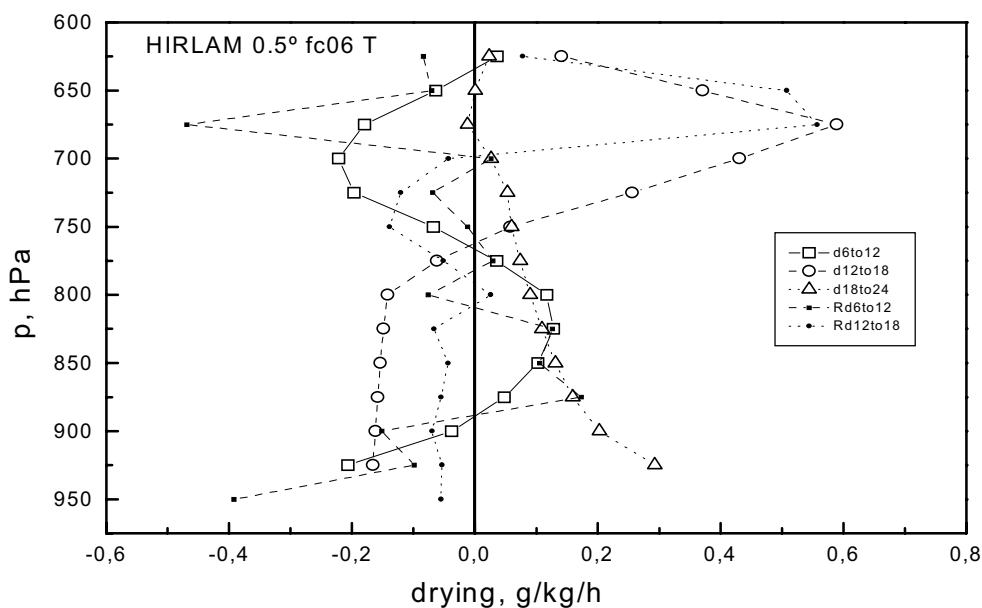


Figure 6-4. As Figure 6-3 for drying and moistening rates.

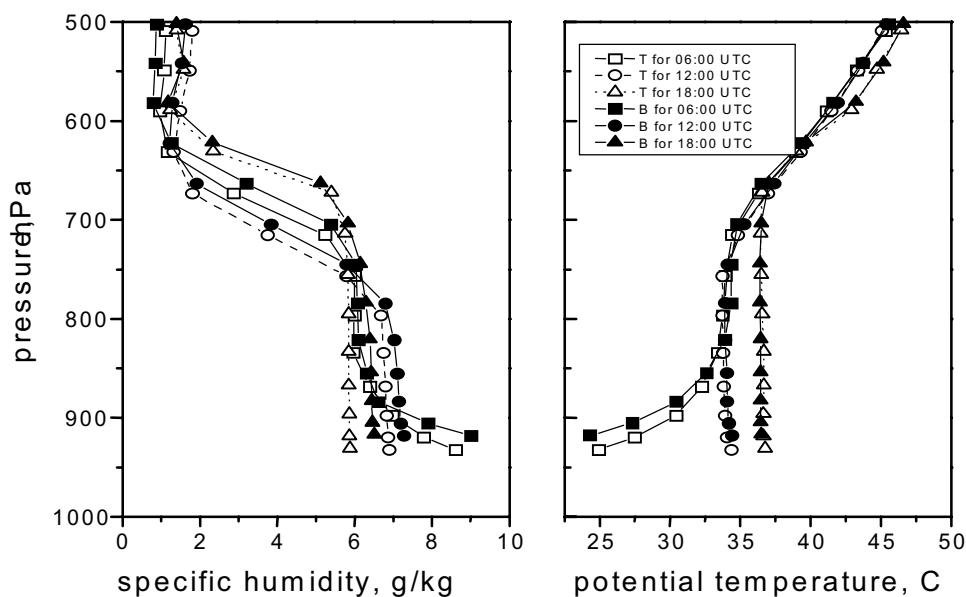


Figure 6-5. Comparison of HIRLAM fc06 profiles at Tomelloso (3°W, 39°N) and Barrax (2.5°W, 39°N) gridpoints.

The general conclusion from the ABL comparison is that there are two categories of differences. One is the general high bias in ML moisture. The other is in the vertical structure itself, since the model does not resolve the RL properly. The first is probably due to problems in the assimilation of moisture in an area of complex topography and close to coastlines, which is unresolved to date. The roots for the second might be found in the vertical model resolution, which is insufficient for this type of landscape, and in the vertical diffusion and

entrainment parameterization. Part of the layered moisture structure observed in the RL is probably due to mesoscale circulations of topographic origin (Jochum et al., 2002; Miao et al., 2002) which obviously are not resolved by the model. Control runs at higher horizontal resolution (0.25°) do not show any significant differences.

6.4 Surface thermodynamic cycle

We are now comparing model data with the site-aggregated surface observations. Based on the assessment of the individual measurement errors and the intra-site variability, differences in temperature and specific humidity exceeding 0.8 K and 1 g kg^{-1} , respectively, are considered to be significant and thus, indicative of model biases.

The model diagnostic package calculates the 2m-temperature and humidity by means of interpolation between the surface (temperature and wetness) and the lowest model level (about 30 m above ground). The special interpolation technique used for this purpose preserves the surface layer similarity profiles (Geleyn, 1988).

The observations of 2m-temperature at Tomelloso (Figure 6-6) show a typical diurnal cycle of a fair weather summer day in continental climate. We find a narrow (2 hour) minimum in the very early morning before sunrise (4:45 UTC), followed by 6 hours of rapid warming until almost noon. The warming slows down then to lead into a broad (4 hours) afternoon temperature maximum. The evening cooling sets on about one hour before sunset (19:49 UTC). The Barrax surface is generally cooler (night, afternoon), but coincides with Tomelloso during the early part of the rapid warming phase. The model reproduces well the midnight and 06 UTC temperatures, although it obviously misses the minimum (possibly due to the 6-hourly output intervals). It performs well for the rapid warming phase, but then stops short of reaching the observed maximum. This means that the morning surface warming slows down and stops earlier in the model than in reality. Consequently, the 18 UTC temperature is slightly too low. The observed high temperature amplitude of the day (17 K) can obviously not be reproduced by the model (which may miss the minimum and does not reach the maximum).

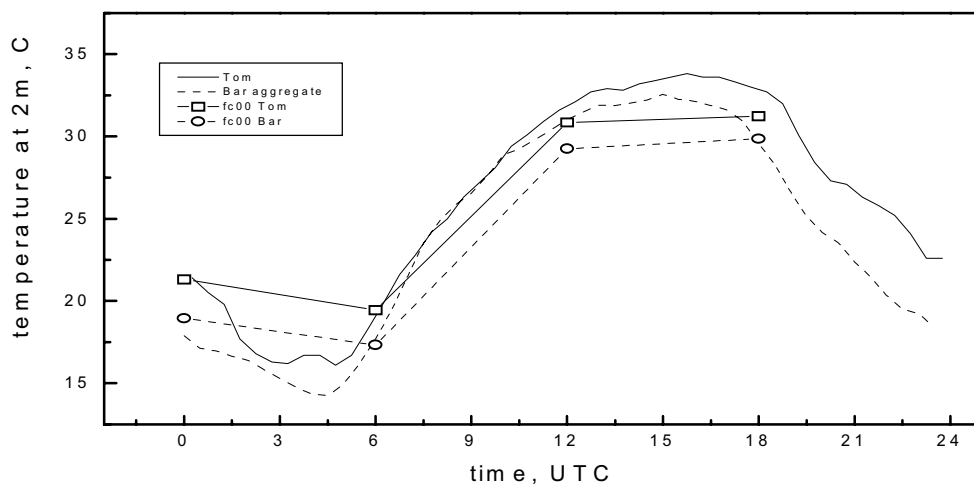


Figure 6-6. Comparison of 2m temperature from model diagnostics and surface observations at Tomelloso (Tom) and Barrax (Bar).

The specific humidity diurnal cycle (Figure 6-7) exhibits a more complex behavior. We observe two maxima, one in the early morning hours and one in the late evening till midnight. The daytime drying is strongest in the late morning, during the rapid ML growth phase, and again in the late afternoon, coinciding with the moment when the plants have closed their stomata. Due to the presence of moisture from irrigated fields, the surface at Barrax keeps moistening or stays at almost constant specific humidity until late afternoon, when some drying sets on. The model reproduces fairly well the daytime dry state and the weak drying from noon to 18 UTC. At night, however, the model overestimates the moistening between 18 and 24 UTC and then keeps moistening until 06 UTC, where it reaches a maximum of 9.5 g/kg (contrasting with the observed morning maximum of about 7 g/kg).

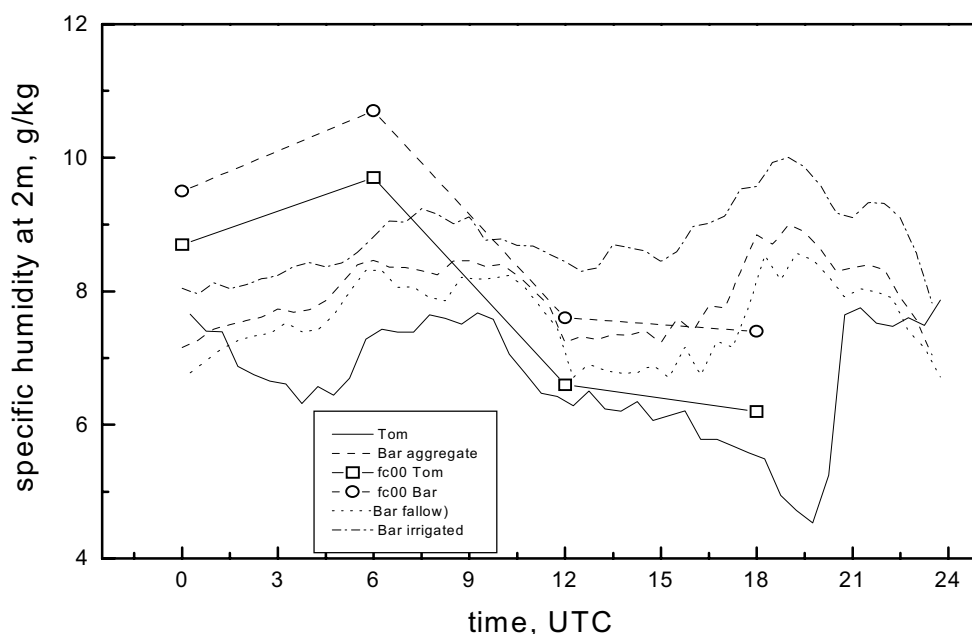


Figure 6-7. Same as Figure 6-6 for specific humidity. For Barrax, the site-aggregate (dashed) is shown as well as the major landuse classes (dotted: fallow; dash-dotted: irrigated crops).

The physical processes contributing to the daytime thermodynamic cycle can be understood from the (θ, q) mixing lines shown in Figure 6-8, where θ is potential temperature. The observations show a decoupling of surface warming and drying processes during the early morning warming period (6-10 UTC). To a lesser extent, this applies also to the late morning drying period (10-12 UTC) (where slight warming does occur) and to the afternoon warming period (where some drying occurs). The model obviously does not resolve these individual periods. Model warming and drying appear as coupled processes with strong drying and strong warming between 6-12 UTC (points 2 to 3 in Figure 6-8). Less drying and very little warming occurs between 12-18 UTC (points 3 to 4 in Figure 6-8).

The observed decoupling of warming and drying processes is essentially due to the complex and inhomogeneous moisture fields in the ABL and above (Michels and Jochum, 1995). During the early morning warming period, there is very little surface evaporation at Tomelloso. With the slowly growing mixed layer (ML), moist air is entrained from the overlying nocturnal stable boundary layer (NBL).

This contributes to a slight moistening of the surface until the shallow NBL is eroded. This is then the start of the rapid ML growth phase, where entrainment of very dry air from the residual layer (RL) contributes to strong surface drying. Entrainment of RL air does not enhance warming, because the RL and ML have about the same potential temperature at that time. When the ML has grown to its maximum top (equal to the RL top), entrainment brings in warm, but not very dry air from the free atmosphere aloft. This again leads to a weak decoupling of warming and drying.

The surface warming/cooling and drying/moistening is generally driven by the heat and moisture exchange at the surface and by entrainment processes reaching downward from the ML top to the surface. Airborne lidar observations and bivariate conditional sampling of airborne fluxes show clearly that entrained air almost reaches the surface layer (Michels and Jochum, 1995).

The model is obviously not able to resolve the observed vertically layered moisture fields and probably does not produce strong enough entrainment. We have discussed the issue in the context of the ABL profiles. Its daytime surface thermodynamic cycle starts at 06 UTC potentially too warm and much too moist. The warming rate is less than observed, which offsets the wrong start and helps the model to catch up with the observed thermodynamic state at noon. During the afternoon forecast period, it seems that the model again does not reproduce the entrainment contribution to warming and drying.

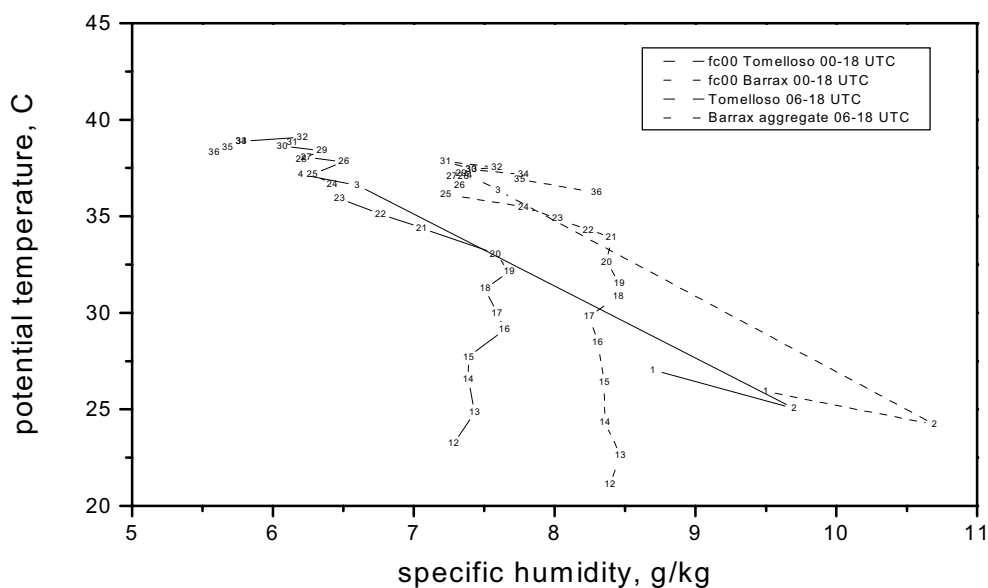


Figure 6-8. (θ, q) mixing lines from model diagnostics and surface observations at Tomelloso and Barrax. Observations are half-hourly values numbered consecutively from 12 (06 UTC) to 36 (18 UTC). Model values (marked 1-4) correspond to forecast hours (00 to 18 UTC).

The observed surface temperature (Figure 6-9) has a wide amplitude diurnal cycle, reaching from a 18 K minimum at sunrise to a noon maximum of 55 K. The model reproduces well the nighttime low values and the 18 UTC value, but fails by far (17 K, 30%) to reach the daytime maximum. This affects both the longwave radiation and the heat and moisture flux. We will return to this issue when discussing the surface fluxes.

The model surface temperature is calculated from a force-restore method, where the forcing is the soil heat flux G (which in turn is obtained directly from the surface energy balance). For the afternoon period (12-18 UTC), the modeled G agrees very well with observations (-6%). This leads to the observed good agreement of surface temperature. The morning G is 36% too high. In addition to other relevant soil parameterization effects, this results in the significant underestimation of surface temperature at noon.

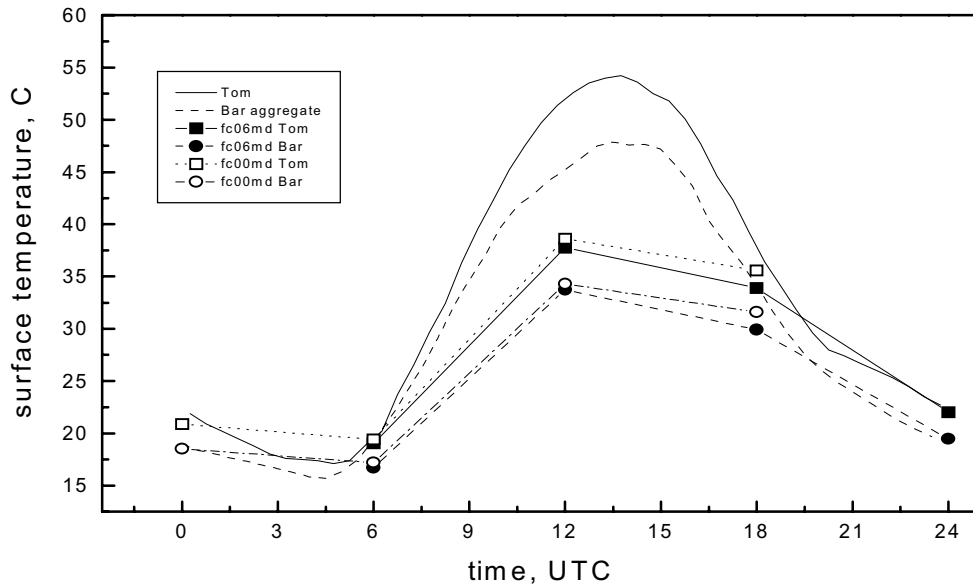


Figure 6-9. Comparison of surface temperature from model first-guess (fc00md), 6-hour forecast (fc06md), and site-aggregated surface observations at Tomelloso and Barrax.

Table 6-3 gives a summary overview of the major findings of this section.

Table 6-3. Differences between surface state of model diagnostics and observations at Tomelloso (T) and Barrax (B).

	00 UTC	06 UTC	12 UTC	18 UTC
2m specific humidity	a bit too moist	much too moist	about right	T too moist B too dry
2m temperature	±ok	±ok	too cool	T too cool B about right
Surface temperature	±ok	±ok	much too cold	T ±ok B a bit less ok
Warming / cooling	cooling ok	overall cooling ok (misses minimum)	±ok, warming slows down earlier	±ok
Drying / moistening	moistening too much	moistening instead of drying, misses minimum	more drying ==> 12 UTC ok	±ok

6.5 Surface radiation and energy budgets

The model output provides surface fluxes accumulated over the 6 hour forecast period at each forecast time (00, 06, 12, 18 UTC). The observations consist of time series of half-hourly flux averages. For comparison with model output data, 6-hour averages were derived from each time series of surface flux observations. Figure 6-12, Figure 6-13, and the set of tables (Table 6-4 to Table 6-7) show the resulting values, normalized by the length of the averaging period. These values represent the mean fluxes during each forecast interval. Figure 6-14 shows the relative contributions of each component in the surface radiation and energy budgets. As explained above, the reference point for the comparison is Tomelloso. Results for Barrax are shown and used whenever they help to gain additional insight.

The site-aggregated observations at Tomelloso show an essentially clear-sky net radiation, slightly reduced in amplitude by light cirrus cloud, peaking at 500 Wm^{-2} shortly before local noon (Figure 6-10). The intra-site variability is around 20 Wm^{-2} , which lies within the range of individual measurement errors of 5%.

The model overestimates net radiation considerably, by 28% in the morning period and 47% in the afternoon period. In order to track the error sources, we first compare the individual terms in the surface radiation budget:

$$R_n = R_{sd} - R_{su} + R_{ld} - R_{lu} \quad (6.1)$$

where R_n is net radiation, R_{sd} downwelling shortwave (SW) or solar radiation, R_{su} upwelling (reflected) SW radiation, R_{ld} downward longwave (LW) radiation, and R_{lu} upward LW radiation. Units used here are energy fluxes (W m^{-2}).

Figure 6-11 shows the observational reference.

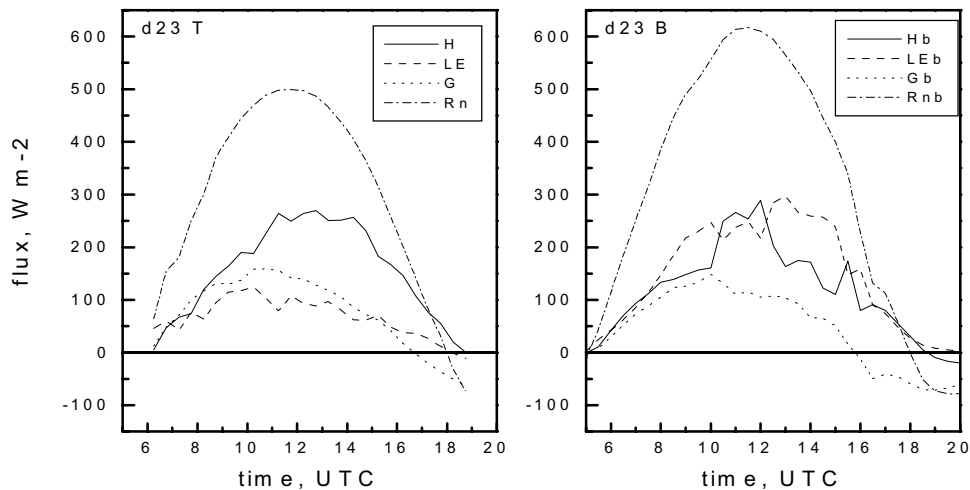


Figure 6-10. Surface energy budget components at Tomelloso (left panel) and Barrax (right) on 23 June 1991. Observations are site-aggregated values (see text).

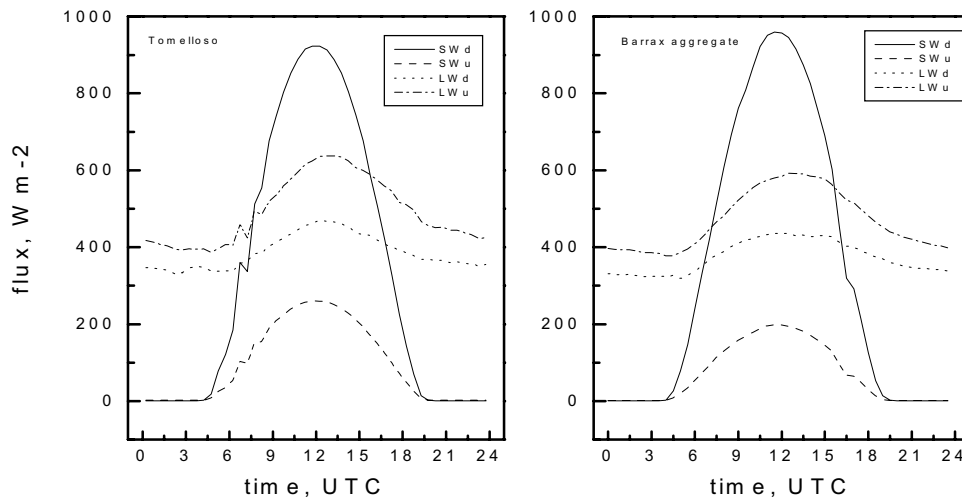


Figure 6-11. Same as Figure 6-10 for surface radiation budget components.

The model overestimates the incoming solar radiation by 10% in the morning and 17 % in the afternoon (Table 6-5 and Figure 6-14). This is surprising for the sign of the bias and even more for its magnitude. The model atmosphere is too moist and slightly too cool (see vertical profiles of water vapor in Figure 6-2). Therefore, one would expect a reduced SW transmission in the model. With a more realistic atmospheric moisture profile, the bias would even be larger. Moene et al. (1995) compared the HIRLAM version 2 with individual station data at Tomelloso and found the same bias. Betts et al. (1993) found a similar (10%) high bias in the T-106 L-19 cycle 39 version of the ECMWF model as compared to FIFE data. They explained it with the cumulative effect of three small biases in the SW radiation code of that model version, the first due to the band-parameterization, the second and third due to the lack of water vapor and aerosol absorption, respectively. With the introduction of aerosols and of the prognostic cloud scheme in the ERA15 reanalysis scheme, the incoming shortwave radiation performed rather well for the FIFE conditions (Betts et al., 1998). Comparison of the ERA15 data with the same EFEDA-Tomelloso observations (not shown here) does indeed show a better agreement of the incoming solar radiation (5% low in the morning, 10% high in the afternoon).

About 1-2/10 of thin cirrus cloud was observed in the area on most days. The model gridpoint Tomelloso does not show any cloud cover on 23 June, whereas at the Barrax gridpoint it gives 0.11 ci at noon. The lack of cloud cover at the model grid point would explain about 2% of the bias.

In order to explore potential sources of the SW high bias found in the Tomelloso comparison, we analyze details of the HIRLAM SW radiation scheme (Sass et al., 1994). The scheme is based on the parameterization of Savijärvi (1990), whose terminology is used here. For cloud-free grid elements, the incoming solar radiation at the surface (in $W m^{-2}$) is expressed as

$$R_{sd} = S \sinh \left\{ 1 - 0.024 (\sinh)^{-0.5} - \alpha \alpha 0.11 (u/\sinh)^{0.25} - \alpha s (0.28/(1+6.43\sinh) - 0.07\alpha) \right\}, \quad (6.2)$$

where a_a and a_s are constants (see below), u is the column-integrated (linearly) pressure-scaled water vapor (in cm), and α is the SW albedo of the ground. The "solar constant" S (in Wm^{-2}) is approximated as

$$S = 1365 \{ 1 + 0.03422 \cos (2\pi d/365) + 0.0013 \sin (2\pi d/365) + 0.000719 (4\pi d/365) \}, \quad (6.3)$$

where d is the running date from 1 January.

The local sun-height angle h is given by

$$\sinh = \sin(h) = \cos(\varphi) \cos(dc) \cos(t_0 + \lambda) + \sin(\varphi) \sin(dc), \quad (6.4)$$

where φ is latitude, λ longitude, t_0 local hour angle, and dc the solar declination angle ($dc = 23.45^\circ \cos \{2\pi (d-172)/365\}$).

The terms in Equation (6.2) represent the reduction of the top-of-the-atmosphere solar radiation ($S \sinh$) by ozone UV and visible absorption in the stratosphere (term II), water and tropospheric ozone and CO_2 absorption (term III), Rayleigh scattering (term IV), and backscattering from the reflected beams (term V). The constants $a_a=1.2$ and $a_s=1.25$ serve to include the effects of aerosol absorption and scattering, with values selected from empirical fits to data in "continental industrialized areas during normal visibility" (Savijärvi, 1990).

EFEDA field visibility records and airborne lidar observations (Jochum, 1993b; Kiemle et al., 1995) suggest that the atmosphere was hazy and visibility was low on most days. Therefore, the aerosol parameterization constants might not be adequate for the area. We have calculated the individual terms of Equation (6.2) from the corresponding model data. Terms II and V are very small (below 3%). Terms III and IV contribute about 20% and 7%, respectively. Enhancing the aerosol absorption coefficient a_a from 1.2 to 1.5 increases the contribution of the corresponding term to 26%, which would result in reducing the high bias by about 6%.

Some of the aerosol may also be of marine origin, especially in the afternoon (brought into the area by the sea-breeze penetrating inland from the Mediterranean coast in the afternoon). This would contribute to enhanced scattering as well, increasing the aerosol scattering coefficient a_s to 1.9 (Paltridge, 1973) and thus, augmenting term IV in Equation (6.2) by 2-3%.

The upwelling (reflected) SW radiation is underestimated by the model. This is clearly due to the low model albedo. Observations show an albedo of 0.28-0.29, whereas the model physiographic database gives a value as low as 0.17. This represents an underestimation of 35-37% (morning-afternoon), which cannot even be offset by the high model incoming solar radiation. The low model albedo is close to that observed at the irrigated fields of Barrax, which is consistent with the moist and cool model surface and atmosphere.

Both LW radiation components are too low in the model, but the resulting total LW radiation is too high (18% in the morning, 12% in the afternoon), which may be responsible for part of the excessive cooling.

The downward LW radiation depends very much on the vertical moisture and temperature profiles. The model ABL is too moist and slightly too cool, which might explain most of the 19-22% low bias of downwelling LW radiation.

The 11-13% low bias in outgoing LW radiation is closely linked to the surface temperature, which is greatly underestimated by the model (Figure 6-9).

We now return to the high bias in net radiation and use Table 6-5 to analyze the relative importance of the errors in the individual radiation components. For the morning period, we see that the total SW bias (-117 W m^{-2}) is much higher than the total LW bias ($+21 \text{ W m}^{-2}$). The relative contribution of the total SW bias to the net radiation bias is -34% (in percent of observed net radiation). This overestimate is slightly offset by the LW bias, which contributes $+6\%$ of the observed net radiation, resulting in a total high bias of 28% for net radiation. The overestimation of incoming SW radiation and the low bias in albedo contribute about equally to the total SW bias.

For the afternoon period, the total LW bias contribution is the same as in the morning ($+6\%$). The total SW bias, however, contributes much more to the overall error (-162 W m^{-2} , corresponding to -53% of observed net radiation) and thus, explains almost entirely the gross overestimation of net radiation (47%). The incoming solar radiation error has the largest share in it.

The nighttime SW fluxes are small (Table 6-7). In the 00-06 UTC period ("night"), the high bias in the incoming SW radiation is 11% . The large low bias in upward SW is due to the low model albedo. The LW fluxes are generally predicted well ($+6\%$, -1% , with good agreement in surface temperature as well). The resulting net radiation bias is essentially caused by the albedo bias. In the 18-24 UTC period ("evening") we find the worst case overestimation of incoming SW (-53%), but the values are small and the error is offset by a small low bias in the LW flux. The resulting error in R_n is zero.

In conclusion, we have identified a high bias in daytime incoming SW radiation (originating from the aerosol description in the radiation code) and a low bias in albedo (rooted in the vegetation class assignment). Both (in descending order of magnitude) cause a large overestimation of net radiation. Model errors in LW radiation components are of smaller magnitude and of less impact on net radiation.

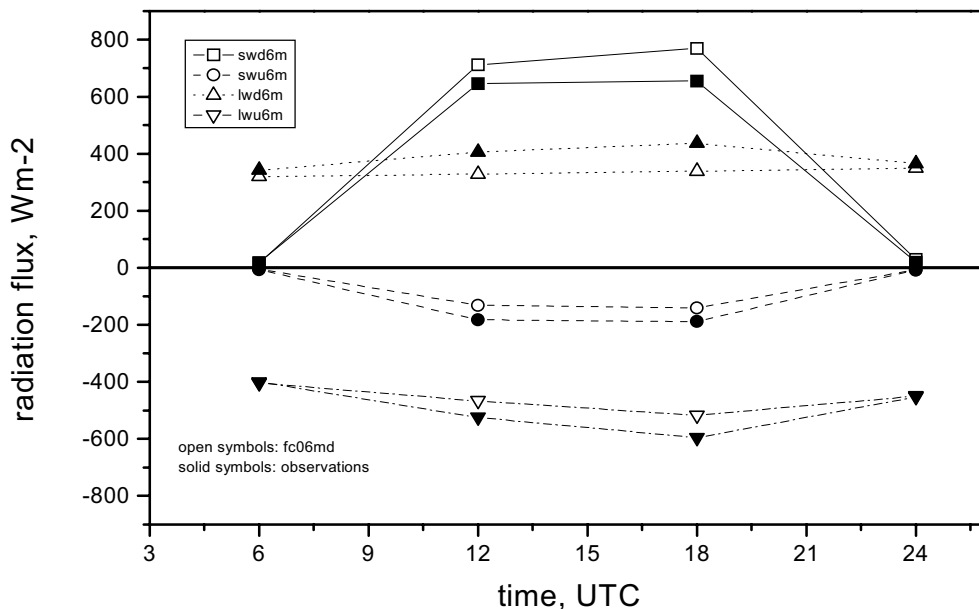


Figure 6-12. Comparison of surface radiation budget components at Tomelloso on 23 June 1991. Open symbols denote model output (fluxes accumulated over 6 hour forecast period, normalized with forecast interval). Solid symbols denote site-aggregated observations (mean values of 6h-period, normalized with forecast interval). swd=SW down; swu=SW up; for LW accordingly.

We now return to look at the surface energy budget. Model and observations agree in that the daytime available energy is dominated by the sensible heat flux (H). The bias in latent heat flux (LE) is smaller in absolute magnitude and changes sign from morning to afternoon. The sensible heat flux is overestimated by 56% in the morning and by 54% in the afternoon.

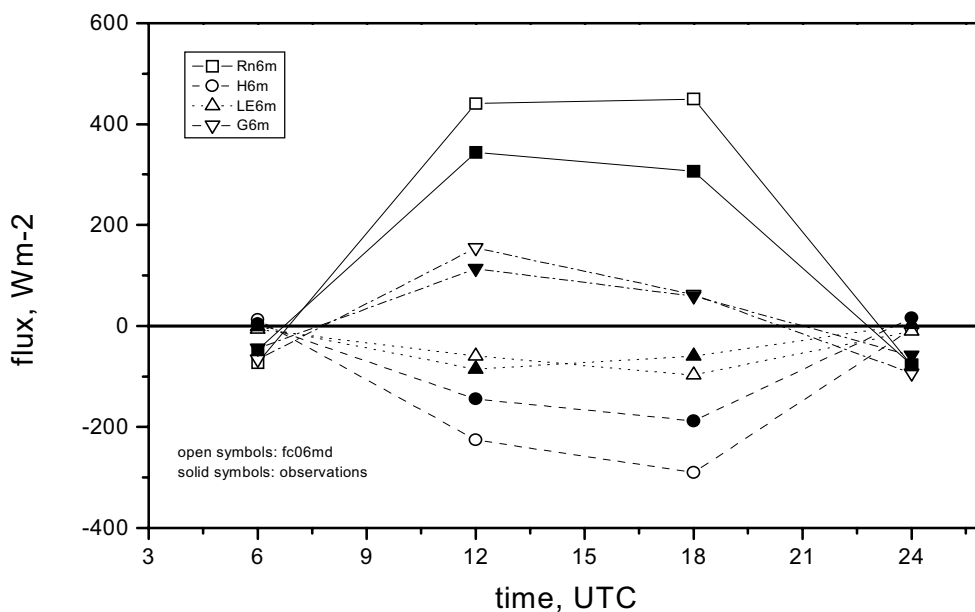


Figure 6-13. Comparison of surface energy budget components at Tomelloso on 23 June 1991. Symbols as in Figure 6-12.

It is difficult and may seem futile to perform a detailed comparison of the surface energy budget in view of the fact that the model surface scheme acts on a stage very different from the actual site setting. The model grid element is entirely covered by rather dense (50% vegetated) deciduous shrub (Table 6-2). Consequently, the key vegetation parameters are very different from observations (Table 6-2). The low albedo, high vegetation fraction, and low surface resistance jointly explain the biases in sensible and latent heat fluxes. We have seen above already that the low albedo explains much of the net radiation bias. The ISBA model has been extended for Mediterranean vegetation and thoroughly validated off-line for the EFEDA area (Braud et al., 1993; Giordani et al., 1996; Noilhan et al., 1996). So there is no question that it works well in this environment, provided it is given the adequate input parameters. Tests with a modified landuse classification are under way at INM, in order to assess the feedbacks in the fully coupled 3-D model. Yet they are not assumed to completely alter the performance of the land-surface scheme. Effects of the model orography and spatial resolution were investigated using the higher resolution model version (0.25°). The results are not significantly different though.

The potential impact of the high bias in H would be increased warming of the ML, but the model ML is slightly too cool. Similarly, the potential impact of the low bias in LE at noon would be a too dry ML, but model ML is very moist. This indicates that the underestimation of ML temperature and especially the overestimation of ML moisture originate from sources other than the surface forcing. As discussed above, the assimilation scheme is the prime candidate here.

The model soil heat flux G is calculated from the surface energy budget

$$R_n = H + LE + G \quad (6.5)$$

In the afternoon period, the errors in the three components R_n , H , and LE offset each other, such that the resulting G is almost unbiased (-6%). This leads to a very good agreement of modeled surface temperature with observations at that time (Figure 6-9). The situation is different in the morning period, where the remaining bias in G is -36%. This overestimation contributes significantly to the large low bias in surface temperature at noon.

G is also too high at night (during both periods), basically as a result of the R_n bias.

Table 6-4. Components of the surface energy budget at Tomelloso on 23 June 1991. ob = site-aggregated surface observation (mean values of 6h period, normalized with forecast interval); fc = HIRLAM 6h forecast (fluxes accumulated over 6 hour forecast period, normalized with forecast interval); del = difference (ob - fc); delp = difference in percent (= del/ob). ava = available energy (H+LE); efra = evaporative fraction (LE/ava). All flux units are Wm^{-2} .

	Accumulation 06 - 12 UTC				Accumulation 12 - 18 UTC			
	ob12	fc12	del12	del12p	ob18	fc18	del18	del18p
Rn	344	441	-97	-28	307	450	-143	-47
ava	231	286	-55	-24	248	387	-140	-56
G	113	155	-41	-36	59	62	-3	-6
LE	86	60	26	30	60	97	-38	-63
H	145	226	-81	-56	188	290	-102	-54
100 * Bowen	161	377	-217	-135	332	299	33	10
100 * efra	43	21	22	51	24	25	-1	-6

Table 6-5. Same as Table 6-4 for surface radiation budget. SWd=SW down; SWu=SW up; for LW accordingly.

	ob12	fc12	del12	del12p	ob18	fc18	del18	del18p
SWd	646	712	-66	-10	655	769	-114	-17
SWu	183	132	51	28	188	141	48	25
100 * albedo	28	18	10	35	29	18	11	37
SW total	463	580	-117	-25	467	629	-162	-35
LW total	-119	-140	21	-18	-160	-179	19	-12
LWd	406	328	78	19	437	338	98	22
LWu	525	467	57	11	597	517	79	13

Table 6-6. Same as Table 6-4 for night (00-06 UTC) and evening (18-24 UTC) periods.

	ob06	fc06	del06	del06p	ob24	fc24	del24	del24p
Rn	-47	-73	25	-53	-77	-77	-1E-3	0
ava	-3	-6	3	-107	-19	17	-36	188
G	-44	-67	22	-50	-58	-94	36	-61
LE	2	7	-5	-319	-3	11	-13	484
H	-4	-13	8	-182	-16	6	-22	137
100 * Bowen	63	-190	254	401	697	56	641	92
100 * efra	50	-111	161	321	18	64	-47	-263

Table 6-7. Same as Table 6-5 for night (00-06 UTC) and evening (18-24 UTC) periods.

	ob06	fc06	del06	del06p	ob24	fc24	del24	del24p
SWd	19	17	2	12	20	31	-11	-55
SWu	7	4	3	44	8	7	1	14
100 * albedo	151	24	126	84	152	23	128	85
LWd	342	320	22	6	365	349	16	4
LWu	401	405	-4	-1	453	450	4	1
SW total	16	13	-3	-19	12	24	-12	-100
LW total	-59	-85	26	-44	-88	-101	13	-15

Since the model surface scheme ISBA was calibrated with Tomelloso data (among many others), we assume that the scheme itself does not have any major deficiencies in that area. The soil scheme appears to perform reasonably as well, within the limits of a one-layer scheme, which does not resolve the diurnal cycle of the upper soil layers (Figure 6-16). The slight high bias of soil moisture (Figure 6-15) and the low bias of soil temperature might be due to the assignment of soil type (5 instead of 3).

The soil heat flux bias is a direct result of the errors in the other three terms of the surface energy budget, which compensate each other in the afternoon period, but not in the morning. There, the high soil heat flux bias propagates directly into the surface temperature calculation and causes a large underestimation.

In summary, we have identified deficiencies in all terms of the surface energy budget. The net radiation is overestimated by 28% in the morning and 47% in the afternoon, which is mainly caused by the high bias in incoming solar radiation, but also by the low model albedo. The high bias in incoming solar radiation has been traced to the aerosol parameterization. The sensible heat flux has a high bias of 56% (morning, 54% afternoon), while the moisture flux bias changes sign from 30% low (morning) to 63% high (afternoon). The discrepancy

essentially results from the vegetation class and subsequent parameter attribution in the model physiographic database, where the Tomelloso grid element is much more densely vegetated than the sparse vine canopy actually growing there. Even at the irrigated site Barrax, the situation is similar.

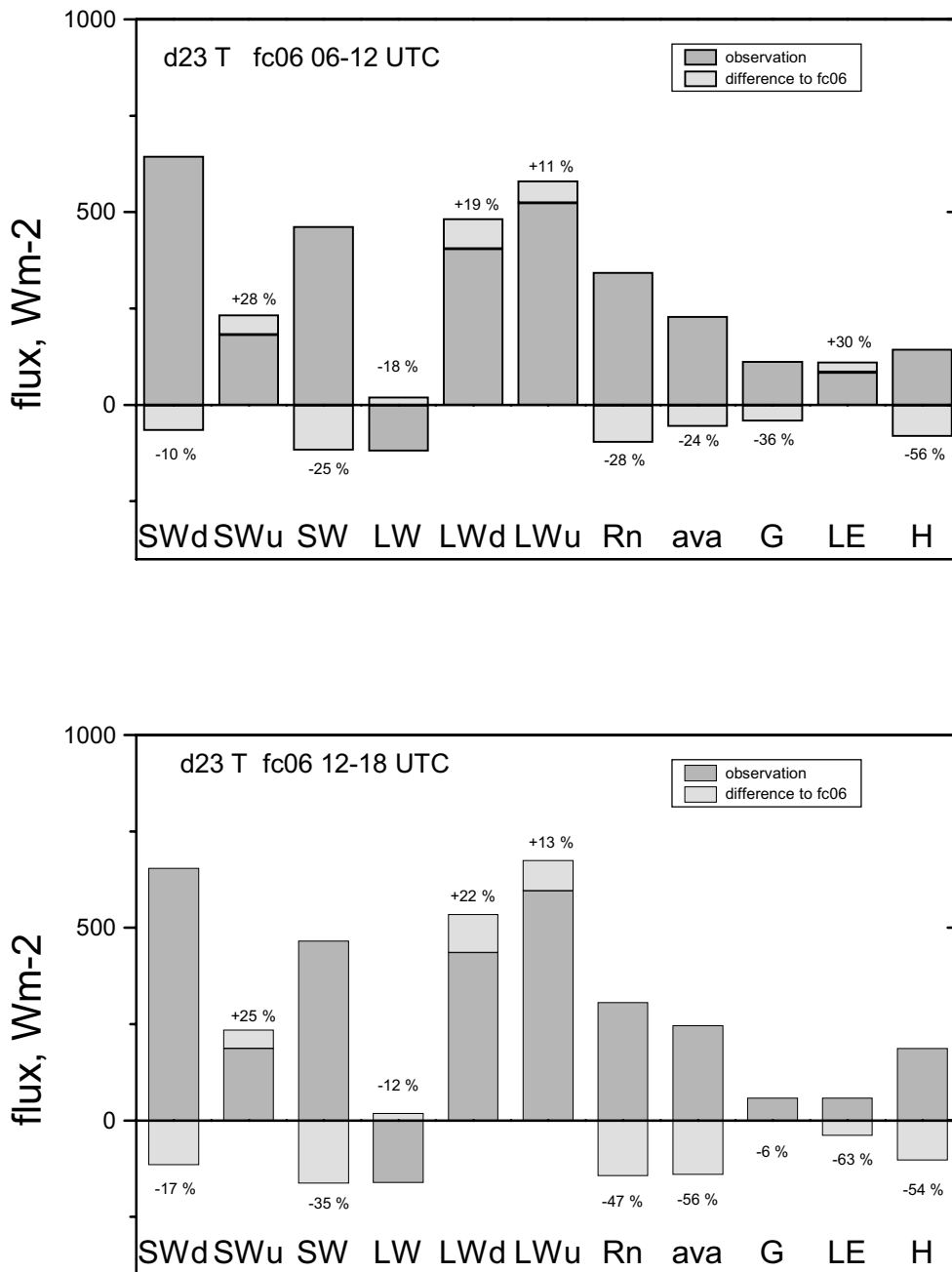


Figure 6-14. Comparison of surface radiation and energy budget components, fc06 vs. site-aggregated observations at Tomelloso. Abbreviations as in Table 6-4 and Table 6-5. Observations are mean values of 6h period, normalized with forecast interval. Model values are fluxes accumulated over 6 hour forecast period, normalized with forecast interval. Difference (grey shading) = observation (color shading) - model forecast. Percent values refer to deviation from observation of individual parameter (not of budget). Negative deviations (forecast > observation) correspond to overestimation, positive to underestimation, respectively.

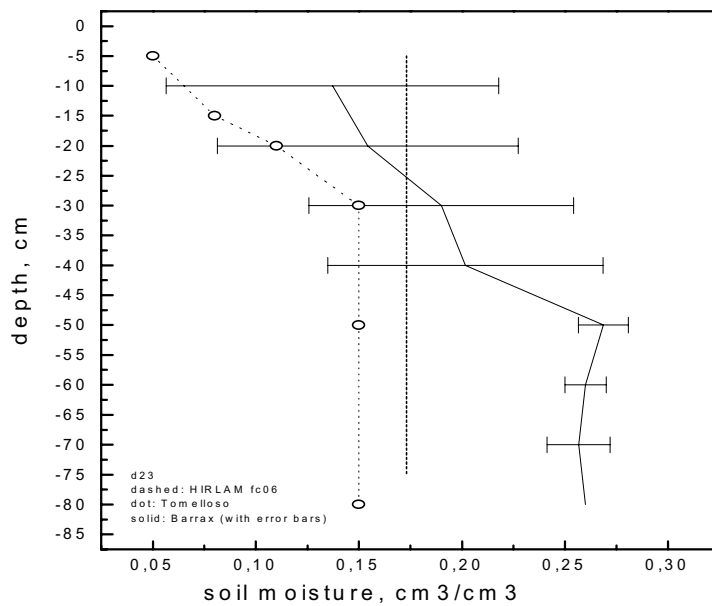


Figure 6-15. Soil moisture comparison of model (dashed vertical line) and observations at Tomelloso (dotted, o) and Barrax (solid curve, error bars give standard deviation of layer mean).

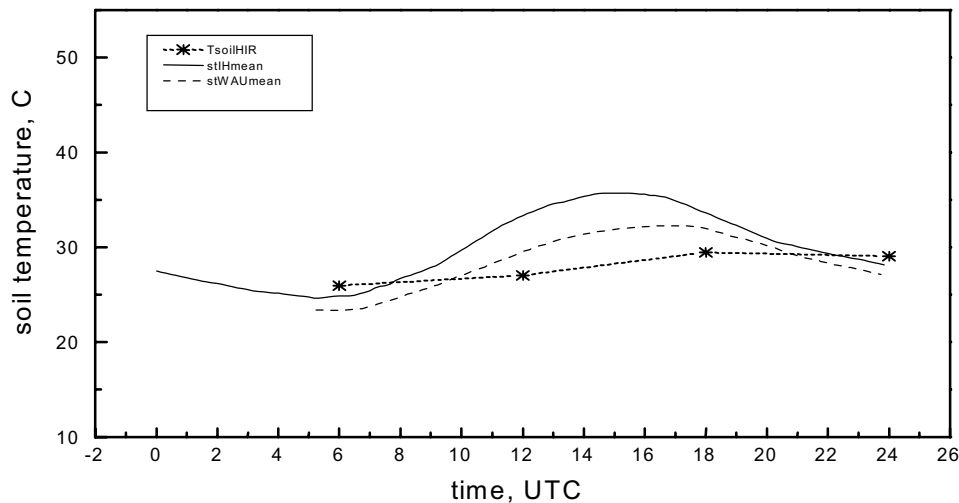


Figure 6-16. Soil temperature comparison with mean observations (averaged over all depths of observations). Solid and dotted curves represent envelope of values found across the Tomelloso site.

Based on this conclusion and knowing that the ISBA scheme has performed well in off-line validations for the same environment, we have not entered in a detailed comparison of the surface energy budget. This will be an interesting task once the model's landuse classification and physiographic database includes an adequate representation of Mediterranean ecosystems. Based on the same EFEDA dataset, we have shown in Chapter 5 that the EFEDA grid-scale aggregated fluxes depend critically on the fraction of irrigated crops in a given grid cell. Consequently, we propose a simple and efficient way to incorporate the corresponding plant phenological parameters into the physiographic database of a

given NWP model, by distinguishing two classes of irrigated crops. Spring-irrigated and summer-irrigated crops have different phenological cycles, their discrimination in multitemporal remote sensing-based landuse classification is straightforward (Martínez and Calera, 2001). The classification of Calera (2000) is a regional-scale example of the approach.

6.6 Conclusions

Observations from the European Field Experiment in a Desertification-threatened Area (EFEDA) were used to evaluate the performance of the land-surface and boundary-layer description of HIRLAM in semi-arid conditions. Analysis and 6-hour forecast data of the fully coupled 3-D model were compared with the comprehensive dataset of a case study representative for a sample of 22 days of anticyclonic conditions.

The model surface, soil, and boundary layer are found to be too moist and slightly too cool during most of the diurnal cycle. The model radiation and surface energy budgets are biased towards more humid conditions.

Summarizing the overall results of the comparison and assigning priorities (based on bias magnitudes and impacts) to the observed discrepancies, we obtain the following picture:

1. Deficiencies in the moisture assimilation procedure result in large errors (up to 50%) of the ABL humidity profiles.
2. Assignment of too dense vegetation leads to biased surface fluxes and net radiation. Yet the surface scheme works well off-line in Mediterranean crops.
3. The incoming solar radiation is overestimated, which results from the aerosol parameterization in the radiation scheme. Modification of the aerosol parameters to account for lower visibility reduces the bias significantly.
4. Assignment of a soil type with too high clay percentage may generate too much soil moisture, although the soil moisture assimilation effects would need to be assessed here as well.
5. The residual layer (RL) is not resolved properly and the entrainment contribution to surface and ML warming and drying is not reproduced adequately, due to the combined effect of vertical model resolution, which is insufficient for this type of landscape, and deficiencies in the vertical diffusion and entrainment parameterization.
6. The high bias in net longwave radiation is probably related to the excess atmospheric moisture and the underestimated surface temperature.

Immediate improvement of the model performance can be expected from the use of a landuse and soil classification (with its associated physiographic database) adapted to Mediterranean landscapes, in combination with the use of aerosol parameters in the radiation scheme, that account for the typically higher aerosol load of arid and semiarid environments.

An adequate landuse classification for Mediterranean landscapes would need to account for sparse dry canopies as well as for two classes of irrigated crops (spring-irrigated and summer-irrigated), with a physiographic database reflecting their different phenological cycles.

7 Practical applications and perspectives⁴

The results obtained in the previous chapters are useful for many purposes in the world of practical applications. Impact assessment, water management and agriculture are perhaps the most widely known. We will focus here on a very immediate and still intermediate application, which is a research topic in itself and intrinsically related with the topics of previous chapters through a number of feedback loops.

Remote sensing has on purpose not been covered in the analysis of the preceding chapters, although EFEDA, along the philosophy of LSEs, included a wealth of remote sensing studies. Not even now, we will enter in remote sensing as such, but rather deal with the data needed by remote sensing as very basic input data into any atmospheric correction procedure. The preceding chapters have created a sound basis from which to evaluate the quality and performance of available atmospheric moisture profiles for the purpose of atmospheric correction.

This brief chapter serves as an application example with the twofold objective,

1. firstly, to provide a brief assessment of the quality of atmospheric moisture profiles and/or column-integrated precipitable water content (PWC) obtained from all available data sources, and
2. secondly, to show the implications of errors in water vapor on the surface biogeophysical parameters retrieved from remote sensing.

Jochum et al. (1999) have performed a detailed assessment of water vapor datasets for atmospheric correction at three different time-space scales, by comparisons of local case studies, of local climatologies, and of horizontal variability, respectively. Here, we briefly introduce the subject, show an example of each and summarize their results. As a final outcome, we will present a list of recommendations and practical guidelines for the selection of the data source(s) most adequate for a given atmospheric correction task.

7.1 Water vapor datasets for atmospheric correction

The variability of atmospheric water vapor complicates the retrieval of biogeophysical parameters of the land-surface from space data. Methods to correct for the signal attenuation by atmospheric moisture in the calculation of surface reflectances and of derived quantities (like surface radiative temperature or vegetation indices) are often limited by the lack of adequate water vapor data. Providing reliable datasets for regional optimization of atmospheric correction is crucial in particular in arid and semi-arid environments, characterized by high space-time variability of atmospheric moisture, such as the Iberian peninsula.

Thermal infrared remote sensing offers the possibility of determining the surface energy budget on regional and global scales (Norman et al., 1995). Spectral reflectances in visible and near-infrared bands and vegetation indices derived from these reflectances provide information about the biospheric state (Myneni et al., 1995). On its way between the satellite and the earth's surface, however, the signal is attenuated by atmospheric constituents. Consequently, the retrieved biogeophysical parameters are strongly influenced by the state of the atmosphere

⁴ Material extracted from manuscript "Regionally optimized atmospheric correction of optical satellite data" (in preparation for Rem. Sens. Environ.)

(Wukelic et al., 1989; Li and Becker, 1993). For the estimation of land-surface temperature in particular the absorption due to water vapor is important (Prata et al., 1995).

The radiometric correction for atmospheric effects has been the topic of intense research for many years. Current methods of atmospheric correction fall basically in two categories. The split-window approach parameterizes the effects of the atmospheric water vapor in terms of the difference in brightness temperature of two adjacent spectral bands. The radiative transfer method explicitly calculates the transmission along the path through the atmosphere (as specified by given profiles of water vapor and other constituents) for each sensor channel. The validation and calibration of the first and the application of the second require spatially resolved vertical profiles of atmospheric water vapor, ozone, aerosol, and temperature.

A wide variety of split-window techniques has been developed as summarized by Prata et al. (1995) and Ottlé et al. (1997). Choudhury et al. (1995) and Choudhury and DiGirolamo (1995) used a database obtained from 24 globally distributed radiosondes to evaluate the relationship between the split window temperature difference (ΔT) and atmospheric precipitable water (PWC). Ottlé et al. (1997) evaluated and calibrated two algorithms (one for land and one for sea pixels) to estimate precipitable water from thermal-infrared split window channels using radiosonde data from the HAPEX-MOBILHY experiment in Southern France (André et al., 1988). The estimated errors are less than 0.5 g cm^{-2} . Li and Becker (1993) performed an error propagation analysis for the retrieval of land-surface temperature. Errors in precipitable water of, e.g., 0.38 g cm^{-2} already produce errors between -3 K and 3.5 K , depending on surface temperature.

Radiative transfer codes have so far been operated using input vertical profiles from radiosonde observations, numerical model output (e.g. Arino et al., 1997) or from a set of standard atmospheres (e.g. McClatchey et al., 1971). Recently we find increasing availability of global gridded data sets from numerical weather prediction models (NWP) and four-dimensional data analyses (4DDA) and from endeavors like the National Air and Space Administration Water Vapor Project (NVAP, Randel et al., 1996). A critical assessment of the various available datasets for the purpose of improving atmospheric correction has not been presented so far.

Water vapor data can be obtained from distinctly different types of data sources, either directly from operational radiosonde observations (unevenly distributed in space) or from global gridded datasets (produced by assimilation of observational data into a regular grid, with or without numerical modeling) or from climatologies. The major available datasets are summarized in Table 7-1, with characteristics relevant for the Iberian peninsula. The ECMWF and HIRLAM models are the most relevant global and regional NWP models for the Iberian peninsula. Similar global and regional models exist at the major operational centers. Among these spatial data, the radiosonde data have the coarsest spatial resolution (eight data points on the Iberian peninsula) and are, furthermore, irregularly spaced (see Figure 6.1 in Chapter 6). A much finer spatial resolution is achieved with NVAP and NWP model data, which are all regularly spaced (even though not all fully equidistant). Corresponding to the model (or other gridded dataset) resolution of 2° , 1.2° , 0.5° or 0.2° , we are dealing with a total of 28, 112, 448 or 2800 data points on the Iberian peninsula.

The NASA Water Vapor Project (NVAP, Randel et al., 1996) is a global gridded dataset derived from a combination of independent observational data with simple two-dimensional assimilation schemes. The data sources are the Television

and Infrared Operational Satellite (TIROS) Operational Vertical Sounder (TOVS, Wittmeyer and Vonder Haar, 1994), the Special Sensor Microwave Imager (SSM/I, Greenwald et al., 1994), and operational radiosonde observations (Ross and Elliott, 1997). The input data are subject to quality control and consistency checks and then are interpolated onto a regular horizontal grid. The basic dataset includes daily total column water vapor and values for three atmospheric layers at a spatial resolution of $1^\circ \times 1^\circ$ for eight years. Gridded water vapor datasets at 2° resolution were also produced from TOVS data alone (Wittmeyer and Vonder Haar, 1994).

Table 7-1. Water vapor data sources. ISCCP: International Cloud Climatology Project, PWC = precipitable water content; LW(3) = layered water content (3 layers). For the Iberian peninsula 1° latitude (longitude) corresponds to roughly 123 km (96 km).

Data source	Horizontal resolution	Data points*)	Time period	Relevant products
Operational radiosonde	300-700 km *)	8	continuous	vertical profiles of specific humidity at 00 and 12 UTC
NVAP	1°	112	1988-1995	daily PWC, LW(3)
ISCCP TOVS	2°	18	1978-present	daily PWC
ECMWF reanalysis (ERA15 and ERA40)	$\sim 1.12^\circ$ lat 1.125° lon	112	1979-1993 and 1957-2001	vertical profiles of humidity; PWC at 00, 06, 12, 18 UTC
ECMWF operational analyses/forecast	2.5°	28	continuous, ≥ 1996 same model as ERA	see ERA
HIRLAM	0.5° 0.2°	448 2800	continuous	see ERA
Climatological reference atmosphere	6 zones globally	1	not applicable	vertical profiles

*) on and around Iberian peninsula

7.2 Assessment of water vapor datasets

The basic reference standard for the case study comparison comes from the EFEDA dataset. As discussed in Chapter 2, the uncertainty of the specific humidity profiles is on the order of 0.7 g kg^{-1} . Operational radiosoundings were used to generalize the comparison beyond EFEDA time and space scales. The associated errors were evaluated on many occasions (e.g., Pratt, 1985). Here they are estimated to be 2-3% relative humidity. The precipitable water content W was calculated from the individual vertical profiles as

$$W = \frac{1}{g} \int_0^{p_s} q dp \quad (7.1)$$

where g is the gravity acceleration, q specific humidity, p pressure, and p_s surface pressure.

The NWP model data needed adjustment of the height above mean sea level. The model topography is defined such as to produce the correct form drag in the model atmosphere (Lott and Miller, 1997). In none of our comparison locations this coincides with the actual elevation of the station.

The basis for the case study assessment is the comparison of NWP model results with EFEDA data (see Chapter 6 for HIRLAM). There we have found deficiencies in the moisture assimilation leading to sometimes large errors in atmospheric humidity. Figure 7-1 gives an example of the differences in PWC resulting from these findings. The agreement between radiosoundings and ERA analyses at the Madrid gridpoint (where the analysis scheme actually uses the operational radiosonde) is good only in the morning and fair in the late afternoon. The midnight analysis overestimates the observed value by 10%, whereas the noon analysis underestimates it by 20%. The Tomelloso radiosonde agrees rather closely with the operational one at Madrid (which is in the same climate regime, at about the same elevation and 200 km from Tomelloso). For the morning hours there are no operational sounding data available to compare with. The ERA15 analysis at the Tomelloso gridpoint, however, is rather poor, giving much too high values of PWC. This is due to the excess moisture in the model ABL as shown in Chapter 6.

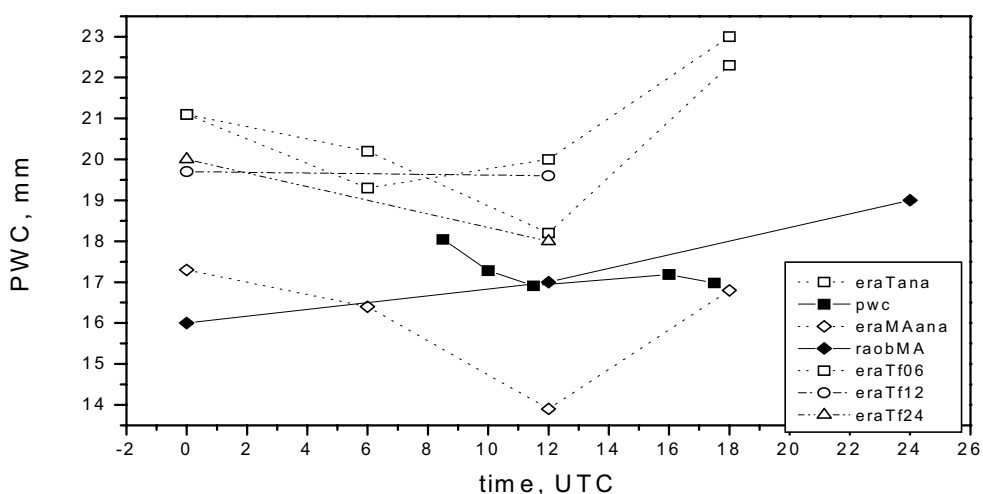


Figure 7-1. Precipitable water content (PWC) on 23 June 1991 at Madrid (solid diamonds from radiosonde, open diamonds from ERA analysis) and Tomelloso (solid squares from radiosonde, open black squares from ERA analysis; open squares, circles, and triangles from ERA 6-, 12-, and 24-hour forecast).

Extending the local 1-D comparison in time, we use the five-year climatology derived from operational radiosonde data (del Pino, 1997) to assess the local performance of the reanalysis and NVAP data on a longer time scale. Since the operational upper-air soundings form part of the input data for both NWP and NVAP, this is obviously not a fully independent evaluation. It is the purpose of this comparison, however, to investigate the effects of the different assimilation procedures (as used in ERA/HIRLAM and NVAP) on a local level and on climatological times scales. As we have seen already in the previous section, significant errors in water vapor are introduced through the NWP assimilation procedure.

Using the five-year climatology of PWC derived from operational radiosonde data (del Pino, 1997) as a reference, we have derived a similar five-year climatology from NVAP and ERA data, using the nearest gridpoint for each of the three locations. From a climate regime point of view, the selection of the gridpoint is not too critical, because the three sites are located well within each of the climate regimes they represent. Table 7-2 summarizes the results obtained from the three

different data sources for all three stations. It compares the overall five-year mean values and standard deviations. The NVAP-derived climatologies agree very well with the radiosonde-based ones. This indicates that the data assimilation procedure followed by NVAP to produce gridded datasets does not introduce additional artificial errors in areas with nearby radiosonde station. The situation is different, however, in the case of the ERA data. There, we find less good agreement, especially for the near-shore locations Murcia and La Coruña (see Figure 6.1 in Chapter 6 for location). In view of the results of the EFEDA evaluation this is not surprising. Looking at some of the individual vertical profiles, we find the same situation here, with boundary layer moisture much too high and the upper air slightly too dry, which results in an overall overprediction of PWC. The moisture assimilation procedure, performed in entire boxes (Gibson et al., 1997) is apparently not able to generate realistic moisture fields in this case. The radiosonde network is concentrated along the coasts. For the interior of the peninsula, the station density and spacing is not sufficient in view of complicating factors like topography and land-sea interfaces.

Table 7-2. Summary of five-year climatology of precipitable water (in mm) at three typical locations as obtained from three different data sources. raob = radiosonde observations; sigma = standard deviation; rel.dev = relative deviation (difference divided by the raob value).

Station	Mean raob	Mean ERA	Mean NVAP	Sigma raob	Sigma ERA	Sigma NVAP	Rel.dev ERA-raob	Rel.dev NVAP-raob
La Coruña	18.0	22.4	17.7	8/7.3	6.8	8.4	24 %	2 %
Madrid	12.4	18.1	13.2	5.5/5.5	5.1	5.6	46 %	7 %
Murcia	16.8	22.1	17.0	8.4/ 8.5	8.0	8.3	32 %	1 %

The PWC varies in the range of 5-30 mm across the Iberian peninsula. The largest variations occur in summer, the lowest in winter. The horizontal distribution of PWC is closely correlated with the topography. The spatial resolution and patterns were investigated using data from four sources, the operational radiosonde network, ERA, NVAP, and HIRLAM. Several methods for spatial interpolation of the radiosonde data were investigated by del Pino (1996). The derived variability depends quite a bit on the kind of statistical technique used in the interpolation. The effect of topography becomes critical. In general, cubic polynomial regression seems to be the most adequate interpolation method for this kind of data set. These two-dimensional fields (maps) of PWC are then compared with the PWC maps as extracted from HIRLAM, ERA, and NVAP data for the same day (Figure 7-2). The most striking feature at first glance is the much higher degree of spatial variability in the NVAP data as compared to ERA which is not explained by the very small difference in grid resolution (1.2-1.25° in ERA, 1° in NVAP). This is related to the effect of topography in connection with the two different ways of assimilating humidity. In ERA, the vertical humidity profiles are assimilated into a grid where topography is defined as the mean grid element elevation. This automatically smoothes the fields. The PWC is then calculated from the model output vertical profiles. In NVAP, all input observations are firstly converted into PWC values, which then are assembled into the corresponding grid element using a priority criterion for the weighting of data from different sources (radiosonde, TOVS or SSM/I). This dataset-inherent difference may be small in

flat areas. But it can be significant in orographically structured regions, where the PWC is largely influenced by the topography.

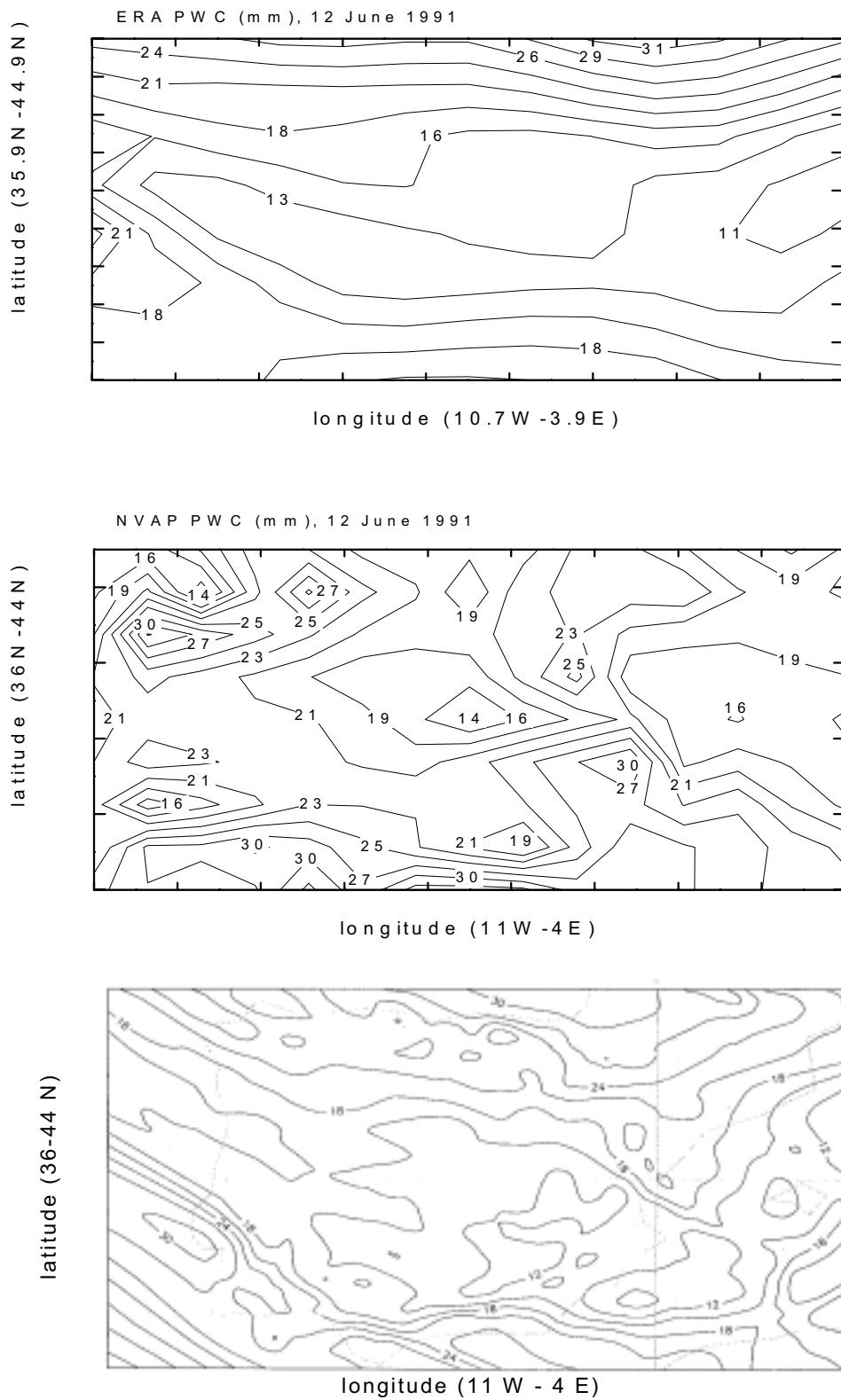


Figure 7-2. Maps of PWC from ERA (top), NVAP (middle), and HIRLAM 0.2° (bottom) on 12 June 1991.

Comparing in more detail the structure and values of the PWC maps (Figure 7-2), we notice a weak resemblance of the overall pattern, with its main orientation axis WNW-ESE direction and the minimum values in the center of the peninsula. The range of absolute values is slightly larger in the NVAP data (13-30 mm as compared to 11-24 in the ERA data). Differences in the spatial structure, however, imply that in special locations the values differ by as much as a factor of 2. Comparing both ERA and NVAP generated PWC fields with those derived from radiosonde observations only, we notice that the minima in the center of the Iberian peninsula are somewhat higher (17 mm). More importantly, they extend much farther to the north-northwest (where, e.g., the observations at Santander give only 15.5 mm). Being aware of the crucial impact of the interpolation method (which obviously also applies to that of the graphics software), we have compared directly (grid-) point values at the radiosonde stations, but show the maps here for brevity.

The performance of the HIRLAM and ERA datasets is determined by the deficiencies in the moisture assimilation procedure, as discussed above. Due to the 4D nature of the NWP assimilation process (as opposite to 2D in NVAP) and to the use of a special grid-mean topography, the moisture fields are smoothed before the PWC is calculated. In consequence, some of the variability gets lost. Sensitivity tests indicate that in mountainous terrain, the adequate incorporation of high-resolution topography can be more important than high-resolution moisture fields in determining maps of PWC.

The NVAP dataset is better capable of reproducing the horizontal variability of PWC across the peninsula. However, the performance of the NVAP dataset obviously depends critically on the kind of source data (radiosonde, TOVS, or SSM/I) available for any particular grid element and day and on the individual performance of these source data in the region of interest. There are eight radiosonde stations (the data source of highest quality) on the Iberian peninsula, of which not all deliver data every day. The remaining NVAP grid elements are then filled with a combination of TOVS (over land) and SSM/I (over sea) data. Now, the TOVS data seem to generally overestimate PWC over the Iberian peninsula. Another problem is related to the near-coast locations, where SSM/I retrieval errors are introduced. A closer inspection of the SSM/I data as used within NVAP (and provided with the NVAP dataset) reveals that PWC is highly overestimated near and over the sea area around the Iberian peninsula.

7.3 Impact of water vapor data errors on retrieved biogeophysical variables

The information needed to perform the atmospheric correction of optical images includes the concentration of the main absorbing gases (water vapor and ozone) and the type, composition and concentration of aerosol particles responsible for scattering. Of the two gases, water vapor is highly variable in space and time. Therefore, rather detailed information is needed and the availability and selection of data is a major issue. Ozone is much less variable. The effects of aerosol scattering are not dealt with here. Due to the lack of global datasets the way to proceed is rather different (see, e.g., Liang et al., 1997).

It is important to note that the use of vertically resolved water vapor profiles improves the accuracy of the correction as compared to the column-integrated value (PWC). This is due to the interaction between aerosol and water vapor and the subsequent coupling of absorption and scattering effects. A more accurate

correction is furthermore achieved through the use of actual pressure and temperature profiles in the determination of the absorption coefficients.

In order to see if the magnitude of errors found in the candidate input datasets is of relevance to the results of atmospheric correction algorithms, Jochum et al. (1999) have estimated those effects for typical situations. For this purpose, a series of simulations was performed using the radiative transfer codes 5S and 6S (Tanré et al., 1990; Vermote et al., 1997) with vertical profiles from the different data sources. Further input data were the US62 standard ozone profile (Tanré et al., 1990) and a visibility range of 15-25 km.

Taking channel AVHRR 2 as an example of the near infrared channel typically used to calculate vegetation indices, atmospheric transmittance (one way) changes by 3-4% (from 0.88 to 0.85, for typical conditions) when the column atmospheric water vapor increases from 10 to 20 mm. The effect is small because the spectral filter of the channels used is already designed to avoid water vapor effects, but even in this case changes due to spatial variability must be taken into account in the atmospheric correction of the data. For example, for a surface with a reflectance of 0.3, the error can be about 6% in the retrieved surface reflectance (del Pino, 1997). The incoming solar radiation can be underestimated by as much as 10% when taking a profile with PWC value of 20 mm instead of 10mm.

In the thermal range, under vertical viewing conditions, an increase in PWC from 10 to 20 mm produces a reduction in atmospheric transmittance of 12-14% (e.g. from 0.89 to 0.78) for channel AVHRR 4, and of 21-27% (e.g. from 0.84 to 0.66) for channel AVHRR 5. These changes are rather significant since they can introduce errors of several Kelvin in the retrieved surface temperature, depending on the air temperature and on the surface emissivity (see e.g. Li and Becker, 1993). The effect is increased for observations far from nadir, due to the longer atmospheric path between the surface and the sensor. Figure 7-3 (from Jochum et al., 1999) shows an example for the Landsat TM channels in more detail. We see that in some channels the apparent reflectance due to the effect of atmospheric water vapor is more than 10% below the actual ground reflectance.

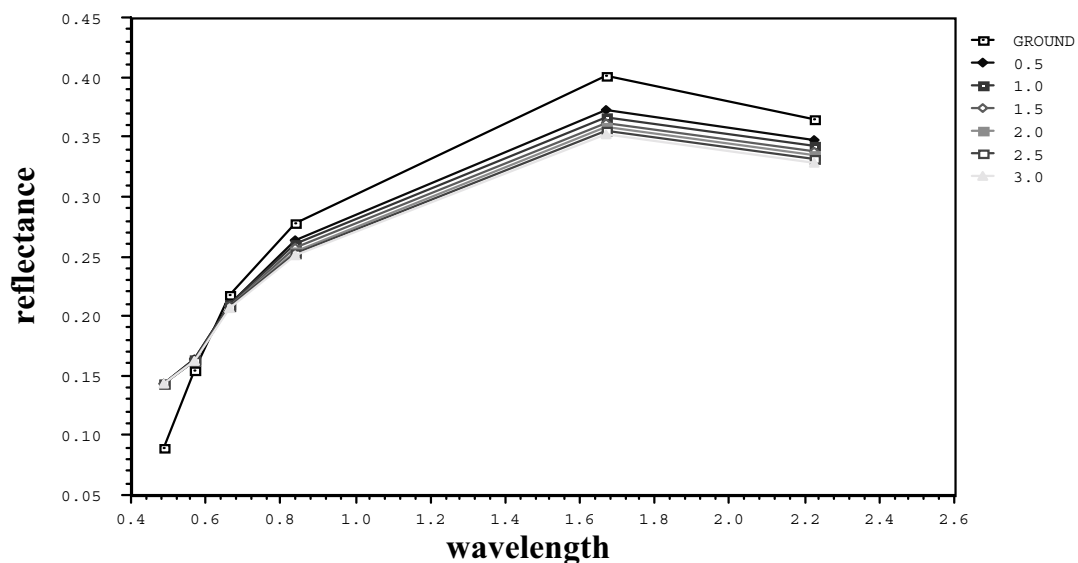


Figure 7-3. Effect of atmospheric water vapor changes over the apparent reflectance at the top of the atmosphere, within the spectral channels of the Landsat TM sensor, as compared to the actual ground reflectance (labeled as "ground"), for a typical soil surface, and for a fixed visibility. Numbers in the legend correspond to different water vapor values (in cm). From Jochum et al. (1999).

It is important here to distinguish the need for absolute or relative accuracy of geo-biophysical parameters. If only information about the variability of a specific parameter across an image area is needed, then the water vapor accuracy is not critical, provided that the retrieval relationship is (almost) linear. Then, the error in the retrieved final parameter will be about the same everywhere in the image. An exception to this would be the vicinity of mountains, which can cause steep moisture gradients. In the case of non-linear retrieval relationships and whenever absolute values of retrieved parameters are needed, the water vapor accuracy is indeed critical.

7.4 Guidelines for finding the regional best choice water vapor data

The following conclusions and recommendations apply to the Iberian peninsula primarily, since the evaluation was performed for this region. The errors in water vapor datasets we have identified are related to complex topography and coastal zones, which are ubiquitous in the Mediterranean basin. Thus we assume that our conclusions are valid for other Mediterranean regions as well.

1. The highest accuracy is obviously achieved by launching extra radiosondes at the time(s) and in the area of interest. This is, of course, not generally feasible, but it is highly recommended for any special intensive field experiment.
2. For a more operational use, the best choice is still the operational radiosonde observation closest in time and space, provided that the image area lies within the same regional climate zone as the radiosonde station and provided that the synoptic situation is not too far from undisturbed. The latter condition in general coincides with the requirement for optical and thermal image data to be almost cloudfree. The former condition can be easily verified from a climate classification atlas (for the Iberian peninsula, e.g., Almarza and Balairón, 1992).
3. The NOAA noon overflight time is close to the operational noon radiosonde, so the AVHRR images can safely be corrected with these data. The Landsat overpass time, however, falls into a period of intense boundary layer growth. So the noon radiosonde data cannot be considered representative. A simple slab model of the atmospheric boundary layer development (like the one used in Chapters 3 and 5) can be used in conjunction with the midnight and noon operational radiosoundings.
4. Global 4DDA data are produced operationally by the ECMWF at 2.5° spatial resolution. A self-consistent set of 4DDA data at 1.2° resolution (using the same model for 15 or 40 years) is available from the ECMWF Reanalysis Project (ERA15 and ERA40). Both data have been increasingly used as input for radiometric correction (e.g. Arino et al., 1997). The errors in the vertical moisture profiles, however, can be significant in semiarid mountainous areas like the Iberian peninsula and the land-part of the entire Mediterranean basin. Depending on the time of day and the location (near-coast or inland), the model atmosphere can be too dry or much too moist, with absolute error magnitudes up to 100% (ERA15).
5. A better choice is the analysis data from a limited area model (LAM), such as HIRLAM. These provide vertical profiles of water vapor, temperature and pressure at regular 3- or 6-hour intervals. The operational HIRLAM version run at ECMWF has a resolution of 0.5°, while the National Weather Services use

higher resolution versions (e.g., 0.2°) adapted to their territory. We have used the HIRLAM 0.2° version currently in operational use at the Spanish Weather Service INM to evaluate the quality and advantages. Due to the higher spatial resolution, the effects of topography are reproduced better. Assimilation-generated errors in water vapor profiles can still be up to 50% in the lower troposphere.

6. Whenever the column-integrated precipitable water content (PWC) only or a 3-layer PWC is considered sufficient in a simplified radiometric correction scheme, the NVAP data (available on global 1° grid for 1988-1995) may be a good alternative. They are also affected by errors, but in general less than NWP analysis data. The errors over land are mainly introduced by the TOVS data subset used in deriving the final PWC product. As such, the NVAP data also represent an improvement over the use of TOVS data only. Caution is indicated, however, in using the NVAP data in coastal zones and over the sea area of the Mediterranean, due to the very large errors (up to 200%) introduced by the SSM/I data. A simple way of controlling the data quality is to inspect the files on data sources (which are available with the main data) for missing radiosonde values, which were substituted with TOVS.
7. In view of the significant errors inherent in presently available global gridded datasets, the use of monthly or seasonal mean vertical profiles from a regional climatology may offer a viable alternative. For the Iberian peninsula, e.g., the variability is largest in April and September, with absolute magnitudes up to 50%. So the achievable accuracy is comparable to that of ERA/ECMWF analysis data. For very large datasets the computational simplicity of this approach may also be appealing.

7.5 Conclusions and perspectives

We have assessed the performance of water vapor datasets from different sources for the purpose of their use in atmospheric correction schemes. The data sources include operational radiosondes and gridded datasets from NWP models (ECMWF/ERA, HIRLAM) and NVAP. Our regional focus is the Iberian peninsula and similar Mediterranean environments. There, we have identified serious deficiencies in the NWP output water vapor profiles. We give a set of recommendations how to find the best regional choice water vapor data for a given atmospheric correction task. Jochum et al. (1999) give further recommendations for the treatment of aerosol effects and the selection of ozone input data. In topographically structured terrain (like most of the land area surrounding the Mediterranean) the second step of downscaling these input data from their respective grid-area to the pixel resolution of the actual image is at least of equal importance for the accuracy of the derived products. Due to the correlation of PWC with topography, higher resolution correction is needed in and near mountainous areas than in extended flat land.

These errors propagate into the derived biogeophysical parameters and need to be taken into account when interpreting the resulting maps of remote-sensing-derived parameters (like NDVI, surface temperature, surface fluxes). Obviously, at present there is hardly any other choice for the operational radiometric correction of large image datasets and/or long-term time series of large images. It is important, however, to be aware of the magnitude of errors induced in the retrieved parameters, which can be, e.g., up to 15% in incoming solar radiation and up to 20% in surface temperature. Propagating these errors further into the application of irrigation scheduling (Jochum and Calera, 2002), we may obtain errors in daily or weekly crop water requirements of up to 20%.

8 Summary and outlook

Land covers a total of 35% of the Earth's surface. Processes at the land-surface represent one of the most important weather and climate forcings. They are equally important for the sustainable management of natural resources.

The issue of land-surface heterogeneity and its impact on ABL processes has received considerable attention for decades. Internationally coordinated research efforts in this area have focused for many years on land-surface experiments (LSEs, Feddes et al., 1998; Jochum et al., 2000) involving considerable resources in terms of ground-, aircraft-, and satellite-based observation systems. The driving forces were the global weather and climate modeling community on one hand (seeking improved and calibrated land-surface parameterizations) and the remote-sensing community on the other (seeking calibration of satellite observing systems and algorithms to derive land-surface-related parameters).

The general context of this thesis is given by one of the major LSEs, the European Field Experiment in a Desertification-threatened Area (EFEDA), which was conducted in 1991 and 1994 in a semiarid landscape in Spain (Bolle et al., 1993). It fills an important gap in the general LSE picture by addressing a unique area of typically Mediterranean heterogeneous land-use and of added complexity due to the simultaneous presence of mountains and the non-local influence of Mediterranean sea-breezes frequently penetrating inland.

The EFEDA area is located on the Castilian high plateau in the Southeast of Spain at an average elevation of 700 m above mean sea level. It is a semiarid area of heterogeneous landuse, surrounded by mountains, where regionally different boundary layers and inhomogeneous moisture fields were observed.

The objectives of this work are defined from a grid-scale perspective of EFEDA. As such, it aims at providing an analysis of the relevant processes and scales and their implications on flux parameterization and aggregation, based on a comprehensive observational dataset. In a second step, it aims at using these results to assess the performance of NPW models and its implications on atmospheric correction procedures in the retrieval of bio-geophysical parameters from optical satellite data. The inherent goal is to go all the way from basic process studies to final practical applications.

Chapter 2 describes the observations. The EFEDA dataset used in this work includes observations from surface flux stations, aircraft, and radiosondes taken by more than 30 research groups. Some kind of homogenization was applied whenever necessary. Based on the surface observations at the supersites, Linder et al. (1996) have developed standardized surface datasets for each of the four major vegetation classes, which are used here to derive various area-aggregates. Aircraft observations provide access to the spatial variability and to regional scales. The DLR Falcon airborne dataset is mainly used here. These data are prepared for subsequent analysis by means of an extended quality control and flux calculation methodology. Turbulent flux errors from four different sources are assessed individually for each flight track ("leg"), in order to assure that flux sampling is adequate ("legs long enough") and to properly identify non-stationarity of time series. High-resolution radiosondes were launched regularly at the Tomelloso and Barrax supersites. The original sounding datasets (Bessemoulin, personal communication; Kalthoff, personal communication) were used here after homogenization to equidistant pressure intervals. A downward-looking near-infrared Differential Absorption Lidar (DIAL) flown onboard the DLR

Falcon gives the aerosol backscatter and water vapor fields within and above the ABL.

Based on the synoptic situation during the experimental period of 1-30 June 1991, the data are stratified into two broad categories of "anticyclonic" and "unstationary" conditions. The "anticyclonic" composite (of 22 cases) is shown to be well represented by the individual day 23 June, which is selected as the prime focus for subsequent case studies.

In **Chapter 3**, we investigate the physical processes that contribute to heat and moisture transport in the EFEDA area by means of an atmospheric boundary layer (ABL) budget study. Mixed layers of different characteristics were observed at rather short geographical distance (80 km) between the two main supersites. Moisture plays the key role here. The Tomelloso site is an extensive wine-growing area representative of semiarid conditions, with a surface energy balance dominated by the sensible heat flux. The Barrax site is characterized by additional moisture supply from two sources, one at the ground from irrigation and one aloft from the Mediterranean sea breeze often penetrating inland in the afternoon. The resulting ABL at Barrax is generally moister, slightly cooler and less deep than at Tomelloso.

Our budget analysis is based on the synergistic combination of a comprehensive observational dataset and a simple coupled canopy-ML model. The observational dataset consists of distributed micrometeorological surface stations, radiosondes, flux aircraft, and an airborne water-vapor differential absorption lidar (DIAL). In particular the unique aircraft dataset includes the four radiation flux components, from which the full radiative divergence can be derived. By providing a large sample of heat and moisture flux observations throughout the ML depth, it supports the analysis of the vertical flux divergences in a ML slab framework.

Airborne DIAL- and radiosonde-derived humidity crosssections and profiles show that the residual layer (RL) above both sites is characterized by a layered moisture structure. The resulting entrainment moisture fluxes vary in magnitude and sign over a large part of the diurnal cycle. The determination of the vertical moisture flux divergence becomes a challenging task under these circumstances.

The ML warming is balanced by a combination of the heat flux divergence and the radiative divergence. While the absolute values of the latter vary only slightly with time and between sites, their relative importance is greater at Barrax and in the afternoon. The magnitudes are consistent with the high aerosol load and low visibility observed in the area most of the time. Temperature advection is found to be small and the heat budgets are fairly closed using aircraft-derived entrainment closure parameters of 0.3 (Tomelloso) and 0.16 (Barrax), respectively.

The evolution of the moisture budgets over the observed period is more complex. It is related to the inhomogeneous moisture structure of the RL, with gradients of changing sign. The ML is drying at both sites, as long as it erodes the dry NBL. As soon as it comes in contact with the positive humidity gradients in the RL, the entrainment flux becomes negative until the moister air has been fully entrained. This midday moistening event lasts only a short time (1-2 hours) before the ML starts drying out again from above. This sequence was clearly identified in the series of four moisture budgets at Barrax. At Tomelloso, it was probably missed by the data, but it is evident in the ML slab model calculation. Thus, the moisture budgets show clearly the influence on non-ABL scales on the moisture transport, which is also reflected in the lack of simple entrainment closure parameterization for moisture flux. A simple model relating the surface and inversion level Bowen ratios is used to derive the moisture flux divergence. With inversion level Bowen

ratios generated by advection (like in the case of the inhomogeneous RLs), the entrainment moisture fluxes are related not only with ABL processes and scales. Accurate high-resolution vertical humidity profiles are needed to properly estimate these fluxes. The coupled canopy-ML slab model proves to be a valuable tool in this complex environment, if it is regularly provided with updated RL gradients.

This non-local characteristic of moisture transport is found at both sites. However, the ML drying or moistening may evolve differently at either site, because it depends on the relative importance of surface vs. entrainment flux. A simple model confirms that the potential for moisture flux divergence and associated ML moistening is higher at Barrax, where irrigation enhances the surface evaporation.

Chapter 4 determines the scales of the landscape and of the ABL and explores the implications on flux parameterization. The scales are reviewed in the framework of Mahrt (1996). We have identified a number of surface heterogeneity features, which condition the scale dependence of flux parameterization in EFEDA-like areas. Momentum transfer becomes scale dependent in the presence of sub-grid velocity variations due to mesoscale motions. Heat transfer is not scale-dependent here, due to the large temperature difference at the air-land interface throughout the area. The moisture transfer scales are linked to the saturation deficit, which is very inhomogeneous across the area, in particular where dry sparse vegetation is adjacent to irrigated fields.

Chapter 5 is dedicated to flux aggregation and regional fluxes. The objective is to obtain area-averaged fluxes for a range of areas including the whole EFEDA area and four relevant HIRLAM grid-cells. Several approaches are discussed on the grounds of the available data. Surface observations provide continuous time series of observational grid-scale fluxes through weighted averaging. A comparison exercise was performed to determine how representative a weighted tower average is and if any adjustments are necessary (for strata, processes, and/or scales not covered). Airborne flux observations provide an area-wide view at single points in time on single days. They offer independent reference values for comparison, often around local noon and on fair-weather days. Radiosondes offer another alternative of areal perspective. In conjunction with a simple ML model framework, they can provide semi-observational continuous regional fluxes during daytime. Mesoscale model data complete the comparison data, once the model has been validated (e.g., Noilhan et al., 1997).

The results of the different methods agree within the range of uncertainty. On some days, the airborne estimate of sensible heat flux is low, which could indicate that either the low-level flux divergence was underestimated or that the ML depth was overestimated. The PERIDOT mesoscale model latent heat fluxes are consistently high, which we suppose is due to a wet bias in its land-use database. The highly sensitivity of the area-aggregated fluxes to the fraction of irrigated land highlights the need of its correct identification (in the land-use classification and in the delineation of the area). Occasionally, large mesoscale moisture flux contributions were observed by the aircraft, which would be consistent with the inhomogeneous moisture fields observed by airborne lidar. We speculate that topography-induced mesoscale circulations are the mechanisms that generate these inhomogeneous structures from the moisture introduced by irrigation and the sea breeze. Mesoscale model calculations (e.g., Miao et al., 2002) confirm the influence of topography.

The grid-scale flux comparison confirms that indeed the consolidated dataset of grid-scale fluxes in EFEDA can be computed on the basis of weighted averages of

the surface observations. Adjustments due to the limited range of "view" of the surface observations, like in the case of other field experiments are not necessary here. However, adjustments will need to be made for the timing in the crop growth and irrigation cycle and (to a lesser extent) for relative cloud cover.

The area-aggregated fluxes (in particular of moisture) depend strongly on the location of the area boundaries, whenever a significant fraction of irrigated land is present. Even though not surprising by itself, this demonstrates clearly the importance to adequately account for tiles of irrigated land in surface schemes and the corresponding physiographic databases of large scale models. A prerequisite is the capability of the land-use classification to properly identify irrigated fields and their water status in different seasons. The simplest way to accommodate a minimum information on plant water status would be via the distinction of two classes of irrigated crops, one of spring and one of summer growth cycles. The classification approach of Martínez and Calera (2001) offers a viable solution for that purpose.

In **Chapter 6** we evaluate the performance of the HIRLAM surface and ABL description in the EFEDA environment. The HIRLAM (High-Resolution Limited Area Model) system is a complete numerical weather prediction (NWP) system including the analysis of observations and a short-range forecasting model. Analysis and 6-hour forecast data of the fully coupled 3-D model were compared with the EFEDA case study of 23 June 1991, representative for a sample of 22 days of anticyclonic conditions.

The model surface, soil, and boundary layer are found to be too moist and slightly too cool during most of the diurnal cycle. The model radiation and surface energy budgets are biased towards more humid conditions. Summarizing the overall results of the comparison and assigning priorities (based on bias magnitudes and impacts) to the observed discrepancies, we obtain the following picture:

Moisture assimilation is problematic for the Iberian peninsula as in any complex topography and near-coastal areas. This results in large errors (up to 50%) of the ABL humidity profiles. The model physiographic database assigns too dense vegetation, which leads to biased surface fluxes and net radiation. With adequate landuse class and data assignment, the surface scheme performs well. The incoming solar radiation is overestimated, which results from the aerosol parameterization in the radiation scheme. Modification of the aerosol parameters to account for lower visibility reduces the bias significantly. A model soil type with too high clay percentage may generate too much soil moisture, which possibly cannot be compensated in the soil moisture assimilation procedure. The residual layer (RL) is not resolved properly and the entrainment contribution to surface and ML warming and drying is not reproduced adequately, due to the combined effect of vertical model resolution, which is insufficient for this type of landscape, and deficiencies in the vertical diffusion and entrainment parameterization. The high bias in net longwave radiation is probably related to the excess atmospheric moisture and the underestimated surface temperature.

Immediate improvement of the model performance can be expected from the use of a landuse and soil classification (with its associated physiographic database) adapted to Mediterranean landscapes, in combination with the use of aerosol parameters in the radiation scheme, that account for the typically higher aerosol load of arid and semiarid environments. An adequate landuse classification for Mediterranean landscapes would need to account for sparse dry canopies as well as for two classes of irrigated crops (spring-irrigated and summer-irrigated), with a physiographic database reflecting their different phenological cycles. The approach of Martínez and Calera (2001) offers a practical solution, as indicated above.

Chapter 7 introduces a practical application of the results obtained in the preceding chapters. The retrieval of biogeophysical parameters at the land surface from remote sensing satellite data requires correction for the signal attenuation by atmospheric constituents, in particular water vapor. Consequently, high-quality water vapor fields are needed as input data into the respective radiometric correction schemes (like MODTRAN or 6S). The performance of water vapor data from the major available data sources is assessed here along with the implications of errors on the retrieved bio-geophysical parameters. The errors introduced by the moisture assimilation procedure of NWP models may result in significant errors in, e.g., global radiation (10%) and surface temperature (20%). Therefore, it is recommended to recur to operational radiosonde data whenever possible and to use 4DDA data from NWP models with care.

Propagating these errors further into the application of irrigation scheduling, we may obtain potential errors in daily or weekly crop water requirements of up to 20%.

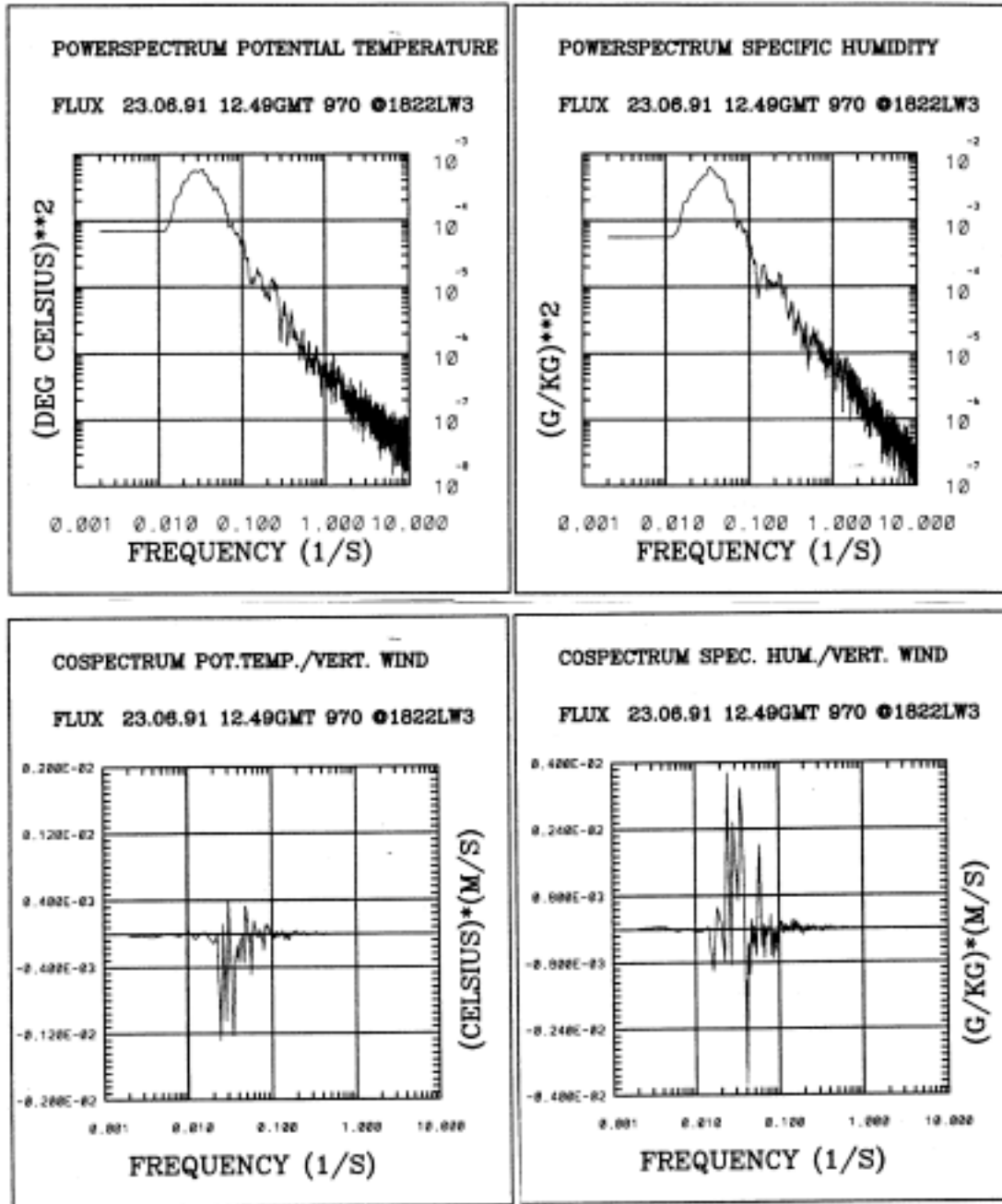
The challenge for the coming decade is in providing high-quality operational 4D global datasets of land-surface and ABL parameters, along with simple tools and models for using them. These datasets are called for by the major international global change programs (IGBP, WCPR, IHDP) and global observing systems (e.g., G3OS, GMES). The only way to achieve this relies heavily on NWP models and remote sensing, which are becoming coupled in increasing ways. In conjunction with these datasets, simple tools like the ML model used in Chapters 3 and 5 maintain their importance. Confidence in the performance of these tools in all major ecosystems and climates is thus required. The land-surface experiments have brought significant improvement for these tools. This work has given several additional clues for the Mediterranean environment, which are now being followed up in operational ways.

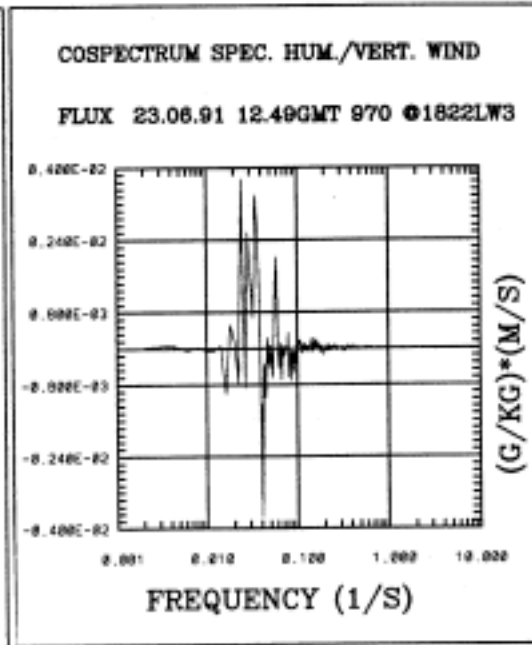
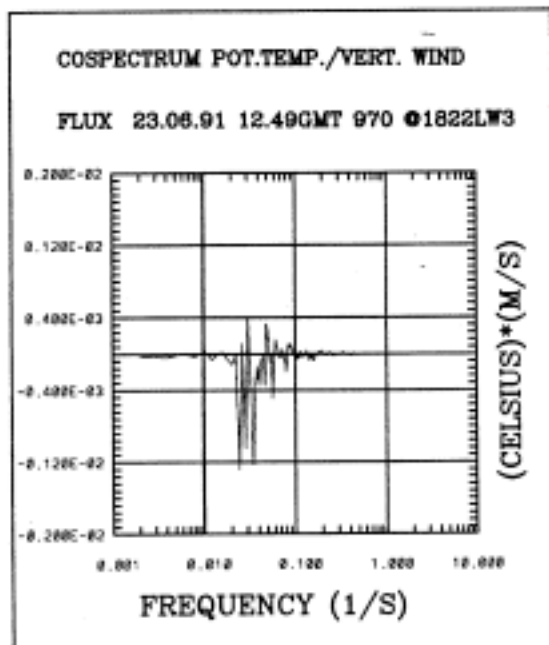
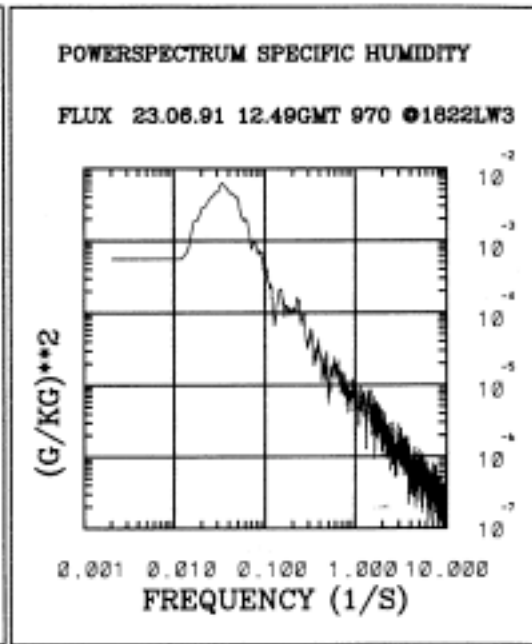
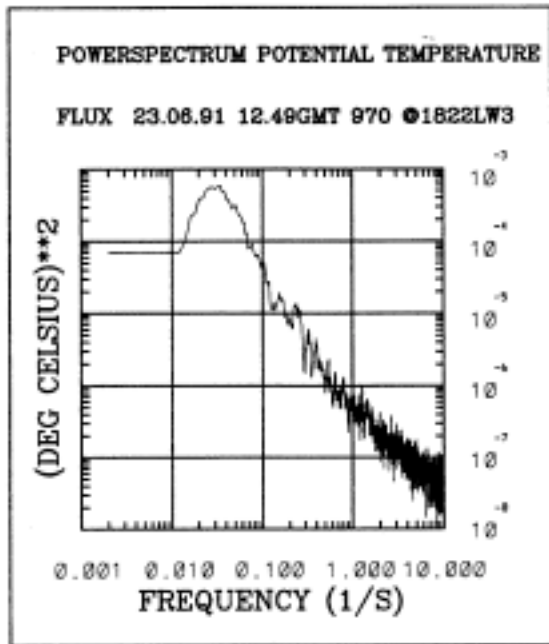
From a global perspective, a new set of experiments is being designed under the auspices of GEWEX and its projects GLASS (Global Land-Atmosphere System Study; Polcher et al., 2000) and GABLS (Global Atmospheric Boundary Layer Study; Holtslag, 2001). The aim is to further improve the description of the land-atmosphere interaction in numerical models by addressing new levels of complexity and coupling.

On the regional level, many practical applications in the realm of sustainable management of natural resources and rural development are calling for advanced decision support systems that operationally accommodate the very same kind of 4DDA and remote-sensing-derived data to complement special tools and data sources tailored to their specific needs. Mediterranean agriculture is an important "information-user" and a key social and economic factor. An example that closes the circle would be the farmer who hosted some EFEDA mast installations years ago and who may benefit from an advanced space-assisted irrigation advisory service (Jochum and Calera, 2002) in the years to come.

Annex A. Example of spectral analysis of airborne turbulence data

Plates A-1 and A-2 show the spectra of potential temperature and specific humidity (top) and the cospectra of vertical wind with potential temperature and specific humidity, respectively (bottom). The example uses two time series of a transect Tomelloso- Barrax flown on 23 June 1991 at midday near inversion (A-1) and in the afternoon at low level (A-2).





Annex B. The mixed layer model

The model is based on the model of Tennekes (1973) with the entrainment formulation of Driedonks (1981). The ML is considered as a one-dimensional vertical slab with well-mixed potential temperature θ and specific humidity q .

The simplified budget equations of heat and moisture (no advection) lead to

$$\frac{d\theta_m}{dt} = \frac{\overline{w'T'_0} - \overline{w'T'_h}}{h} + Q_{rad} \quad (\text{B.1})$$

$$\frac{dq_m}{dt} = \frac{\overline{w'q'_0} - \overline{w'q'_h}}{h} \quad (\text{B.2})$$

where Q_{rad} is the radiative warming and the notation as in Chapter 3.

The entrainment fluxes are expressed as

$$\overline{w'T'_h} = -\Delta\theta \left(\frac{dh}{dt} - w_h \right) \quad (\text{B.3})$$

$$\overline{w'q'_h} = -\Delta q \left(\frac{dh}{dt} - w_h \right). \quad (\text{B.4})$$

where w_h is the subsidence velocity.

The budgets for the entrainment layer lead to prognostic equations for the inversion-level jumps

$$\frac{d\Delta\theta}{dt} = \gamma_\theta \left(\frac{dh}{dt} - w_h \right) - \frac{d\theta_m}{dt} \quad (\text{B.5})$$

$$\frac{d\Delta q}{dt} = \gamma_q \left(\frac{dh}{dt} - w_h \right) - \frac{dq_m}{dt}. \quad (\text{B.6})$$

Assuming that the surface fluxes $\overline{w'T'_0}$ and $\overline{w'q'_0}$ are known as well as γ_θ , γ_q and w_h , the set of equations (B.1)-(B.6) has 7 unknowns (h , θ_m , q_m , $\Delta\theta$, Δq , $\overline{w'T'_h}$ and $\overline{w'q'_h}$) and only 6 equations. We need to make one closure assumption.

For conditions where turbulence is generated only by surface heating, i.e. mechanically generated turbulence is absent, it is assumed that $\overline{w'T'_h}$ is proportional to $\overline{w'T'_0}$:

$$\overline{w'T'_h} = -A \overline{w'T'_0}, \quad (\text{B.7a})$$

where the empirical constant A is often set to 0.2 (Stull, 1988).

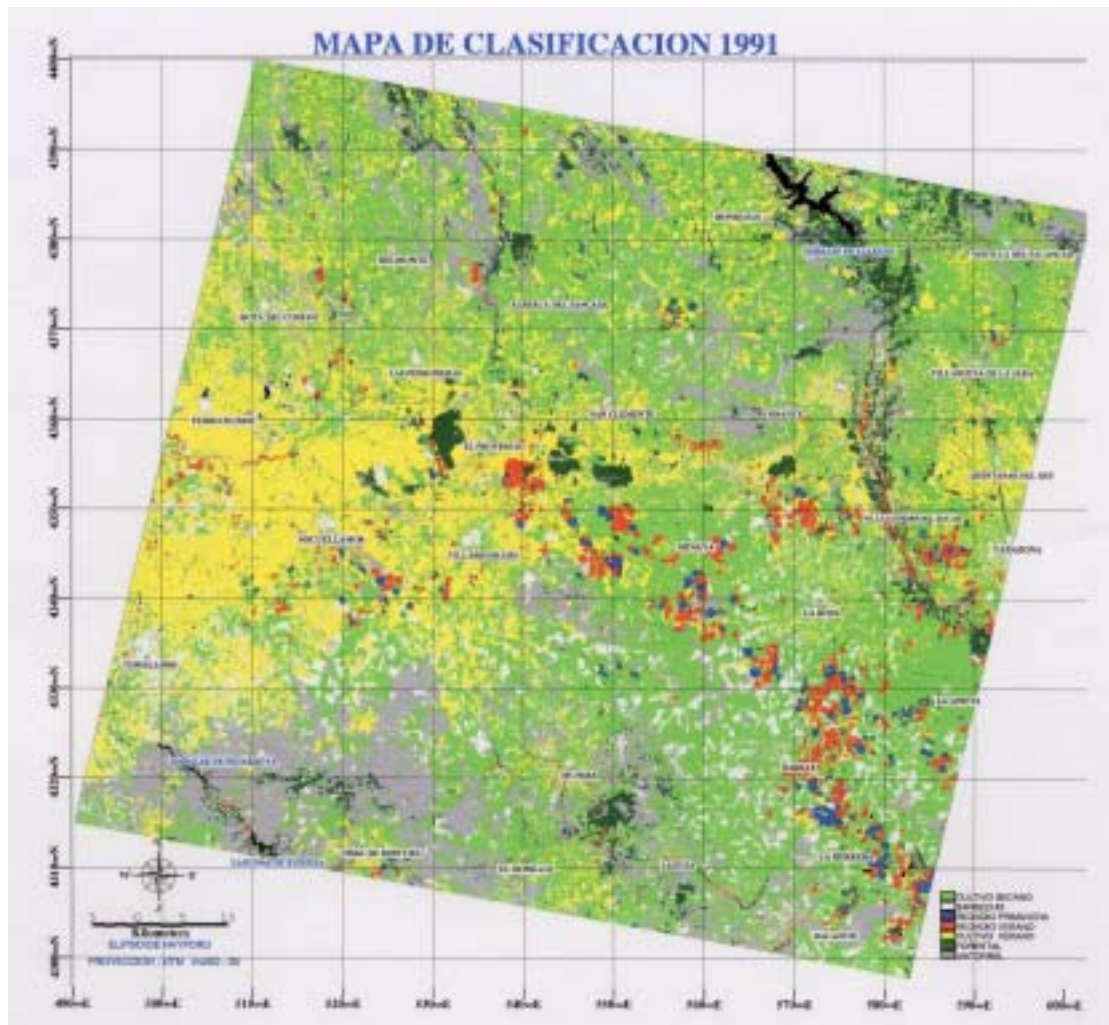
A more general closure assumption (Driedonks, 1981) takes shear generation of turbulence into account:

$$\overline{w'T'_h} = -A\overline{w'T'_0} + A'\frac{u_*^3 T_0}{gh} \quad (\text{B.7b})$$

where A' is another empirical constant.

Annex C. Landuse classification of EFEDA area

This plate shows the landuse classification of the EFEDA area for 1991 from Calera (2000) (courtesy of A. Calera). For definition of classes, see Chapter 2.



Annex D. List of Acronyms

4DDA	4-dimensional data assimilation
ABL	Atmospheric boundary layer
AVHRR	Advanced Very High Resolution Radiometer
BOREAS	Boreal Forest Study
CASES	Cooperative Atmosphere-Surface Exchange Study
CODE	California Ozone Deposition Experiment
CORINE	CoORdination of INformation on the Environment
DIAL	Differential absorption lidar
DLR	Deutsches Zentrum für Luft- und Raumfahrt (German Aerospace Centre)
ECMWF	European Centre of Medium-Range Weather Forecast
EFEDA	European Field Experiment in a Desertification-Threatened Area
ERA	ECMWF Re-Analysis
EZ	Entrainment zone
FA	Free atmosphere
FIFE	First ISLSCP Field Experiment
GEWEX	Global Energy and Water Experiment
GCM	General circulation model
GIS	Geographical information system
GMES	Global Monitoring of Environmental Security
GPS	Global Positioning System
HAPEX	Hydrologic-Atmospheric Pilot Experiment
HIRLAM	High-Resolution Limited-Area Model
INM	Instituto Nacional de Meteorología
IGBP	International Geosphere Biosphere Program
IHDP	International Human Dimensions Program
ISBA	Interaction Soil-Biosphere-Atmosphere
ISLSCP	International Satellite Land Surface Climatology Project
LBA	Large-Scale Biosphere-Atmosphere Experiment
LOTREX	Longitudinal Traverse Experiment
LSE	Land-Surface Experiment
ML	Mixed layer
MOBILHY	Modélisation du Bilan Hydrologique
NASA	National Aeronautic and Space Administration
NBL	Nocturnal boundary layer
NDVI	Normalized Differential Vegetation Index
NOPEX	Northern Hemisphere Climate Processes Land-Surface Experiment
NVAP	NASA Water Vapor Project
NWP	Numerical Weather Prediction
PI	Principal investigator
RL	Residual layer
SEB	Surface energy budget
SEBAL	Surface Energy Balance Algorithm for Land
SR	Simple Ratio
SVAT	Soil-Vegetation-Atmosphere Transfer
TOVS	Tiros Operational Vertical Sounder
WCRP	World Climate Research Program

References

- Abdumumin, S., L.O. Myrup, and J.L. Hatfield, 1987: An energy balance approach to determine regional evapotranspiration based on planetary boundary layer similarity and regularly recorded data. *Water Resources Res.*, **23**, 2050-2058.
- Allen, R.A., L.S. Pereira, D. Raes, and M. Smith, 1998: *Crop evapotranspiration. Guidelines for computing crop water requirements*. FAO Irrigation and Drainage Paper 56. 300 pp.
- Almarza Mata, C., and L. Balairón Ruiz, Coordinators, 1992: Atlas Nacional de España. Sección II, Grupo 9: Climatología. Instituto Geográfico Nacional, Madrid.
- Almarza Mata, C., and J.A. López Díaz, 1996: Análisis de homogeneidad y variabilidad de la serie de precipitación de Murcia. In: *Clima y agua: la gestión de un recurso climático* (M.V. Marzol, P. Dorta, and P. Valladares, Eds.), La Laguna, Madrid.
- André, J.C., et al., 1988. HAPEX-MOBILHY: first results from the special observing period. *Ann. Geophys.*, **6**, 477-492.
- André, J.C., P. Bougeault, and J.-P. Goutorbe, 1990: Regional estimates of heat and evaporation fluxes over non-homogeneous terrain; examples from the HAPEX-MOBILHY program. *Boundary-Layer Meteorol.*, **50**, 77-108.
- Angevine, W.M., 1999: Entrainment results including advection and case studies from the Flatland boundary layer experiments. *J. Geophys. Res.*, **104**, 30947-30963.
- Angevine, W.M., A.M. Grimsdell, S.A. McKeen, and J.M. Warnock, 1998: Entrainment results from the Flatland boundary layer experiments. *J. Geophys. Res.*, **103**, 13689-13701.
- Anthes, R.A., 1984: Enhancement of convective precipitation by mesoscale variations in vegetative covering in semiarid regions. *J. Clim. Appl. Meteorol.*, **23**, 541-554.
- Arain, A.M., W.J. Shuttleworth, Z.L. Yang, J. Michaud, and J. Dolman, 1997: Mapping surface-cover parameters using aggregation rules and remotely sensed cover classes. *Q. J. R. Meteorol. Soc.*, **123**, 2325-2348.
- Arino, O., E. Vermote, and V. Spaventa, 1997: Operational atmospheric correction of Landsat TM imagery. *Earth Observation Quarterly*, 56-57, 32-35.
- Avissar, R., 1992: Conceptual aspects of a statistical-dynamical approach to represent landscape subgrid-scale heterogeneities in atmospheric models. *J. Geophys. Res.*, **97**, 2729-2742.
- Avissar, R., and R.A. Pielke, 1989: A parameterization of heterogeneous land surfaces for atmospheric numerical models and its impact on regional meteorology. *Mon. Wea. Rev.*, **117**, 2113-2136.
- Avissar, R., and T. Schmidt, 1998: An evaluation of the scale at which ground-surface heat flux patchiness affects the convective boundary layer using large eddy simulation. *J. Atmos. Sci.*, **55**, 2666-2689.
- Ball, F.K., 1960: Control of inversion height by surface heating. *Quart. J. Roy. Meteor. Soc.*, **86**, 483-494.
- Bange, J., F. Beyrich, and D.A.M. Engelbart, 2002: Airborne measurements of turbulent fluxes over heterogeneous terrain with Helipod and Do 128 - Error analysis and comparison with ground-based systems. *15th Sympos. on Boundary Layers and Turbulence, 15-19 July 2002, Wageningen*. Amer. Meteorol. Soc., 378-381.
- Barr, A.G., and A.K. Betts, 1997: Radiosonde boundary layer budgets above a boreal forest. *J. Geophys. Res.*, **102**, 29,205-29,212.
- Barr, A.G., A.K. Betts, R.L. Desjardins, and J.I. MacPherson, 1997: Comparison of regional surface fluxes from boundary-layer budgets and aircraft

- measurements above a boreal forest. *J. Geophys. Res.*, **102**, 29,213-29,218.
- Barr, A.G., A.K. Betts, T.A. Black, J.H. McCaughey, and C.D. Smith, 2001: Intercomparison of BOREAS northern and southern study area surface fluxes in 1994. *J. Geophys. Res.*, **106**, 33,543-33,550.
- Bastiaanssen, W.G.M., 1995: *Regionalization of surface flux densities and moisture indicators in composite terrain*. Ph.D. Thesis, Wageningen Agricultural University. 271 pp.
- Bastiaanssen, W.G.M., H. Pelgrum, P. Droogers, H.A.R. de Bruin, and M. Menenti, 1997: Area-average estimates of evaporation, wetness indicators and top soil moisture during two golden days in EFEDA. *Agric. For. Meteorol.*, **87**, 119-137.
- Batchvarova, E., and S.-E. Gryning, 1994: An applied model for the height of the daytime mixed-layer and the entrainment zone. *Boundary-Layer Meteorol.*, **71**, 311-323.
- Beljaars, A.C.M., 1994: The parameterization of surface fluxes in large-scale models under free convection. *Quart. J. Roy. Meteorol. Soc.*, **121**, 255-270.
- Beljaars, A.C.M., and A.A.M. Holtslag, 1991: Flux parameterization over land surfaces for atmospheric models. *J. Appl. Meteorol.*, **30**, 327-341.
- Bellamy, J.C., 1949: Objective calculations of divergence, vertical velocity, and vorticity. *Bull. Amer. Meteor. Soc.*, **30**, 45-49.
- Berger, M., 1997: *Flächenmittel der Energieflüsse in einem semiariden Testgebiet*. Ph.D. thesis, Freie Universität Berlin, 163pp.
- Betts, A.K., 1973: A composite mesoscale cumulonimbus budget. *J. Atmos. Sci.*, **30**, 597-610.
- Betts, A.K., 1992: FIFE atmospheric boundary layer budget methods. *J. Geophys. Res.*, **97**, 18 523-18 531.
- Betts, A.K. and J.H. Ball, 1995: The FIFE surface diurnal cycles climate. *J. Geophys. Res.*, **100**, 25,679-25,693.
- Betts, A.K. and J.H. Ball, 1998: FIFE surface climate and site-averaged dataset 1987-89. *J. Atmos. Sci.*, **55**, 1091-1108.
- Betts, A.K., R.L. Desjardins, J.I. McPherson, and R.D. Kelly, 1990: Boundary-layer heat and moisture budgets from FIFE. *Boundary-Layer Meteorol.*, **50**, 109-137.
- Betts, A.K., R.L. Desjardins, J.I. McPherson, and R.D. Kelly, 1992: Budget analysis of the boundary layer grid flights during FIFE 1987. *J. Geophys. Res.*, **97**, 18 533-18 546.
- Betts, A.K., J.H. Ball, and A.C.M. Beljaars, 1993: Comparison between the land-surface response of the ECMWF model and the FIFE-1987 data. *Q.J.R. Meteorol. Soc.*, **119**, 975-1001.
- Betts, A.K., F. Chen, K.E. Mitchell, and Z.I. Janjic, 1997: Assessment of the land-surface and boundary layer models in two operational versions of the NCEP Eta model using FIFE data. *Mon. Wea. Rev.*, **125**, 2896-2916.
- Betts, A.K., P. Viterbo, and A.C.M. Beljaars, 1998: Comparison of the land-surface interaction in the ECMWF reanalysis model with the 1987 FIFE data. *Mon. Wea. Rev.*, **126**, 186-198.
- Betts, A.K., J.H. Ball, and J.H. McCaughey, 2001: Near-surface climate in the boreal forest. *J. Geophys. Res.*, **106**, 33,529-33,542.
- Betts, A.K., P. Viterbo, A.C.M. Beljaars, and B.J.J.M. van den Hurk, 2001: Impact of BOREAS on the ECMWF forecast model. *J. Geophys. Res.*, **106**, 33,593-33,603.
- Blümel, K., 1992: *Modellierung der Wärmeflüsse am Erdboden mit Berücksichtigung von Vegetation*. Ph.D. thesis, Freie Universität Berlin, 186pp.
- Blyth, E.M., 1995: Using a simple SVAT scheme to describe the effect of scale on aggregation. *Boundary-Layer Meteorol.*, **72**, 267-285.

- Bögel, W., and R. Baumann, 1991: Test and calibration of the DLR Falcon wind measuring system by maneuvers. *J. Atmos. Ocen. Tech.*, **8**, 5-18.
- Bolle, H.-J., J.-C. André, J.L. Arrue, H.K. Barth, P. Bessemoulin, A. Brasa, H.A.R. de Bruin, G. Dugdale, E.T. Engman, D.L. Evans, R. Fantecchi, F. Fiedler, A. van de Griend, A.C. Imeson, A. Jochum, E. López-Baeza, E. Meliá Miralles, L.S. Muniosguren, F. Nerry, J. Noilhan, H.R. Oliver, R. Roth, J. Sánchez Díaz, F.M. de Santa Olalla, W.J. Shuttleworth, H. Soegaard, H. Stricker, J. Thornes, M. Vauclin, and D. Wickland, 1993: EFEDA: European Field Experiment in a Desertification-threatened Area. *Ann. Geophys.*, **11**, 173-189.
- Bolle, H.-J., and B. Streckenbach, 1993: *EFEDA Final Report*. Institut für Meteorologie, Freie Universität Berlin, 461 pp.
- Bosveld, F.C., A. van Ulden, and A.C.M. Beljaars, 1999: *A comparison of ECMWF Re-Analysis data with fluxes and profiles observed in Cabauw*. ECMWF Re-Analysis Project Report Series, **8**, 42 pp.
- Brandt, C.J., and J.B. Thornes, Eds., 1995: *Mediterranean Desertification and Land Use*. Wiley, 554 pp.
- Brasa-Ramos, A., F. Martin de Santa Olalla, V. Caselles, A. Jochum, 1999: Comparison of evapotranspiration estimates by NOAA-AVHRR images and aircraft flux measurements in a semiarid region of Spain. *J. agric. Engng Res.*, **70**, 285-294.
- Braud, I., J. Noilhan, P. Bessemoulin, P. Mascart, R. Haverkamp, and M. Vauclin, 1993: Bare-ground surface heat and water exchanges under dry conditions: Observations and parameterizations. *Boundary-Layer Meteorol.*, **66**, 173-200.
- Bringfelt, B., 1996: *Test of a new land-surface treatment in HIRLAM*. HIRLAM Technical Report 23, SMHI, Norrköping. 72 pp.
- Bringfelt, B., M. Heikinheimo, N. Gustavson, V. Perov, and A. Lindroth, 1999: A new land surface treatment for HIRLAM - comparisons with NOPEX measurements. *Agric. For. Meteorol.*, **198-199**, 239-256.
- Brutsaert, W.H., 1982: *Evaporation into the Atmosphere*. D. Reidel, 299 pp.
- Brutsaert, W.H., and W.P. Kustas, 1985: Evaporation and humidity profiles of neutral conditions over rugged hilly terrain. *J. Clim. Appl. Meteorol.*, **24**, 915-923.
- Brutsaert, W.H., and M. Sugita, 1991: A bulk similarity approach in the atmospheric boundary layer using radiometric skin temperature to determine regional surface fluxes. *Boundary-Layer Meteorol.*, **51**, 1-23.
- Calera Belmonte, A., 2000: *Seguimiento mediante teledetección de la cubierta vegetal de los cultivos de secano y su relación con variables climáticas en Castilla La Mancha*. Ph.D. Thesis, University of Valencia, 315 pp.
- Carson, D.J., 1973: The development of a dry inversion-capped convectively unstable boundary layer. *Quart. J. Roy. Meteorol. Soc.*, **99**, 3129-3134.
- Cervantes Saavedra, M. de, 1605: *El Ingenioso Hidalgo Don Quijote de la Mancha*. J. de la Cuesta, Madrid. 664 pp.
- Cervantes Saavedra, M. de, 1615: *Segunda Parte del Ingenioso Caballero Don Quijote de la Mancha*. J. de la Cuesta, Madrid. 584 pp.
- Champeaux, J.L., and J.P. Jullien, 1993: *Cartographie de la végétation sur l'Espagne à partir de données AVHRR*. Technical Report #19, Météo France, CNRM/GMME.
- Chen, F., and R. Avissar, 1994: The impact of land-surface wetness heterogeneity on mesoscale heat fluxes. *J. Appl. Meteorol.*, **33**, 1323-1340.
- Choudhury, B.J., and N.E. DiGirolamo, 1995: Quantifying the effect of emissivity on the relations between AVHRR split window temperature difference and atmospheric precipitable water over land surfaces. *Remote Sens. Environ.*, **54**, 313-323.
- Choudhury, B.J., T.J. Dorman, and A.Y. Hsu, 1995: Modeled and observed relations between the AVHRR split window temperature difference and

- atmospheric precipitable water over land surfaces. *Remote Sens. Environ.*, **51**, 281-290.
- Claussen, M., 1991: Estimation of areally-averaged surface fluxes. *Boundary-Layer Meteorol.*, **54**, 387-410.
- Claussen, M., 1995: Flux aggregation at large scales: on the limits of validity of the concept of blending height. *J. Hydrol.*, **166**, 371-382.
- Cleugh, H.A., 1991: Predicting catchment scale evaporation using a coupled boundary layer growth/canopy evaporation model. *Vegetatio*, **9**, 135-148.
- Cleugh, H.A., and C.S.B. Grimmond, 2001: Modelling regional scale surface energy exchanges and CBL growth in a heterogeneous, urban-rural landscape. *Boundary-Layer Meteorol.*, **98**, 1-31.
- Cuxart, J., P. Bougeault, and J.L. Redelsperger, 2000: A turbulence scheme allowing for mesoscale and large-eddy simulations. *Q. J. R. Meteorol. Soc.*, **126**, 1-30.
- de Bruin, H.A.R., 1983: A model for the Priestley-Taylor α . *J. Climate Appl. Meteorol.*, **22**, 572-578.
- de Bruin, H.A.R., 1987: Physical aspects of the planetary boundary layer with special reference to regional evapotranspiration. In: *Estimation of Areal Evapotranspiration* (T.A. Black, D.L. Spittlehouse, M.D. Novak, and D.T. Price, Eds.). IAHS Publ. no. 177.
- de Bruin, H.A.R., and Coauthors, 1993: *Surface fluxes measured during EFEDA*. In: Bolle and Streckenbach (1993), 141-227.
- del Pino Corredera, J., 1996: *Estudio de la distribución del vapor de agua en la atmósfera para su aplicación en la corrección de imágenes de satélite*. Tesis de Licenciatura, Universitat de València. 112 pp.
- Desjardins, R.L., and Coauthors, 1997: Scaling up flux measurements for the boreal forest using aircraft-tower combinations. *J. Geophys. Res.*, **102**, 29 125-29 134.
- Dickinson, R.E., A. Henderson-Sellers, P.J. Kennedy, and M.F. Wilson, 1986: *Biosphere-Atmosphere Transfer Scheme (BATS) for the NCAR Community Climate Model*. NCAR Tech. Note TN-275+STR, 69 pp.
- Doran, J.C., W.J. Shaw, and J.M. Hubbe, 1995: Boundary layer characteristics over areas of inhomogeneous surface fluxes. *J. Appl. Meteorol.*, **34**, 559-571.
- Doran, J.C., J.M. Hubbe, J.C. Liljegren, W.J. Shaw, G.J. Collatz, D.R. Cook, and R.L. Hart, 1998: A technique for determining the spatial and temporal distributions of surface fluxes of heat and moisture over the Southern Great Plains Cloud and Radiation Testbed. *J. Geophys. Res.*, **103**, 6109-6121.
- Douville, H., J.-F. Mahfouf, S. Saarinen, and P. Viterbo, 1998: *The ECMWF surface analysis: diagnostics and prospects*. ECMWF Technical Memorandum 258, 51 pp.
- Driedonks, A.G.M., 1982: Models and observations of the growth of the atmospheric boundary layer. *Boundary-Layer Meteorol.*, **23**, 283-306.
- Duan, J., M. Bevis, P. Fang, Y. Bock, S. Chiswell, S. Businger, C. Rocken, F. Solheim, T. van Hove, R. Ware, S. McClusky, T. A. Herring, and R.W. King, 1996: GPS Meteorology: Direct estimation of the absolute value of precipitable water. *J. Appl. Meteorol.*, **35**, 830-838.
- ECMWF, 2001: *The ERA-40 Archive Plan*. <http://www.ecmwf.int/research/era>.
- EFEDA, 1995: EFEDA CD-ROM Data Bank. Freie Universität Berlin.
- Ehret, G., C. Kiemle, W. Renger, and G. Simmet, 1993: Airborne remote sensing of tropospheric water vapor with a new near-infrared differential absorption lidar system. *Applied Optics*, **32**, 4534-4551.
- Feddes, R.A., P. Kabat, A.J. Dolman, R.W.A. Hutjes and M.J. Waterloo, 1998: Large scale field experiments to improve land surface parameterisations. In: Dooge J.H. et al. (Eds), *Climate and Water - A 1998 Perspective*. Proc. 2nd Int. Conf. on Climate and Water, Espoo, Finland (1998), 619-647.

- Fiedler, F., J. Grunwald, and N. Kalthoff, 1993: *The boundary layer evolution at the Barrax and Tomelloso site during the "golden days"*. In: Bolle and Streckenbach (1993), 257-267.
- Fiedler, F., G. Adrian, M. Baldauf, and A. Müller, 1996: Mesoscale and microscale circulations. In: *Desertification processes in the Mediterranean area and their interlinks with global climate: Surface processes and atmospheric modelling* (J. Noilhan, Ed.). Final report of the EFEDA group 6, EU contract EV5V-CT93-0269 (available upon request to J. Noilhan, CNRM, 42 Ave. Coriolis, 31057 Toulouse Cedex, France). 44 pp.
- Fimpel, H.-P., 1987: The DFVLR meteorological research aircraft Falcon-E: Instrumentation and examples of measured data. *Proc. of the Sixth Symp. on Meteorological Observations and Instrumentation*, New Orleans, LA, Amer. Meteorol. Soc., 113-116.
- Frech, M., and A. Jochum, 1999: The evaluation of flux aggregation methods using aircraft measurements in the surface layer. *Agricultural and Forest Meteorology*, **98-99**, 121-143.
- Frech, M., P. Samuelsson, M. Tjernström, and A. Jochum, 1998: Regional surface fluxes over the NOPEX area. *J. Hydrol.*, **212-213**, 155-171.
- Gao, W., 1995: Parameterization of subgrid-scale land surface fluxes with emphasis on distributing mean atmospheric forcing and using satellite-derived vegetation index. *J. Geophys. Res.*, **100**, 14305-14317.
- Garratt, J.R., 1992: *The Atmospheric Boundary Layer*. Cambridge University Press, 316 pp.
- Geleyn, J.F., 1988: Interpolation of wind, temperature and humidity values from the model levels to the height of measurement. *Tellus*, **40A**, 347-351.
- Gibson, J.K., P. Kallberg, S. Uppala, A. Hernandez, A. Nomura, and E. Serrano, 1997: *ERA description*. ECMWF Re-Analysis Project Report Series, 1. 71pp.
- Giordani, H., J. Noilhan, P. Lacarrère, P. Bessemoulin, and P. Mascart, 1996: Modelling the surface processes and the atmospheric boundary layer for semi-arid conditions. *Agricultural and Forest Meteorology*, **80**, 263-287.
- Gottschalk, L., E. Batchvarova, S.-E. Gryning, A. Lindroth, D. Melas, Y. Motovilov, M. Frech, M. Heikinheimo, P. Samuelsson, A. Grelle, and T. Persson, 1999: Scale aggregation - comparison of flux estimates from NOPEX. *Agricultural and Forest Meteorology*, **98-99**, 103-119.
- Goutorbe, J.P., et al., 1997: An overview of HAPEX-Sahel: a study in climate and desertification. *J. Hydrol.*, **188-189**, 4-17.
- Greenwald, T.J., G.L. Stephens, T.H. Vonder Haar, and D.L. Jackson, 1993: A physical retrieval of cloud liquid water over the global oceans using SSM/I measurements. *J. Geophys. Res.*, **98**, 18471-18488.
- Grossman, R.L., 1984: Bivariate conditional sampling of moisture flux over a tropical ocean. *J. Atmos. Sci.*, **41**, 3238-3253.
- Grossman, R.L., 1992a: Convective boundary layer budgets of moisture and sensible heat over an unstressed prairie. *J. Geophys. Res.*, **97**, 18,425-18,438.
- Grossman, R.L., 1992b: Sampling errors in the vertical fluxes of potential temperature and moisture measured by aircraft during FIFE. *J. Geophys. Res.*, **97**, 18,439-18,443.
- Grossman, R.L., and N. Gamage, 1995: Moisture flux and mixing processes in the daytime continental convective boundary layer. *J. Geophys. Res.*, **100**, 25,665-25,674.
- Grunwald, J., N. Kalthoff, U. Corsmeier, and F. Fiedler, 1996: Comparison of areally averaged turbulent fluxes over non-homogeneous terrain. *Boundary-Layer Meteorol.*, **77**, 105-134.
- Grunwald, J., N. Kalthoff, F. Fiedler, and U. Corsmeier, 1998: Application of different flight strategies to determine areally averaged turbulent fluxes. *Contr. Atmos. Phys.*, **71**, 283-302.

- Gryning, S.-E., and E. Batchvarova, 1999: Regional heat flux over the NOPEX area estimated from the evolution of the mixed layer. *Agric. For. Meteorol.*, **98-99**, 159-167.
- Gustafsson, D., and coauthors, 2002: Boreal forest surface parameterization in the ECMWF model - 1D tests with NOPEX long-term data. *J. Appl. Meteorol.*, **42**, 95-112.
- Habets, F., 1994: *Modélisation régionale de la couche limite convective et des processus de surface. Application aux 28 et 29 juin de la campagne EFEDA 1991*. DEA report, Université Paul Sabatier, Toulouse. 29 pp.
- Halldin, S., L. Gottschalk, A.A. van de Griend, S.-E. Gryning, M. Heikinheimo, U. Högström, A.M. Jochum, and L.-C. Lundin, 1998: NOPEX - a northern hemisphere climate processes land-surface experiment. *J. Hydrol.*, **212-213**, 172-187.
- Halldin, S., S.E. Gryning, L. Gottschalk, A.M. Jochum, L.-C. Lundin, A.A. Van de Griend, 1999: Energy, water and carbon exchange in a boreal forest landscape - NOPEX experiences. *Agricultural and Forest Meteorology*, **98-99**, 5-29.
- Hasager, C., and N.O. Jensen, 1999: Surface-flux aggregation in heterogeneous terrain. *Quart. J. Roy. Meteorol. Soc.*, **125**, 2075-2102.
- Hipps, L.E., E. Swiatek, and W.P. Kustas, 1994: Interactions between regional surface fluxes and the atmospheric boundary layer over a heterogeneous watershed. *Water Resources Res.*, **30**, 1387-1392.
- Holtslag, A.A.M., 2001: GABLS: A new GEWEX activity on atmospheric boundary layers. *GEWEX News*, 11-2001, p.18.
- Howell, J., and L. Mahrt, 1997: Multiresolution flux decomposition. *Boundary-Layer Meteorol.*, **83**, 117-137.
- Hu, Y., and S. Islam, 1997: Effects of spatial variability on the scaling of land-surface parameterizations. *Boundary-Layer Meteorol.*, **83**, 441-461.
- Hu, Y., S. Islam, and L. Jiang, 1999: Approaches for aggregating heterogeneous surface parameters and fluxes for mesoscale and climate models. *Boundary-Layer Meteorol.*, **93**, 313-336.
- Hubbe, J.M., J.C. Doran, J.C. Liljegren, and W.J. Shaw, 1997: Observations of spatial variations of boundary layer structure over the Southern Great Plains Cloud and Radiation Testbed. *J. Appl. Meteorol.*, **36**, 1221-1231.
- Jacobs, C.M.J., 1994: *Direct impact of atmospheric CO2 enrichment on regional transpiration*. Ph.D. Thesis, Wageningen Agricultural University. 178 pp.
- Jochum, A.M., 1993a: Estimation of area-averaged fluxes from aircraft measurements using different observational techniques. *Proc. Eighth Symposium on Meteorological Observations and Instrumentation, Anaheim, Amer. Meteorol. Soc.*, 469-472.
- Jochum, A.M., 1993b: Evaporation and energy fluxes during EFEDA: Horizontal variability and area averaging. In: *Exchange Processes at the Land-Surface for a Range of Space and Time Scales* (H.J. Bolle, J. Kalma, and R. Feddes, Eds.). IAHS Publ. no. 212, 373-380.
- Jochum, A., and A. Calera Belmonte, 2002: Tecnologías de observación de la Tierra en los Servicios de Asesoramiento de Riegos. III Congreso Ibérico sobre Gestión y Planificación del Agua. 10 pp.
- Jochum, A.M., N. Entstrasser, B.I. Michels, G. Ehret, and C. Kiemle, 1992b: *EFEDA aircraft operations. DLR Falcon Data Report*. DLR Internal Report, 216 pp.
- Jochum, A.M., J. Moreno, J.D. del Pino, 1999: *Meteorological and climate data in support of the Land-Surface Change Indicator (LCI)*. Final Report RESYSMED (Synthesis of Change Detection Parameters into a Land-Surface Change Indicator for Long-Term Desertification Studies). European Commission Contract ENV4-CT97-0683. 45 pp.
- Jochum, A.M., P. Kabat, and R. Hutjes, 2000: The role of remote sensing in land-surface experiments within BAHC and ISLSCP. In: *Observing Land from*

- Space: Science, Customers and Technology*. M. Verstraete, M. Menenti and J. Peltoniemi, Eds., Kluwer Academic Publishers. 91-103.
- Kabat, P., R.W.A. Hutjes, and R.A. Feddes, 1997: The scaling characteristics of soil parameters: From plot scale heterogeneity to subgrid parameterizations. *J. Hydrol.*, **190**, 363-396.
- Källén, E., Ed., 1996: *HIRLAM Documentation Manual, System 2.5*. SMHI, Norrköping. 178 pp. + 55 pp. appendix.
- Kain, J.S., and J.M. Fritsch, 1993 Convective parameterization for mesoscale models: The Kain-Fritsch scheme. In: *The representation of cumulus convection in numerical models* (K.A. Emanuel and D.J. Raymond, Eds.). *AMS Monograph*, **46**, 245 pp.
- Kelly, R.D., E.A. Smith, and J.I. MacPherson, 1992: A comparison of surface sensible and latent heat fluxes from aircraft and surface measurements in FIFE 1987. *J. Geophys. Res.*, **97**, 18 445-18 453.
- Kiemle, C., M. Kästner, and G. Ehret, 1995: The convective boundary layer structure from lidar and radiosonde measurements during the EFEDA'91 campaign. *J. Atmos. Oceanic Technol.*, **12**, 771-782.
- Koster, R.D., and M.J. Suarez, 1992a: Modeling the land surface boundary in climate models as a composite of independent vegetation stands. *J. Geophys. Res.*, **97**, 2697-2715.
- Koster, R.D., and M.J. Suarez, 1992b: A comparative analysis of two land surface heterogeneity representations. *J. Climate*, **5**, 1379-1390.
- Kratzsch, T., 1994: Messung turbulenter Flüsse mit einem Forschungsflugzeug während EFEDA. *Meteorol. Zeitschr., N.F.* **3**, 319-332.
- Kratzsch, T., A. Jochum, and R. Busen, 1993: *Intercomparison of aircraft flux measurements*. In: Bolle and Streckenbach (1993), 239-243.
- Krikke, R.K., 1994: *Quickset Manual*. Dept. of Meteorology, Wageningen Agricultural University. 19 pp.
- Kustas, W.P., and W. Brutsaert, 1987a: Budgets of water vapor in the unstable boundary layer over rugged terrain. *J. Climate Appl. Meteorol.*, **26**, 607-620.
- Kustas, W.P., and W. Brutsaert, 1987b: Virtual heat entrainment in the mixed layer over very rough terrain. *Boundary-Layer Meteorol.*, **38**, 141-157.
- Kustas, W.P., L.E. Hipps, and K.S. Humes, 1994: Calculation of basin-scale surface fluxes by combining remotely sensed data and atmospheric properties in a semiarid landscape. *Boundary-Layer Meteorol.*, **73**, 105-123.
- LeMone, M.A., and Coauthors, 2000: Land-atmosphere interaction research: Early results and opportunities in the Walnut River watershed in southeast Kansas: CASES and ABLE. *Bull. Amer. Meteorol. Soc.*, **81**, 757-779.
- LeMone, M.A., R.L. Grossman, R.T. McMillen, K.-N. Liou, S.C. Ou, S. McKeen, W. Angevine, K. Ikeda, and F. Chen, 2001: CASES-97: Late morning warming and moistening of the convective boundary layer over the Walnut River watershed. *Boundary-Layer Meteorol.*, **104**, 1-52.
- Lenschow, D.H., Ed., 1986. Probing the Atmospheric Boundary Layer. Amer. Meteorol. Soc., Boston, 269 pp.
- Lenschow, D.H., and B.B. Stankov, 1986: Length scales in the convective boundary layer. *J. Atmos. Sci.*, **12**, 1198-1209.
- Lenschow, D.H., H. Mann, and L. Kristensen, 1994: How long is long enough when measuring fluxes and other turbulence statistics? *J. Atmos. Ocean. Technol.*, **11**, 661-673.
- Lhomme, J.-P., A. Chehbouni, and B. Monteny, 1994: Effective parameters of surface energy balance in heterogeneous landscape. *Boundary-Layer Meteorol.*, **71**, 297-309.
- Lhomme, J.-P., B. Monteny, and P. Bessemoulin, 1997: Inferring regional surface fluxes from convective boundary layer characteristics in a Sahelian environment. *Water Resources Res.*, **33**, 2563-2569.

- Li, Z.-L., and F. Becker, 1993: Feasibility of land surface temperature and emissivity determination from AVHRR data. *Remote Sens. Environ.*, **43**, 67-85.
- Liang, S., H. Fallah-Adl, S. Kalluri, J. J, Y. Kaufman, and J.R.G. Townshend, 1997: An operational atmospheric correction algorithm for Landsat Thematic Mapper imagery over the land. *J. Geophys. Res.*, **102**, 17,173-17,186.
- Linder, W., J. Noilhan, M. Berger, K. Bluemel, E. Blyth, and G. Boulet, 1996: *Intercomparison of surface schemes using EFEDA flux data*. CNRM Report N 39, Mteo France, 86pp.
- Lopez Gomez, J., 1979: El clima en Espaa segun la clasificacion de Koppen. Instituto Juan Sebastian Elcano (CSIC), Madrid.
- Lott, F., and M.J. Miller, 1997: A new subgrid-scale orographic drag parameterization: Its formulation and testing. *Q. J. R. Meteorol. Soc.*, **123**, 101-127.
- Louis, J.F., 1979: A parametric model of vertical eddy fluxes in the atmosphere. *Boundary-Layer Meteorol.*, **17**, 187-202.
- Louis, J.F., M. Tiedtke, and J.F. Geleyn, 1982: A short history of the PBL parameterization at ECMWF. ECMWF Workshop on Planetary Boundary Layer Parameterization, 59-80.
- Lynn, B.H., D. Rind, and R. Avissar, 1995: The importance of mesoscale circulations generated by subgrid-scale landscape heterogeneities in general circulation models. *J. Climate*, **8**, 191-205.
- Mahfouf, J.-F., and J. Noilhan, 1996: Inclusion of gravitational drainage in a land surface scheme based on the force restore method. *J. Appl. Meteorol.*, **35**, 987-992.
- Mahfouf, J.-F., A.O. Manzi, J. Noilhan, H. Giordani, and M. Deque, 1995: The land surface scheme ISBA within the Meteo-France climate model ARPEGE. Part I: Implementation and preliminary results. *J. Climate*, **8**, 2039-2057.
- Mahrt, L., 1996: The bulk aerodynamic formulation over heterogeneous surfaces. *Boundary-Layer Meteorol.*, **78**, 87-119.
- Mahrt, L., 1998: Flux sampling errors for aircraft and towers. *J. Atmos. Oceanic Tech.*, **15**, 416-429.
- Mahrt, L.J., and J. Paumier, 1984: Heat transport in the atmospheric boundary layer. *J. Atmos. Sci.*, **41**, 3061-3075.
- Mahrt, L., and M. Ek, 1993: Spatial variability of turbulent fluxes and roughness lengths in HAPEX-MOBILHY. *Boundary-Layer Meteorol.*, **65**, 381-400.
- Mahrt, L.J., and J. Sun, 1995a: Dependence of surface exchange coefficients on averaging scale. *Quart. J. Roy. Meteorol. Soc.*, **121**, 1835-1852.
- Mahrt, L.J., and J. Sun, 1995b: The subgrid velocity scale in the bulk aerodynamic relationship for spatially averaged scalar fluxes. *Mon. Wea. Rev.*, **123**, 3032-3041.
- Mahrt, L., J.I. MacPherson, and R.L. Desjardins, 1994a: Observations of fluxes over heterogeneous surfaces. *Boundary-Layer Meteorol.*, **67**, 345-367.
- Mahrt, L., J. Sun, D. Vickers, J.I. MacPherson, J.R. Pederson, and R.L. Desjardins, 1994b: Observations of fluxes and inland breezes over a heterogeneous surface. *J. Atmos. Sci.*, **51**, 284-2499.
- Mahrt, L., D. Vickers, J. Sun, and J.H. McCaughey, 2001: Calculation of area-averaged fluxes: Application to BOREAS. *J. Appl. Meteorol.*, **40**, 915-920.
- Mann, J., and D.H. Lenschow, 1994: Errors in airborne flux measurements. *J. Geophys. Res.*, **99**, 14519-14526.
- Manzi, A.O., and S. Planton, 1994: Implementation of the ISBA parameterization scheme for land surface processes in a GCM - an annual cycle experiment. *J. Hydrol.*, **155**, 353-387.
- Martın de Santa Olalla, F., A. Brasa Ramos, C. Fabeiro Cortes, D. Fernandez Gonzalez and H. Lopez Corcoles, 1999: Improvement of irrigation

- management towards the sustainable use of groundwater in Castilla-La Mancha, Spain. *Agricultural Water Management*, **2-3**, 195-206.
- Martínez, C., and A. Calera, 2001: Irrigated crop area estimation from thematic map using Landsat TM imagery in La Mancha (Spain). *Photogrammetric Engineering and Remote Sensing*, **67**, 1177-1184.
- Mascart, P., J. Noilhan, and H. Giordani, 1993: *Etude des caractéristiques des sols dans la zone EFEDA-91*. Technical Report 14, Météo France, CNRM/GMME.
- Mason, P.J., 1988: The formulation of areally-averaged roughness lengths. *Quart. J. Roy. Meteorol. Soc.*, **114**, 399-420.
- McClatchey, R.A., R.W. Fenn, J.E.A. Selby, F.E. Volz, and J.S. Garing, 1971: *Optical properties of the atmosphere*. AFCRL-TR-71-0279, Enviro. Research Papers, No 354.
- McNaughton, K.G., and T.W. Spriggs, 1986: A mixed-layer model for regional evaporation. *Boundary-Layer Meteorol.*, **34**, 243-262.
- Miao, J.-F., L.J.M. Kroon, J. Vilà-Guerau de Arellano, and A.A.M. Holtslag, 2003: Impacts of topography and land degradation on the sea breeze over Eastern Spain. *Meteorol. Atmos. Phys.*, in press.
- Michaud, J.D., and W.J. Shuttleworth, 1997: Executive summary of the Tucson Aggregation Workshop. *J. Hydrol.*, **190**, 176-181.
- Michels, B.I., 1992: *Fluxes of heat and water vapour in a convective mixed layer during EFEDA*. DLR Report FB 92-21, 77 pp.
- Michels, B.I., and A.M. Jochum, 1995: Heat and moisture flux profiles in a region with inhomogeneous surface evaporation. *J. Hydrol.*, **166**, 383-407.
- Moene, A.F., 1992: *Intercomparison of energy fluxes measured during EFEDA*. Internal Manuscript. Dept. of Meteorology, Wageningen Agricultural University, Wageningen, 33 pp.
- Moene, A.F., H.A.R. de Bruin, A.A.M. Holtslag, 1995: *Validation of the surface parameterization of HIRLAM using surface-based measurements and remote sensing data*. Scientific report WR 95-07. KNMI, de Bilt. 45 pp.
- Moore, K.E., D.R. Fitzjarrald, and J.D. Ritter, 1993: How well can regional fluxes be derived from smaller-scale estimates? *J. Geophys. Res.*, **98**, 7187-7198.
- Morcrette, J.-J., 1990: Impact of changes to the radiative transfer parameterization plus cloud optical properties in the ECMWF model. *Mon. Wea. Rev.*, **118**, 847-873.
- Muniosguren, L.S., 1993: *Results of radiosonde measurements undertaken by INM*. In: Bolle and Streckenbach (1993), 268-279.
- Munley, W.G., and L.E. Hipps, 1991: Estimation of regional evaporation for a tallgrass prairie from measurements of properties of the atmospheric boundary layer. *Water Resources Res.*, **27**, 225-230.
- Myneni, R.B., S. Maggion, J. Jaquinta, J.L. Privette, N. Gobron, B. Pinty, D.S. Kimes, M.M. Verstraete, and D.L. Williams, 1995: Optical remote sensing of vegetation: Modeling, caveats, and algorithms. *Remote Sens. Environ.*, **51**, 169-188.
- Nobre, C.A., et al., 1996: *The Large Scale Biosphere-Atmosphere Experiment in Amazonia (LBA)*. Concise Experiment Plan. LBA Project Office, CPTEC/INPE.
- Noilhan, J., 1996: Desertification processes in the Mediterranean area and their interlinks with global climate: Surface processes and atmospheric modelling. Final report of the EFEDA group 6, EU contract EV5V-CT93-0269 (available upon request to J. Noilhan, CNRM, 42 Ave. Coriolis, 31057 Toulouse Cedex, France).
- Noilhan, J., and S. Planton, 1989: A simple parameterization of land surface processes for meteorological models. *Mon. Wea. Rev.*, **117**, 536-549.
- Noilhan, J., P. Lacarrère, A.J. Dolman, and E.M. Blyth, 1997: Defining area-average parameters in meteorological models for land surface with mesoscale heterogeneity. *J. Hydrol.*, **190**, 302-326.

- Norman, J.M., M. Divakarla, and N.S. Goel, 1995: Algorithms for extracting information from remote thermal-IR observations of the earth's surface. *Remote Sens. Environ.*, **51**, 157-168.
- Oliver, H.R., and K.J. Sene, 1992: Energy and water balances of developing vines. *Agric. Forest Meteorol.*, **61**, 167-183.
- Ottlé, C, S. Outalha, C. François, and S. Le Maguer, 1997: Estimation of total atmospheric water vapor content from split-window radiance measurements. *Remote Sens. Environ.*, **61**, 410-418.
- Paltridge, G.W., 1973: Direct measurements of water vapor absorption of solar radiation in the free atmosphere. *J. Atmos. Sci.*, **30**, 156-160.
- Paulson, C.A., 1970: The mathematical representation of wind speed and temperature profiles in the unstable surface layer. *J. Appl. Meteorol.*, **9**, 857-861.
- Pelgrum, H., and W.G.M. Bastiaanssen, 1996: An intercomparison of techniques to determine the area-averaged latent heat flux from individual in situ observations: A remote sensing approach using the EFEDA data. *Water Resources Res.*, **32**, 2775-2786.
- Peters-Lidard, C., and L.H. Davis, 2000: Regional flux estimation in a convective boundary layer using a conservation approach. *J. Hydrometeorol.*, **1**, 170-182.
- Peters-Lidard, C., M.S. Zion, and E.F. Wood, 1997: A soil-vegetation-atmosphere transfer scheme for modeling spatially variable water and energy balance processes. *J. Geophys. Res.*, **102**, 4303-4324.
- Polcher, J., and coauthors, 2000: GLASS: Global Land-Atmosphere System Study. *GEWEX News*, 05-2000. 3-5.
- Portela, A., and M. Castro, 1996: Summer thermal lows in the Iberian peninsula: A three-dimensional simulation. *Q. J. R. Meteorol. Soc.*, **122**, 1-22.
- Prata, A.J., 1993: Land surface temperature derived from the Advanced Very High Resolution Radiometer and the Along-Track Scanning Radiometer: 1. Theory. *J. Geophys. Res.*, **98**, 16689-16702.
- Pratt, R.W., 1985: Review of radiosonde humidity and temperature errors. *J Atmos. Oceanic Technol.*, **2**, 404-407.
- Randel, D.L., T.H. Vonder Haar, M.A. Ringerud, G.L. Stephens, T.J. Greenwald, and C.L. Combs, 1996: A new global water vapor dataset. *Bull. Amer. Meteorol. Soc.*, **77**, 1233-1246.
- Raupach, M.R., 1991: Vegetation-atmosphere interaction in homogeneous and heterogeneous terrain: Some implications of mixed-layer dynamics. *Vegetatio*, **91**, 105-120.
- Raupach, M.R., 1993: The averaging of surface flux densities in heterogeneous landscapes. *IAHS Publ.*, **212**, 343-355.
- Raupach, M.R., 1995: Vegetation-atmosphere interaction and surface conductance at leaf, canopy, and regional scales. *Agric. For. Meteorol.*, **73**, 151-179.
- Raupach, M.R., and J.J. Finnigan, 1995: Scale issues in boundary-layer meteorology: Surface energy balances in heterogeneous terrain. *Hydrol. Processes*, **9**, 589-612.
- Rodríguez, E., Navascues, B, Ayuso, J.J., and Jarvenoja, S., 2003: *Analysis of surface variables and parameterization of surface processes in HIRLAM. Part I: Approach and verification by parallel runs*. HIRLAM Technical Report No. 58. HIRLAM-5 Project. SMHI. [Available from Per Unden, SMHI, S-601 76 Norrkoeping, Sweden].
- Rodríguez-Camino, E., and R. Avissar, 1999: Effective parameters for surface heat fluxes in heterogeneous terrain. *Tellus*. **51A**, 378-399.
- Rodríguez-Camino, E., and J.A. García-Moya, 1992: *Synoptic weather atlas during the EFEDA experimental phase (June 1991)*. Instituto Nacional de Meteorología, 136 pp.

- Ronda, R.J., 2002: *Modeling the exchange of water and energy over natural land surfaces*. Ph.D. thesis, Wageningen University, 114pp.
- Ronda, R.J., and H.A.R. de Bruin, 1999: A note on the concept of the "effective" bulk exchange coefficients for determination of surface flux densities. *Boundary-Layer Meteorol.*, **93**, 155-162.
- Rontu, L., K. Sattler, and R. Sigg, 2002: *Parameterization of subgrid-scale orography effects in HIRLAM*. HIRLAM Technical Report, submitted.
- Ross, R. J., and W.P. Elliott, 1996: Tropospheric water vapor climatology and trends over North America: 1973-93. *J. Climate*. **9**, 3561-3574.
- Rubio Caballero, E.M., 1997: *Hacia la optimización de la medida de la emisividad y la temperatura en teledetección*. Ph.D. Thesis, Universidad de Valencia. 272 pp.
- Saïd, F., J.L. Attié, B. Bénech, A. Druilhet, P. Durand, M.H. Marciniak, and B. Monteny, 1997: Spatial variability in airborne surface flux measurements during HAPEX-Sahel. *J. Hydrol.*, **188-189**, 878-911.
- Samuelsson, P., and M. Tjernström, 1999: Airborne flux measurements in NOPEX: comparison with footprint estimated surface heat fluxes. *Agric. For. Meteorol.*, **98-99**, 205-226.
- Sánchez, J., R. Boluda, A. Artigao, C. Morell, J.C. Colomer, and R. Guardado, 1994: Suelos. In: *Desertificación en Castilla La Mancha. El proyecto EFEDA* (F. Martín de Santa Olalla, Ed.). Ediciones Universidad de Castilla La Mancha, 97-139.
- Sass, B.H., L. Rontu, and P. Räisänen, 1994: *HIRLAM-2 Radiation Scheme: Documentation and Tests*. HIRLAM Technical Report 16, SMHI, Norrköping. 42 pp.
- Savijärvi, H., 1990: Fast radiation parameterization schemes for mesoscale and short-range forecast models. *J. Appl. Meteorol.*, **29**, 437-447.
- Schmid, H.P., 1994: Source areas for scalars and scalar fluxes. *Boundary-Layer Meteorol.*, **67**, 293-318.
- Schmid, H.P., and B. Bünzli, 1995: The influence of surface texture on the effective roughness length. *Q. J. R. Meteorol. Soc.*, **121**, 1-21.
- Sellers, P.J., Y. Mintz, Y.C. Sud, and A. Dalcher, 1986: The design of a Simple Biosphere model (SiB) for use within general circulation models. *J. Atmos. Sci.*, **43**, 505-531.
- Sellers, P.J., F.G. Hall, G. Asrar, D.E. Strelbel, and R.E. Murphy, 1992: An overview of the First ISLSCP Field Experiment. *J. Geophys. Res.*, **97**, 18 345-18 372.
- Sellers, P.J., et al., 1995: The Boreal Ecosystem-Atmosphere Study (BOREAS): An overview and early results from the 1994 field year. *Bull. Am. Meteorol. Soc.*, **76**, 1549-1577.
- Shaw, W.J., and J.C. Doran, 2001: Observations of systematic boundary layer divergence patterns and their relationship to land use and topography. *J. Climate*, **14**, 1753-1764.
- Shuttleworth, W.J., 1988: Macrohydrology: the new challenge for process hydrology. *J. Hydrol.*, **100**, 31-56.
- Shuttleworth, W.J., 1991: Evaporation models in hydrology. In: *Land Surface Evaporation; Measurements and Parameterization* (T.J. Schmugge and J.C. André. Eds.). Springer, New York, 93-120.
- Shuttleworth, W.J., 1993: The Soil-Vegetation-Atmosphere Interface. In: *Energy and Water Cycles in the Climate System* (E. Raschke and D. Jakob, Eds.). Proc. NATO-ASI, Glücksburg, Germany.
- Smith, E.A., and Coauthors, 1992: Area-averaged surface fluxes and their time-space variability over the FIFE area. *J. Geophys. Res.*, **97**, 18599-18622.
- Sorbjan, Z., 1989: *Structure of the Atmospheric Boundary Layer*. Prentice Hall, 308 pp.

- Sugita, M., and W. Brutsaert, 1990: Regional surface fluxes from remotely sensed skin temperature and lower boundary layer measurements. *Water Resources Res.*, **26**, 2937-2944.
- Sugita, M., T. Hiyama, and I. Kayane, 1997: How regional are the regional fluxes obtained from lower atmospheric boundary layer data? *Water Resources Res.*, **33**, 1437-1445.
- Sun, J., W. Massman, and D.A. Grantz, 1999. Aerodynamic variables in the bulk formulation of turbulent fluxes. *Boundary-Layer Meteorol.*, **91**, 109-125.
- Sundqvist, H., 1993: Inclusion of ice-phase of hydrometeors in cloud parameterization for mesoscale and largescale models. *Contr. Atm. Phys.*, **66**, 137-147.
- Stull, R.B., 1988: *An introduction to boundary layer meteorology*. Kluwer Academic Publishers, Dordrecht, 666pp.
- Tamayo, J., 1994: *Relación entre las precipitaciones y el Índice de Vegetación Diferencia Normalizada (NDVI) en áreas en riesgo de desertificación. Aplicación a la zona de estudio en el proyecto EFEDA*. Ph.D. Thesis, University of Valencia.
- Tennekes, H., 1973: A model for the dynamics of the inversion above a convective boundary layer. *J. Atmos. Sci.*, **30**, 558-567.
- Tennekes, H., and A.G.M. Driedonks, 1981: Basic entrainment equations for the atmospheric boundary layer. *Boundary-Layer Meteorol.*, **20**, 515-531.
- Tiedtke, M., 1989: A comprehensive massflux scheme for cumulus parameterization in large-scale models. *Mon. Wea. Rev.*, **117**, 1779-1800.
- Tiedtke, M., 1993: Representation of clouds in large-scale models. *Mon. Wea. Rev.*, **121**, 3040-3061.
- Tjernström, M., and A.-S. Smedman, 1993: The vertical turbulence structure of the coastal marine atmospheric boundary layer. *J. Geophys. Res.*, **98**, 4809-4826.
- Trenberth, K.E., and C.J. Guillemot, 1998: Evaluation of the atmospheric moisture and hydrological cycles in the NCEP/NCAR reanalyses. *Climate Dynamics*, **14**, 213-231.
- Unden, P., and coauthors, 2002: *The HIRLAM model (version 5.2)*. HIRLAM-5 Project. SMHI. [Available from Per Unden, SMHI, S-601 76 Norrköping, Sweden].
- Uppala, S., 1997: *Observing System Performance in ERA*. ECMWF Re-Analysis Project Report Series, 3. 261 pp.
- USGS, 1999: Global 30 Arc-second Elevation Dataset. <http://edcwww.cr.usgs.gov/products/elevation/gtopo30.html>.
- Vachalek, R.E., 1987: *Case studies of divergence and vertical velocities calculated using different sensing systems*. M.Sc. Thesis, University of Wisconsin-Madison. 176 pp.
- van den Hurk, B.J.J.M., 1996: *Sparse canopy parameterizations for meteorological models*. Ph.D. thesis, Wageningen Agricultural University, 270 pp.
- van den Hurk, B.J.J.M., and A.A.M. Holtslag, 1997: On the bulk parameterization of surface fluxes for various conditions and parameter ranges. *Boundary-Layer Meteorol.*, **82**, 119-134.
- van den Hurk, B.J.J.M., P. Viterbo, A.C.M. Beljaars, and A.K. Betts, 2000: *Offline validation of the ERA40 surface scheme*. ECMWF Technical Memorandum 295, 42 pp.
- Vesperini, M., 1998: Humidity in the ECMWF model: Monitoring of operational analyses and forecasts using SSM/I observations. *Q.J.R. Meteorol. Soc.*, **124**, 1313-1327.
- Vickers, D., and L. Mahrt, 1997: Quality control and flux sampling problems for tower and aircraft data. *J. Atmos. Oceanic Technol.*, **14**, 512-526.
- Viterbo, P., 1996: *The Representation of Surface Processes in General Circulation Models*. Ph.D. thesis, University of Lisbon. 201 pp.

- Viterbo, P., and A.C.M. Beljaars, 1995: A new land surface parameterization scheme in the ECMWF model and its validation. *J. Climate*, **8**, 2716-2748.
- Wendling, P., R. Wendling, W. Renger, D.S. Covert, J. Heintzenberg, and P. Mörl, 1985: Calculated radiative effects of arctic haze during a pollution episode in spring 1983 based on ground based and airborne measurements. *Atmos. Environ.*, **19**, 2181-2193.
- Wieringa, J., 1986: Roughness-dependent geographical interpolation of surface wind speed averages. *Quart. J. Roy. Meteorol. Soc.*, **112**, 867-889.
- Wittmeyer, I.L., and T.H. Vonder Haar, 1994: Analysis of the global ISCCP TOVS water vapor climatology. *J. Climate*, **7**, 325-333.
- Wood, E.F., and V. Lakshmi, 1993: Scaling water and energy fluxes in climate systems: Three land-atmosphere modeling experiments. *J. Climate*, **6**, 839-857.
- Wood, E.F., M. Sivaplan, K.J. Beven, and L. Band, 1988: Effects of spatial variability and scale with implications to hydrologic modeling. *J. Hydrol.*, **102**, 29-47.
- Wood, N., and P.J. Mason, 1991: The influence of static stability on the effective roughness for momentum and heat transfer. *Quart. J. Roy. Meteorol. Soc.*, **117**, 1025-1056.
- Wukelic, G.E., D.E. Gibbons, L.M. Martucci, and H.P. Foote, 1989: Radiometric calibration of Landsat thematic mapper thermal band. *Remote Sens. Environ.*, **28**, 339-347.
- Yates, D.N., F. Chen, M.A. LeMone, R. Qualls, S.P. Oncley, R.L. Grossman, and E.L. Brandes, 2001: A CASES dataset for analyzing and parameterizing the effects of land-surface heterogeneity on area-averaged surface heat fluxes. *J. Appl. Meteorol.*, **40**, 921-937.
- Yucel, I., W.J. Shuttleworth, and J. Washburne, 1998: Evaluating NCEP Eta Model-derived data against observations. *Mon. Wea. Rev.*, **126**, 1977-1991.
- Zipser, E.J., and R.H. Johnson, 1998: Systematic errors in radiosonde humidities: A global problem? *Proc. 10th Symposium on Measurements, Observations, and Instrumentation*, Phoenix, AZ, Amer. Meteorol. Society, 72-73.

Samenvatting en doelstelling

Het aardoppervlak bestaat voor 35% uit land. De processen boven dit landoppervlak bepalen in belangrijke mate de forcering van weer en klimaat en zijn van belang voor een duurzaam gebruik van natuurlijke hulpbronnen.

De heterogeniteit van het landoppervlak en de invloed daarvan op atmosferische grenslaag processen staat al tientallen jaren aanzienlijk in de belangstelling. Internationaal gecoördineerd onderzoek op dit gebied richt zich al vele jaren op landoppervlak-georiënteerde experimenten (LSEs) (Feddes et al., 1998; Jochum et al., 2000), waarbij belangrijke instrumentaria betrokken worden m.b.t. grond, luchtvaart en satelliet-gerelateerde waarnemingssystemen. De drijvende krachten achter dit type onderzoek waren aan de ene kant de mondiale weer- en klimaatmodellereurs (op zoek naar verbeterde en gekalibreerde land-oppervlakte parameters) en aan de andere kant de remote-sensing aanhangers (op zoek naar kalibratie van satelliet-waarnemingssystemen en algoritmes om land-oppervlakte parameters af te leiden).

De algemene context van dit proefschrift wordt gevormd door één van de grootste land-oppervlakte experimenten: EFEDA. Het Europese experiment werd gedurende 1991-1994 uitgevoerd in een semi-aride gebied in Spanje, dat door verwoestijning bedreigd wordt (Bolle et al., 1993). Het vult een belangrijk hiaat op in het bestaande LSE-framework, door gebruik te maken van een uniek gebied met een typisch Mediterraan heterogeen landgebruik. Daarbij komt ook nog eens de extra complexiteit als gevolg van de aanwezigheid van bergen en als gevolg van de niet-lokale invloed van Mediterrane zeewinden die regelmatig het binnenland binnendringen.

Het gebied van het EFEDA-experiment is gesitueerd op het hooggelegen plateau van Castilië in het zuidoostelijk deel van Spanje op een gemiddelde hoogte van 700 m boven zeeniveau. Het is een semi-aride gebied met heterogeen landgebruik, omgeven door bergen. Bovendien zijn in het gebied regionaal verschillende grenslagen en inhomogeen verdeelde nattere gebieden/percelen geobserveerd.

De doelstelling van het huidige werk wordt feitelijk bepaald door EFEDA vanuit een schaal-perspectief te bekijken. Als zodanig poogt dit werk een analyse te geven van de relevante processen en de relevante schalen alsmede de implicaties daarvan te onderzoeken m.b.t. parameterizatie en aggregatie van fluxen, door gebruik te maken van de zeer uitgebreide waarnemings-dataset. Daarnaast worden deze resultaten gebruikt, om de prestaties van numerieke weermodellen te evalueren alsmede de implicaties daarvan op atmosferische correctieprocedures, welke gebruikt worden bij de afleiding van bio-geofysische parameters uit optische satellietmetingen. Daarbij is het inherente doel om de hele weg te volgen: startende vanuit de basisprocessen tot en met de uiteindelijke praktische toepassingen.

Hoofdstuk 2 geeft een beschrijving van de waarnemingen. De EFEDA-dataset die in dit werk gebruikt is bevat onder meer waarnemingen van oppervlaktefluxstations, vliegtuigen, en radiosondes, welke verzameld zijn door meer dan 30 onderzoeksgroepen. Daar waar nodig is enige vorm van homogenisatie toegepast op de metingen. Gebaseerd op de oppervlaktewaarnemingen boven de "super-terreinen", hebben Linder et al. (1996) een gestandaardiseerde dataset ontwikkeld voor elk van de vier belangrijkste vegetatieklassen. Deze zijn hier gebruikt om de verschillende gebiedsaggregaties af te kunnen leiden. De beschikbaarheid van vliegtuigwaarnemingen geeft toegang tot informatie over ruimtelijke variabiliteit en regionale schalen. Hier is vooral de DLR Falcon vliegtuig-dataset gebruikt. Door uitgebreide kwaliteitscontrole en door fluxberekeningen toe te passen, zijn deze data geschikt gemaakt voor verdere analyse. Voor vier verschillende foutenbronnen zijn de afzonderlijke effecten op de uiteindelijke fouten in de turbulente fluxen afgeschat en dat dan vervolgens voor elke afzonderlijke "flight-track". Dit is gedaan om zeker te weten dat er voldoende "sampling" is (flight-tracks lang genoeg), alsmede om de mate van niet-stationariteit van de gemeten tracks te kunnen afschatten.

Op vaste tijdstippen zijn hoge-resolutie-radiosondes gelanceerd op de Tomelloso and Barrax "supersites". De oorspronkelijk 'sounding-datasets' (Bessemoulin, persoonlijke mededeling;

Kalthoff, persoonlijke mededeling) zijn gebruikt nadat eerst homogenisatie is toegepast, zodat gelijkmatig verdeelde drukintervallen resteerden.

Een omlaag gerichte nabij-infrarood Differentieel Absorptie Lidar (DIAL) aan boord van de DLR Falcon verschaft informatie over de aërosol "backscatter" en waterdampvelden in en boven de atmosferische grenslaag (ABL).

Uitgaande van de synoptische situatie gedurende de experimentele periode van 1-30 juni 1991, zijn de data ruwweg onderverdeeld in twee categorieën nl.: "anti-cyclonale" en "niet stationaire" condities. De anticyclonale compositie (van 22 gevallen) blijkt goed gerepresenteerd te worden door de dag van 23 juni, die daarom de focus zal krijgen in verdere case-studies.

In **hoofdstuk 3** onderzoeken we de fysische processen die bijdragen aan warmte en vochttransport in het EFEDA gebied door een budget-studie van de atmosferische grenslaag. Op relatief korte geografische afstand (80 km) tussen de twee belangrijkste supersites zijn gemengde lagen met verschillende karakteristieken waargenomen. Vocht speelt hierbij de sleutelrol. Het Tomelloso terrein is een extensief wijng gebied, representatief voor semi-aride omstandigheden, waarbij de totale oppervlakte-energiebalans voornamelijk bepaald wordt door de voelbare warmteflux. Het Barrax- terrein wordt daarnaast gekarakteriseerd door vochttransport afkomstig van twee bronnen: één vanuit de bodem door irrigatie en één vanuit de lucht welke aangevoerd wordt door de Mediterrane zeewind die vaak 's middags het binnenland binnendringt. Derhalve is de atmosferische grenslaag (AGL) bij Barrax in het algemeen vochtiger, iets koeler en minder diep dan in Tomelloso.

Onze budget-analyse is gebaseerd op een synergie voortkomend uit een uitgebreide observatie-dataset en een eenvoudig gekoppeld vegetatie-atmosferische menglaag model. De observatieset bestaat uit een netwerk van micrometeorologische stations, radiosondes, een fluxvliegtuig en een waterdamp differential absorption lidar (DIAL) welke vanuit de lucht opereert. In het bijzonder wordt de vliegtuig-dataset genoemd met daarin elk van de vier stralingsfluxcomponenten, waardoor de volledige stralingsdivergentie bepaald kan worden. Doordat de flux-observaties van vocht en warmte voorzien in een hoge 'sampling-frequentie' kan een analyse gemaakt worden van de verticale fluxdivergenties, te gebruiken in een menglaagmodel-framework.

De horizontale dwarsdoorsneden en verticale vochtigheidsprofielen welke zijn afgeleid uit de DIAL- en radiosonde-observaties laten zien dat de 'residual layer' (RL) boven beide locaties gekarakteriseerd kunnen worden door een gelaagde vochtigheidsstructuur. De vocht-entrainment-fluxen variëren qua grootte en qua teken gedurende een groot gedeelte van de dagelijkse cyclus. Het is een uitdagende taak om de verticale flux-divergentie van vocht te bepalen onder deze omstandigheden.

De opwarming van de atmosferische menglaag (ML) wordt gebalanceerd door een combinatie van fluxdivergentie (turbulente warmteflux) en de stralingsdivergentie. Hoewel de absolute waarde van de stralingsdivergentie weinig variatie vertoont in de tijd en tussen de meetlocaties onderling, is haar relatieve aandeel groter bij Barrax en tegen het einde van de middag. De orde van grootte van de stralingsdivergentie is consistent met de hoge aërosolbelasting en de geringe visibiliteit in dit gebied gedurende het grootste deel van de tijd. Temperatuuradvectie blijkt gering te zijn en de sluiting van de warmtebudgetten is behoorlijk. Bij deze sluiting is gebruik gemaakt van de volgende entrainmentparameters: 0,3 (voor Tomelloso) en 0.16 (voor Barrax), in beide gevallen bepaald uit vliegtuiggegevens.

De ontwikkeling van vochtbudgetten over de observatieperiode vertoont een zeer complex beeld. Dit hangt samen met de inhomogene vochtstructuur in de RL, waarbij de lokale vochtgradiënten wisselend van teken zijn. Voor beide locaties geldt dat de menglaag droog is, zolang ze nog bezig is om de nachtelijke grenslaag te eroderen. Zodra de menglaag echter in contact komt met de positieve vochtgradiënten in de RL, wordt de entrainmentflux negatief, totdat deze vochtigere lucht volledig 'ge-entrained' is. Deze bevochtigingsgebeurtenis rond het middaguur houdt slechts korte tijd aan (1-2 uur), totdat de ML weer van bovenaf begint uit te drogen. Een dergelijke sequentie is duidelijk waargenomen in vier verschillende budget-tijdreeksen bij Barrax. In Tomelloso is het effect als zodanig waarschijnlijk niet herkenbaar in

de data, maar komt het wel duidelijk naar voren in de berekeningen met het slab-model. Derhalve laten de vochtbudgetten duidelijk zien dat de niet-grenslaag-schalen het vochttransport beïnvloeden, hetgeen ook terugkomt in het gebrek aan simpele entrainmentparameterizaties als het gaat om vochtfluxen. Er is een eenvoudig model gebruikt om de divergentie van de vochtflux af te schatten. Het model relateert de Bowen ratio aan het aardoppervlak aan die ter hoogte van de inversie. De Bowen ratio op de inversiehoogte wordt daarbij gegenereerd door advectie (als in het geval van een niet-homogene RL) en waarmee de entrainmentfluxen niet uniek zijn gerelateerd aan de atmosferische grenslaagprocessen/schalen. Om goede fluxschattingen te kunnen maken, zijn nauwkeurige verticale vochtprofielen met een hoge resolutie vereist. Het gekoppelde vegetatie-menglaag(slab)model blijkt een waardevol hulpmiddel te zijn in een dergelijk complexe omgeving, wanneer het regelmatig wordt gevoed met geactualiseerde RL gradiënten.

Op beide locaties wordt deze typische niet-locale karakteristiek van vochttransport waargenomen. Op elk van de afzonderlijke locaties kan uitdroging of bevochtiging van de ML zich anders ontwikkelen, afhankelijk van het relatieve belang van de oppervlaktefluxen t.o.v. de entrainmentflux. Met het simpele model is bevestigd dat het potentiëel voor vochtfluxdivergentie en de samenhangende bevochtiging van de ML groter is bij Barrax , omdat de irrigatie daar de oppervlakteverdamming verhoogt.

Hoofdstuk 4 bepaalt de schalen van het landschap en van de atmosferische grenslaag en onderzoekt de implicaties hiervan voor fluxparameterizaties. De schalen worden bestudeerd aan de hand van het framework van Mahrt (1996). We hebben een aantal oppervlakte-heterogeniteitskenmerken geïdentificeerd, welke de schaalafhankelijkheid van fluxparameterizaties in EFEDA-achtige gebieden conditioneren. In de aanwezigheid van subgrid snelheidsfluctuaties als gevolg van mesoschaal stromingen, zal de overdracht van impuls schaal-afhankelijkheid vertonen. Het warmtetransport daarentegen is niet schaalafhankelijk omdat er over het hele gebied sterke temperatuurverschillen aanwezig zijn over de scheidslijn tussen land en zee. De transportschalen m.b.t. vocht zijn verbonden aan het verzadigingsdeficit, dat zich kenmerkt door een sterke mate van inhomogeniteit, in het bijzonder wanneer gebieden met schaarse vegetatie direct grenzen aan geïrrigeerde velden.

Hoofdstuk 5 is gewijd aan regionale fluxen en flux-aggregatie. Het doel is om gebiedsgemiddelde fluxen te verkrijgen voor een heel scala aan gebieden, het EFEDA gebied en de vier relevante HIRLAM grid-cellen inbegrepen. Tegen de achtergrond van de beschikbare data worden verschillende methoden van aanpak worden besproken. Door een gewogen middeling toe te passen kunnen continue tijdreeksen van 'geobserveerde' grid-gemiddelden worden geconstrueerd uit de afzonderlijke oppervlakte waarnemingsreeksen. Tevens is een vergelijkingstest uitgevoerd om vast te stellen in hoeverre zo'n gewogen mast-gemiddelde representatief is en, indien nodig, of er nog correcties dan wel bijstellingen nodig zijn (bv. voor niet-opgeloste schalen/processen). Flux observaties vanuit de lucht geven informatie in de vorm van een 'helikopterview' op bepaalde tijdstippen en op bepaalde dagen. Als zodanig bieden zij een onafhankelijke referentie welke vergelijking mogelijk maakt met name rondom het middaguur en op onbewolkte dagen. Vanuit een ruimtelijk perspectief gezien, wordt een alternatief geboden door het gebruik van radiosondes. Radiosondes kunnen nl. voorzien in continue regionale semi-geobserveerde fluxreeksen (overdag), wanneer zij worden gecombineerd met het simpele ML model-framework. Tenslotte wordt de vergelijkingsdataset compleet gemaakt door data afkomstig van een gevalideerd mesoschaalmodel (bv. Noilhan et al., 1997).

Binnen een bepaalde onzekerheidsmarge zijn de resultaten van de verschillende methoden in overeenstemming met elkaar. Op bepaalde dagen zijn de schattingen van de sensibele warmtestroom vanuit de lucht aan de lage kant, hetgeen kan duiden op een onderschatting van de 'low-level' flux divergentie ofwel op een overschatting van de dikte van de ML. De latente warmtefluxen van het PERIDOT mesoschaal model zijn constant hoog, hetgeen, naar we veronderstellen, waarschijnlijk veroorzaakt wordt door een voorkeur voor natte gebieden in de landsgebruik database. De hoge gevoeligheid van de gebiedsgeaggregeerde fluxen m.b.t. de fractie geïrrigeerd land, laat zien dat een correcte identificatie van deze fractie noodzakelijk is (zowel qua landgebruikclassificatie als in de afbakening van het gebied). Zo nu en dan worden er grote vochtfluxen op mesoschaal waargenomen, hetgeen consistent zou kunnen zijn met de

inhomogene vochtvelden, gemeten met de lidar vanuit de lucht. We speculeren hierbij dat deze inhomogene vochtvelden gegenereerd worden door topografisch gestuurde mesoschaal circulaties, waarbij het vocht uiteindelijk afkomstig is van irrigatievelden en/of wordt aangevoerd door de zeewind. Berekeningen met een mesoschaal model (e.g. Miao et al., 2002) bevestigen de invloed van topografie op dergelijke mesoschaalcirculaties.

Vergelijking van de fluxen op grid schaal bevestigen dat de geconsolideerde dataset van de grid-schaal fluxen in EFEDA inderdaad berekend kan worden op basis van een gewogen gemiddelde van de afzonderlijke oppervlakteflux-waarnemingen. Aanpassingen om rekening te houden met de beperkte 'waarnemingsblik' van de afzonderlijke waarnemingen, zoals uitgevoerd bij andere veldexperimenten, bleek in dit geval niet noodzakelijk. Aanpassingen zullen echter wel noodzakelijk zijn om rekening te houden met de timing in het groeiseizoen, de timing in de irrigatiecyclus en (in mindere mate) om rekening te houden met de relatieve bedekkingsgraad van bewolking.

Wanneer de fractie geïrrigeerd land significant groot is, dan hangt de gebiedsgeaggregeerde flux (in het bijzonder van vocht) sterk af van de locatie van de gebiedsgrenzen. Hoewel dit op zichzelf niet verrassend is, laat het wel duidelijk zien dat het belangrijk is rekening te houden met het mozaïekpatroon van geïrrigeerde gebieden bij toepassing van oppervlakteschema's en de bijbehorende physiographische databestanden in grootschalige modellen. Daarbij is de bekwaamheid van het landgebruik-classificatiesysteem om op een juiste manier de geïrrigeerde velden en hun water status in verschillende seizoenen te identificeren een belangrijke voorvereiste. Een simpele manier om in minimale informatie over de waterstatus van een plant te voorzien, zou kunnen zijn via het onderscheid in twee afzonderlijke klassen geïrrigeerd gewas: een lente- en een zomercyclus. Een bruikbare oplossing in die richting wordt gegeven door de klassificatie-aanpak van Martínez en Calera (2001).

In **hoofdstuk 6** evalueren we het resultaat van de HIRLAM oppervlakte- en grenslaagbeschrijvingen in het EFEDA gebied. Het HIRLAM (High-Resolution Limited Area Model) systeem is een totaal numeriek weerverwachtingssysteem (NWP), inclusief de analyse van waarnemingen en een korte-termijn verwachtingsmodel. Analyse en 6-uurs verwachtingsdata van het volledig gekoppelde 3-D model zijn vergeleken met de EFEDA case-study van 23 juni 1991, welke representatief is voor een meetperiode van 22 dagen onder een hogedruksituatie.

De resultaten laten zien dat het oppervlak, de bodem en de grenslaag in het model te vochtig en ook ietsje te koud zijn over het grootste gedeelte van de dagelijkse gang. De oppervlakte-energiebalans en de straling neigen naar meer vochtige condities. Het totale plaatje van de resultaten ziet er als volgt uit, rekening houdend met prioriteiten wat betreft waargenomen discrepanties (grootte van de invloed en van de 'bias'):

Net als in elk kust-gebied en elk gebied met complexe topografie vormt de assimilatie van vocht een probleem voor het Iberische schiereiland. Dit resulteert in grote fouten (tot 50%) als het gaat om vochtprofielen in de grenslaag. De fysiografische database van het model genereert te dichte vegetatie, hetgeen leidt tot onjuiste oppervlaktefluxen en straling. Het oppervlakteschema van het model presteert goed wanneer de juiste landsgebruik-classificaties worden opgelegd. De inkomende zonnestraling wordt overschat, hetgeen het gevolg is van de aërosol-parameterisatie in het stralingsschema. Een aanpassing van de aerosol-parameters om rekening te houden met de beperkte zichtbaarheid, resulteert in een aanzienlijke fout-reductie. Een te hoog klei-percentages in het model-bodemtype kan leiden tot een te hoog vochtgehalte, dat mogelijk niet gecompenseerd kan worden in de bodemvocht assimilatieprocedure. De RL wordt onvoldoende beschreven en de bijdrage van entrainment aan de opwarming van het oppervlak en de menglaag wordt onvoldoende gereproduceerd. Dit komt door een combinatie van gebrekkige verticale resolutie in het model, welke onvoldoende is voor dit type landschap, en door tekortkomingen in de parameterisatie van verticale diffusie en entrainment. De hoge 'bias' in de netto straling is waarschijnlijk gerelateerd aan het overschot aan vocht in de atmosfeer en de onderschatting van de oppervlaktetemperatuur.

We verwachten dat een onmiddellijke verbetering in de prestatie van het model kan worden bereikt indien landgebruik en bodemclassificaties (samen met de daaraan verbonden fysiografische database) worden gebruikt welke zijn aangepast aan de Mediterrane landschappen. Hetzelfde geldt indien in het stralingsschema aërosolparameters worden

gebruikt die direct rekening houden met de typische hogere aërosolbelasting in aride en semi-aride gebieden. Om tot een adequate classificatie van landsgebruik voor Mediterrane landschappen te komen, dient rekening te worden gehouden met zowel de schaars-verdeelde droge vegetatie als voor de twee klassen geïrrigeerde gewassen (lente- en zomer-geïrrigeerd), waarbij de fysiografische database de verschillen in hun fenologische cycli verdisconteert. Zoals eerder genoemd, biedt de benadering van Martínez en Calera (2001) een praktische oplossing voor dit probleem.

Hoofdstuk 7 introduceert een praktische toepassing van de in de voorgaande hoofdstukken verkregen resultaten. De afschatting van biogeofysische parameters van het landoppervlak door gebruik te maken van remote sensing satellietgegevens vereist een correctie voor de signaalafzwakking veroorzaakt door de aanwezigheid atmosferische gascomponenten, in het bijzonder waterdamp. Als gevolg hiervan zijn hoge kwaliteit waterdampvelden vereist als inputdata, om radiometrische correctieschema's te kunnen toepassen (zoals bv. MODTRAN of 6S). Het modelresultaat m.b.t. de waterdampdata bepaald uit de belangrijkste beschikbare databronnen is geëvalueerd. Daarnaast is de invloed van fouten in de afschatting van biogeofysische parameters op het resultaat onderzocht. De fouten die geïntroduceerd worden door de vochtassimilatieprocedure binnen de NWP modellen, kunnen leiden tot significante fouten in, bv. de globale straling (10%) en in de oppervlakte temperatuur (20%). Daarom wordt aanbevolen om, indien mogelijk, toevlucht te nemen tot operationele radiosonde data en om voorzichtigheid te betrachten met het gebruik van 4DDA data van NWP modellen. Door voortplanting van de fouten in de toepassing van irrigatieschema's, verwachten we dat fouten in de dagelijkse of wekelijkse waterbehoefte van het gewas kunnen oplopen tot zo'n 20%.

Het is een uitdaging voor de komende jaren om op globale schaal hoge-kwaliteit 4D-datasets te ontwikkelen, met name in relatie tot landoppervlak en atmosferische grenslagen. Dit tezamen met eenvoudige hulpmiddelen en modellen om deze te gebruiken. Er is een behoefte voor dit soort datasets vanuit de grote internationale klimaatsveranderings-programma's (IGBP, WCPR, IHDP) en globale observatiesystemen (G3OS, GMES). De enige manier om dit te bereiken is sterk afhankelijk van NWP modellen en remote sensing, welke meer en meer aan elkaar gekoppeld zullen worden. In samenhang met deze datasets zullen eenvoudige modellen als in hoofdstuk 3 en 5 hun waarde behouden. Het is daarom belangrijk om vertrouwen te hebben in deze eenvoudige hulpmiddelen binnen alle grote ecosystemen en klimaten. De landoppervlakte experimenten hebben in belangrijke mate bijgedragen aan de verbetering van deze hulpmiddelen. Het huidige werk heeft geresulteerd in verschillende leidraden, die geldig zijn in de Mediterrane omgeving, welke momenteel verder ontwikkeld worden voor operationele doeleinden.

Vanuit een mondiaal perspectief, is een nieuwe set experimenten ontworpen onder auspiciën van GEWEX en diens projecten GLASS (global Land-Atmosphere System Study; Polcher et al., 2000) en GABLS (Global Atmospheric Boundary Layer Study; Holtslag, 2001). Het doel is de beschrijving van de land-atmosfeer interacties in numerieke modellen verder te verbeteren door nieuwe complexiteit- en koppelingsniveau's aan te pakken.

Op het regionale niveau, vragen veel praktische toepassingen op het gebied van duurzaam beheer van natuurlijke bronnen en rurale ontwikkeling om geavanceerde besliskundige systemen. Deze systemen dienen operationeel aangepast te zijn aan dezelfde soort 4DDA en remote-sensing data als aanvulling op de speciale 'tools' en databronnen welke aangepast zijn aan de specifieke behoefte van deze systemen. Mediterrane landbouw is een belangrijke "informatie-gebruiker" en vormt als zodanig een sociale en economische sleutelfactor. De agrariër die jaren geleden de EFEDA masten op zijn grondgebied toestond en in de toekomst zal kunnen profiteren van het geavanceerde ruimte-ondersteund irrigatie advies (Jochum and Calera, 2002) vormt daarvan misschien wel het mooiste voorbeeld, waarmee de cirkel uiteindelijk weer rond is,...

Curriculum vitae

Maria Anna Regine Jochum

Born on 29 July 1948 in Munich (Germany).

1967-1976

Higher education in physics and mathematics, Universities of Munich (Germany) and Grenoble (France).

1977-1987

Research scientist at DLR (German Aerospace Research Establishment; now: German Aerospace Centre), Oberpfaffenhofen (Germany).

1988-1997

Head of Atmospheric Instrumentation Division at DLR, Oberpfaffenhofen (Germany).

1998-2003

Ph.D. student at Wageningen University, Meteorology and Air Quality Department, Wageningen (The Netherlands).

1997-present

Founder and Managing Director of ALFAclima Asesoramiento Medioambiental, Albacete (Spain).